Atomic force microscopy-based nanoscopic studies of epoxy/boehmite nanocomposites

Vorgelegt von

M.Sc.

Media Ghasem Zadeh Khorasani

ORCID: 0000-0002-0885-8314

an der Fakultät III - Prozesswissenschaften

der Technischen Universität Berlin

zur Erlangung des akademischen Grades

Doktor der Ingenieurwissenschaften
Dr. -Ing.

genehmigte Dissertation

Promotionsausschuss:

Vorsitzender: Prof. Dr.-Ing Harald Kruggel-Emden

Gutachter: Prof. Dr.-Ing. Dietmar Auhl

Gutachter: Prof. Dr. rer. nat. Heinz Sturm

Tag der wissenschaftlichen Aussprache: 27. November 2019

Berlin 2020

Table of content

Acknowledgement

Zusammenfassung

Die Entwicklung von Leichtbauteilen aus faserverstärkten Polymerverbundwerkstoffen für die Luft- und Raumfahrt sowie die Automobilindustrie stand in den letzten Jahrzehnten im Mittelpunkt vieler Studien. Nanofüllstoffe, die den in solchen Verbundteilen verwendeten Epoxidmatrizen zugesetzt werden, führen zu einer bemerkenswerten Verbesserung der matrixdominierten Eigenschaften. Die Bildung von Interphasen zwischen anorganischen Nanofüllstoffen und Polymermatrices hat bekanntlich einen dominanten Einfluss auf die Eigenschaften des Nanokomposits. In manchen Fällen ist die Wirkung von Nanofüllstoffen auf die Eigenschaften der Matrix nicht nur auf die unmittelbare Umgebung beschränkt, sondern es kann auch zu einer weitreichenden Eigenschaftsänderung des Matrixpolymers kommen. Die Unterschätzung der Auswirkungen solcher kurz- und weitreichenden Wechselwirkungen zwischen Nanofüllstoffen und Polymermatrices auf die Eigenschaften des Nanokomposits führt zu einer Fehlinterpretation des Materialverhaltens.

In dieser Arbeit ist das Hauptziel, die Interaktion zwischen Nanofüllstoffen und der Epoxidmatrix zu verstehen, die Interphase und ihre Eigenschaften zu untersuchen und schließlich die nanoskaligen Eigenschaften mit dem makroskopischen Verhalten des Materials zu korrelieren. Aufgrund der Größenbeschränkungen verschiedener Analysemethoden ist es eine Herausforderung, die Eigenschaften von Nanofillern und deren Interphasen zu bestimmen. Diese Arbeit zeigt, dass durch den Einsatz von Rasterkraftmikroskopie-Methoden (AFM) Informationen über physikalische, chemische und mechanische Eigenschaften eines Nanokomposits im Nanometerbereich zugänglich werden und mit dem makroskopischen Verhalten korreliert werden können. Die Verwendung von hochauflösendem Intermodulations-AFM (ImAFM) führt zur Aufnahme kompletter Kraft-Weg-Kurven von jedem Pixel des gescannten Bereichs. Durch die Auswertung sowohl der berührungslosen als auch der kontaktierenden Anteile dieser Kurven erhält man neben Steifigkeitskarten auch bildgebende Messungen der elektrostatischen Kräfte und der Van-der-Waals-Kräfte, die neben den mechanischen Eigenschaften auch ergänzende Informationen über die Materialzusammensetzung liefern. Die Kelvin-Sonde Mikroskopie (SKPM) liefert Potenzialkarten, die mit den chemischen Strukturen des heterogenen Materials korrelieren. Darüber hinaus wird die AFM-basierte nano-Infrarotspektroskopie (AFM-IR) eingesetzt, um die chemische Struktur der Interphasen und der heterogenen Phasen der Matrix zu untersuchen.

Im Rahmen dieser Arbeit wurden Böhmit-Nanopartikel (BNPs) als Nanofüllstoff für die Epoxidmatrix ausgewählt. Die Ergebnisse dieser Dissertation belegen die Existenz von kurz- und weitreichenden Wechselwirkungen der BNPs im Epoxid. Es wurde beobachtet, dass BNPs einen weitreichenden Einfluss auf die Vernetzung des Epoxids haben und dadurch eine versteifende Wirkung auf das Epoxid haben. Der Kurzreichende Einfluss auf die Interphase zwischen BNPs und Epoxid ist dem entgegengesetzt und die Interphase ist viel weicher als das Epoxid selbst. BNPs beeinflussen die Netzwerkstruktur der Matrix, indem sie die Vernetzungsdichte verringern. Untersuchungen an Grenzflächenmodellsystemen zeigen die Bildung chemischer Interphasen, die mehr als eine Größenordnung größer sind als mechanische Interphasen bei kurzreichenden Wechselwirkungen. Es konnte weiterhin gezeigt werden, dass eine solche weitreichende chemische und strukturelle Veränderung des Epoxids das Ergebnis einer präferentiellen Absorption des Härters am BNP ist. Diese führt zu einer Störung des stöchiometrischen Verhältnisses zwischen Epoxid und Härter, einer Veränderung der Chemie der Aushärtung und damit zur Modifizierung der makroskopischen Eigenschaften der ausgehärteten Matrix.

Abstract

Development of lightweight parts made of fiber-reinforced polymer composites for aerospace and automotive industry has been focus of many studies over the past several decades. Nanofillers added to the epoxy matrices used in such composite parts results in remarkable improvement of matrix-dominated properties. Formation of interphases between inorganic nanofillers and polymer matrices is usually known to have a dominant impact on the properties of the nanocomposite. Sometimes, the effect of nanofillers on the properties of the matrix is not only limited to the immediate vicinities, but a long-range property alteration of the bulk polymer may occur. Underestimating the effect of such short- and long-range interactions between nanofillers and polymer matrices on properties on the nanocomposite, result in misprediction of material behavior.

In this thesis the main goal is to understand the interaction between nanofillers and the epoxy matrix, to probe the interphase and its properties and eventually to correlate the nanoscale properties to the macroscopic behavior of the material. Due to size limitations of various analytical methods it is difficult to determine properties of nanofillers and their interphases. This thesis shows that by using multiple atomic force microscopy (AFM) methods, information about physical, chemical and mechanical properties of the nanocomposite at nanometer scale are provided and can be correlated to the macroscopic behavior. Using high resolution intermodulation AFM (ImAFM) results in recording complete force-distance curves from each pixel of the scanned area. By evaluation of both non-contact and contact regions of these curves, maps of electrostatic and van der Waals forces are obtained in addition to stiffness maps, providing complementary information about material composition in addition to the mechanical properties. Scanning Kelvin probe microscopy (SKPM) provides us with maps of potential which correlate to chemical structures of the heterogeneous material. Furthermore, infrared spectroscopy AFM (AFM-IR) is used to investigate the chemical structure of the interphase and heterogenous phases of the bulk matrix.

Within the scope of this work, boehmite nanoparticles (BNPs) were selected as nanofillers for the epoxy matrix. The results of this dissertation prove the existence of both short- and long-range interactions of BNPs in epoxy. It was observed that BNPs have a long-range stiffening effect on the bulk epoxy. The short-range influence on the interphase between BNPs and epoxy shows the opposite behavior; the interphase is much softer than the epoxy itself. BNPs affect the network structure of bulk matrix by lowering the crosslinking density.

Investigations on interfacial model systems demonstrate the formation of a long-range chemical interphase more than one order of magnitude larger than the short-range mechanical interphase. In the end, it is demonstrated that both the soft interphase and long-range chemical alteration of epoxy result from the preferential absorption of the curing agent (anhydride) towards BNPs. This leads to disturbance of the epoxy-hardener stoichiometric ratio, alteration of curing mechanisms, and modification of bulk properties of the cured matrix.

List of Publications

This thesis is based on four publications listed below:

Paper I   Fankhänel, Johannes; Silbernagl, Dorothee; **Ghasem Zadeh Khorasani, Media**; Daum, Benedikt; Kempe, Andreas; Sturm, Heinz and Rolfes, Raimund. "Mechanical properties of boehmite evaluated by atomic force microscopy experiments and molecular dynamic finite element simulations." *Journal of Nanomaterials* 2016 (2016)

Paper II   **Ghasem Zadeh Khorasani, Media**., Silbernagl, D., Szymoniak, P., Hodoroaba, V. D., & Sturm, H. "The effect of boehmite nanoparticles (γ-AlOOH) on nanomechanical and thermomechanical properties correlated to crosslinking density of epoxy". *Polymer* 164 (2019): 174-182

Paper III **Ghasem Zadeh Khorasani, Media**; Silbernagl, Dorothee; Platz, Daniel; Sturm, Heinz. 2019. "Insights into Nano-Scale Physical and Mechanical Properties of Epoxy/Boehmite Nanocomposite Using Different AFM Modes." *Polymers* 11, 2 (2019): 235

Paper IV   **Ghasem Zadeh Khorasani, Media**; Elert, Anna-Maria; Hodoroaba, Vasile-Dan; Agudo Jácome, Leonardo; Altmann, Korinna; Silbernagl, Dorothee; Sturm, Heinz. "Short- and Long-Range Mechanical and Chemical Interphases Caused by Interaction of Boehmite (γ-AlOOH) with Anhydride-Cured Epoxy Resins." *Nanomaterials* 9.6 (2019): 853

Conference contribution

The content of this thesis has been presented in form of poster and oral presentations in conferences listed below:

Poster presentations

- **M. Ghasem Zadeh Khorasani**, D. Silbernagl, H. Sturm. *Long-Range influence of boehmite nanoparticles on the nanomechanics of epoxy matrix Used in Carbon-Fiber Composites,* The 5th International Symposium Frontiers in Polymer Science 2017 (Sevilla, Spain)

- **M. Ghasem Zadeh Khorasani**, D. Silbernagl, H. Sturm. *Studies on interphase formation of cured epoxy resin near boehmite surface,* ICCS20 – 20th International Conference on Composite Structures (Paris, France)

- **M. Ghasem Zadeh Khorasani**, D. Silbernagl, H. Sturm. *Mechanical and chemical alteration of polymer matrix induced by nanoparticles in epoxy-boehmite nanocomposites,* HYMA 6th International Conference on Multifunctional, Hybrid and Nanomaterials 2019 (Sitges, Spain)

Oral Presentations

- **M. Ghasem Zadeh Khorasani**, D. Silbernagl, H. Sturm. *Application of Scanning Kelvin Probe Microscopy together with Intermodulation Force Microscopy for probing boehmite nanoparticles in polymer nanocomposites*, EUROMAT 2017 (Thessaloniki, Greece)

- **M. Ghasem Zadeh Khorasani**, D. Silbernagl, P. Szymoniak, H. Sturm, A. Schönhals *Effect of boehmite nanoparticles on the mechanical properties and network architecture of epoxy* DPG- Deutsche Physikalische Gesellschaft 2018 (Berlin, Germany)

- **M. Ghasem Zadeh Khorasani**, D. Silbernagl, H. Sturm. *Interphase formation of cured epoxy resin near boehmite surface* Junior EUROMAT 2018 (Budapest, Hungary)

- **M. Ghasem Zadeh Khorasani**, A. Elert, D. Silbernagl, H. Sturm *Combination of advanced atomic force microscopy methods to investigate mechanical and chemical interphases in epoxy-boehmite nanocomposites.* EUROMAT 2019 (Stockholm, Sweden)

Introduction

The demand for developing optimized materials with customized mechanical, thermal electrical and optical properties is tremendously increasing. In many industries such as aerospace and automotive, the requirement is to develop material with high-stiffness and toughness which weigh as light as possible. These contradictory requirements can only be achieved by producing composite materials which are made by combination of two or more components with oppositional properties. Composite materials are abundantly used by nature in biological structures like sea shells and bones, providing high mechanical performances. These biological structures mainly consist of stiff components with high aspect ratio such as long molecules, fibers and platelets imbedded in a soft polymeric matrix, providing high mechanical performance which inspires numbers of bio-inspired structure developments [1].

Followed by the discovery of carbon fibers in 1964 [2], a new class composite material named as carbon fiber-reinforced polymers (CFRPs) was developed in which woven-carbon fibers are embedded in a polymeric matrix which function as a binding material. This class of composites has found a broad range of applications in aircraft industry, allowing them to displace conventional material such as aluminum and aluminum titanium alloys [3]. More recent development of CFRPs demonstrated that this class of material can be up to 70 percent lighter than steel [4] which broadened the potential application of CFRPs in aerospace, wind energy, automotive and many other industries. Meanwhile the carbon-fibers with diameter of 5-10 microns and Young's modulus of up to approx. 1000 GPa provide the remarkable stiffness and tensile strength of the composite, the polymer matrix enables easy fabrication and shaping of complex designs. Besides the rigidity and tensile strength of the composite which are mainly dominated by fiber properties, the compressive strength, dimensional stability, fracture toughness, impact strength and fatigue are dominated by the properties of matrix and fiber-matrix interphase. Therefore, choosing the right material as matrix in CFRPs is crucial for increasing the performance of the composite.

A variety of polymers can be used in CFRPs, from thermoplastic polymers such as polypropylene, Nylon 6.6, PMMA and PEEK to thermoset polymers as epoxy, polyester, phenolic and polyimide resins. [3, 5]. Thermosetting epoxies are more conventionally used in CFRPs with applications in aerospace, due to their high temperature stability, high stiffness and tensile strength. However thermosetting epoxies are not as damage tolerant as thermoplastics. To improve matrix dominated and interphase dominated properties of fiber

reinforced composites, nano-scale fillers (less than 100 nm in size) or simply called nanoparticles (NPs) are added to the polymer matrix. The resulting polymer nanocomposites (PNCs) have shown remarkable improvements in mechanical, thermal and electrical properties [6, 7]. Nanoparticles such as carbon nanotubes, graphene and clay have shown significant improvements in tensile strength and stiffness compared to the unfilled material [7-9]. Increase of damage tolerance and crack resistance of the matrix are among the most important mechanical improvements of in the polymer matrices after inclusion of nanoparticles. This is commonly related to energy absorbing and dissipating mechanisms at the interphase.

Besides the intrinsic properties of NPs such as their size, morphology, Young's modulus, compositional structure, the effectiveness of NPs in property improvement of PNCs strongly depends on their chemical and physical interactions with the polymer matrix. For instance, when the adhesion between particles and polymer is poor, particles tend to form large agglomerates which result in formation of defect centers and inhomogeneous dispersion in the polymer matrix. Homogeneous dispersion and high adhesion at the interphase of nanoparticles and polymers can be achieved by surface functionalization of the nanoparticles. Depending on the NPs, surface functionalization adds costs to the production and may make the PNCs unaffordable for many applications. Moreover, strong bonding between NPs and polymer can cost the toughness of the composite. Therefore, it is necessary to find the balance based on the application requirements. In **Chapter 1**, different theoretical aspects of PNC characteristics and interphase formation between organic and inorganic phases are introduced**.** For an in-depth investigation of the interactions between nanofillers and polymers and their effect on the mechanics of the composites, mechanical properties of each phase (matrix, nanofiller and the interphase) is requires to be investigated at the nanoscopic level. A variety of atomic force microscopy (AFM) methods can be used to describe not only the surface structure but also the composition and properties, especially the mechanical properties. In **Chapter 2**, AFM and its various modes and approaches are described as main characterization methods for PNCs in this dissertation.

Boehmite nanoparticles (BNPs) have recently received a great deal of interest after being used as the nanofiller in several PNCs [10]. Low production costs, high dispersibility in most of polymeric matrices with or without surface modification, large specific surface area makes BNPs a suitable nanofiller in variety of polymers especially thermosetting resins. Recent studies on the effect of BNPs on epoxies used as matrix for CFRPs showed a remarkable

enhancement of mechanical properties including tensile and flexural strength as well as fracture toughness [11-16]. It was also observed that inclusion of BNPs in epoxy matrix in CFRP samples results in stronger adhesion of carbon fiber to epoxy matrix and a higher energy dissipation at the interphase. In **Chapter 3** a broad literature review of similar composite systems and their characteristics as well as different hypotheses regarding the interaction mechanisms between epoxy and BNP are presented. Some of these hypotheses assume that boehmite as an inorganic crystal has a relatively high modulus compared to epoxy and this is the key factor of reinforcement and property enhancement of BNPs in epoxy nanocomposites. However due to the lack of reliable experimental measurements on the Young's modulus of boehmite, the first goal of this work is to investigate the mechanical properties of pure boehmite experimentally by means of atomic force microscopy (AFM)-based force measurement methods. The results of this investigation which is part of the **Paper I** (Fankhänel, J., Dorothee Silbernagl, M. Ghasem Zadeh Khorasani, B. Daum, A. Kempe, Heinz Sturm, and R. Rolfes. "Mechanical properties of boehmite evaluated by atomic force microscopy experiments and molecular dynamic finite element simulations." *Journal of Nanomaterials* 2016 (2016)), presented in **Chapter 4**, shows over one order of magnitude difference between the previously assumed Young's modulus values and the experimental one. This new finding is the basis of hypotheses for the reinforcement mechanism and interaction between BNPs and epoxy matrix which are further proposed and investigated in further chapters.

Chapter 5 is based on **Paper II** (Ghasem Zadeh Khorasani, M., Silbernagl, D., Szymoniak, P., Hodoroaba, V. D., and Sturm, H. "The effect of boehmite nanoparticles (γ-AlOOH) on nanomechanical and thermomechanical properties correlated to crosslinking density of epoxy". *Polymer* 164 (2019): 174-182). The focus here is probing the local alteration of bulk epoxy in epoxy/BNP nanocomposite samples as result of interacting with BNPs. In this chapter the shortcomings of AFM force-distance curves in probing samples with heterogeneities in scales of few ten nanometers are demonstrated and the Intermodulation AFM (ImAFM) which is a dynamic AFM force measurement method is introduced as the suitable method to probe local mechanical properties. It was also hypothesized that the interaction of BNPs with epoxy during the curing process results in alteration of the network architecture and crosslink density of the epoxy matrix. This hypothesis is studied by systematic dynamic mechanical thermal analysis (DMTA) on epoxy/BNP samples with different particle mass fractions.

Chapter 6 is based on **Paper III** (Ghasem Zadeh Khorasani, Media; Silbernagl, Dorothee; Platz, Daniel; Sturm, Heinz. 2019. "Insights into Nano-Scale Physical and Mechanical Properties of Epoxy/Boehmite Nanocomposite Using Different AFM Modes." *Polymers* 11, 2 (2019): 235**)**. The main goal is to probe the epoxy/BNP interphase in nanocomposite samples. In this chapter scanning Kelvin Probe microscopy (SKPM) is introduces as a suitable method to be combined with ImAFM in order to precisely locate the nanoparticles and distinguish them from the matrix and the interphase. Other information channels such as energy dissipation and work of van der Waals (W_{vdW}) forces provided with ImAFM are also used to characterize the sample. Based on the results presented in this chapter, it was hypothesized that the interaction between epoxy and BNPs has both short and long-range effects. However, the size and geometry of the nanoparticles and due to the effect of buried interphases, the long-range interphase must be preferably studied on a model sample with simplified geometry.

Chapter 7 is based on **Paper IV** (Ghasem Zadeh Khorasani, Media; Elert, Anna-Maria; Hodoroaba, Vasile-Dan; Agudo Jácome, Leonardo; Altmann, Korinna; Silbernagl, Dorothee; Sturm, Heinz. "Short- and Long-Range Mechanical and Chemical Interphases Caused by Interaction of Boehmite (γ-AlOOH) with Anhydride-Cured Epoxy Resins." *Nanomaterials* 9.6 (2019): 853**)**. In this chapter, a layered model sample consisting of an easy-to-access interfacial region between boehmite layer and an interacting epoxy is presented as a suitable approach to probe both short and long-range interphases. In This chapter, ImAFM stiffness maps, electrostatic forces as well as van der Waals forces are investigated for short-range interphases. Besides the mechanical interphase, the chemical interphase is also investigated referring as the long-range interphase. The investigations on long-range chemical interactions are studies with SKPM and AFM-infrared spectroscopy (AFM-IR). The results presented in this chapter are further correlated to the hypotheses presented in **Chapter 5** and **Chapter 6** regarding the chemical alteration of epoxy due to the preferential interactions with boehmite while curing.

The correlation between the presented results and hypotheses to the macroscopic behavior of the epoxy/BNP nanocomposites are finally discussed in **Concluding Remarks**.

Chapter 1: Theoretical Background

1.1 Thermosetting polymers

There are generally two recognized classes of polymers regarding their structure: thermosets and thermoplastic. Thermoplastics consist of long linear or branched polymer chains. They can be either amorphous or semi-crystalline depending on their molecular structure, position and size of their side-groups. For instance, an isotactic polypropylene forms crystalline region whereas atactic polypropylene is mainly amorphous. Degree of crystallization affects the mechanical, optical and thermal properties of a thermoplastic polymer. Thermoplastics can be softened and reshaped when reaching their glass transition temperature T_g. With further increase of temperature, melting temperature range T_m is reached (for semi-crystalline polymers) which is the temperature where the ordered crystalline parts of the polymer are deconstructed. This results in considerable viscosity decrease and the polymer reaches the state of flow.

Thermosetting polymers consist of an irreversibly crosslinked polymer network made from a prepolymer resin. Crosslinking or curing process can be induced by heating, radiation, and mixing with a curing agent. Unlike thermoplastics it is not possible to melt or reshape the cured thermosets. The glass transition region T_g in thermosets is where the polymer changes from a solid glassy state to a more compliant rubbery state. Further increase of temperature usually results in thermal decomposition of the polymer.

1.1.1 Epoxy resins

Most important classes of thermosetting polymers are epoxies, phenolic resins and polyurethanes. Thermally cured epoxies have a wide range of applications in many industries such as adhesives, construction parts, electronic insulations, medical devices, sport and leisure equipment and 3D printing, mainly due to their excellent mechanical properties, thermal and chemical resistance while being easily formable to complex shapes.

Like all thermosets, epoxy resins are made from initially produced, low-molecular monomers and oligomers. In order to have a crosslinked system, the resin monomer must have at least two functional groups. One of the most commonly used epoxy resin monomers, is bisphenol A diglycidyl ether (DGEBA) which is a linear bifunctional epoxy resin with two oxirane groups at both ends of the monomer. Other common epoxy monomers are phenol-formaldehyde Novalac resins, hydrogenated DGEBA (H-DGBEBA), glycidyl imides and epoxidized plant-based oils such as soy bean oil (ESBO) [17]. The most common way to

synthesize DGEBA is by the reaction of bisphenol A with epichlorohydrin in the presence of a strong base catalyst such as NaOH [18]. Fig.1.1 shows the chemical structure of DGEBA monomer.
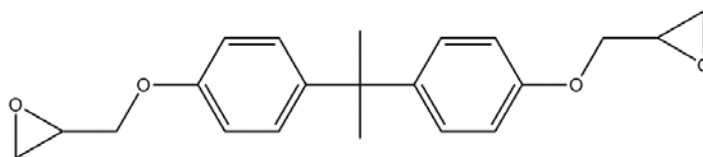
Fig.1. 1 Chemical structure of bisphenol A diglycidyl ether (DGEBA)

1.2.2 Curing mechanism of epoxy with anhydride hardener

Addition of a curing agent to epoxy resin results in a chemical reaction and formation of a three-dimensional polymer network. Curing parameters such as curing time, temperature and type of curing agent and especially the degree of curing strongly affect the final mechanical, chemical and thermal properties of the epoxy. Typical curing agents for DGEBA are primary amines and anhydride [19-21]. Primary aliphatic amines such as diethylenetriamine (DETA) and aromatic amines such as *m*-phenylenediamines (MPD) are most commonly used curing agents for epoxy resins. Where a higher temperature stability of epoxy thermosets is required, acid anhydride curing agents such as methyl tetrahydrophthalic anhydride (MTHPA) are better candidates than primary amine curing agents. The low viscosity of anhydride curing agents makes them more preferential for using epoxies compared to amines since no diluent or solvents are required in the thermoset production. Chemical structure of MTHPA is presented in Fig.1.2.
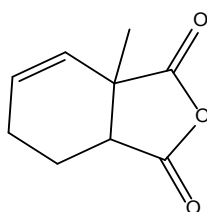
Fig.1. 2 Chemical structure of methyl tetrahydrophthalic anhydride (MTHPA)

Curing of epoxy resins with either amine or anhydride hardeners usually takes place by the ring opening of the oxirane group with either an electrophilic attack on the oxygen atom or a nucleophilic attack on one of the carbon atoms of the oxirane ring [18]. Despite the well-understood curing mechanism of epoxy with amine hardeners which has been studied extensively, the curing mechanism of epoxies with anhydride is found to be complex due to many competitive reactions involved [20] . The curing of DGEBA with an anhydride hardener is usually in the presence of a tertiary amine which functions as an initiator. As

6

depicted in Fig.1.3, tertiary amine can initiate the reaction by nucleophilic attack to either the oxirane ring on DGEBA or to the carbonyl group of the anhydride.
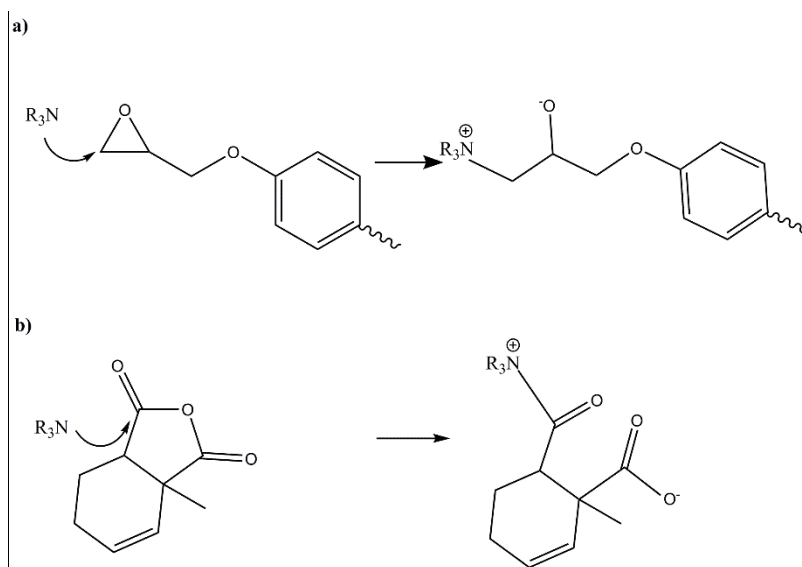
Fig.1. 3 Initiation step of curing DGEBA -MTHPA with tertiary amine by a) nucleophilic attack to the oxirane ring and b) carbonyl group of the anhydride [20].

Considering the initiation mechanism in Fig.1.3 a and Fig.1.3 b, the propagation step happens as shown in Fig.1.4 a and Fig.1.4 b, respectively. As presented in Fig.1.4 c, the propagation is also possible by nucleophilic attack of the alkoxide anion to another epoxy group, which can be the case with existence of excess epoxy (locally or in total). Since the curing reaction of epoxy-anhydride is not a living polymerization [22], regeneration of tertiary amine with different possible mechanism provides a better description of network formation on epoxy-anhydride systems [23].

An important side reaction is the reaction of hydroxyl groups with anhydrides and formation of carboxylic acid groups which can further react with epoxy (Fig.1.5). These hydroxyl groups can be the product of regeneration of tertiary amine or in case of an external source such as water or nanoparticles with hydroxyl groups on their surface.

Due to all these side reaction pathways, assumption of simple alternating anionic copolymerization is not able to describe cure kinetics of the network built up mechanism. Thus, other characterization based on physical and thermomechanical properties are required to complement the investigations on the network architecture.

7
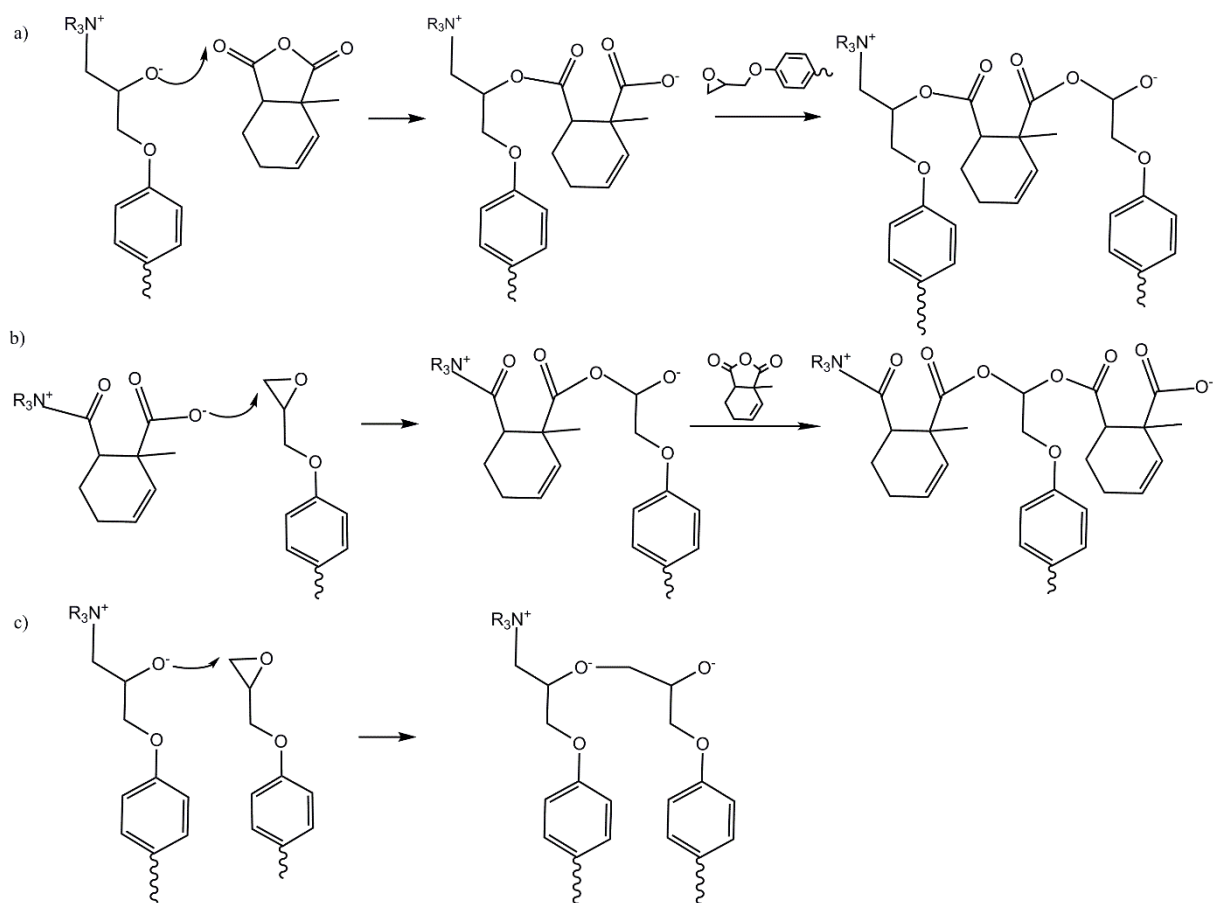
Fig.1. 4 Propagation of the curing reaction of DGEBA- MTHPA by a) nucleophilic attack of alkoxide anion to anhydride b) nucleophilic attack of carboxylate anion to oxirane group and c) nucleophilic attack of the alkoxide anion to another oxirane group [24]
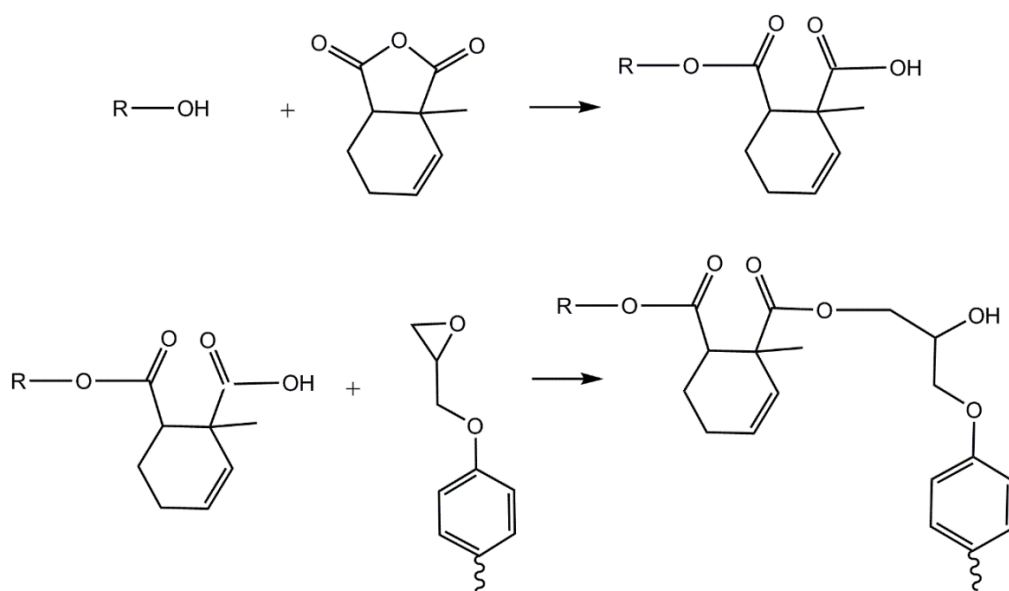
Fig.1. 5 Polycondensation pathways initiated by the hydroxyl groups.

1.2 Structure-property relationship in thermosetting epoxies

The degree of cure and crosslink density are important parameters which have high impact on mechanical, optical, thermal and electrical properties of cured epoxies. Below the definition of both degree of cure and crosslink density are presented together with their common measurement techniques.

1.2.1 Degree of cure

Degree of cure and crosslink density are substantially different by definition. The degree of cure is usually defined as the conversion degree achieved during the curing reaction, whereas crosslink density is defined by the number of chain segments, which connect two parts of the polymer network, per unit volume. The degree of cure is usually determined by indirect methods such as differential scanning calorimetry (DSC) or directly by near-infrared (NIR) and mid-infrared (MIR) spectroscopic methods.

In spectroscopic methods such as NIR, the degree of cure is directly determined by the conversion degree of epoxy [19, 25]. In this approach, the concentration of epoxy is obtained from the epoxide combination band at 4528 cm^{-1}. The investigations on evolution of the area of the peak over time results in determination of degree of conversion:

$$X_{NIR}=1-A(t)/A(0) \qquad \textbf{Eq.1.1}$$

where X_{NIR} is the degree of conversion, $A(t)$ is the actual area and $A(0)$ is the initial area of peak (See Fig.1.6).
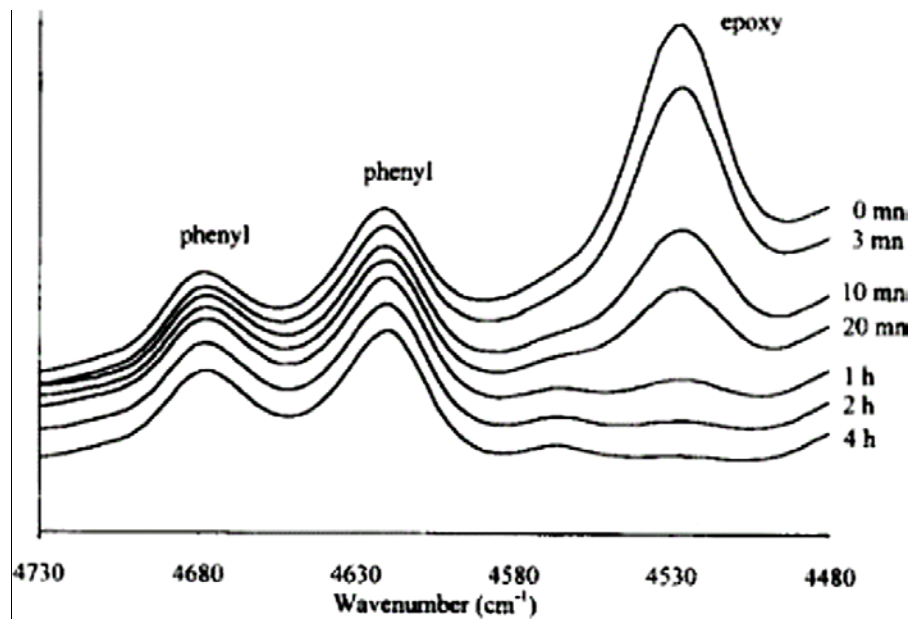
Fig.1.6 NIR spectra of DGEBA-amine during the reaction and the evolution of epoxy peak at 4528 cm^{-1} with the time of reaction [25].

9

In DSC, the degree of cure of a partially crosslinked sample determined by:

$$\alpha = 1 - \Delta H_R / \Delta H \qquad \qquad \textbf{Eq.1.2}$$

where α is the degree of cure (between 0 t0 1), ΔH_R is residual enthalpy of post-curing and ΔH is the total reaction enthalpy during the isothermal curing and post-curing. An example for determination of degree of curing from DSC plots is presented Fig.1.7.
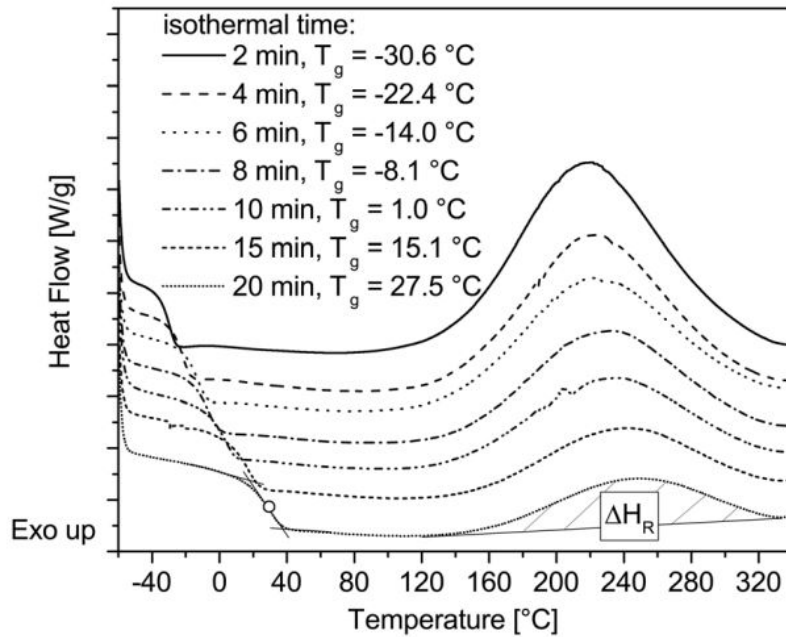
Fig.1. 7 DSC measurement of isothermal curing of epoxy-amine at 160 ˚C [26]

It is noteworthy that both time and temperature of curing significantly affect the degree of curing. If the T_g of the epoxy-anhydride is higher than the curing temperature, vitrification of the mixture may occur during the curing. In this case, due to mobility restrictions, curing may not reach completion [20]. Thus, post-curing at higher temperatures may be necessary to reach final network structure and desired properties.

1.2.2 Crosslink density.

In a polymer networks, crosslink density is defined by the number of chain segments, which connect two parts of the network, per unit volume. Many properties of thermosetting epoxies including their glass transition temperature, fracture toughness and crack propagation arise from the crosslink density and network architecture of the polymer network. Therefore, precise understanding of the network properties of the epoxy, resulted by certain curing conditions, is crucial to optimize the properties of the material for desired applications.

Compared to characterization of the molecular weights in linear polymers, measuring the molecular weight of the segments between the crosslinks is more complex and only an average density of crosslinks can be calculated or qualitatively studied by the available methods. Since the crosslink reactions of the epoxy resins are highly dependent on curing conditions, presence of additives and type of curing agents, the estimation of crosslink density based on chemistry of the system is usually inaccurate. In the following, some of the most common empirical methods of studying network structures in polymers are introduced:

Swelling solvents:

A crosslinked polymer swells in a solvent in which the same polymer when un-crosslinked is soluble [27]. Swelling measurements based on Flory swelling equations [28] has been long used for determination of crosslink density of polymers and afterwards additional modifications has been applied to this equation to describe different polymer networks [29]. The physical measurements include the determination of the volume and weight changes after the maximum swelling is reached. The method is commonly used for loosely crosslinked systems such as rubbers. However, Kenyon and Nielson demonstrated that the theoretical equation of swelling does not hold for highly crosslinked systems as epoxies [30]. They also observed that the swollen epoxy-amine samples are fragile which indicates that although epoxy-amine networks are highly crosslinked, the network structure of such polymers are less perfect than vulcanized rubbers.

Nuclear magnetic resonance (NMR):

Solid state ^{1}H NMR is a common technique to determine crosslink density of crosslinked polymers networks [31]. The principle of this method is to relate the molecular motion to network properties based on a theory suggesting the relation between hydrogen spin-spin relaxation time T_2 to crosslink density. The dominant interaction in polymers in solid state is the hydrogen dipole-dipole interaction. At elevated temperatures when the rubbery plateau is reached, fast molecular motions with rates higher than T_2^{-1} is induced. By further heating, due to an anisotropy of chain segmental motions in a crosslinked system, the molecular motion is constraint and the hydrogen dipole-dipole interactions between monomeric units are not averaged out by the molecular motion. As a result, T_2 increases with increasing the temperature and reaching a plateau value T_2^P which is inversely proportional to the crosslink density [32].

Shift of glass transition:

11

An indirect approach of qualitative approximation of crosslink density is to investigate the shifts of glass transition temperature T_g. Variation of crosslink density results in variations of the long-range segmental mobility and thus resulting in shifts of T_g. In a thermosetting polymer which is cured by copolymerization of the resin with the curing agent the T_g. shift is due two either alteration of the degree of crosslinking or the changes in chemical composition of the polymer due to copolymer effect [27]. This makes the interpretation of the T_g shifts rather challenging. Many empirical equations have been proposed for determination of crosslink density from T_g [33, 34]. However, there is not enough data available which shows their degree of reliability. Still, for qualitative comparisons between polymer networks with different crosslink densities, study of T_g variation with dynamic mechanical thermal analysis (DMTA) is a common method. Details regarding changes in the mechanical behavior of the polymer network when reaching the glass transition is provided further in the next section.

Kinetic theory of rubber-like elasticity:

Based on theory of rubber elasticity [35], crosslink density v can be estimated from the modulus in rubbery plateau (temperatures well above T_g) G_r measured by dynamic mechanical thermal analysis (DMTA):

$$G_r = \Phi v R T \qquad \textbf{Eq.1.3}$$

where R is the molar gas constant and T is the absolute temperature. The actual value of the front factor Φ is uncertain. However, it is suggested that in case of $G_r < 10^7$ Pa, Φ is close to unity and if $G_r > 10^7$ Pa, the non-Gaussian characteristic of the network becomes more dominant and the Eq.2 may not hold [27, 36]. The Eq.1.3 is commonly used for the lightly crosslinked networks where the elasticity is driven entropically. In tight networks such as in thermoset epoxies, although the kinetic theory of rubbers is not valid, the elastic modulus at high temperatures is independent from the chemical structure and mostly depends on the crosslink density [27]. Thus, using the kinetic theory of rubbers is still a good empirical method for relative determination of crosslink density in epoxies.

1.2.3 Dynamic mechanical behavior of epoxies and determination of crosslinking density
DMTA methods are rapid and sensitive to detect the glass transition temperature and crosslink density of polymer-based materials. The mechanical parameters detected macroscopically are related to the molecular motions which are functions of temperature [37].

Typical dynamic mechanical behavior of thermosetting polymers is illustrated as function of temperature in Fig.1.8. Starting at low temperatures where the sample is in the glassy state,

the storage modulus E' is high whereas the loss modulus E'' shows low values. With increasing temperature, the storage modulus is decreased and the loss modulus reaches a maximum value At this point the main relaxation process (α-relaxation) is reached which is related to the segmental motions of the backbone chains [37]. This temperature range is called glass transition region. In DMTA measurements, glass transition temperature is determined in three ways: a) the dramatic decrease of storage modulus b) The maximum peak of loss modulus and c) the maximum peak of damping ratio (loss tangent or *tan δ*). T_g values obtained from E', E'' and *tan δ*, sometimes differ considerably and therefore it is important to use one analysis method to provide comparable results. It is noteworthy that the width and shape of *tan δ* peak provide information about the molecular behavior and crosslinking density. For instance, broadening of the *tan δ* peak in the first heating is either due to an ongoing crosslinking reaction which indicates that the system was not fully cured or there is a large distribution of molecular weight of segments between crosslinks. Bimodal *tan δ* peak is usually an indication of the heterogeneity or crosslinked structures [38].
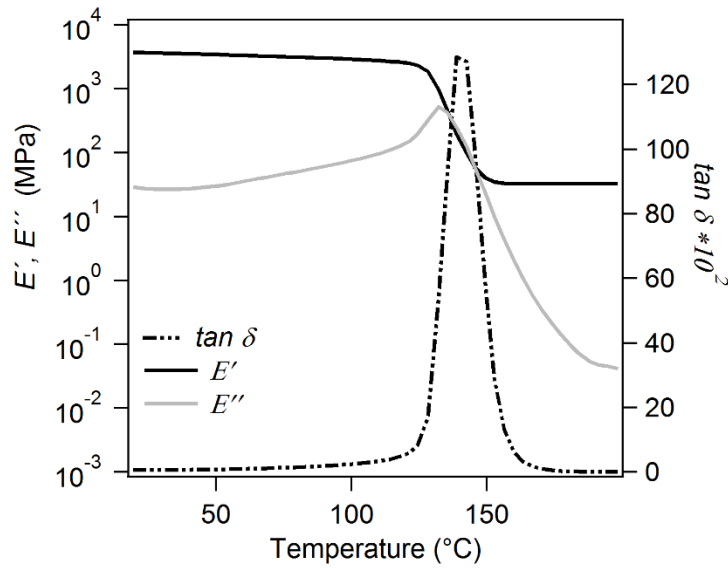
Fig.1. 8. Typical dynamic mechanical properties of a crosslinked epoxy. The solid black line is the storage modulus E', the solid gray line is the loss modulus E'' and the dashed line is the damping ratio *(tan δ)*.

It is well-known that below T_g, where the material is in the solid (glassy) state, the crosslinking has little effect on E', whereas above T_g, the modulus is depending strongly on the network architecture and the degree of crosslinking [27, 39]. Therefore, as previously mentioned, the kinetic theory of rubber elasticity can be used for modulus changes above T_g to determine the crosslinking density. It is noteworthy that for determination of crosslink

density, the elastic modulus must be converted to the shear modulus, otherwise DMTA modes such as the torsional mode must be used which directly measures the change of the shear modulus as function of temperature. For an isotropic material elastic modulus E is connected to shear modulus G by [35]:

$$2\,G\,(1+v_P)=E \qquad\qquad \textbf{Eq.1.4}$$

Here, v_P is the Poisson's ratio. For epoxy matrices the Poisson's ratio varies between 0.33 to 0.40 [40].

Based on earlier studies on the crosslink density of different polymer networks, it has been demonstrated that the kinetic theory of rubber elasticity may not hold for highly crosslinked systems with G_r values higher than 10^7Pa [27]. Thus; an empirical equation was suggested for highly crosslinked polymers [27, 36]:

$$\log G_r = 7 + 293\,(d/M_C) \qquad\qquad \textbf{Eq.1.5}$$

Where the d is the density and M_C is the average molecular weight of chains between crosslink points. The **Eq.1.5** is only valid if the modulus is measured well above (30-50K) T_g. For many epoxy thermosets which have high T_g values, it is sometimes impossible to reach the rubbery plateau at 50K above T_g, since the increase of temperature can be immediately followed by decomposition of the polymer.

At the rubbery state, when a polymer network is subjected to an applied force, a large deformation occurs due to uncoiling of the polymer chains and gaining a certain orientation towards the axis of elongation. This results in an elastic response due to decrease of entropy via elongation. In this case, the longer the chains segments between crosslinks, the larger the entropic elasticity [41]. However, in a highly crosslinked system, where chains are shorter, and the chains can establish nonbonded intra- and intermolecular interactions with neighboring chains, the elasticity is not only entropic, but the energetic elasticity must be taken into account. As Pohl et al. suggested, the energetic part of modulus G_e in crosslinked systems can be determined using the following equation [42].

$$G_r = G_e + \Phi v R T \qquad\qquad \textbf{Eq.1.6}$$

Based on this definition, by extrapolating the modulus to absolute zero temperatures, the energetic elasticity can be measured which is either a positive or a negative value. Fig.1.9 presents an example of such extrapolation to measure the contribution of energetic elasticity

on the shear modulus of a cured epoxy system. The y-intercept of the linear fit corresponds to the G_e and the slope is proportional to the crosslink density v.
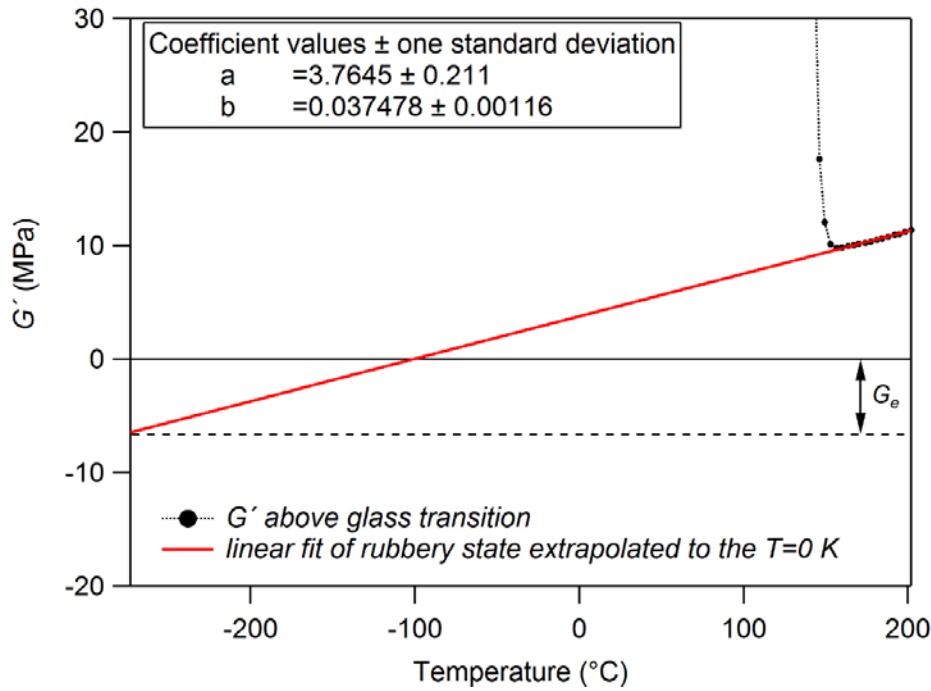
Fig.1. 9 Temperature dependency of storage shear modulus G' for an anhydride-cured epoxy. The extrapolation of the linear fit in rubbery region to the absolute zero temperature determines the intercept "a" which is correlated to G_e and the slope "b" which is proportional to crosslink density v. values of a and b are presented in the graph inset.

Structural information such as crosslink density and the non-bonded energy interactions can only be accessed by measurements of modulus well above the glass transition. Therefore, studying the mechanical behavior in the rubbery state is one focus in examining the structure-property relationship of our epoxy nanocomposite system. Investigating the variation of crosslink density and energetic elasticity with introduction of BNPs can help us to understand how the molecular structure of polymer network contributes to the variation of fracture toughness and damage tolerance.

1.3 Polymer nanocomposites (PNCs)

Traditionally, inorganic fillers such as talc and carbon black were used in polymeric products to reduce their costs. However, with time it became clear that in case of using small particles, the mechanical properties of the composite material improves, significantly [43]. Edwards reported that fillers with sizes below 100 nm exhibit the highest reinforcement effect compared to micron size particles.

One important parameter is the concentration of the nanofillers in the polymer matrix. Unlike micron size fillers, only low concentrations of nanofillers are sufficient to achieve a significant property improvement in the polymer. The variation of nanofiller concentration does not always show a linear relationship with property enhancements such as tensile strength [44, 45]. One of the reasons is the re-agglomeration of the nanofillers at high concentrations. Large agglomerations act as stress centers which reduce the mechanical properties of the polymer.

Nanofillers with variety of geometries and dimensions has been used as fillers of polymer matrices. Using low concentration (less than 2 % in weight) of a 1-dimensional nanowire or nanotube such as carbon nanotubes CNTs with high aspect ratio and extremely high (1 TPa) Young's modulus (in one direction) results in significant reinforcement of the polymer matrices [6, 46]. 2-dimensional nanofillers with platelet and layered structures such as graphene [47] and clay [48] exhibit high specific surface area when intercalated and exfoliated, resulting in improvement of the mechanical properties of the polymer. Among 3-dimensional (e.g. spherical) nanoparticles, the effect of silica [49, 50], carbon black [50], gold [51] and silver [50] nanoparticles as well as metal oxides and hydroxides such as alumina [52] and boehmite [10, 14] on a variety of polymers matrices have been studied and in most of the cases overall improvement in mechanical behavior was reported when compared to neat polymer. In the following sections, the general theoretical models on mechanics of PNCs and the interphase formations mechanism are briefly discussed. Further in **Chapter 3**, the effect of nanofiller especially boehmite nanoparticles (BNPs) on properties of epoxy matrices is broadly discussed based on data collection from previous reports.

1.3.1 Mechanical models for PNCs

As mentioned above, one of the reasons for adding fillers to polymers is to increase the modulus of the material. Over several decades, theoretical models have been developed for predicting the properties of composites. The simplest model, the rule of mixture (ROM)

describing the elastic modulus of continuous fiber composites, is presented in the following equation:

$$E_c = E_m \phi_m + E_f \phi_f$$

<div align="right">E.q.1.7</div>

where E_m and E_f are the elastic moduli of the matrix and the fiber, respectively; Φ_m and; Φ_f are the volume fraction of the matrix and the fiber.

This equation was further developed to match the characteristics of polymer nanocomposites in which the aspect ratio of the filler is also taken into account. Halpin-Tsai [53] is a commonly used theoretical model to describe the elastic modulus of unidirectional composites. In the Halpin-Tsai theory the modulus of the composite E_c is describe as:

$$E_c = E_m \left(\frac{1 + \xi \eta \phi_f}{1 - \eta \phi_f} \right)$$

<div align="right">Eq.1.8</div>

$$\xi = 2 \left(\frac{l}{d} \right)$$

<div align="right">E.q.1.9</div>

$$\eta = \frac{\left(\frac{E_f}{E_m} \right) - 1}{\left(\frac{E_f}{E_m} \right) + \xi}$$

<div align="right">Eq.1.10</div>

where ξ is the shape parameter, l is the length, d is the diameter and Φ_f is the volume fraction of the filler. For spherical nanoparticles, $\xi = 2$ is considered.

With more complex calculations, Mori-Tanaka [54] model was developed to describe the elastic modulus of a composite containing ellipsoidal particles. In all theoretical models describing composites, for simplicity reasons the components are assumed to act independent from each other, which means matrix and filler have the same properties as if the other component was not there [55]. Therefore, these models only take the simple reinforcement effect into account, based on the volume fraction and orientation of the filler and differences between young's moduli of the components. However, based these simple reinforcement effects, in most of polymer nanocomposites, the interphase and its properties (modulus and the volume fraction) also influence on the properties of the composite. In addition to these complexities, precise determination of properties such as aspect ratio, elastic modulus, density and shape factor of many complex nanofillers is alone a challenge and many simplifications in the assumptions are required [55]. Despite all these shortcomings in application of theoretical models in PNCs, these calculations help to understand whether the property changes in the composite is mainly due to the simple reinforcement or other mechanisms have

a major role. For instance, in a study on nylon6/ clay PNC, theoretical values of elastic modulus calculated by Halpin-Tsai and Mori-Tanaka as function of volume fraction of the clay are in good agreement with experimental values [56]. Therefore, it can be concluded that in nylon6/clay PNC, the major effect is the simple reinforcement and the nano-effects are relatively minor.

In thermoplastic PNCs the deviations of experimental modulus from theoretically calculated values are mainly due to nano-effects such as non-uniform dispersion of particles (i.e. particle agglomeration), strong particle-polymer interphase or in some cases percolation of interphases. In more recent studies, modified models of composite theory have been presented for PNCs, by taking the interphase properties (i.e. elastic modulus and volume fraction) into account [57] or the inclusion interphase percolation [58]. Due to the complexity of determination of interphase thickness and assigning an absolute value for the interphase elastic modulus with gradient properties, using these models is usually difficult. The main shortcoming of these modified models especially for thermosetting PNCs is neglecting the alteration of matrix properties in the presence of the filler component. Property alteration of the matrix component during the curing reaction may be the result of preferential absorption of hardener on the surface of the filler or contribution of the nanoparticles in the curing reaction and alteration of network architecture.

1.4 Organic-inorganic interphases

The overall mechanical behavior of PNCs - especially the damage tolerance and fracture strength - depends on the stress transfer at the polymer-filler interface. The interface is defined as the boundary between two phases. This boundary is rarely well-defined and usually as result of chemical and physical interactions between phases, a third phase is formed with chemically and/or mechanically altered properties. This is what is referred as the interphase [59].
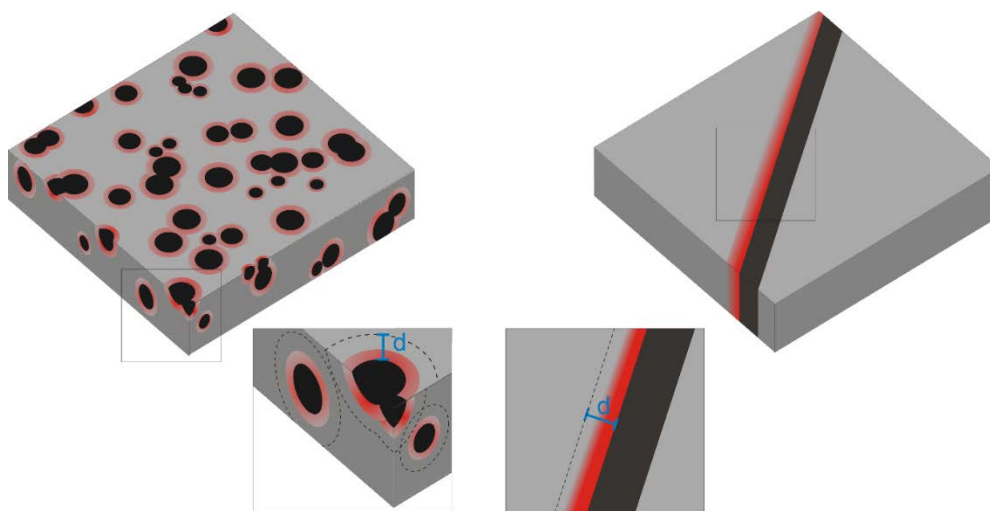
Fig.1.10 Schematic of formation of an interphase between polymer and inorganic species in a nanocomposite (left) and a layered sample (right). The effective radius or interphase thickness d is shown by blue marker.

Formation of both soft interphases [60-62] and stiff interphases [63-65] have been reported in studies on composite materials. Interphases may be homogenous or may exhibit a gradient behavior of mechanical or chemical alteration [66]. Depending on the interphase formation mechanisms (discussed further in this section), type of the matrix and the structure of the nanoparticles, the thickness of the interphase can vary from few nanometers to several micrometers [63, 67, 68].

1.4.1 Interphase formation mechanisms

The mechanism of interphase formation varies with thermoplastic or thermosetting nature of the matrix. In case of a thermoplastic matrix, previously polymerized long chains interact with the surface of the filler. In case of strong interaction between the surface of the filler and the polymer chains, either with the whole length (in case of short chains) or partial length of the chain are absorbed on the surface of the filler. In case of broad molecular weight distribution in the polymer matrix and the existence of both short and long chains, surface of the filler may induce a molecular weight segregation. In this case short chains are more prone to be

19

absorbed on the filler surface [69]. This results in restrict mobility of the polymer in the vicinity of the filler surface. In some cases, the absorbed chains tend to crystalize and thus the degree of crystallinity of the interphase may differ from the bulk [70].

The interphase formation in thermosets is substantially different. Thermosets like epoxies usually made of two or three components including resin, hardener and sometimes a small amount of accelerator. During curing, these low molecular weight components go through the polymerization reaction in the presence of an external component, the nanofiller. In this case, three scenarios can possibly occur: 1) due to the confinement effect, the crosslinking of the polymer is inhibited in the vicinity of the filler surface, resulting in formation of an interphase with different network architecture than the bulk [55]. 2) In case of a stronger affinity of one component toward the nanofiller, the concentration of that component varies with the distance from the filler surface. This preferential absorption causes a stoichiometric imbalance. Being above or below stoichiometry can result in significant alteration of material properties including modulus, T_g and crosslinking density [71, 72].The preferential absorption of amine hardener onto surface of carbon fibers [73] [74], metals and metal oxide substrates [66, 75, 76] has been previously reported. In anhydride-epoxies which were cured in contact with aluminum substrates it was noticed that the anhydride-based hardener is adsorbed onto the surface of the aluminum oxide, forming surface carboxylate [77]. 3) Nanofillers contribute to the curing reaction, thus becoming part of the network. This was observed in silsesquioxanes (POSS)-based inorganic–organic PNCs, demonstrating that nanofillers with a defined surface composition can even be used as structural elements forming network nodes [62, 78]. In many cases these three mechanisms coexist with different magnitude of influence on the properties of the interphase or may result in formation of multiple mechanical and chemical interphases with different thicknesses.

1.4.2 Determination of interphase properties

Determination of the elastic modulus and thickness of interphases is highly important in the prediction of the composite behavior. Numerical approaches [79] as well as empirical approaches, such as single fiber pull-out tests (SFPO) [67], atomic force microscopy force-distance curves (FDC) and force modulation mode [80] and nanoindentation [68] have been applied to determine the interphase properties in micrometer-size fiber reinforced polymers. The limitations in spatial resolution of those empirical methods, make it impossible to probe nanometer-sized particles and interphases in PNC samples. Studies on interphase properties in PNCs have been mainly carried out using numerical approaches [81, 82]. However, most

20

existing models are not able to explain the behavior of the many nanocomposite systems since in those models, a perfectly-bonded interphase is assumed. Therefore, especially in case of thermosetting matrices the long-range effects on the polymer matrix, as well as local changes in the stoichiometric ratio caused by preferential absorptions are not taken into account. Therefore, a combination of simulation and experimental measurements of interphase properties provides a more precise prediction of the material's behavior.

Chapter 2: Nanoscale characterization methods based on atomic force microscopy

Obtaining information about the local property contrasts across the surface of heterogeneous materials especially nanocomposites is crucial for understanding and optimizing material behavior. This resulted in development of advanced scanning probe methods allow to measure various material properties such as local mechanical, thermal and electrical properties as well as local chemical composition of the surfaces. In this chapter, first the principle of atomic force microscopy and common force measurements methods are introduced. Among the described methods, FDC, ImAFM and tapping mode are used as experimental methods in this dissertation. Further the complementary-based methods used in this dissertation such as SKPM and AFM-IR are introduced. Other non-AFM complementary methods are explained separately in other chapters.

2.1 Atomic force microscopy

Atomic force microscopy (AFM) is classified under the collective term scanning probe microscopy (SPM) in which the surface of the sample is scanned with a physical probe by means of a x,y piezo stage. Depending on the diameter of the physical probe (tip) and surface roughness the resolution of the images varies but can provide atomic resolution. The diameter of the cantilever's tip is usually in range of 5 to 20 nms. A piezoelectric actuator precisely controls the motion of the cantilever in z-direction and results in highly accurate images with nanometer resolution. In general, three main tasks of AFM are the following: 1) to measure the topography and surface imaging. Exploiting the control of applied force via the cantilever deflection 2) force measurements and 3) surface lithography are possible. Although, in some cases other methods of surface imaging such as electron microscopies provide higher resolution image compared to AFM, among the force measurement techniques, AFM-based methods are outstanding with the ability to apply forces in the range of 10^{-12} to 10^{-4} N with a lateral resolution in the range of Angstroms. Unlike scanning tunneling microscopy which can be only implemented on conductive samples, AFM can be applied on the surface of all type of material with a smooth surface. These advantages make this method suitable especially for nanoscale analysis of a wide range of organic and biological surface.

The schematic of an AFM is illustrated in Fig.2.1. The laser beam is pointed on the back side of the cantilever with a reflective coating and the beam is reflected to a quadrant photo diode detector. The sample is mounted on a piezoelectric X, Y, and Z positioning stage which

moves the sample with nanometer to picometer precision. When the tip scans over the surface of the sample, the motion of the cantilever is detected by the photodiode and used as the topographical feedback when sent to a controlling feedback unit to control the distance in z-direction during the scan. Hence, a control signal is derived from the cantilever deflection and fed to the Z-piezo so that the tip-sample interaction, e.g. the contact forces, which varies due to the topography, is kept constant. After length calibration, the control signal for the Z-piezo produces the image of the topography.
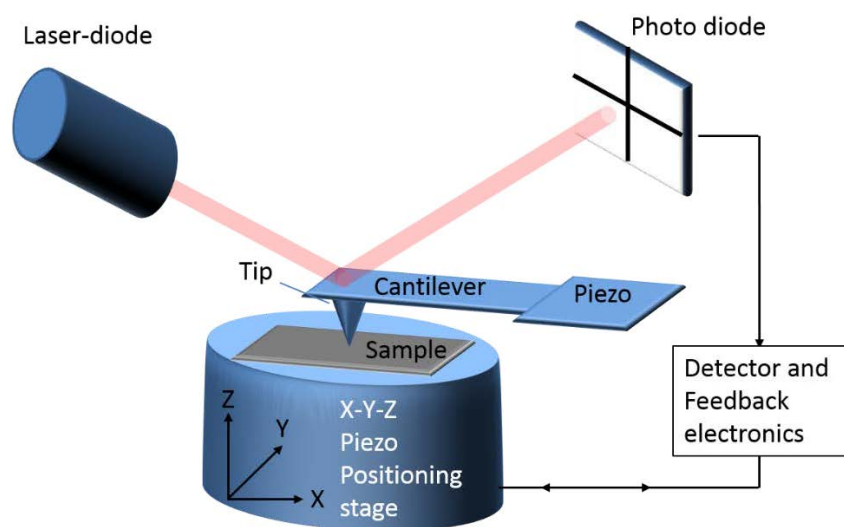
Fig.2. 1 Schematic of the AFM set up

AFM measurements can be operated in different modes. In the contact mode, the tip is in mechanical contact with the sample. If the tip moves further towards the sample, as result of repulsive forces between the tip and surface, the cantilever is deflected according to the topography of the sample. During scanning, the control loop has the task of keeping the laser position on the photo-diode, therefore the cantilever bending and thus the contact force is kept constant. The disadvantage of contact mode is possible damaging of the sample and contamination of the tip by adsorbing parts of sample during the measurement

In dynamic mode, using a piezoelectric element, the cantilever oscillates at or near its resonance frequency f_0. The amplitude of oscillation is usually selected to be small (less than 100 nm). Choosing the right cantilever with low spring constant and by controlling the set point, the sample will not be damaged by the oscillating tip during the measurements. On the other hand, high amplitudes can also lead to the possibility of geometrically changing the surface, achieving a bond fracture of polymers and changing the chemical composition of the

surface [83]. Due to the tip-surface interactions the oscillation is damped, resulting in alteration of the amplitude and phase of the oscillation.

2.1.1 AFM probes and their characteristics:

Most commonly used AFM cantilevers have a rectangular shape although triangle cantilevers are also used. The cantilever's backside is coated with a thin metallic layer to enhance the reflectivity. The spring constant of the cantilever is an important parameter and must be chosen carefully based on the AFM operation mode and the sample properties. For sensitive measurements and probing small tip-sample interactions such as in living cells, the cantilevers with low spring constants (less than 0.01 N/m) are often used. For hard substrates such as polymers in glassy state, high spring constant cantilevers (higher than 40 N/m) can be suitable. Cantilevers are usually made of silicon and silicon nitride (approx. 300 GPa), however diamond cantilevers with very high young's moduli (approx. 1000 GPa) are also used for AFM measurements. The theoretical estimation of the cantilever's spring constant based on their geometry and material properties is not precise since the structural defects are usually neglected. Therefore, calibrations are required for precise estimation of the spring constant which is further required for force measurements. Both the spring constant and the resonance frequency of the cantilever are determined via calibration by thermal noise method [84]. This calibration method includes gathering the undamped amplitude of an oscillating tip due to thermal noise by means of a lock-in-amplifier, leading to a power density spectrum (PDS). At the resonance frequency and higher harmonics of the cantilever the PDS shows maxima. The area of the peak corresponds to the power of the oscillation, P and the spring constant k_c can be estimated from:

$$k_c = K_B T / P$$ **Eq.2.1**

Where K_B is the Boltzmann constant and T is the temperature.

Another important parameter in AFM cantilevers especially for dynamic mode measurements is the quality factor or Q-factor. Q-factor is a dimensionless parameter which determines the damping behavior of a harmonic oscillator. Q-factor is also determined from the resonance peak in frequency domain from:

$$Q = f_0 / \Delta f$$ **Eq.2.2**

Where f_0 is the resonance frequency and the Δf is the half power band width of the resonance peak. Controlling the Q-factor is especially important in Dynamic AFM approaches and needs to consider the sample surface properties. for instance, in tapping mode, the tapping force is

inversely proportional to Q [85]. Therefore, with a high Q-factor probe, the force applied on the surface is kept small, resulting in less damage during the scan. On the other hand, since the high Q-factor probe has lower energy dissipation in each oscillation cycle, their response is slower. Thus, the scan speed must be kept lower than for the low Q-factor AFM probes. The Q-factor depends strongly on the dimensions of the cantilever and the medium that the measurement is carried out. Reducing the dimensions of cantilever and operating in vacuum results in increase of quality factor.

2.2 AFM force measurement methods

Static indentation methods are among the best-established methods to evaluate the hardness and stiffness of the material. Micro indentation in which spherical or a triangular pyramid made of metal or diamond indents into the surface of the sample [86]. Despite being one of the most common methods to evaluate the mechanical properties, it cannot be applied on small specimens, thin films and for nanoscale evaluation of mechanical properties. Nanoindentation is a common method for evaluating mechanical properties of thin films with the indentation depth in the scale of nanometer. In this method a pointed indenter is forced to the surface by applying a certain load (10^{-6} -10^{-3} N) and is hold for a few seconds followed by unloading. However, besides the measurement's errors due to substrate stiffness, the indenter effective shape and the residual imprints on the surface after measurement, this method does not have the lateral resolution required for measuring nanoscale areas on the surface [87].

2.2.1 Force distance curves (FDC)

The AFM static AFM force-distance curve (FDC) is a well-established method for measuring local mechanical properties of compliant and soft samples, such as polymers and duromeres [88]. Compared to conventional indentation methods, it provides significantly high lateral (25 nm), vertical (1 Å) and force (1 pN) resolution [89].

In this method, the X, Y position is kept constant during the recording of one curve. During the measurement of one curve, the sample is brought into contact with the tip and the cantilever deflection δ is recorded in dependence of the Z-piezo displacement. For a cantilever with a known spring constant k_c, the applied force F is determined based on Hooks law:

$$F=k_c\delta \qquad\qquad \textbf{Eq. 2.3}$$

In order to estimate the mechanical properties, the deformation of the sample D needs to be calculated:

$$D= Z - \delta \qquad\qquad \textbf{Eq. 2.4}$$

It is common that data obtained from FDC is plotted as deflection vs. displacement as depicted in Fig.2.2. Approaching (red line) and retracting (blue line) traces are usually not identical and especially in polymers a hysteresis is present due to viscoelastic or viscoplastic properties of the material.
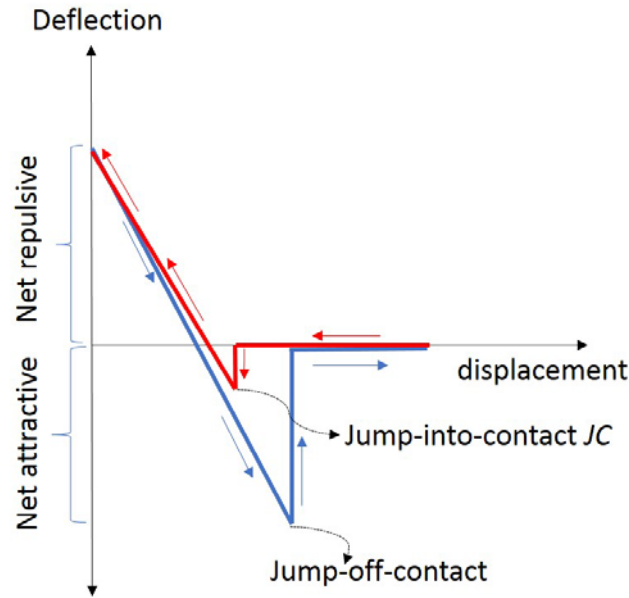
Fig.2.2 Schematic diagram of AFM force-distance curves. The red line indicates the approach and blue like corresponds to retract curve. The arrows show the direction of motion of the cantilever

Before the tip comes into contact with the surface, it is affected by tip-surface attractive forces causing a deflection towards the sample. When the gradient of attractive surface forces exceeds the spring constant, the tip jumps into contact. It must be noted that jump-to-contact (JC) is caused by the sum of attractive forces including van der Waals and electrostatic forces while jump-off-contact which is observed in retract curve is mainly due to adhesion and capillary forces [88]. Forces of jump-off contact are difficult to be considered as the pure material property since capillary forces mainly caused by the water layer on the surface are inevitable and difficult to be distinguished from pure surface adhesion forces. However, JC forces mainly originate from van der Waals forces which are caused by dipole-dipole and dipole-induced dipole interactions between the tip and surface. During the contact line the repulsive forces dominate and hence the deflection becomes positive. The repulsive regime provides information about the elastic behavior of the material; during the contact part, the applied force F is in equilibrium with the elastic deformation of the sample, given by the deformation D and the samples spring constant k:

$$k\,|D| = k_c\,|\delta| \qquad\qquad \textbf{Eq.2.5}$$

26

When Eq.2.4 is applied

$$kZ = k\delta + kD = k\delta + k_C\delta \implies k_c\delta = -\frac{k_c k}{k_c + k} Z = k_{eff} Z \qquad \textbf{Eq.2.6}$$

Since stiffness is defined as $S = \delta F/\delta D$, it becomes clear, that the slope of a FDC's contact part $\frac{k_c k}{k_c + k}$ is a measure of stiffness k_{eff}. Where the cantilever is much stiffer than the sample $(k_c >> k)$, the $k_{eff} \sim k$ and where the sample is much stiffer than the cantilever $(k >> k_c)$, then $k_{eff} \sim k_c$ [88]. Therefore, when the spring constant of the cantilever is much lower than the measured sample, the force-distance curves only measure the stiffness of cantilever. This must be taken into account in choosing the right cantilever with suitable spring constant for different surfaces. k_{eff} is related to elastic modulus of the sample by:

$$k_{eff} = \frac{3}{2} a E_{tot} \qquad \textbf{Eq.2.7}$$

where E_{tot} is the reduced elastic modulus. E_{tot} is related to the elastic modulus of the material by:

$$\frac{1}{E_{tot}} = \frac{3}{4}\left(\frac{1 - v_{tip}^2}{E_{tip}} + \frac{1 - v_s^2}{E}\right) \qquad \textbf{Eq.2.8}$$

with v_{tip} being the Poisson's ratio of the tip, v_s is the Poisson's ratio of the sample and R the tip radius [88].

Contact mechanic models

Several theoretical models have defined the elastic deformation and the relation between the applied force and the contact radius between a spherical tip and a plane surface. The Hertz model which was introduced at the end of 19th century, is based on the elastic contact of two spheres with different diameters [90]. For AFM force-distance curves, Hertz theory can be applied with the assumption that a) the tip has a half spherical shape and b) the adhesion between tip and the sample is negligible.
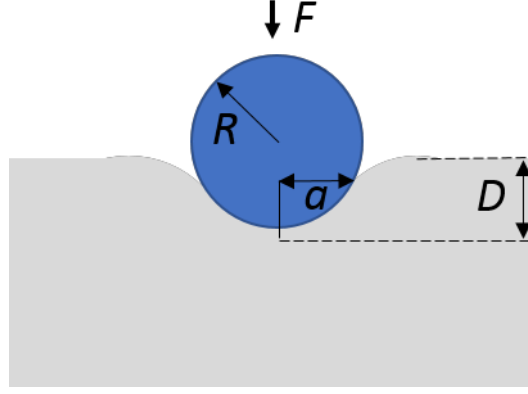
Fig.2. 3 Schematic of the deformation D of a plane specimen by a stiff spherical tip with radius R. The contact radius a of the two solids is presented based on Hertz theory

In the Hertz model, the contact radius a_{Hertz} of a sphere with the radius of R is determined by:

$$a_{Hertz} = \sqrt[3]{\frac{RF}{E_{tot}}} \qquad \text{Eq. 2.9}$$

According to the geometrical calculations the deformation can be calculated from:

$$D = \frac{a_{Hertz}^2}{R} \qquad \text{Eq.2.10}$$

and the **Eq.2.10** is rewritten:

$$D = \left(\frac{F}{R^{1/2}E_{tot}}\right)^{2/3} \qquad \text{Eq. 2.11}$$

In theoretical model of Johnson, Kendall and Robert (JKR) [91] and Derjaguin, Muller and Toporov (DMT) [92], the work of adhesion W is taken into account which can be calculated from the Jump-off contact. The contact radius based on DMT model is the determined by:

$$a_{DMT} = \sqrt[3]{\frac{R(F+2\pi RW)}{E_{tot}}} \qquad \text{Eq.2.12}$$

and JKR model determines the contact radius by:

$$a_{JKR} = \sqrt[3]{\frac{R(F+3\pi RW + \sqrt{6\pi RWF + (3\pi RW)^2}}{E_{tot}}} \qquad \text{Eq.2.13}$$

JKR model is suitable for measurements with large tips and soft samples, whereas DMT can be applied to small tips and stiff samples with small adhesion. The Hertz theory can be applied in case the adhesion force is much smaller than the maximum force ($F>>W$).

As previously mentioned, contact (static) mode force measurements such as FDC have the disadvantage of imprinting holes on the sample surface especially on soft surfaces due to plastic deformations. Moreover, determination of Young's modulus is depending strongly on knowing the exact contact area *a*. The above-mentioned theoretical models are all approximations and the determination of the real contact area may be challenging in rough samples with more complex geometries.

Dynamic force measurement method which are introduced later are much faster in comparison to FDC, providing maps with nanoscale lateral resolution with no imprinting and surface damage and thus, they are more suitable for nanoscale force measurements. Additionally, those dynamic methods which provide topography imaging and force spectroscopy simultaneously are advantageous over static measurements by enabling the investigation of the relationship between the structure and property.

2.2.2 Force Volume mode

The principle of force volume mode (FV) is similar to FDC mode. Instead of obtaining force-curves from selected points of the sample, force volume obtains force curves from every pixel of the AFM image. The real time or post processed analysis results in two-dimensional maps of adhesion, electrostatic forces and a relative elasticity between two points of the surface [88]. This method has been broadly used for imaging biological surfaces and allowed material identification [93]. Composite materials such as carbon-fiber reinforced epoxies have also benefit from this method by probing local property variations between filler and the matrix [94].

The main limitation of FV mode is the long acquisition time. This is especially problematic in case of loose samples with high drift which results in mismatches of force maps with the topography maps. Sometimes the irreversible deformation of the sample at one scan point will affect the adjacent measuring point. Therefore, acquisition of high number of data points per scan is challenging and the lateral resolution in the force map is sacrificed.

2.2.3 Tapping mode atomic force microscopy

Tapping or intermittent-contact mode AFM is the most common dynamic AFM method in which the cantilever is excited by a single frequency near its resonance frequency f_0 and oscillates while the tip is in intermittent contact with the surface of the sample. The feedback can be achieved by keeping the damped vibration amplitude or the frequency constant. In addition to topography information, the phase image contains information about surface

mechanical properties of the material, but unfortunately also contains the dissipation caused by the water film and the above-mentioned capillary forces. The free oscillation phase of a cantilever at its resonance frequency f_0 is $\pi/2$. When the cantilever is engaged with the sample surface the oscillation characteristics of the cantilever changes due to tip-sample interactions. Changes of oscillation phase are recorded as phase image. The contrast in phase image is usually attributed to viscoelasticity and tip-sample adhesion [87]. Magonov et.al. describes the correlation between phase image contrast and stiffness of the sample [95]. However, due to complexity of the correlation of phase shift with topographic artifacts and experimental parameters such as set point and tapping frequency, interpreting the stiffness of the material based on the phase imaging is only qualitative.

2.2.4 Pulsed force mode atomic force microscopy

Another single frequency AFM-based method developed for force measurements is pulsed-force mode (PFM-AFM) [96]. In this method, the z-piezo induces an oscillation in which at the highest point of the oscillation, the tip is in full contact with the surface which defines the maximum cantilever deflection [88]. The lowest point of oscillation is where the tip is not in contact with the surface. Selected points from the recorded deflection are taken and evaluated as mechanical properties (Fig.2.5). The sampling frequency is far below the resonance frequency of the cantilever. Unlike tapping mode which keeps the amplitude constant, in PFM the maximum positive deflection (Point B) which represented the maximum force is kept constant to be used as the feedback control. The point C is a user defined point with a certain distance from the point B. The difference in the values at B and C is proportional to the force-distance slope and thus is a measure of stiffness. The point D in which the tip detaches from the surface is recorded as adhesion force.
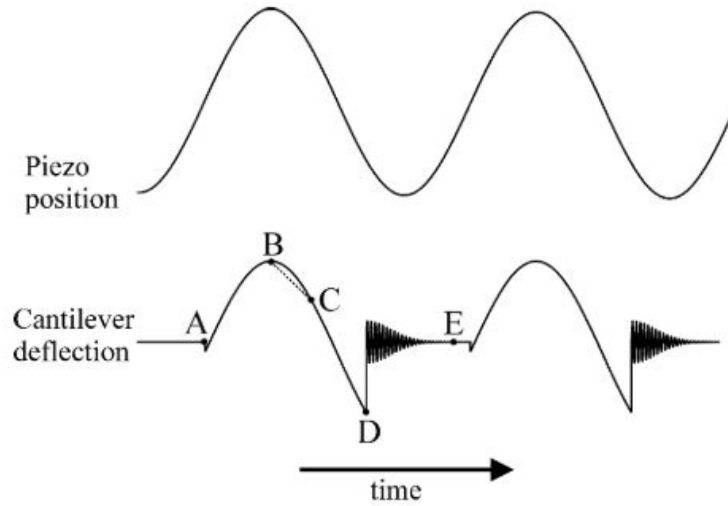
Fig.2.4 Schematic of the tip movement and cantilever deflection in Pulsed force mode [88]

This method provides real-time images of adhesion and stiffness properties of the sample in addition to topography images in a short time. The modulation oscillation is at a frequency of maximum 2kHz which means from point A to E is about 0.5ms [88]. The intermittent contact with the surface makes it suitable for measuring soft surfaces without damaging the surface. However, the mechanical property information obtained by this method is limited to few selected points in comparison with static FDC which provides a full force-distance curves including additional information such as viscoelastic behavior, van der Waals forces and yielding points. Moreover, since only stiff cantilevers can be used for PFM mode to ensure the tip-surface detachment, the force resolution of this method is relatively low (10^{-9} N) compared to single FDC curves taking in the static mode [88, 97].

2.2.5 Peak Force quantitative nanomechanical mapping

Peak Force quantitative nanomechanical mapping (PeakForce QNM) which is an extension of PFM mode, provides the complete force curve and improved force resolution (10^{-10} N) compared to PFM [97, 98]. The principle of PeakForce is similar to PFM where the tip and surface are intermittently brought to contact for a short time and the maximum force (Peak force) is kept constant by the system's feedback. The main difference between PFM and PeakForce QNM is the analysis and evaluation of acquired force curve. An example of force curve analysis by PeakForce is provided in Fig.12. At each contact point (each pixel of the image) force curves if trace and retrace is recorded. The deformation (the amount of compression of the sample), energy dissipation (shaded area in Fig.12) and the adhesion images are acquired parallel to topography image. The Young's modulus is obtained by fitting the retrace force curve in the contact region to DMT model.

31
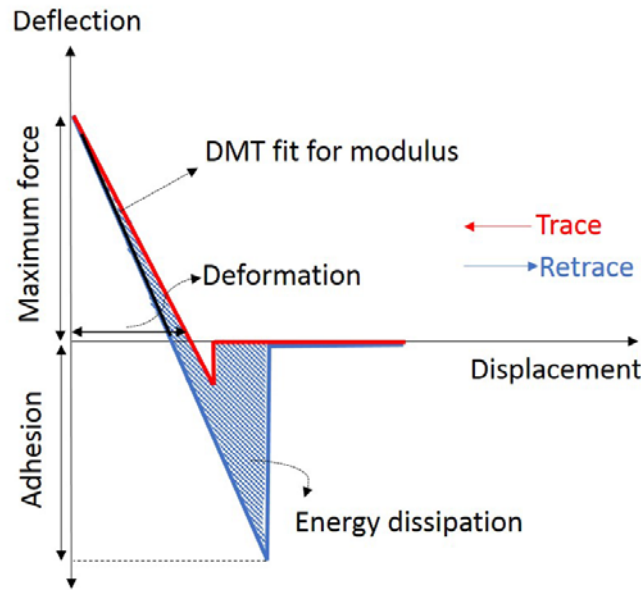
Fig.2. 5 Schematic of one Force-displacement cycle in PeakForce QNM.

The limitation of this method is the reliability of the obtained Young's modulus values due to the requirements of the contact mechanic models which may not be suitable for some surfaces [87, 98]. As the Pulsed force mode, the Peak force QNM is, related to the cantilever, a sub-resonance method.

2.2.6 Force modulation microscopy (FMM)

AFM measurements in FMM mode, where the feedback is form the contact mode type, has been long used for probing mechanical contrast in inhomogeneous surfaces [99, 100]. In this mode, the tip scans over the surface in the contact mode with a feedback loop which keeps the deflection (force) constant. Additionally, a sinusoidal signal called as "driving signal" is applied to the z-piezo voltage inducing an oscillation with a small amplitude to the sample and the tip. The motion of the tip is recorded as an electrical signal which includes both DC and AC component. The DC component is the deflection of the tip which is used for the Z the feedback loop. The AC component which shows the changes in cantilever's oscillation is affected by the sample's mechanical properties [101]. The amplitude of the AC signal known as FMM amplitude is sensitive to sample's elasticity and the contrast in FMM amplitude image is a qualitative measure of the stiffness of the sample. Soft surfaces damp the oscillation, resulting in low amplitude, whereas the cantilever oscillates with higher amplitude above stiff surfaces. An example of the changes in the amplitude of the response signal is illustrated in Fig.2.7

32
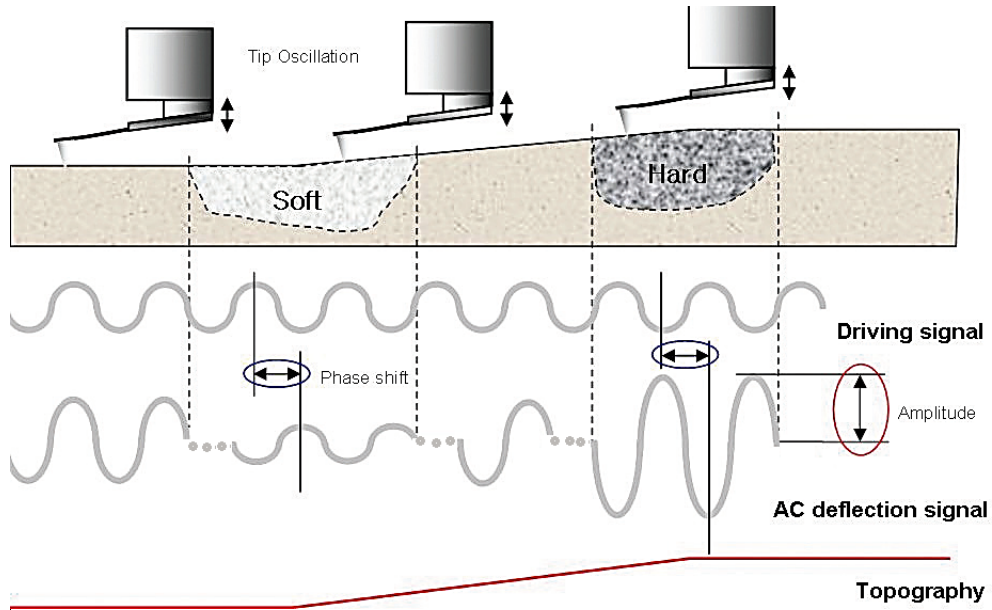
Fig.2. 6 Schematic of the tip movement and changes of the phase and amplitude on soft and hard surfaces in FMM mode [102]

2.2.7 Intermodulation AFM

Intermodulation AFM (ImAFM) is an intermittent-contact dynamic method for probing surface nanomechanical properties similar to the tapping mode. It was developed by Platz et.al in 2008 [103]. In this method the cantilever is excited with two tones at different frequencies close to the resonance frequency f_0 of the cantilever. For example, if f_0 is 174 kHz, f_1 is 173.7 and f_2 is 174.2 spaced by 0.5 kHz. This results in the beating wave form of the tip motion (Fig.2.8 a). The feedback is achieved by keeping the damped vibration amplitude constant at frequency f_1. When the oscillating tip comes close to the sample, the non-linear tip-surface interaction results in frequency mixing or intermodulation (Fig.2.8 b). As result of this frequency mixing, intermodulation products (IMPs) are generated at new non-drive frequencies (Fig.2.8 d). In acoustic circuits, the intermodulation commonly occurs which is undesired and known as intermodulation distortion of the acoustic signal. However, in Intermodulation AFM, by monitoring the intermodulation distortion products from a known input signal, the non-linear tip-surface forces can be reconstructed.
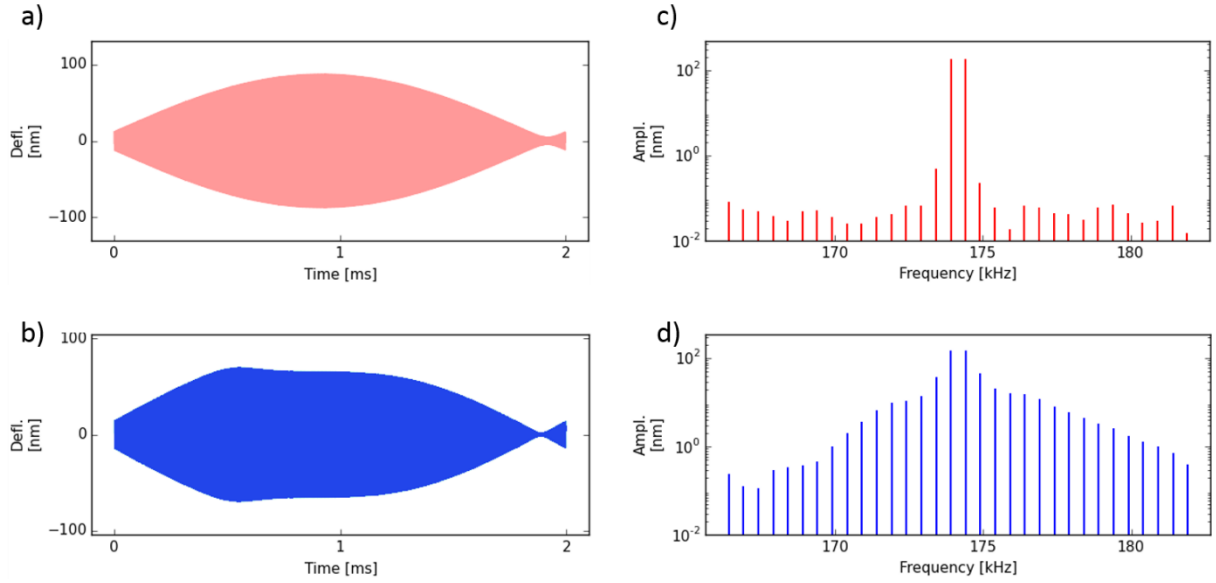
Fig.2. 7 Cantilever's a) free oscillation and b) when engaged with the surface of an epoxy sample in the time domain. The amplitude of free oscillation and when engaged in the frequency domain is shown in c) and d) respectively.

The intermodulation peaks appear (Fig.2.8 d) at linear combination of two driving frequencies [87]:

$$f_{IMP}=m\, f_1 - n\, f_2 \qquad\qquad \textbf{Eq.2.14}$$

where n and m are integers. The spacing between the driving frequencies Δf defines the time of the measurement by $T = \Delta f^{-1}$. As seen in Fig.2.8 a and b, a complete spectrum is recorded in 2 milliseconds. Due to the tip-surface forces F_{ts} the amplitude of the freely oscillating cantilever is damped. The amplitudes and phases of IMPs are measured during scanning with a multi-frequency lock-in amplifier. At each surface position i.e image pixel, hundreds of oscillations are carried out starting from low amplitudes, reaching a maximum and decreased back to zero.

Reconstruction of tip-surface forces:

In static and quasi-static force measurement methods, the cantilever force is equal to the tip-surface force:

$$F_c = -F_{ts} \qquad\qquad \textbf{Eq.2.15}$$

and the deflection d is related to the F_c by Hooks law:

$$d = -\frac{F_c}{k_c} \qquad\qquad \textbf{Eq.2.16}$$

However, in dynamic force measurements the driving force F_{drive} is taken in account:

34

$$F_c(t) = -F_{ts}(t) - F_{drive} \qquad\qquad \textbf{Eq.2.17}$$

the Hook's law equivalent is:

$$\hat{d} = -\frac{1}{k_c} \widehat{G}(\omega)\widehat{F}_c(\omega) \qquad\qquad \textbf{Eq.2.18}$$

the hat symbol refers to the complex numbers, where G is the transfer function which can be determined by:

$$\widehat{G} = \left(1 - \frac{\omega^2}{\omega_0^2} + \frac{i\omega}{\omega_0 Q} \right)^{-1} \qquad\qquad \textbf{Eq.2.19}$$

G can be determined, if ω_0 is known, which can be calculated from $\omega = 2\pi f$ and quality factor Q, which can be obtained from thermal noise calibration. The driving force F_{drive} is measured from the response of the free oscillating cantilever ($F_{ts}=0$) which can be written:

$$F_{drive} = k_c \widehat{G}^{-1} \hat{d}_{free} \qquad\qquad \textbf{Eq.2.20}$$

The tip motion signal is composed of an in-phase and a quadrature component as any other amplitude modulated sinusoids:

$$\hat{d}(\omega) = d_I(\omega) + i\, d_Q(\omega) \qquad\qquad \textbf{Eq.2.21}$$

where the subscript I means the in-phase with the oscillation and Q means phase-shifted by $\pi/2$ from the reference oscillation [104].

A model-free analysis method of the intermodulation response with goal of force reconstruction has been developed by Platz et .al known as amplitude-dependence force microscopy (ADFS) [105]. By extracting the Fourier coefficients of the F_{ts} at a high frequency near resonance $\overline{\omega}$, F_{ts} can be given as function of amplitude A at fixed probe height [104]:

$$\widehat{F}_{ts}(\overline{\omega}, A) = F_I(A) + i\, F_Q(A) \qquad\qquad \textbf{E.q.2.22}$$

$$F_I(A) = \frac{1}{T}\int_0^T F_{ts}(t)\, cos(\overline{\omega}t)\, dt \qquad\qquad \textbf{Eq.2.23}$$

$$F_Q(A) = \frac{1}{T}\int_0^T F_{ts}(t)\, sin(\overline{\omega}t)\, dt \qquad\qquad \textbf{Eq.2.24}$$

F_I, which is the in-phase force quadrature, contains information about conservative forces experienced by the cantilever. Similar to force-distance curves it contains a net attractive regime followed by a net repulsive regime. However, $F_I(A)$ cannot be treated directly as

35

force-distance curves since the force is plotted as a function of oscillation amplitude rather than tip position. Amplitude-dependence force spectroscopy (ADFS) uses the inverse Abel transform to converts $F_I(A)$ to a traditional force-tip position curve[105]. Therefore, the conservative force between tip and the surface as function of tip position is rewritten as:

$$F_c(-z) = \frac{1}{z}\frac{d}{dz}\int_0^{z^2} \frac{\sqrt{\tilde{A}}F_I(\sqrt{\tilde{A}})}{\sqrt{(z^2-\tilde{A})}}\ d\tilde{A} \qquad\qquad \textbf{Eq.2.25}$$

where $\tilde{A}=A^2$ and z is the tip position.

The other force quadrature F_Q which is out of phase with the oscillation or in other words in-phase with velocity, is a measure of dissipative forces and energy losses by the cantilever. The energy dissipation is obtained from:

$$E_{dis}(A) = 2\pi A\ F_Q(A) \qquad\qquad \textbf{Eq.2.26}$$

Knowing that F_I and F_Q are obtained for each pixel of the scanning area (see the example in Fig.2.9), matrices of complete force-displacement curves together with dissipative forces enables to reconstruct maps of different physical and mechanical properties such as stiffness, van der Waals and electrostatic force as well as energy dissipation caused by the viscous nature of the surface. In this thesis, ADFS method is used as the main approach to obtain physical and mechanical properties of the epoxy/BNP nanocomposites.
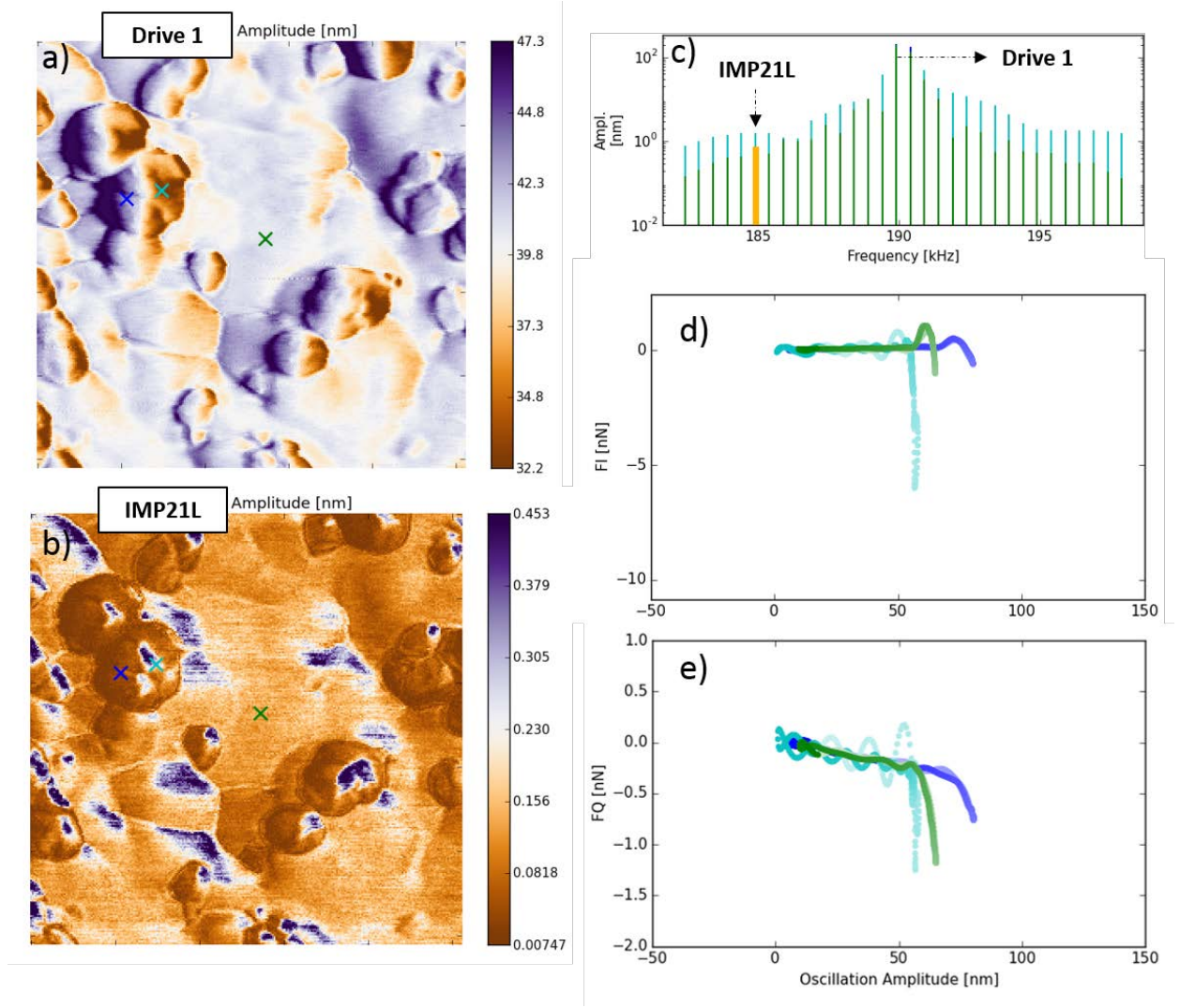
Fig.2. 8 an ImAFM measurement on an epoxy/BNP nanocomposite sample with a scan area of 1μm².
a) The amplitude image of the first driving frequency (Drive 1). the Feedback system takes the amplitude of Drive 1 to keep constant, thus this image represented the error signal. b) The amplitude image of one of the intermodulation products (IMP21L) is the result of tip-surface interaction and thus shows a material contrast independent from topography artifacts. c) the amplitude of drive frequencies and IMPs are plotted for two different measurement points (green and light blue markers). d) Conservative F_I and e) dissipative force$s$ F_Q (right-bottom) as function of amplitude measured on marked area in a) and b).

2.3 Scanning Kelvin probe microscopy

Scanning Kelvin probe microscopy (SKPM) which has been first introduced in 1991, is used to probe potential difference between the conductive tip and the sample (mostly metal or semiconductor) with high resolution [106].

Fig.2.10 shows the schematic of the physics behind the Kelvin probe approach. Work function Φ is defined as the energy required to remove an electron from the surface of the atom to the vacuum. When two surfaces with different Fermi levels are brought into contact,

37

the Fermi levels align to reach the equilibrium. This Fermi alignment causes an electric field and a potential difference which can be compensated by applying an external DC bias.
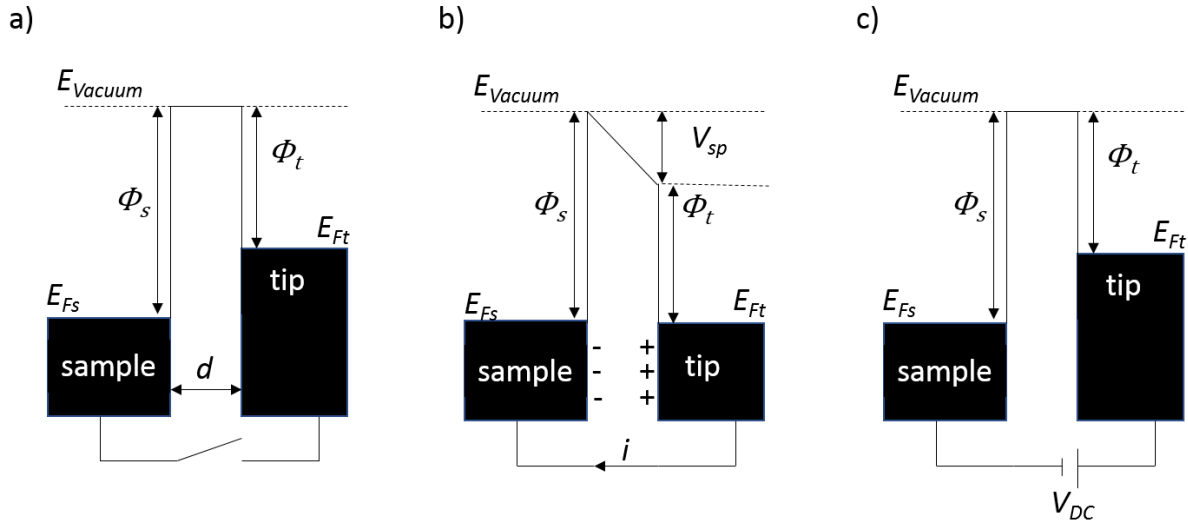
Fig.2. 9 Schematic of Kelvin Probe physics: a) Electronic energy levels of the sample and the tip when separated by the distance d and no electrical contact. b) Tip and sample are electrically connected, and the electrons flows until the Fermi levels are aligned, which cause an electric field between the sample and the tip. c) By applying an external bias, the potential difference which is measured as the surface potential V_{SP} is compensated and both surfaces are uncharged again.

In SKPM, the tip and the surface behave like a parallel plate capacitor with air as the dielectric in between. An AC bias is applied to the probe near or at its resonance frequency. As result of difference between the work function of tip and the sample, the AC bias produces an oscillatory electrostatic force which is defined as:

$$F=\frac{1}{2}\frac{\partial C(z)}{\partial z}\Delta V^2 \qquad \textbf{Eq.2.27}$$

in which C is the capacitance, ΔV is the applied voltage and z is the distance between tip and sample. The total potential difference between tip and sample in SKPM has three components, when an AC voltage V_{AC} plus a DC voltage V_{DC} is applied to the tip:

$$\Delta V=V_{sp}+V_{tip}=V_{DC}\mp V_{sp}+V_{AC}\sin \omega t \qquad \textbf{Eq.2.28}$$

where V_{sp} is the surface potential difference between the sample and the tip. The sign $\mp$ of V_{sp} depends on whether the DC bias is applied to the sample (+) or the tip (-) [107]. For further calculations, the case of DC bias applied to the tip is considered. V_{DC} is the voltage which must be applied as the feedback voltage which nulls out the oscillation of the cantilever induced by the electrostatic force. By inserting the **Eq.2.28** to the **Eq.2.27** and knowing that $sin^2x=1/2(1-cos2x)$,the electrostatic force can be rewritten as [108]:

$$F=\frac{1}{2}\frac{\partial C}{\partial z}\left(\left[(V_{DC}\text{-}V_{sp})^2\right]+2\left[(V_{DC}\text{-}V_{sp})V_{ac}\sin(\omega t)\right]+\left[\frac{1}{4}V_{AC}^2[\cos(2\omega t)\text{-}1]\right]\right)\qquad \textbf{Eq.2.29}$$

Based on this equation, the electrostatic force between tip and sample is divided into three parts: the first part is responsible for the static deflection of the tip. The second part with frequency ω is used to probe V_{sp} and the third part with frequency 2ω is used for capacitance microscopy [107]. In SKPM, only the second part of the force is used. In case of a non-zero potential difference between tip and the sample, the oscillatory force can be cancelled out when the applied DC voltage is equal to the surface potential when $V_{DC}=V_{sp}$. used as the feedback loop. Thus, the applied DC voltage is captured and reported as the surface potential V_{sp}. This value is measured for each point on the sample surface and a map of surface potential is generated. It is noteworthy that V_{sp} collected in SKPM is the superposition of both work function difference, and trapped charges. Therefore, this method is mainly used as a qualitative approach to probe material contrast in heterogenous systems.

SKPM is usually carried out as a two-pass approach, performing two scans per line on the selected scan area. As shown in Fig.2.11, the first pass which includes the mechanical excitation of the cantilever (tapping mode) yields the topography of the line. In the second pass, which is known as lift or nap mode, the topography information is used to maintain a defined distance from the surface which is known as nap height.
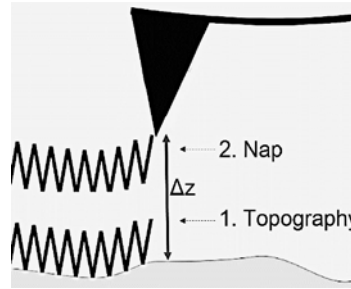
Fig.2. 10 Schematic of SKPM nap mode: first the topography is captured for each scan line followed by retracing the same topography line in order to keep the distance Δz constant between tip and surface.

Both amplitude modulation (AM) and frequency modulation (FM) modes are used to detect the electrostatic force applied to the tip. In AM mode. the force is measured by the amplitude of the electrostatically induced oscillation and V_{DC} is applied to the tip to cancel out the measured amplitude. In FM mode, the force is measured by deterring the shift of the frequency from the initial ω and an V_{DC} is applied to the tip to cancel out the frequency shift. The spatial resolution of AM-SKPM is usually in the nanometer scale (25 nm), whereas FM-SKPM can resolve sub-nanometer features depending on the tip apex and the surface [107].

2.4 AFM-Infrared spectroscopy (AFM-IR)

AFM-based infrared spectroscopy (AFM-IR) is a photothermal induced resonance (PTIR) technique where the combination of high-resolution AFM and infrared (IR) spectroscopy provides chemical characterization of surfaces at the spatial resolution of AFM [109-112]. In this method, rapid pulses from a tunable laser source illuminates the surface of the sample underneath the AFM tip. The absorbed light results in a thermal expansion of the sample. The thermal expansion causes an oscillation probed by the cantilever. Plotting either the amplitude of the oscillation after fast Fourier transform or the peak-to-peak deflection of the cantilever ring down spectrum for various IR pulses at different wavelengths, results in spectra analogous to conventional FT-IR spectra [112]. The principle of AFM-IR is illustrated and summarized in Fig.2.12.

AFM-IR technique overcomes the resolution limits of conventional IR microscopy such as FT-IR, where the lateral resolution depends on the wavelength of light. By setting the laser to a certain wavelength corresponding to one absorption wavelength of the sample and scanning a certain area, chemical maps based on different absorption wavelengths can be constructed with sub 100 nanometer resolution. Since the duration of each pulse is 20ns with a repetition rate as fast as 1 kHz, chemical maps can be obtained in only few minutes [113, 114].
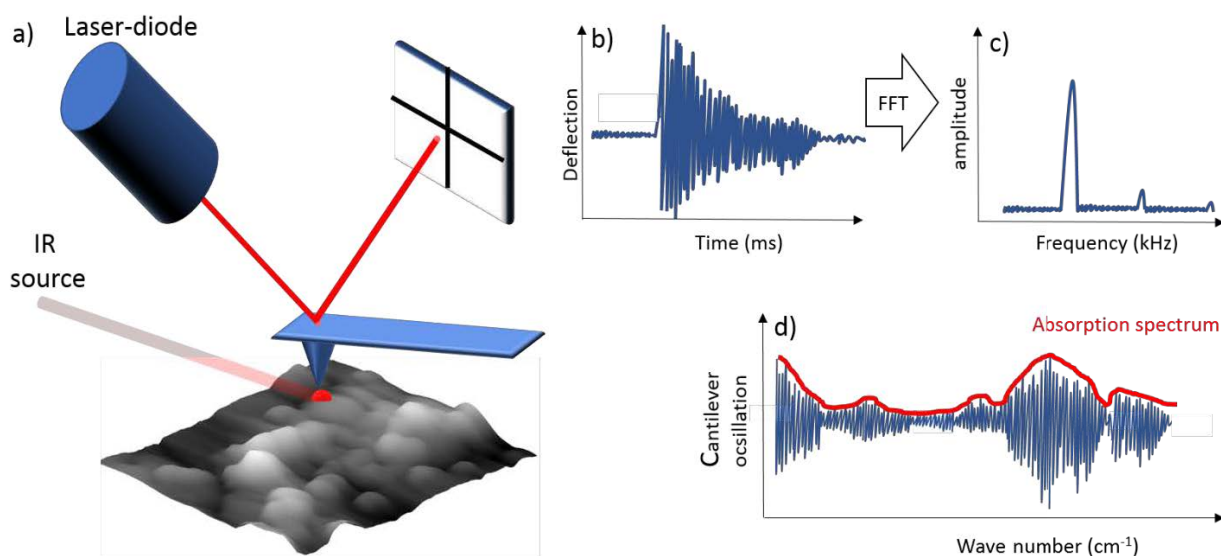
Fig.2. 11 Principle of AFM-IR: a) The laser beam is focused on the sample in the region of the AFM tip. By tuning the wave length of the IR beam to an absorbing band of the sample, the heat released from this absorption causes the thermal expansion of the sample and results in oscillation of the cantilever. The amplitude of this oscillation is measured and is correlated to absorption coefficient.

Conclusion

In order to probe the structure and properties of polymer nanocomposites at nanometer scale, first of all, an overview of the surface has to be made very frequently. Due to vapor deposition with gold or carbon and modification by the implanted electrons, SEM is unsuitable in the first step. The search for special features and the examination of the quality of surface optimization such as polishing or a cut with the microtome must be possible more quickly. For this reason, tapping mode AFM usually provides the first overview images and results. Loose particles or insufficient preparation can be recognized immediately, also because the method is very sensitive to contaminations. The tapping mode becomes additionally valuable because the surface potential can be measured locally in a two-step procedure. As we will see, in chapter 6 and 7 this is an excellent way to analyze the surface composition, unaffected by the local stiffness: the tip does not touch the surface in SKPFM. The advantage of the FDC method used in chapter 4 in this work, is the very good calibration capability and the well accepted models for calculating the local modulus. The disadvantage of the low lateral resolution only allows for questions where no short-range interfacial interactions or the nanoparticles themselves have to be searched for. In contrast, intermodulation AFM, as will be shown in the course of this work (chapter 5,6 and 7), allows a large amount of additional information on the surface properties. Only the time-consuming and sometimes very difficult optimization of the feedback prevents it from completely replacing the somewhat faster conventional tapping mode. For the evaluation of the local chemical composition the method of AFM-IR is indispensable. As will be shown in chapter 7, even a chemical element analysis carried out subsequently in SEM using EDX does not reach the depth of knowledge of nano-IR AFM.

Chapter 3: State of the research

3.1 Epoxy nanocomposites

Nanofillers are commonly added to epoxies to enhance their mechanical properties. In some cases, the enhancement of one property such as elastic modulus as result of inclusion of stiff nanofillers results in sacrificing other properties such as the fracture toughness. Fracture toughness of polymer nanocomposites strongly depends on the mobility and dynamics of polymer chains and energy dissipating mechanisms between nanofiller and the matrix. The chain segmental dynamics which are associated to glass transition may become slower, faster or remain unchanged, depending on the polymer-nanofiller interaction, nanofiller size and morphology (degree of dispersion). The chain mobility in nanocomposites is affected due to several competing mechanisms: a) in some nanocomposites, chain mobility in the network is decreased due to the confinement effect caused by presence of nanofillers. b) on the other hand, chain dynamics is increased due to plasticizing effect of the nanofillers. In this case, nanofillers cause an increase of free volume as result of loosening the molecular packing of the chains [115].

In thermosetting polymers such as epoxies, besides the above-mentioned mechanisms, the alteration of the curing reaction and the network architecture may occur as result of nanofiller inclusion. This can be resulted from certain functional groups on the nanofiller, causing a variation of chain length between the crosslinks. In most literature examples with thermoplastic matrices, only a modest change in T_g values ($\Delta T_g < 10$ °C) are reported [55]. However, in case of having nanocomposites with thermosetting matrices, larger T_g changes are possible as result of possible changes in crosslink density in the presence of nanoparticles and/or preferential interactions of the curing agent with the surface of the nanoparticles.

In Table 3.1, some of previous studies on thermomechanical properties of epoxy nanocomposites are listed, including changes in T_g and room temperature elastic modulus values in comparison with the neat polymer. The reports on the trend of T_g changes among different epoxy nanocomposites are controversial. Some reported the increase of T_g when nanofillers are introduced to epoxy, whereas others reported the opposite. For instance, inclusion of silica particles in epoxy results in a very slight (4 °C) T_g increase [116]. However in another study the same nanoparticle causes a drastic negative shift (30 °C) of T_g [50]. One argumentation for this contradictory observation can be the different filler concentrations. At

high concentrations, fillers sometimes act as plasticizer, resulting in more free volume by changing in the architecture of the polymer and disturbing the crosslinking process.

Table 3. 1 Literature review of epoxy nanocomposites: ΔT_g is the change of glass transition temperature and ΔE is the change of room temperature elastic modulus of epoxy nanocomposites compared to neat epoxy.

Epoxy resin/curing agent	Nanofiller type and concentration	ΔT_g (K)	ΔE (%)	Observations and arguments	Ref.
DGEBA/ amine	Silica (10 wt%)	+ 4	+58	Contribution of silica in the network (increase of crosslink density)	[116]
DGEBA/ amine	MMT Clay (wt 25%)	-5	+35	Enhancement of the overall toughness (the values are not specified)	[117]
DGEBA/ amine	Alumina (Al$_2$O$_3$) (16 volume%)	+6	+60	The crosslink density decreases with increasing alumina content	[118]
DGEBA/ amine	Alumina (Al$_2$O$_3$) (10 wt%)	+15	+45	120% increase of fracture toughness. Increase of crosslink density	[119]
DGEBA/ amine	Carbon black (2 wt%)	+13	+0.1	Above 0.5 wt %, T_g decreases with increasing the filler content	[120]
DGEBA/ amine	Pure CNT (0.2 wt%)	+4	+9	Increase of thermal stability	[121]
DGEBA/ amine	NH$_2$-CNT (0.2 wt%)	+8	+16	Amine modification of CNT improves the interphase	[121]
DGEBA/ amine	Polycarboxyl-OPS (12 wt%)	-40	-9	Fillers are covalently bonded to the network, reducing the crosslink density	[78]
DGEBA/ anhydride	silica NPs (40 wt%)	-30	+45	The absorbed water on the hydrophilic surface of silica results in depression of T_g	[50]
DGEBA/ anhydride	Silver NP (75 wt%)	-30	Not specified	T_g decrease is related to weak resin-filler interphase	[50]
DGEBA/ anhydride	Carbon black (2 wt%)	-10	Not specified	T_g decrease is due to increased interfacial area due to longer sonication	[50]
DGEBF/ anhydride	Fluorinated-CNT (0.5 wt%)	-70	+30	Stoichiometric imbalance induced by the filler results the drastic T_g decrease.	[122]
DGEBA/ anhydride	MMT clay (10 wt%)	-35	+50	Surface modification allows higher degree of intercalation	[123]

Another important observation when comparing T_g values listed in Table 3.1 is the difference between ΔT_g depending on the curing agent. The T_g values in nanocomposites with amine-cured epoxies usually shows a slight positive shift, whereas with anhydride-curing epoxies negative shifts (up to 70 ˚C) were reported. For instance, addition of carbon black to amine-curing epoxy resulted in positive shift of T_g [120], whereas the same concentration of carbon black introduced to anhydride cured epoxy results in negative T_g shift [50]. This may be due to the reasons that the presence of nanofillers affect the molecular architecture of epoxy-anhydride in a different way than of epoxy-amine systems. Miyagawa et.al explained the drastic T_g depression of fluorinated CNT in anhydride-curing epoxy as the result of stoichiometric imbalance between anhydride and epoxy induced by the preferential absorption of the nanofiller [122].

Comparison of the elastic moduli listed in Table 3.1 shows the elastic modulus of epoxy nanocomposites often increases with inclusion of nanoparticles. The degree of the modulus increase varies strongly with the nanofiller type and concentration, whereas no correlation to the curing agent is observed. For instance, with silica and alumina nanoparticles it is possible to reach 45-60% increase in the elastic modulus in both anhydride and amine-curing epoxy matrices.

The exceptional case observed in Table 2.1 is polycarboxyl-OPS nanofillers in amine-curing epoxy in which a slight decrease (9%) in elastic modulus compared to neat epoxy is reported [78].Wang et.al argumentation for such controversial result is alteration of the network architecture due to bulkiness of OPS molecules covalently bonded OPS fillers to the epoxy, resulting in a low crosslink density system.

3.2 Epoxy/BNP nanocomposites

As discussed before, strong polymer-nanofiller interaction plays a crucial role in the final mechanical performance of the nanocomposite. The interaction between some epoxy matrices and many nanofillers such as CNTs and nanoclay is relatively weak. Therefore, functionalized groups or polymer chains and are grafted to the surface of these nanofillers to improve the interfacial interactions [124]. Surface modifications usually adds high costs and complexity to the production of nanofillers on large industrial scale. Therefore, it is more feasible to use nanofillers which have interactive functional groups in their structure.

Boehmite nanoparticles (BNPs), also known as boehmite alumina (BA) have recently received a great deal of interest after being integrated as filler in several thermoplastic and

thermosetting polymers [10]. Low production costs, high dispersibility in most of polymeric matrices and large specific surface area (up to 260 m^2/g [125]) makes BNPs a suitable nanofiller for a variety of polymers. The hydroxyl groups on the outer surface of boehmite allow strong interaction with polymers and result in easy dispersion of nanoparticles in the polymer matrix even without surface modifications. Where the surface modification is necessary, the existence of these hydroxyl groups also allows for grafting of functionalized groups on the surface of the particle. Depending on the polymer matrix type, the effect of BNPs on the properties of the nanocomposite is versatile. In thermoplastic polymers, inclusion of BNPs often results in increase in Young's modulus [126-133], improved thermal degradation [134-138] and toughness [139-141], as well as increase of fire retardancy [132, 142, 143].

In thermosetting polymer matrices, the addition of BNPs resulted in controversial property alterations. Some of these studies are summarized in Table 3.2.

Table 3. 2 Literature review of epoxy/BNP nanocomposites:

Epoxy resin/ curing system	BNP-based nanofiller type/mass fraction	methods	Property changes of the nano-composite compared to neat epoxy	Ref.
DGEBA/ amine	Unmodified (D40) modified with p-toluenesulfonic acid (OS1) and modified with benzenesulfonic acid (OS2)/ 0-5 wt%	DMTA, viscometer, and BDS	-Higher viscosity increase for unmodified BNPs due to high particle-particle interactions -Modification of BNP lowers the particle-particle interaction, which results in better dispersion -E' decreases above and below T_g - Slight T_g decreases (1-6 °C) -Fracture toughness increases	[115]
DGEBA/ amine	Unmodified and APTES modified BNPs/ 0-7 wt%	XRD, FTIR, and DSC	-Increase in tensile strength as function of BNP loading -T_g increases with small filler quantities (up to 5 wt%). Further loading results in decrease of T_g.	[144]
DGEBA/ amine	Unmodified BNPs/0-4 wt%	Tensile test and SEM fractrography	-Increase in tensile modulus, tensile and flexural strength -Enhancement of ductility and fracture toughness	[145]
DGEBA/ amine	Carboxylate alumoxane modified BNPs/0-16 wt%	SEM, EDS and tensile tests	-Decrease of tensile and flexural modulus and strength especially at high loadings (> 5wt%) due to poor resin-fiber interphase interaction.	[146]
Cycloaliphatic epoxy + hyperbranched polyester / UV curing	BNP Modified with p-toluenesulfonic acid (OS1) /5-20 wt%	Rheometer	-Increase in viscosity with increasing filler content	[147]

Cycloaliphatic epoxy oligosiloxane (CEOS)/ UV curing	Un-modified HP14 and Modified with p-toluenesulfonic acid (OS1) / 1-10 wt%	FT-IR, DSC, and TGA	- Unmodified BNP increases the T_g up to 24 °C for and modified BNP up to 43 °C. - T_g maximum appears with 2 wt%. - Improved thermal stability due to attractive particle/resin interactions.	[148]
Cycloaliphatic epoxy/ UV curing	Unmodified BNPs/ 1-7 wt%	FTIR, DMTA, and electrical tests	-Slight decrease of epoxy conversion in the presence of BNPs -Increase in T_g (up to 40 °C) and crosslink density. -Increase in electrical breakdown strength and decrease of space charge accumulation	[149]
DGEBA/ anhydride	Taurine modified BNPs (HP14T)/ 7.5 wt%	Tensile and fiber pull-out tests	-Incorporation of this nanocomposite with carbon fibers resulted in improved tensile properties of the carbon-fiber composite. -The bonding between carbon fiber and epoxy is improved in the presence of HP14T.	[16]
DGEBA/ anhydride	Unmodified (HP14), taurine (HP14T) 4-hydroxybenzoic acid (HP14HBS) and hexanoic acid (HP14Hex) modified BNPs. /0-15 wt%	IR, SEM, Rheometer, DSC, and DMTA	-Low interaction between HP14T and the resin results in significant decrease of viscosity -Increase of bending strength and flexural modulus -Decrease of T_g and crosslink density for all filler types. -Surface modification of BNPs shows no significant effect on mechanical properties of the cured material.	[15]
DGEBA/ anhydride	Taurine modified BNPs (HP14T)/0-15 wt%	DSC and DMTA	-Increase in flexural modulus -Increase of degree of curing -Slight decrease of T_g with increase of the filler content - Decrease of the thermal expansion coefficient of the epoxy - Increase of thermal conductivity	[14]
DGEBA/ anhydride	Acetic acid-modified BNPs/ 0-15 wt%	DSC and rheometer	-Decrease of total reaction enthalpy with increase of filler content -Remarkable decrease of T_g after curing -Viscosity decrease with increasing filler content.	[150]
DGEBA/ anhydride	Unmodified BNPS and acetic acid modified BNPs /0-15 wt%	MDFEM, Tensile test and SEM Fractography	- Increase in tensile modulus and fracture toughness with increase of filler content - No remarkable difference between the properties of unmodified and acetic acid modified BNPs nanocomposites. - A slight increase of Young's modulus and critical stress energy with decrease of agglomerate size.	[11, 12]

The presented data in Table.3.3 shows that the reinforcement of thermosetting epoxies with inclusion of BNPs including the increase of tensile and flexural moduli as well as increase of fracture toughness have been broadly reported. However, the presented hypotheses for the reinforcement mechanisms of BNPs in epoxies vary among different studies. For instance, in the study of Wu et al., the increase in tensile modulus and fracture toughness is attributed to the formation of a rigid interphase between matrix and particles [145]. On the other side, Jux et al. assumed that increase of fracture toughness in epoxy/BNP nanocomposites is due to the formation of soft interphase surrounding the particles, resulted from the disturbance of the network formation [12]. To the author's best knowledge, no further investigations on the interphase properties between epoxy matrices and BNPs are found on the literature.

One of the controversial property changes observed with inclusion of BNPs in epoxy matrices relates to the network density and T_g. Meanwhile drastic increases in T_g were observed for UV curing epoxy/BNP nanocomposites [148, 149], negative T_g shifts are commonly reported of anhydride curing epoxy/BNPs [14, 15, 150]. The T_g changes of amine-curing epoxies in the presence of BNPs seems to be much smaller compared with other epoxy systems. These observations show that the curing agent and their interaction with BNPs have a decisive role in the structure and mobility of the final polymer network.

Some cases of surface modifications of BNPs have shown to decrease viscosity of epoxy resin and enhancement of the dispersion [115, 150]. However, especially in case of anhydride curing epoxies, there are no signs of a considerable improvement of thermal and mechanical properties of the cured composites with modified BNPs in comparison with unmodified BNPs [12, 15].

3.3 Hypotheses and aims of this work:

The reinforcement effect of BNPs on properties of epoxies is attributed to several hypotheses.

Hypthesis.1: inclusion of BNPs as stiff fillers with higher Young's modulus than that of the epoxy matrix results in increase of the composite Young's modulus.

This argumentation is based on the simple theoretical mechanical models for polymer nanocomposites described in Chapter 1, section 1.4.1. For a realistic investigation of theoretical mechanical models in epoxy/BNP nanocomposites, knowledge about material properties including precise Young's moduli of all composite components including boehmite, epoxy and possibly the interphase are required. The calculated Young's modulus of boehmite using numerical approaches yields a value between 82 GPa to 97 GPa. However, no reliable experimental measurement of the Young's modulus of boehmite is available in the literature.

Aim 1: Due to lack of knowledge about mechanical properties of boehmite, the first goal of this work is determination of the mechanical properties of pure boehmite. FDC is used as a suitable method to probe a geological crystal and nanometer size BNPs embedded in epoxy, respectively. This investigation is presented in Chapter 4 which is based on results published in **Paper I**.

Hypothesis 2: The inclusion of BNPs in epoxy, results in alteration of the structure and properties of bulk epoxy, including the crosslinking density and Young's modulus.

In all theoretical models describing mechanics of composites, for simplicity reasons, the assumption is hold that composite components act independent from each other, which means matrix and filler has the same properties as where the other component was not there [55]. This assumption may hold to some extent for some thermoplastic polymer matrices which has no considerable interaction with the nanofiller. In case of a thermosetting epoxy nanocomposites, the bulk properties of the matrix phase, (e.g. the crosslink density and Young's modulus) may alter during the curing reaction as result of its interaction with the nanofiller.

Aim 2: determination of the local mechanical properties of bulk matrix in epoxy/BNP nanocomposites with different BNP loadings by means of high-resolution AFM-based force measurement methods. Moreover, determination of thermomechanical properties of nanocomposite provides information about crosslink density and the network structure

alteration of the epoxy in presence of BNPs. These investigations are demonstrated in Chapter 5 which is based on the published results of **Paper II.**

Hypothesis 3: *the increase of fracture toughness and failure resistance in epoxy/BNP nanocomposites is mainly due to formation of a soft interphase with different network structure than the bulk. Formation of a soft interphase results in enhancing the energy dissipation and damping mechanisms in the nanocomposite.*

Aim 3: investigation of the interphase between epoxy matrix and BNPs and its properties including thickness, stiffness, attractive forces and energy dissipative by means of combination of microscopy methods such as SKPM and ImAFM. These investigations are presented in **Chapter 6** which is based on **Paper III**.

Hypothesis 4: *The preferential absorption of epoxy components (resin or the hardener) toward BNPs results in formation of an interphase with different chemical structure than the bulk. In this case, the interphase may consist of either excess epoxy or hardener molecules which did not participate in the crosslinking reaction of bulk epoxy. Moreover, such preferential absorbance results in formation and coexistence of multiple interphases (chemical and mechanical) with different thicknesses.*

The comparison of the reports listed in previously on Table 3.2, shows that the type of curing (i.e. the curing agent) has a major role in property alteration of different epoxy/BNP nanocomposites. In thermosetting matrices like epoxy, in case of a stronger affinity of one component toward the filler, the concentration of the absorbed component varies with the distance from the filler surface, causing a stoichiometric imbalance. Being above or below stoichiometry can result in significant alteration of material properties including modulus, T_g and crosslinking density [65, 71, 72]. The preferential absorption of amine hardener to surface of carbon fibers [73, 74], metal and metal oxide substrates [66, 75, 76] has been previously reported. In a study on an anhydride-curing epoxy which was cured in contact with an aluminum substrate, it was noticed that the anhydride-based hardener is adsorbed onto the surface of the aluminum oxide, forming surface carboxylate [77]. In case of such preferential absorption in epoxy/BNP nanocomposite, coexistence of multiple interphases with different mechanical, chemical and even electrical properties is possible.

Aim 4: determination of the chemical composition of the interphase. investigation and distinguishing the coexisting chemical, electrical and mechanical interphases and their effective radii (interphase thickness) using combination of methods such as AFM-IR, SKPM

and ImAFM. For this purpose, a model sample with simplified geometry and a combination of analytical methods are required to probe different physical properties at different distances to the boehmite. The results of this investigation are demonstrated and discussed in Chapter 7 which presents the published work of **Paper IV.**

Chapter 4: Mechanical Properties of Boehmite Evaluated by Atomic Force Microscopy Experiments

This chapter is reproduced with permission from the accepted manuscript of: Fankhänel, J., Dorothee Silbernagl, **M. Ghasem Zadeh Khorasani**, B. Daum, A. Kempe, Heinz Sturm, and R. Rolfes. "Mechanical properties of boehmite evaluated by atomic force microscopy experiments and molecular dynamic finite element simulations." *Journal of Nanomaterials* 2016 (2016).

This chapter only presents parts of this publication (AFM measurements on boehmite geological crystal) which are relevant to the focus of this dissertation. Due to lack of relevance, the simulation part and other complementary experiments presented in the publication were excluded from the content of this chapter.

DOI: http://dx.doi.org/10.1155/2016/5017213

Research Article

Mechanical Properties of Boehmite Evaluated by Atomic Force Microscopy Experiments and Molecular Dynamic Finite Element Simulations

J. Fankhänel,[1] **D. Silbernagl,**[2] **M. Ghasem Zadeh Khorasani,**[2] **B. Daum,**[1] **A. Kempe,**[1] **H. Sturm,**[2] **and R. Rolfes**[1]

[1]*Institute of Structural Analysis, Leibniz Universität Hannover, Appelstraße 9A, 30167 Hannover, Germany*
[2]*Bundesanstalt für Materialforschung und -prüfung, Unter den Eichen 87, 12205 Berlin, Germany*

Correspondence should be addressed to J. Fankhänel; j.fankhaenel@isd.uni-hannover.de

4.1. Introduction

The structural properties of boehmite have been widely studied: experimentally through X-ray diffraction by Bokhimi et al. [151] or by means of Raman spectroscopy by Kiss et al.[152]; numerically through quantum mechanics calculations by Tunega et al. [153]and Noel et al. [154]. However, there are very few reports on the mechanical properties of boehmite, especially concerning the Young's modulus. Streller [155] reported a value of approx. 120 GPa from nanoindentation tests using a sample of APYRAL AOH20 (Nabaltec AG) boehmite with a diameter of 1 μm. However, the applicability of nanoindentation of boehmite is questionable. As discussed further, monocrystalline boehmite does not appear to be stable in sufficient size to perform nanoindentation measurements. The diameter of the boehmite crystal should be at least higher micron range, since the maximum indentation depth should not exceed 10% of the sample height in order to get undisturbed results. Additionally, the sample surface is assumed to be an infinite plane, which allows for a region of inelastic deformation in the proximity of the indent. To the authors best knowledge there are no measurements of the mechanical properties of verifiable monocrystalline boehmite to be found in literature, which is apparently due to the fact that macroscopic monocrystalline boehmite is very hard to obtain.

Tunega et al. [153] calculated the bulk modulus of boehmite using density functional theory and density functional based tight binding method obtaining values of 93 GPa and 82 GPa, respectively. Assuming, for simplicity, an isotropic behavior and a Poisson's ratio of 0.22, the Young's modulus can be estimated to fall within the range of 138 to 156 GPa.

Due to the lack of literature, the goal of the present study is the determination of the mechanical properties of boehmite. Since both approaches, experimental and numerical, have obstacles to overcome, a combination of these methods appears most promising.

4.2 Boehmite

Boehmite is a mineral of aluminum with an orthorhombic unit cell (a = 3.693 Å, b = 12.221 Å, c = 2.865 Å), classified as oxyhydroxide (γ-AlO(OH)). Its crystal structure, shown in Fig.4.1, consists of double layers of oxygen octahedrons with a central aluminum atom. The outfacing oxygen is bonded via hydrogen bonds to the hydroxyl group of the adjacent layer of octahedrons [156].
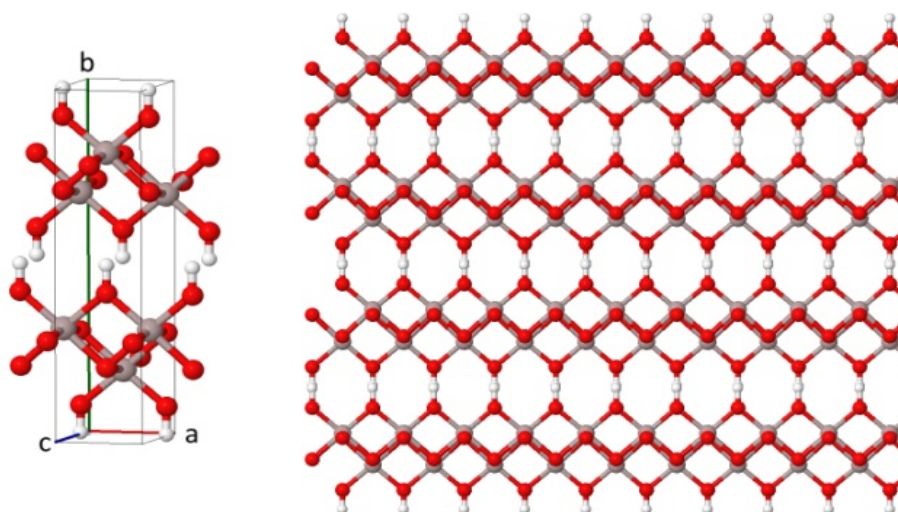
Fig.4. 1 Crystal structure of boehmite (unit cell and material excerpt); Pictures of atomistic structures created with Jmol [157]

Due to the weak bonds boehmite is prone to intercalation, i.e. the inclusion of small molecules, usually water, in between these layers. This causes a larger spacing in [010] direction and a perfect cleavage perpendicular to the general direction of the hydrogen bonding. Boehmite has a preferred growing direction in the a-c plane, which corresponds to the (010) plane [158] and is also prone to dissolving [159, 160]. Therefore, monocrystalline boehmite is not stable in mm range and the boehmite crystal shows a high susceptibility to lattice defects, typically slit-like cracks and domains of amorphous boehmite. Boehmite with an increased spacing in the [010] direction is referred to as pseudo-boehmite, whereas amorphous boehmite is usually referred to as gel. Boehmite can be found in nature or precipitated and grown from solution of aluminum salts and alumina under hydrothermal conditions.

The point of origin for the studies presented in the following was the investigation of commercially available spray dried boehmite nanoparticles (HP14 Sasol, Germany) [125] for their mechanical properties. The results indicated a conspicuously lower stiffness values than expected. Three possible explanations for the low stiffness are considered and discussed in the present work: a) effects related to the crystal size b) slippage of weakly linked boehmite sheets and c) presence of amorphous boehmite domains.

In order to distinguish between these effects, the mechanical properties of a geological sample of boehmite that is comprised of crystalline domains in a μm range is investigated. In this case, effects related to the sample size and influence of an amorphous phase can be ruled out, leaving the slippage of weakly linked sheets.

4.3. Experimental

Boehmite crystals were prepared from a geological sample (denoted as GeoB, on Nathrolith, Saga quarry, Tveidalen, Norway) and mounted on a glass substrate. The crystal is roughly 80 μm in diameter. Since the plane of the preferred crystal growth direction is the largest flat area of the crystal, the double octahedral sheets are parallel to the substrate surface and, therefore, the measurement is taken approx. in [010] direction, i.e. perpendicular to the (010) plane. Mechanical measurements are shown in section 4.3.

All Atomic Force Microscopy (AFM) measurements were carried out with an MFP-3D microscope (Asylum Research, Santa Barbara, CA). Tapping mode and force-distance curves (FDC) AFM were used for topography and mechanical measurements, respectively. The AFM probe used for FDC was from Nanosensors Pointprobe-Plus-NCHR (Nanosensors, Neuchatel, Switzerland) with spring constant k_c of 50 N/m, resonance frequency f_0 of 320kHz and tip radius R of 40 nm.

FDCs were chosen as a well-established method [89, 161] to determine the mechanical properties of boehmite. FDCs have been shown to be a reliable tool to obtain mechanical properties, by probing very little sample volume. This is important, since monocrystalline boehmite can only be obtained in small quantities, too little for other methods, e.g. nanoindentation. In order to record an FDC a microfabricated tip with a radius R, which is mounted on a cantilever with a spring constant k_c is used as a probe. Since the cantilever is assumed to behave linear and elastic, Hook's law relates the applied force F to the cantilever deflection δ:

$$F = k_c \times \delta. \hspace{3cm} \textbf{Eq.4.1}$$

The sample deformation D can be calculated from the deflection δ and the position of the sample Z in Z-direction, which is controlled by the AFM's Z-piezo: $D = Z - \delta$.

From a fit of the Hertz Equation (4.2), using the relation for the reduced Young's Modulus E_{tot} with the samples Poisson's ratio v_s, the tip radius R can be determined, when the Young's modulus E is known, and *vice versa* [88].

$$D = \left(\frac{F}{\sqrt{R} \times E_{tot}} \right)^{2/3} \hspace{2.5cm} \textbf{Eq.4.2}$$

$$\frac{1}{E_{tot}} = \frac{3}{4} \left(\frac{1 - v_{tip}^2}{E_{tip}} + \frac{1 - v_s^2}{E} \right) \hspace{2cm} \textbf{Eq.4.3}$$

Reference measurements on glass substrates were used for this purpose since the mechanical properties of glass are well known (E = 70 GPa, v_s = 0.3). Once the tip radius R is known, the experimental parameters are set and the Young's modulus of any sample can be estimated.

4.4 Results and discussion

FDC measurements of GeoB were conducted on a plateau step, which means that forces were applied roughly perpendicular to the octahedral double planes. As can be seen in the topography of GeoB, shown in Fig.4.2, the surface of the sample is contaminated with amorphous material.
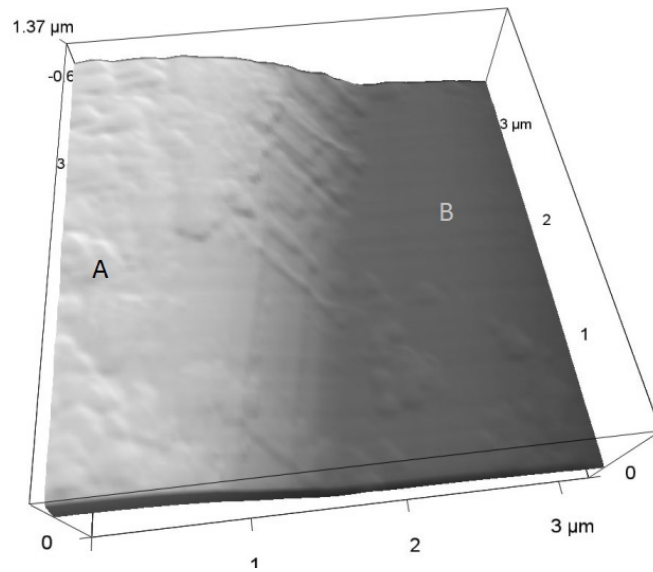
Fig.4. 2 Tapping mode topography of the surface of geological boehmite crystal. The left side (A) is the contaminated surface (or consisting of amorphous boehmite) and the right side of the step (B) is the pure boehmite surface

It cannot be determined if this is amorphous material is boehmite. Only curves on clean spots of the sample were accepted and averaged. From averaged FDCs, the deformation was calculated from the cantilever deflection and the sample position and plotted versus the cantilever deflection which is proportional to the applied force (GeoB curve in Fig.4.3). These experimental curves can be fitted by Hertz, Equation 4.2., yielding a reduced Young's modulus E_{tot}. Applying Equation 4.3 the Young's moduli E_{Epoxy} and E_{GeoB} can be calculated, assuming the Poisson's ratios for epoxy and boehmite to be v_{Epoxy}=0.3 and v_{GeoB}=0.25. The AFM tip's elastic constants are E_{Tip} = 245 GPa and v_{Tip}=0.25. For reference, FDC measurements on glass substrates and epoxy were conducted (Fig.4.3). The results of calculation of the E_{GeoB} reveals that Young's modulus of boehmite is approx. 11 GPa,

confirming that boehmite is much more complaint than expected from the literature values in which $E_{boehmite}$ was predicted to be in the range of 136 to 267 GPa.
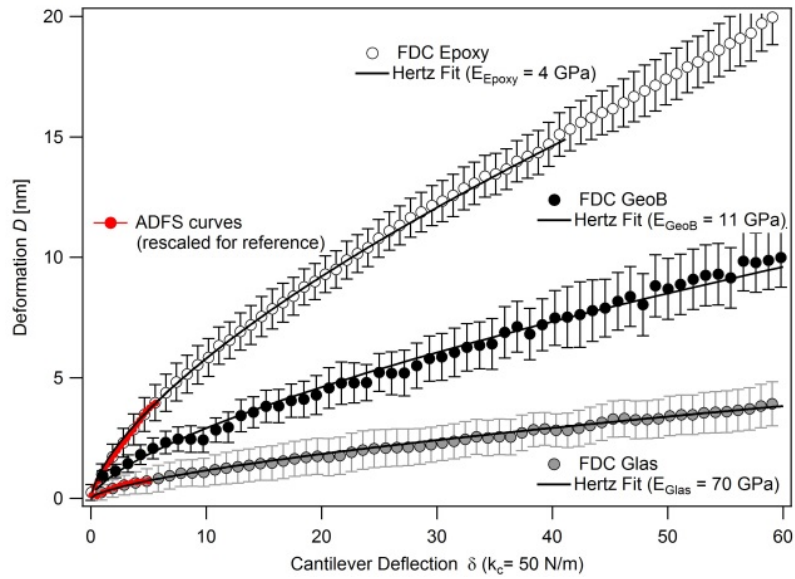
Fig.4. 3 Averaged deformation versus cantilever deflection: experimental curves of glass (grey circles), GeoB (filled circles) and epoxy (blank circles). Standard deviation of the average curve is shown as error bars. The Hertz fit of each experimental curve yields the Young's modulus. For comparison the ADFS curves on glass and epoxy were rescaled and added to the plot (red markers).

in Fig.4.2, force distance curves at two different spots (marked as A and B in Fig.4.3) on GeoB are shown. The hysteresis of the approaching and the retracting part of the curves on (A) spot is considered to reveal inelastic deformations. It should be noted that the deformations at an uncontaminated spot (B) are solely elastic, since there is no hysteresis apparent and only such hysteresis-free curves were accepted for generating the average curve shown in Fig.4.3. It should be also noted that all curves shown in Fig.4.3 are in agreement with the Hertz theory, which also implies that only elastic deformations are induced, since the Hertz theory only considers elastic deformations.
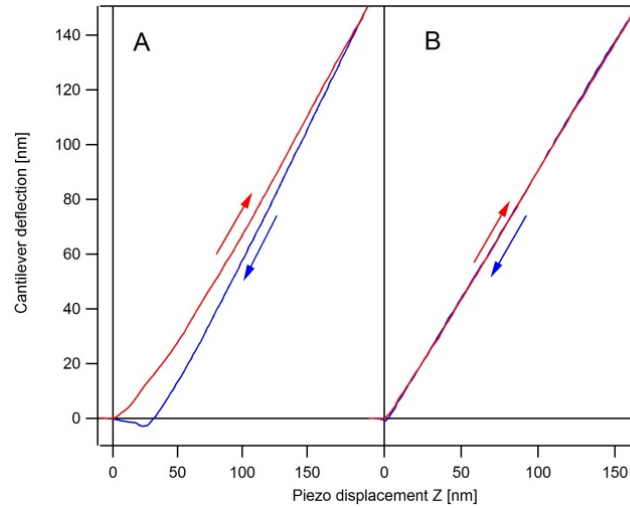
Fig.4.4 FDCs (approach red, retract blue) taken on the spots A (contaminated) and B (clean) in Fig.4.3. Curve A shows a considerable hysteresis. Curve B shows no hysteresis; therefore, purely elastic deformations can be assumed.

The authors hypothesize that in the case of a macroscopic, monocrystalline boehmite (GeoB) the induced deformation leads to local lattice distortions due to plane slippage which will be equilibrated by the far-field lattice structure after the applied force is removed. This is only possible because a) the (010) layers are rather stiff in comparison with the weak bonds between the layers and b) the volume effected by the deformation is small compared to the monocrystalline domain. The compression created in the (010) layers due to the deformation is spread along the whole plane and – acting like a spring- can restore the lattice structure in the deformed volume. The deformations, therefore, appear to be elastic. In case of the nanoparticle's deformations are permanent since there is no unaffected far-field lattice structure. However, for both the micro- and macroscopic boehmite the measured stiffness is much lower than expected due to plane slippage. This hypothesis, on the other hand, is corroborated by simulations emulating the actual AFM test conditions of a particle embedded in epoxy resin. The simulated measurements resulted in substantially lower stiffnesses, 32.5 to 40 GPa, comparable to the experiments on GeoB, when the loading direction did not coincide with [010]. It seems likely that to some extend the stiffness mismatch can be attributed to inevitable load-misalignments in the experiments. Inelastic layer slippage triggered by misalignment of the loading direction is, therefore, identified as the probable cause of the very low stiffness in certain situations (for more details about simulation results, see [162])

4.5 Conclusion

The anisotropic Young's moduli of the perfect boehmite crystal determined by means of MDFEM simulations have values of 232, 136 and 267 GPa in the directions [100], [010] and

[001] respectively. Results of AFM experiments on boehmite nanoparticles, in contrast, showed drastically reduced and seemingly elastic moduli in the range of 10 GPa. Possible causes of the significantly lower values were identified by experiments on complementary types of boehmite, i.e. geological and hydrothermally synthesized samples, and further simulations of imperfect crystals and combined boehmite/epoxy models. Concluding from these investigations, the mechanical behavior of boehmite is dominated by the slippage of weakly linked boehmite layers. The experimental approaching and retracting part of the FDC of the geological sample exhibit no visible hysteresis and hence the behavior appears to be purely elastic. However, further simulations revealed that the inelastic process of layer slippage can be reversed by certain effects, as e.g. for the geological sample, in which the deformations were small compared to the size of the crystal, we hypothesize the conformation of the deformed areas to the far field lattice structure.

Chapter 5: The effect of boehmite (AlOOH) on nanomechanical and thermomechanical properties correlated to crosslinking density of epoxy in epoxy/boehmite nanocomposites

The effect of boehmite nanoparticles (γ-AlOOH) on nanomechanical and thermomechanical properties correlated to crosslinking density of epoxy

Media Ghasem Zadeh Khorasani[a,b,*], Dorothee Silbernagl[a], Paulina Szymoniak[a,b], Vasile-Dan Hodoroaba[a], Heinz Sturm[a,b]

[a] *Bundesanstalt für Materialforschung und -prüfung (BAM), D-12205, Berlin, Germany*
[b] *Technical University Berlin, D-10587, Berlin, Germany*

HIGHLIGHTS

- Boehmite nanoparticles enhance the properties of epoxy by inducing structural changes and alteration of network architecture of epoxy matrix.
- High resolution ImAFM force measurements revealed a significant stiffening effect of boehmite nanoparticles on epoxy matrix.
- High contents of boehmite nanoparticles results in decrease of crosslinking density, meanwhile the stiffness of the nanocomposite is improved.

Abstract

We show that the complex physical and chemical interactions between boehmite nanoparticles and epoxy drastically affect matrix properties, which in the future will provide tuning of material properties for further optimization in applications from automotive to aerospace. We utilize intermodulation atomic force microscopy (ImAFM) for probing local stiffness of both particles and polymer matrix. Stiff particles are expected to increase total stiffness of nanocomposites and the stiffness of polymer should remain unchanged. However, ImAFM revealed that stiffness of matrix in epoxy/boehmite nanocomposite is significantly higher than unfilled epoxy. The stiffening effect of the boehmite on epoxy depends on the particle concentration. To understand the mechanism behind property alteration induced by boehmite nanoparticles, network architecture is investigated using dynamic mechanical thermal analysis (DMTA). It was revealed that although with 15 wt% boehmite nanoparticles the modulus at glassy state increases, crosslinking density of epoxy for this composition is drastically low.

Keywords: boehmite nanoparticles, epoxy resin, nanomechanical properties, atomic force microscopy, intermodulation, crosslinking density

5.1 Introduction

Epoxy resins are well-known for their excellent mechanical properties and being especially good adhesives. Therefore, they are used as matrix in fiber-reinforced composite material for applications such as light-weight construction material [163]. The most important commercially available epoxy resin is diglycidyl ether of bisphenol A (DGEBA). Primary amines and anhydrides are typically used as curing agent [164]. Depending on the final application, the curing agent type, its ratio to the epoxy and the curing time and temperature are varied to reach the optimum mechanical performance. The main challenge with epoxy is the inherent brittleness and low fracture toughness [165]. Boehmite nanoparticles (BNP) are potential candidates to improve the fracture toughness of epoxy while enhancing its modulus at room temperature. The effect of BNPs on a large group of polymers has been already studied [10]. Previous studies report the reinforcing effect of BNPs on epoxy such as increase of shear strength, shear modulus and compressive strength while improving the fracture toughness [11-13, 15, 145, 146]. Jux and coworkers demonstrated that the degree of such enhancements depends strongly on particle concentration. They reported an increase of 26% in tensile modulus and 62% in fracture toughness with adding 15 wt% BNPs to epoxy [12]. Arlt reported a decrease in glass transition temperature (T_g) of epoxy with increasing BNP

concentration and suggested that curing is sterically hindered by BNPs, which results in decrease of crosslinking density in cured epoxy [13]. An in-depth investigation of network density and nanomechanical properties of composite phases is still needed to prove these mechanisms.

Recent works in polymer nanocomposites demonstrated that particles, even in low mass fractions, can result in alteration of bulk polymer properties [166]. It is generally accepted that T_g attributes to molecular mobility. The increase of crosslinking density results in decrease of mobility of chain segments between crosslinks and thus leads to increase of T_g. A simple approximation of network architecture is based on rubbery-like elasticity theory which correlates the crosslinking density to the storage modulus in rubbery state [27]. In thermoplastic nanocomposites, T_g shifts are usually contributed to formation of an interphase [167]. However, in nanocomposites with thermosetting matrices, particularly with crosslinked epoxies, the average crosslinking density can be influenced due to the effect of nanoparticles on the chemistry of curing. In this case, the effect of particles is no longer limited to the nearest polymer layer (interphase) and thus, the bulk alteration of the matrix becomes a dominant effect.

Depending on their physical and chemical properties, nanoparticles can alter the chemistry of curing which results in either decrease or increase of crosslinking density and network homogeneity of the matrix. Here are some examples on the effect of various nanoparticles on epoxy systems: a study has shown that iron particles affect the curing kinetics of epoxy matrix and result in increase of the crosslinking density [168]. Other studies on modified carbon nanotubes have revealed a significant increase in the shear modulus of epoxy above and below T_g as a result of increased crosslinking density [121, 169]. Nevertheless, contradictory results were reported from studies on silica-based particles in epoxy. One study has demonstrated that despite of improvement in elastic modulus, the bulk network structure of epoxy shows regulation by integration of silica resulting in looser network compared to neat epoxy [78]. On the other hand, another study on layered silicate-epoxy nanocomposites suggested the participation of particles in curing reaction which leads to increase of crosslinking density of the epoxy [116].

The aim of the present work is to investigate the effect of boehmite nanoparticles on the nanostructure, local stiffness and crosslinking density of epoxy system. Understanding the nanostructure of epoxy/boehmite nanocomposites can be achieved by performing high resolution AFM-based force measurements, characterizing not only the morphology but also

local mechanical properties. Intermodulation AFM (ImAFM) - a multi-frequency dynamic method - provides us with quantitative force measurements with nanoscale resolution [103]. Dynamic mechanical thermal analysis (DMTA) provides us with information about the crosslinking density of the epoxy matrix. The low strain modulus in glassy state is correlated to the stiffness values obtained from ImAFM while mechanical properties at high temperatures over T_g are related to network architecture of epoxy matrix. In conclusion, we suggest a complementary mechanism to the hypotheses presented in work of others.

5.2 Experimental

5.2.1 Material

Epoxy system used in this study is bisphenol-A-diglycidyl ether (DGEBA, Araldite® LY 556, Huntsman) cured with an anhydride curing agent, methyl tetrahydrophtalic acid anhydride (MTHPA, Aradur® HY 917, Huntsman) and accelerated by an amine, 1-methyl-imidazole (DY070, Huntsman). The mixture of epoxy, hardener and accelerator is 100:90:1 part per weight, respectively. Commercially available spray dried boehmite nanoparticles with orthorhombic shape and primary particle size of 14 nm (DISPERAL HP14, SASOL, Germany) were used. Fankhänel and coworkers have determined the experimental average elastic modulus of boehmite to be approx. 10 GPa [162].With respect to the plane orientation, this value can show deviations from 10 GPa. Suspensions of 30 wt% BNP are blended with DGEBA and diluted with DGEBA to reach certain weight percentiles (0, 2.5, 5, 10, 15 wt%). Mixtures are cured for 4 hours at 80 ˚C to reach gelation and 4 hours at 120˚C for post-curing as suggested by the manufacturer to obtain a fully cured system.

For all measurements in this study, cured nanocomposite samples were prepared by the German Aerospace Center (DLR), Braunschweig, Germany). Details about particle dispersion and curing process of the samples used in this study are described in detail elsewhere [11, 12] Here, the anhydride-cured epoxy DGEBA/MTHPA/DY070 with the mixing ratio of 100:90:1 are named as EP, and the nanocomposites as EP/BNPx (x corresponds to the weight percentage of BNPs).

5.2.2 Methods

All AFM measurements (tapping mode and ImAFM) were conducted with an MFP-3D AFM (Asylum Research, Santa Barbara, CA). The AFM probe used is Mikromasch, HQ:NSC35 (Wetzlar, Germany). Here we implemented a lock-in amplifier and a software designed by Intermodulation Products (Sagersta, Sweden) added to the MFP-3D AFM setup to perform dynamic force curves (Amplitude-dependence force spectroscopy- ADFS). For the analysis of

ADFS curves and creating stiffness images we used software developed in our group. The resonance frequency and spring constant of the cantilever are determined by non-invasive thermal noise method [84]. The cantilever has a spring constant k_c of 13 N/m, resonance frequency f_0 of 202 kHz and tip radius R of approx. 23 nm. Surface polishing and plasma cleaning were carried out to prepare the surface of samples for AFM measurements.

In ImAFM mode, the cantilever is driven by two frequencies above and below its resonance, $f_0 \pm 0.5$ kHz. As a result, the cantilever movement contains both frequencies leading to a beating waveform of the amplitude. When engaged with the surface, the linear response of a free cantilever is distorted due to the non-linear tip-surface interaction and two frequencies mix with each other (intermodulation) which yields responses at new frequencies. These responses which are called intermodulation products (IMP) are collected using a multi-frequency lock-in amplifier. For each image pixel within the scan in X and Y direction, the amplitudes and phase shifts of each IMP frequency comb are extracted by Fourier transformation of the oscillating deflection $d(t)$. Since the amplitude of the oscillation is directly correlated to the force F, two force quadrature curves with dependency on amplitude can be constructed: 1) in-phase with the cantilever's motion which is conservative and describes the elastic behavior of the material. 2) out-of-phase which describes the dissipative forces. Amplitude-dependence force spectroscopy (ADFS) curves obtained from the conservative part of tip-surface force can be treated as conventional force-distance curves (FDC) [103, 105].

Dynamic thermal mechanical analysis (DMTA) spectra were recorded using a ATM3 torsion pendulum (Myrenne, Roetgen, Germany). In this method a clamped sample is loaded with an oscillating pendulum. The sinusoidal shear deformation induces a free oscillation of the pendulum at frequency of 1 Hz with 1° strain. The measured oscillation period and damping are used to calculate the complex modulus G^*. The storage and loss moduli, G' and G'' are determined as a function of temperature. In this work, the temperature is ramped up from 20 to 200°C with the heating rate of 1 K/min. The maximum temperature 200°C was chosen carefully to avoid any degradation (see SM4). The measurement is carried with the presence of nitrogen gas in the chamber. DMTA torsion pendulum was chosen over other DMTA modes (e.g. three-point bending or compression) due to high sensitivity and applying low strain which allows to stay in the linear regime through the entire measurement. DMTA measurements are carried out on epoxy samples containing 0, 1, 2.5, 5, 10 and 15 wt% BNP content. Sample dimensions are 32 mm x 5 mm x 1 mm. Each sample was measured through

first heating up (first run), cooling down and second heating up (second run). Both heating cycles are evaluated.

Thermogravimetric analysis (TGA) was performed using a STA7000 Series Thermogravimetric Analyzer (Hitachi, Chidoya, Japan), employed with a horizontal dual balance beam, enabling a microgram-level weight change detection. Samples of 8-13 mg were heated in alumina pans from room temperature up to 1000 °C at a heating rate of 10 °C min^{-1}. Nitrogen was used as a purge gas up to approximately 600 °C to avoid oxidation reactions, thus ensuring that the sample reacts only to temperature during decompositions. At temperatures from 600 to 1000 °C, above standard pyrolysis temperatures, oxygen was used in order to oxidize the remaining pyrolytic char.

The spatial distribution of BNPs in EP/BNP15 was investigated by scanning electron microscopy (SEM) using a Zeiss Supra 40 microscope (Zeiss, Germany) equipped with a high-resolution cathode of Schottky type and conventional Everhart-Thornley (ET) and In-Lens secondary electron (SE) detectors. For better observation of the nanoparticles in the sample volume, the SEM was operated in the transmission mode, i. e. the so-called T-SEM mode [170] , which offers a superior material contrast. For this purpose, free-standing 100 nm thin sections of EP/BNP15 were prepared by ultramicrotomy and deposited carefully on typical carbon TEM grid. It was not necessary to apply a conductive thin layer onto the microtome-cut sections, as they were sufficiently electrically conductive.

5.3 Results

The spatial distribution of BNPs in epoxy was evaluated from T-SEM micrographs as exemplary presented in Fig.5. 1. First, it must be noticed that the high-resolution T-SEM used allows the (expected) identification of individual embedded primary nanoparticles of 14 nm. Application of high-resolution, surface-sensitive SEM with the InLens detector is confronted with the problem to distinguish clearly the buried nanostructures from potential morphological artifacts at the sample surface. Based on the T-SEM images, besides a few larger agglomerates, the overall distribution of the nanoparticles within the matrix can be considered as homogeneous. Particles mainly form agglomerates in the range of 100-200 nm size and single particles with the primary size of 14 nm are only rarely recognized.
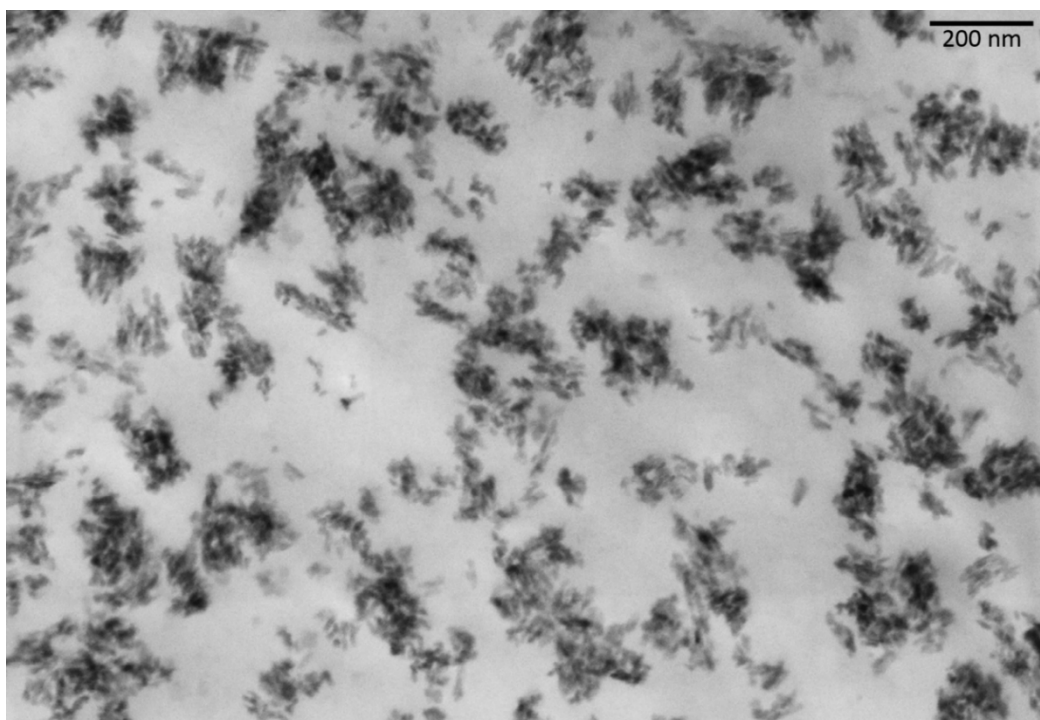
Fig.5.1 20 kV T-SEM micrograph of BNPs in anhydride-cured epoxy prepared as ultramicrotomed section.

Tapping mode AFM topography images of different scanned sizes of EP/BNP15 are presented in Fig.5. 2.a and b. Here, the morphology of agglomerates and distribution of the particles are similar to those observed by T-SEM. Here, besides the topography, a compositional contrast is also required to distinguish between particles and other topographical artifacts due surface contamination or the well-known nodular morphology of epoxy matrix [171, 172]. Thus, we consider the oscillation phase contrast to verify the location of particles as for a small scanned area presented in Fig.5. 2.c. This area is further evaluated by ImAFM.
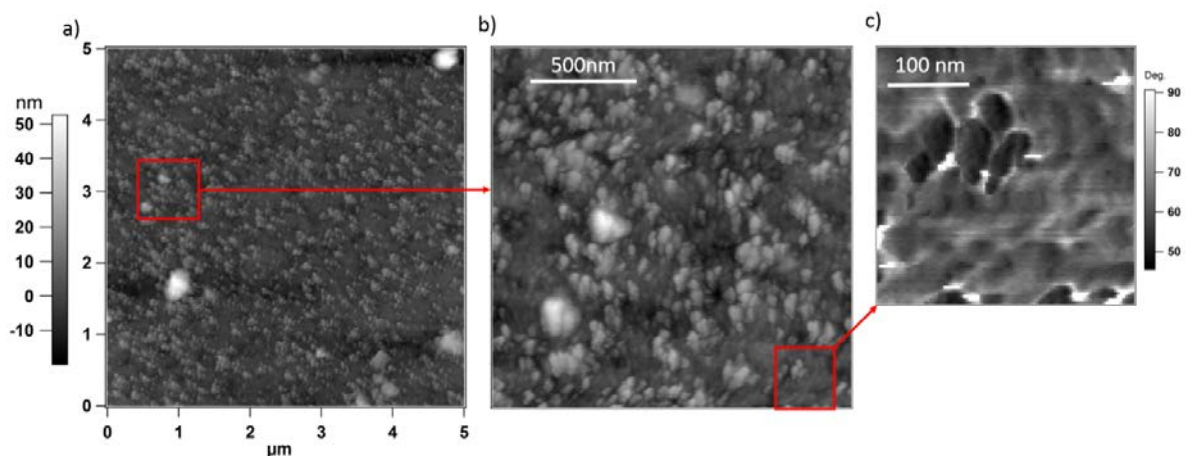
Fig.5. 2. a) and b) tapping mode AFM topography and c) phase image of anhydride/cured epoxy with 15wt% boehmite nanoparticles (EP/BNP15).

5.3.1 Intermodulation AFM:

For probing the mechanical properties of each component of the nanocomposite separately, the scan size for ImAFM needs to be small and carefully selected to include both small particles and areas of undisturbed matrix. From each pixel of the ImAFM scanned area, an ADFS force curve is obtained which can be treated similar to conventional force-distance curves. The slopes in the repulsive regime are correlated to the stiffness and the area of net attractive regime corresponds to attractive forces (mainly Van der Waals) between the tip and the sample. In addition to topography image, the work of attractive force W_{attr} is used as an additional channel to precisely locate the particles and separate their force curves from force curves of matrix. The maps of stiffness and W_{attr} together with corresponding topography of the scanned area of EP/BNP15 are shown SM1.1. Here we only focus on two main components of the nanocomposite, particles and matrix. In-depth investigations of interphase properties include more complex analysis of ImAFM data which will be published elsewhere [173].

Fig.5. 3 presents the stiffness histograms of bulk matrix and BNPs separated from the overall stiffness histogram of the scanned area in EP/BNP15. The scanned points from which the stiffness values are taken, are shown in colored pixels in the 3-D topography inset image of Fig.5. 3. Surprisingly, the stiffness values corresponding to epoxy are higher than of BNPs. To investigate this effect, the stiffness of neat epoxy and other concentrations requires be determined using the similar approach and compared to EP/BNP15. The lowest concentration that we could reliably locate nanoparticles with the scanned volume is 2.5 wt%. Below this concentration spotting the nanoparticles is very challenging. Since the scanned areas by ImAFM have typically a size of below 500 x 500 nm, the particle concentration varies extremely in such an area, as can be seen for example in Fig.5. 1. Thus, it is not possible to distinguish the effect of particle content between 2.5 or 5 and 10 or 15 wt% respectively from a local effect. Therefore, systematic study of changes in concentration is only possible with comparing two extremes of concentrations, here 2.5 and 15 wt% with neat epoxy. Topography, map of stiffness and W_{attr} for EP/BNP2,5 and EP are presented in SM1.2 and SM1.3, respectively.
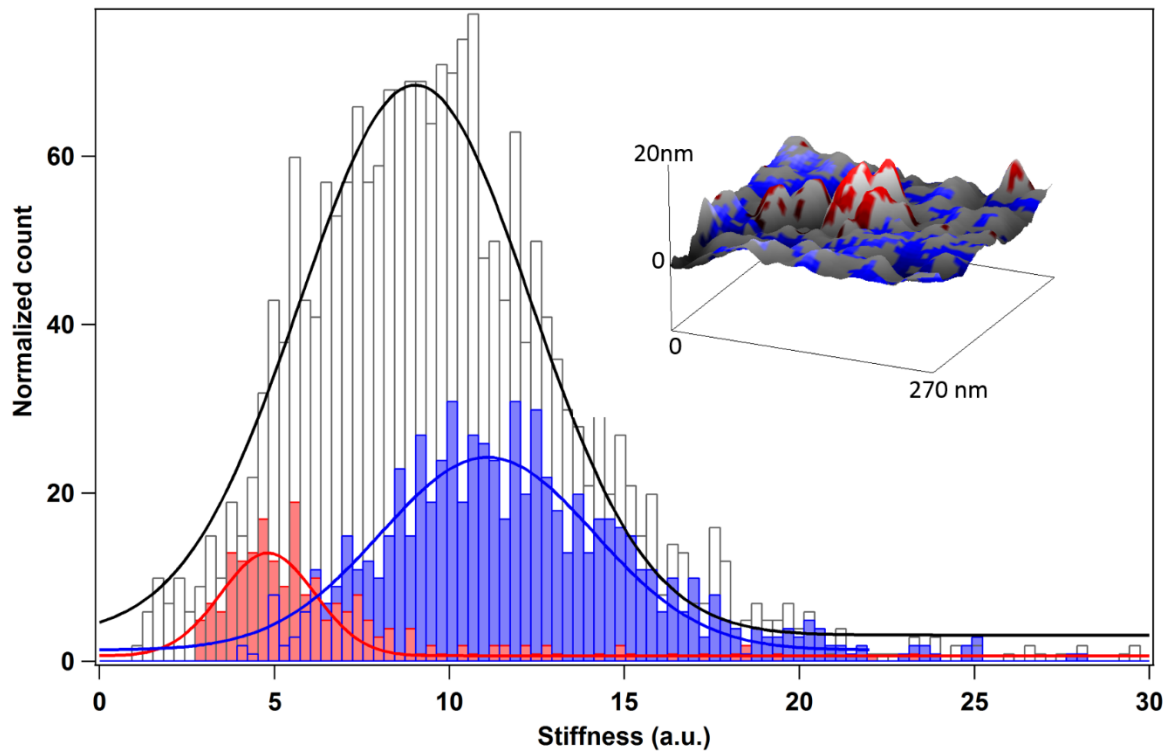
Fig.5. 3. Stiffness histogram from ImAFM measurements on EP/BNP15 from the overall scanned area shown in the 3D topography (white bars). Only the selected pixels shown in color red and blue of the inset image where taken as stiffness values of BNPs and epoxy, respectively, which are shown as stiffness histograms. Blue bars are related to epoxy phase (blue regions) and red bars are related to BNPs (red regions) of the inset 3D image. Gaussian fits are shown as solid lines.

In Fig.5. 4, comparison of the stiffness values related to bulk epoxy in EP, EP/BNP2.5 and EP/BNP15 clearly shows the stiffening effect of boehmite on the bulk epoxy matrix which increases with increasing particle content. The stiffness of neat epoxy is considerably lower than of BNPs as expected from the initial Young's modulus values of epoxy (3.3 GPa [12]) and boehmite (10 GPa [162]). However, the stiffness of epoxy increases with introducing BNPs. The stiffening effect of nanoparticles on crosslinked matrices have been previously reported [174]. Huang and coworkers demonstrated that the bulk PDMS in the presence of silica particles has a higher stiffness compared to that of neat PDMS. However, in our study, the stiffening effect of BNPS on epoxy matrix at high particle concentration (here, 15 wt%) is in such an extent that local stiffness value of epoxy exceeds the stiffness of BNP particles, results in an inversed composite property. In this case, BNPs act as plasticizers in a highly stiff epoxy matrix. It is noteworthy that despite of increase in maximum stiffness values of epoxy matrix, the width of the stiffness distribution (the error bar in inset Fig.5. 4) increases with increasing particle concentration. This implies that although the overall stiffness is increasing, the epoxy matrix in the presence of high concentrations of boehmite exhibits a

more heterogeneous behavior compared to neat epoxy. Heterogeneities are known to help dissipating energy and prevent crack propagation and brittle fracture. The increase of fracture toughness with increasing BNP concentration in composite system similar to this study has been e reported elsewhere [12].
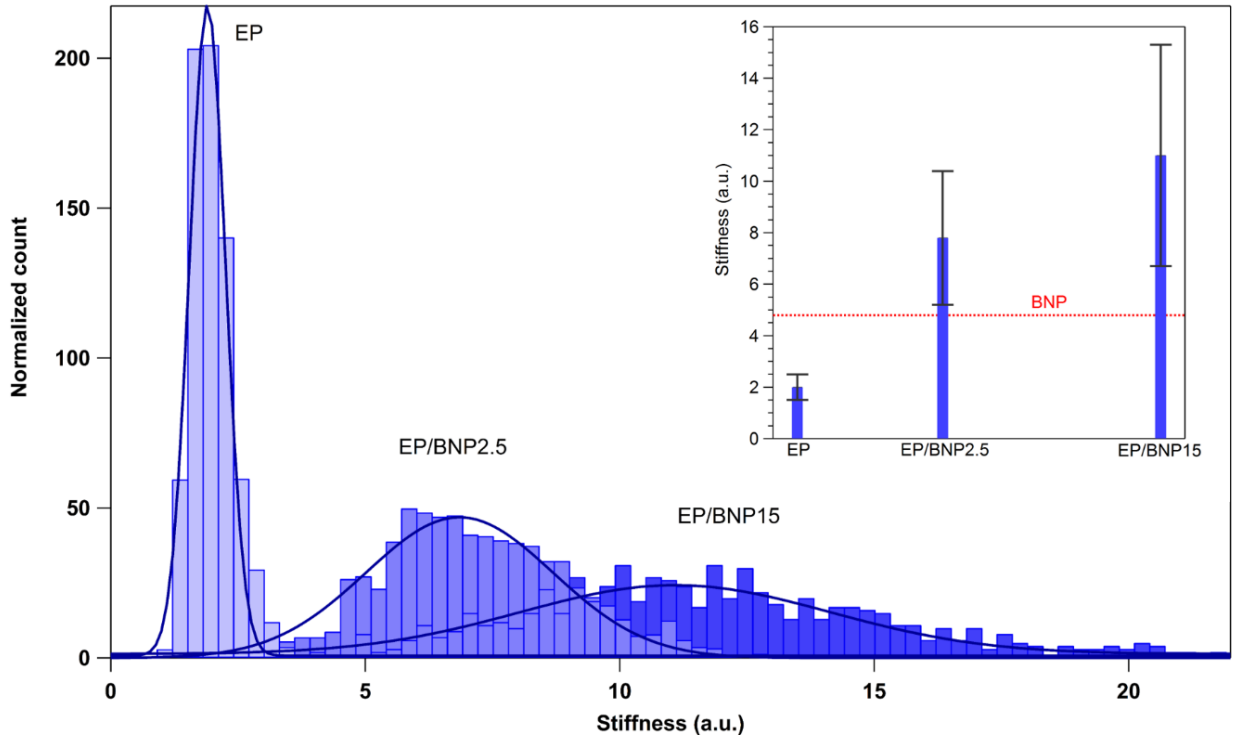
Fig.5. 4. Stiffness histogram from ImAFM of exclusively epoxy matrix, in EP/BNP2.5 and EP/BNP15 compared to neat epoxy EP. The inset plot compares the average stiffness values and the standard deviation are shown with error bars obtained from the gaussian fit (solid lines) of the stiffness histograms. The red dashed line in inset plot corresponds to the average stiffness value of BNPs in EP/BNP15 shown in Fig.5. 3.

An important remark on the stiffening effect of boehmite on epoxy, is that the Young's modulus of epoxy matrix is changed accordingly and therefore the assumption from previous studies that the increase in the modulus of elasticity is exclusively due to the contribution of particle modulus must be revised [12, 13, 15]. Considering that the Young's modulus of the matrix phase is no longer a constant but a variable of the particle concentration, theoretical micromechanical models such as Halpin-Tsai [53, 57] fail to explain the behavior of this material. Comparison of experimental elastic modulus with Halpin-Tsai for various particle concentrations for EP/BNP15 is presented in supplementary material (SM2).

Since the ImAFM measurements are carried out at room temperature, the stiffness values qualitatively correlate to low-strain moduli of epoxy at glassy state. It is known that the glassy state moduli of epoxy systems are mainly related to chain interactions, intra- and

intermolecular noncovalent bonding and intermolecular packing [71, 175]. The decrease of crosslinking density results in better chain packings and thus increases the glassy state modulus. Thus, we hypothesize that the stiffening effect of BNPs on epoxy is due to inducing changes to crosslinking chemistry of epoxy and anhydride. Information about crosslinking density can be obtained from dynamic mechanical analysis at elevated temperatures by evaluation of material response at glass transition and rubbery state which presented further in DMTA section.

5.3.2 DMTA measurements

DMTA measurements are performed to investigate the effect of BNP concentration on thermomechanical properties of EP/BNP nanocomposite and approximation of crosslinking density of epoxy matrix. All measurements are carried out on samples with 0, 1, 2.5, 5, 10 and 15 wt% boehmite content. The mechanical responses of nanocomposites were obtained as a function of temperature starting from the glassy state, through glass transition and reaching rubbery state. The temperature ramp was done twice for each sample, further referred as "first run" and "second run". The modulus values obtained from only the first heating is comparable to stiffness values obtained from ImAFM and tensile modulus tests provided previously in literature [12, 13, 15]. Since samples experience elevated temperatures during the first DMTA ($T > T_g$), the results of second DMTA measurements are evaluated separately to demonstrate the effect of temperature treatment on thermomechanical properties of the nanocomposites.

5.3.2.1 Effect of BNP concentration (first run)

The storage shear modulus(G') and loss tangent (*tan δ)* as function of temperature for samples with different particle concentrations are presented in Fig.5. 5.a and b, respectively. The storage modulus at glassy state is correlated to material stiffness under shear deformation. An increase in glassy state modulus with increase of BNP concentration is clearly observable (Fig.5. 5.a). The same tendency was reported on static mechanical properties (tensile modulus) of similar composite systems [12].

69
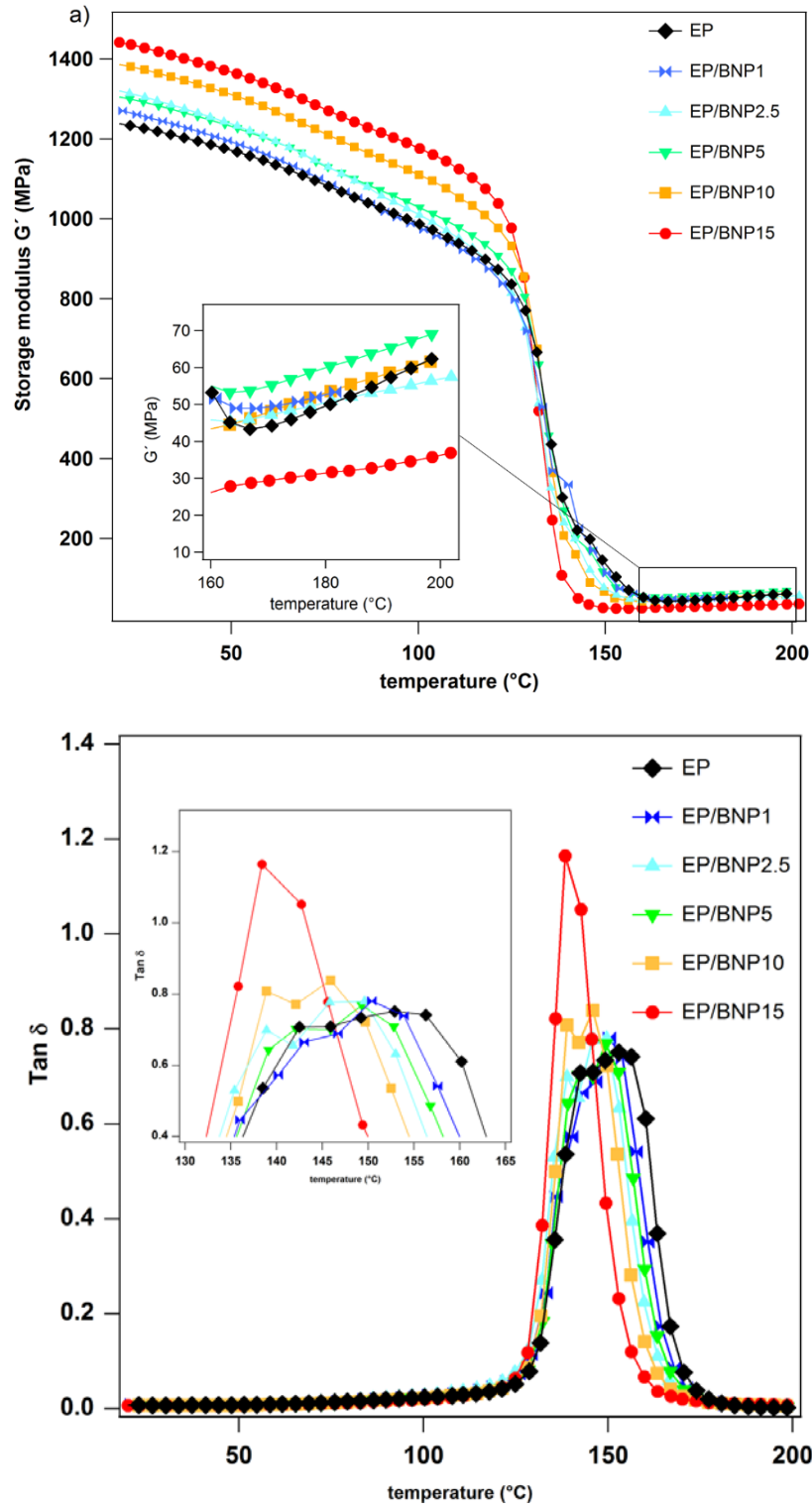
Fig.5. 5. a) storage shear modulus and b) loss tangent *tan* δ versus temperature for anhydride-cured epoxy nanocomposites EP/BNPs with different boehmite nanoparticle concentrations.

However, in the rubbery state, the storage shear modulus shows a different behavior: the inset image of Fig.5. 5.a shows that for EP/BNP15 the storage modulus in the rubbery plateau drastically decreases. There is an approximation of crosslinking density based on theory of

rubber elasticity, in which crosslinking density v, is correlated to the storage shear modulus G' at rubbery state, R is the gas constant and T is the absolute temperature [35, 36, 176]:

$$G'=vRT \qquad \qquad \textbf{Eq.5.1}$$

Eq.1 is proposed for lightly crosslinked systems such as rubbers in which the elasticity is purely entropic, or the energy contribution of elasticity is negligible. In case of a highly crosslinked system with heterogenous phases consisting of nanoparticles, the intra- and intermolecular forces cannot be neglected and therefore the contribution of energetic elasticity needs to be considered. By taking energetic elasticity G_e into account, correlation between modulus G' and crosslinking density v can be approximated via Eq.2 [42].

$$G'=G_e+vRT \qquad \qquad \textbf{Eq.5.2}$$

As suggested by Pohl and coworkers [42], by extrapolating the rubbery plateau to absolute zero temperature, the axis intercept represents G_e which can have both negative or positive values. The slope of $G'(T)$ at rubbery state is taken as an approximation for v .

G', v and G_e values are calculated for all measured nanocomposites and listed in Table.5. 1. EP/BNP15 has the lowest crosslinking density while showing the highest modulus at glassy state. At first glance, the behavior of EP/BNP15 appears counterintuitive. However, as discussed before, the glassy state modulus is not correlated to crosslinking density. The glassy state modulus is mainly governed by non-covalent intra- or intermolecular interactions and intermolecular packing. In contrast, rubbery state modulus relates to the actual covalent crosslinks occur during the curing process. Here, the increase in glassy state modulus of the nanocomposite is partially related to the mechanical properties of particles. The other part is related to changes in the inherent properties of epoxy (as observed with ImAFM) which resulted in increase of intermolecular packing due existence of less covalent crosslinks and inter and intra-chain hydrogen bonding which may be caused by BNPs.

It is observed for all nanocomposites that G_e shifts to smaller values compared to unfilled epoxy, although no linear dependence to the particle concentration is observed. The magnitude of G_e shows its minimum at highest nanoparticle concentration (EP/BNP15). This comparison indicates that with high particle concentrations, following the argumentation of Pohl and coworkers, the response of the network at high temperatures is more entropy driven. According to the theory of rubber elasticity [35], an entropy driven network response is typical for rubbers, i.e. more lightly crosslinked networks. In lightly crosslinked networks,

71

segmental chains have high mobility and less inter- and intramolecular forces compete with entropic elasticity. This means that in EP/BNP15, the matrix is comprised of a more lightly crosslinked network compared to unfilled epoxy.

The *tan δ* spectra obtained from the nanocomposites with different particle concentrations are presented in Fig.5. 5.b. For the determination of the glass transition temperature T_g with DMTA, it is common to take either the maximum value of loss modulus or of *tan δ*. In this work the latter was chosen (the loss modulus spectra are presented in SM3.1). The analysis of *tan δ*, namely the position of peak maximum (T_g), peak height and width of half-height for each composition is presented in Table.5. 1. It can be observed that T_g decreases with increasing BNP concentration. This is in the agreement with the trend observed in T_g values obtained from DSC [15]. Decrease of T_g is another indication of decreasing the crosslinking density [177].

The shape of *tan δ* peak including height and width also provide additional information about network structure. It is observed that besides T_g shift to lower values, *tan δ* peak also gets narrower with increasing BNP content. Broad *tan δ* peak indicates a wide distribution of molecular weight between crosslinks and therefore high heterogeneities of the network. The heterogeneous nature of cured epoxy were previously reported [38, 171]. Kishi and coworkers attributed the heterogeneities to formation of local regions with low crosslinking densities[38]. Here, the bimodal peak observed for unfilled epoxy indicates that the polymer is a heterogeneous mixture of two distinguishable phases. As BNP content increases, the peak gets narrower and consequently a high sharp unimodal peak appears for 15wt% BNP content. Table.5. 1 shows that for EP/BNP15, the width of half-height reduces up to 50% compared to EP. The sharp unimodal peak of EP/BNP15 shows that with high BNP concentration, the chemical network of epoxy becomes more homogenous although the crosslinking density is low. The changes in the height of *tan δ* peak for high particle concentration is also noteworthy. This value for EP/BNP15 shows approx. 60% increase compared to the height value in EP. The height of *tan δ* is associated with segmental mobility of network [175]. This implies that in EP/BNP15, polymer segments between crosslinks has a higher mobility compared to EP which can be caused by formation of a network with lower crosslinking density. Another reason can be the existence of high number of free chain ends in the network of EP/BNP15 or high number of unreacted monomers between the chains, which has higher mobility than the chains between crosslinks. Evidences on existence of a small fraction of

unreacted monomers in EP/BNP with increasing BNP concentration has been observed with thermogravimetric analysis (SM4).

Table.5. 1. Analysis of storage shear modulus, *tan δ* curves and the approximation of crosslinking density for each nanocomposite obtained from DMTA (first run).

composition	Storage modulus G' at room temperature (MPa)	Absolute value of Energetic elasticity G_e (MPa)	Crosslinking density ν (mol m^{-3}) $*10^6$	Glass transition temperature T_g (˚C)	Width of half-height (K)	Peak Height (a.u.)
EP	1239	232	7.7	153	28	0.75
EP/BNP1	1270	111	7.3	150	25	0.78
EP/BNP2.5	1322	98	6.9	149	23	0.77
EP/BNP5	1307	163	8.7	149	23	0.78
EP/BNP10	1388	171	7.7	146	20	0.84
EP/BNP15	1442	69	4.4	140	14	1.17

5.3.2.2 Effect of temperature (second run)

So far, observations show that boehmite distorts the curing process and consequently alter the network density of epoxy, particularly at higher particle concentrations. The heterogeneous nature of epoxy network which appears as wide bimodal T_g peak in the first run can be due to existence of segments which are not fully reacted. In this case it is expected that exposure to high temperatures during the first run causes an additional post-curing and consequently the matrix system will become more homogeneous with higher crosslinking density. Since boehmite has a higher thermal conductivity than epoxy, the question arises about the role of boehmite in the curing process by regulating the curing temperature. To investigate this effect, DMTA measurements from the second run are evaluated and compared with the first run. The storage modulus and *tan δ* spectra obtained from the second run were quantitatively analyzed and presented in SM3.2 and SM3.3, respectively.

In Fig.5. 6, *tan δ* peak of EP and EP/BNP15 from the first run are compared to those from the second run. As mentioned before, the bimodal *tan δ* spectrum for EP is an indication of two segmental motions which represent two different network characteristics which we here call "*network A*" with T_g of 155 ˚C and "*network B*" with T_g of 141 ˚C. In the second run, the

temperature affected the *network B* and what remains is the *network A* (T_g of 155). This indicates that EP went through additional curing during the first run. The network with low crosslinking density (*network B*) is hypothesized to be formed due to existence of not covalently bonded segments of the network. During the DMTA measurement the material, for the first time after the preparation, experiences temperatures higher than its T_g. It seems that at $T > T_g$, epoxy goes through a post-curing which leads to formation of additional chemical crosslinks and the network becomes homogeneous. The peak related to *network A* does not show any changes with exposure to high temperatures and hence this part of epoxy network has already reached its maximum crosslinking.
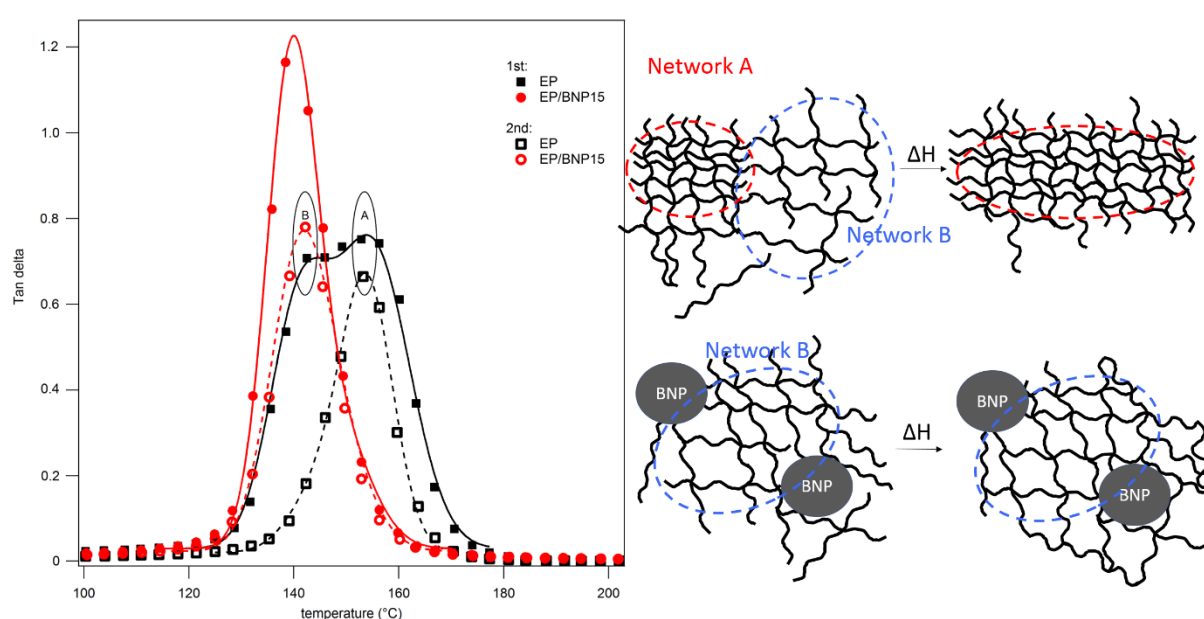
Fig.5. 6. Left: *tan* δ peak in first (filled red circles) and second (unfilled red circles) run of anhydride cured epoxy with 15wt% boehmite (EP/BNP15) compared with those of unfilled epoxy (EP). Right: simplified schematic of the effect of temperature on unfilled epoxy and EP/BNPs on the network topology of the epoxy.

In the first run for EP/BNP15, *tan* δ peak is sharp and narrow, showing a maximum value close to that of the *network B* observed in EP. In the second run, unlike the neat epoxy, for EP/BNP15 the maximum and the width of the peak remains constant. It is expected that the low-crosslinked network of EP/BNP15 goes through the same post-curing as observed for *network B* in EP. However, based on these observations, EP/BNP15 has already reached its maximum crosslinking density during the preparation and further at elevated temperatures, no major crosslinking occurs. According to TGA-MS measurements (SM4), there is a larger number of unreacted anhydrides and DGEBA monomers in EP/BNP15 compared to EP. Although the mobility of these unreacted species increases at elevated temperatures, they are confined by the presence of large particles, thus the participation in further polymerization

74

and formation of network is less possible for the confined monomers. Based on TGA measurements, at temperatures higher than 150 ˚C, the unreacted anhydride molecules desorb from the material, decreasing the chances of post-curing.

5.4 Discussion

We observed that BNPs induce changes in the epoxy matrix which lead to increase in stiffness of bulk matrix at room temperature (glassy state) while the network density is decreased. At first glance, this seems counterintuitive. However, a number of studies have demonstrated that in epoxy systems, the low strain modulus in glassy state is predominately correlated with intramolecular hydrogen bonding, free volume and intermolecular packing, while crosslinking density is the main factor of mechanical behavior at rubbery state [71, 175, 178]. Therefore, the mechanism behind the behavior in these two regions must be addressed separately.

Generally, three different mechanisms are proposed for the effect of particles on the curing behavior of epoxy[166]: 1) Particles with higher thermal conductivity than the polymer, function as a temperature regulator within the matrix and consequently the curing behavior is changed. 2) Particles disturb the polymer network due to steric limitations which results in decrease of crosslinking density. 3) Due to attractive forces between particle and matrix, the mobility of polymer chains are restricted which results in changes in curing by local alteration of stoichiometric ratio of resin and the hardener in the curing mixture in different distances from the particle. Here we discussed these three possibilities:

Since boehmite has a higher thermal conductivity than epoxy, it was proposed that BNP affects the curing process by homogenizing the temperature in the reaction volume. However, the comparison between the first and second runs of DMTA measurements, shows that BNP and temperature treatment influence the post-curing in a significantly different way and result in different thermomechanical behavior. While boehmite decreases the crosslinking density of the epoxy, exposure to high temperatures results in increase of crosslinking density. Therefore, the effect of boehmite as a temperature regulator is insufficient to describe the mechanical behavior and crosslinking density of anhydride-cured epoxy nanocomposite.

The increase in the number of unreacted monomers of epoxy and hardener with increasing the BNP content was observed with TGA-MS. Therefore, it is probable that BNPs decrease the crosslinking density of epoxy by sterically hindering diffusivity of monomers during the curing process. The steric hindrance of crosslinking by particles is a physical phenomenon which is related to the size and structure of particles and polymer. Therefore, it is expected to

be observed in all boehmite-epoxy nanocomposites. However, in other studies on BNPs in a different epoxy system (with amine hardener) different behaviors were reported [115, 149]. The DMTA results in these studies showed that neither T_g nor the crosslinking density was decreased. In some cases, the opposite effect was reported. It is clear, that the contradictory observation between these reports and observations in this study is due to chemical and physical interaction between BNPs and the matrix components. Therefore, in addition to sterically hindering the diffusion of monomers within the curing volume, the decrease of crosslinking density can be due to preferential absorption of anhydride on the surface of BNPs. This preferential absorption can lead to covalent bonding or hydrogen bridging between the carbonyl and hydroxyl group. The evidences of strong interaction between BNPs and anhydride will be published elsewhere[179]. Another consequence of BNP- anhydride interaction is formation of phase segregation near the BNP interphase which results in less reactive groups of anhydrides to be available for epoxy to react. Therefore, the unbalanced stoichiometric ratio is expected to result a reduced crosslinking density.

5.5 Conclusion

Local nanomechanical properties of anhydride-cured epoxy- BNP nanocomposite has been evaluated using ImAFM. The high resolution of this method allowed us to compare the stiffness of epoxy matrices in samples with different nanoparticle content by precisely distinguishing the force curves related to nanoparticles and polymer. It was observed that BNPs has a significant long-range stiffening effect on bulk epoxy matrix which increases with increasing particle concentration. At higher concentrations of BNP, the stiffening effect of epoxy is in such an extent that the stiffness value of epoxy can locally exceeds the stiffness of particles resulting in an inverse configuration in which particles act as plasticizer for the stiff matrix. The stiffening effect of BNP on epoxy is hypothesized to be due to alteration of network density during the curing process as a result of strong particle-polymer interaction Using DMTA, investigations of crosslinking density of epoxy network in the presence of BNPs were carried out by evaluating the loss tangent peak characteristics and the rubbery state modulus. It was revealed that at high nanoparticle concentrations (15wt%) T_g and consequently the crosslinking density of epoxy network decreases significantly. The stiffened matrix together with contribution of the modulus of nanoparticles results in total enhancement of modulus of this nanocomposite compared to unfilled epoxy Meanwhile in 15wt% nanocomposite, a looser network with higher mobility of segmental chains together with existence of unreacted monomers results in significant increase of fracture toughness and

hinderance of crack propagation. The second run DMTA reveals that meanwhile the unfilled epoxy does not reach its maximum crosslinking by the suggested curing temperature program, the network density and T_g of 15wt% nanocomposite does not show a considerable change during the temperature cycles, which indicates that the maximum crosslinking for this composition can be reached with lower curing temperatures.

Based on evidences in this work and an ongoing investigations of chemical interactions between boehmite and epoxy resin and hardener, we suggest a mechanism for nanoparticle-polymer interaction in epoxy-boehmite nanocomposites which explains the decrease of crosslinking density meanwhile the increase of stiffness of matrix: The high number of hydroxyl groups on the surfaces of boehmite results in absorption of anhydride hardener (MTHPA) on the surface of nanoparticles via hydrogen bonding or covalent bonding. Thus the curing chemistry of epoxy will be affected by i) promoting a different polymerization pathway by initiation of hydroxyl groups [180] ii) changes in stoichiometric ratio of hardener and epoxy and consequently formation of a network with different architecture (lower crosslinking density). An epoxy network which is loosely crosslinked due to chemical and physical interference of BNPs is able to form higher number of intra- and intermolecular noncovalent bondings and enhance the chain packings, resulting in higher stiffness compared to a highly crosslinked epoxy network The local chemical composition of epoxy matrix and interphase using AFM-IR techniques, the interaction between boehmite and epoxy mixture components and a systematic study on mechanical properties of networks with varied stochiometric ratio are subjects of further studies.

Acknowledgement

Chapter 6: Insights into nano-scale physical and mechanical properties of epoxy/boehmite nanocomposite using different AFM modes

This chapter is reproduced with permission from the accepted manuscript of: **Ghasem Zadeh Khorasani, Media**; Silbernagl, Dorothee; Platz, Daniel; Sturm, Heinz. 2019. "Insights into Nano-Scale Physical and Mechanical Properties of Epoxy/Boehmite Nanocomposite Using Different AFM Modes." *Polymers* 11, 2 (2019): 235.

*Supporting information is given in Appendix II

Media Ghasem Zadeh Khorasani [1,2,*], Dorothee Silbernagl [1], Daniel Platz [3] and Heinz Sturm [1,4]

[1] Bundesanstalt für Materialforschung und -prüfung (BAM), Div. 6.6, D-12205 Berlin, Germany; dorothee.silbernagl@bam.de (D.S.); heinz.sturm@bam.de (H.S.)
[2] Department Polymertechnik/Polymerphysik, Technical University of Berlin, D-10587 Berlin, Germany
[3] TU Wien, Institute of Sensor and Actuator Systems, A-1040 Vienna, Austria; Daniel.Platz@tuwien.ac.at
[4] Department Mechanical Engineering and Transport Systems, Technical University of Berlin, D-10587 Berlin, Germany
* Correspondence: media.ghasem-zadeh-khorasani@bam.de

check for updates

Abstract

In boehmite-epoxy nanocomposites, it is crucial to understand the interaction between the matrix and nanoparticles and the properties of interphase to understand the mechanism behind the enhancements of macroscopic properties such as Young's modulus and fracture toughness. Here, we demonstrate benefits of using multifrequency intermodulation atomic force microscopy (ImAFM) to obtain information about conservative, dissipative and van der Waals tip-surface forces and probing local properties of nanoparticles, matrix and the interphase. We utilize scanning kelvin probe microscopy (SKPM) to probe surface potential as a tool to visualize material contrast with a physical parameter which is independent from the mechanics of the surface. Combining the information from ImAFM stiffness and SKPM surface potential resulted in a precise characterization of interfacial region, demonstrating that the interphase is softer than epoxy and boehmite nanoparticles.

Further, we investigated the effect of boehmite nanoparticles on the bulk properties of epoxy matrix. ImAFM stiffness maps revealed the significant stiffening effect of boehmite nanoparticles on anhydride-cured epoxy matrix. The energy dissipation of epoxy matrix locally measured by ImAFM shows a considerable increase compared to that of neat epoxy. These measurements suggest a substantial alteration of epoxy structure induced by the presence of boehmite.

Keywords: Nanomechanical properties; boehmite; epoxy nanocomposites; atomic force microscopy; intermodulation; interphase.

6.1 Introduction

Epoxy materials are used as matrix in carbon-fiber reinforced polymers to produce light-weight constructions for applications such as in automotive, aerospace and construction industries. Despite of excellent properties such as high strength, high modulus, good adhesion, high chemical and heat resistance [164], the main challenge to overcome is the brittleness and low fracture toughness of cured epoxy matrix [165]. Among commercially available inorganic nanoparticles, boehmite nanoparticles (BNPs) have shown enhancements of mechanical properties of matrix in several polymer-based nanocomposites [13, 133, 145, 181, 182]. Particularly, BNPs shows significant reinforcing effect on epoxy matrices such as increasing shear strength, shear modulus and compressive strength while improving the fracture toughness [11-13]. The underlying mechanism of toughening effect of BNPs on epoxy matrix is hypothesized to be due to formation of a *soft interphase* between epoxy and

boehmite. However, the direct investigations on interphase properties of such nanocomposite system is not yet addressed.

The interfacial region between a filler and bulk matrix, which exhibits different chemical, physical and mechanical properties compared to bulk, is referred as interphase. It is widely accepted that the mechanical properties of composites are strongly influenced by the properties of their interphase [101]. The nature of interphase in thermoplastic and thermosetting matrices are substantially different. In thermoplastics, the interphase consists of immobilized polymer chains which exhibit less flexibility than the bulk. In thermosetting matrices however, the crosslinking chemistry at the interphase as well as in the bulk can be altered by the presence of particles. The interphase can have sizes from few nanometers up to few microns [66, 68, 183]. It may exhibit a property gradient or may be homogeneous [66].

Determination of interphase properties using experimental approaches is challenging due to resolution limitations in conventional mechanical characterization methods. Formation of interphases has been investigated widely in different studies using numerical methods [58, 82, 184, 185] and or with experimental methods, for instance with temperature modulated differential scanning calorimetry (TMDSC) [186]. A direct approach to investigate mechanical properties of interphases is atomic force microscopy (AFM). AFM force-distance curve (FDC) is the most common approach to probe mechanical properties of small volumes. Especially, the ability to apply well-known models from contact mechanics (Hertz, DMT and JKR)[88] makes this method suitable for quantitative measurements of polymers. This method, has a high spatial resolution and therefore it is suitable to probe the interphase between heterogeneous layers of material [161]. However, FDC substantially lacks the lateral resolution required to probe nano-scale domains of interphase in nanocomposites. For probing smaller volumes and resolving single nanoparticles, dynamic AFM-based approaches are required. The most common dynamic AFM mode is tapping mode which is mostly used to obtain high resolution surface topography images with additional compositional information in the tip oscillation phase image. Some studies demonstrated that the phase shift is correlated to surface stiffness [95]. However, in most cases, quantitative determination of mechanical properties is not possible with tapping mode phase image. A novel dynamic AFM technique is intermodulation AFM (ImAFM) in which a multi-frequency method provides more information about the tip-surface interaction forces than aforementioned approaches. Besides providing force curves which are equivalent to conventional FDCs, ImAFM yields information about energy dissipated by the tip-sample interaction giving insight to the viscous

80

behavior of the material. ImAFM provides high resolution stiffness maps which makes it suitable for visualizing and quantitative probing of nanoscale heterogeneous phases in polymer nanocomposites. Along with stiffness maps, a second channel of information are required to distinguish the heterogenous phases (e.g. polymer and nanoparticles) and assign the mechanical properties to them. Using topography images for this purpose is not sufficiently precise particularly when the dispersed phase is too small. Moreover, mechanical approaches can be affected by topographic changes and therefore affecting the accuracy in distinguishing the border between the phases [101]. Therefore, along with ImAFM, another information channel which probes a material property independent from its mechanics, can provide higher reliability of data analysis. Scanning kelvin probe microscopy (SKPM) is commonly applied on semiconductors and conducting systems to determine the work function. So far, SKPM has been widely used to characterized electrical contacts, semiconductors ,devices like transistors for purposes such as determination of work function [107]. It has been also used to localize corrosion in metal alloys [187] or to measure electrical surface charges of biological samples [188]. In recent years, this method is used to probe embedded materials with different physical properties in insulating polymer matrices [189].The electrical surface potential obtained from SKPM can be used as an information channel to visualize heterogeneous phases, even with sub-surface sensitivity [189].

In the present work, we aim to study the effect of BNPs on anhydride-cured epoxy resin. First, we focus on visualizing and mechanical characterization of interphase by combining different information channels of ImAFM together with SKPM. Second, we investigate the effect of BNPs on bulk matrix (away from particles) including stiffness, and dissipating energy. Finally, we compare the results with macroscopic mechanical analysis of these nanocomposites reported in other works and propose a describing model.

6.2 Materials and methods

6.2.1 Materials and sample preparation

The epoxy system used in this study is bisphenol-A-diglycidyl ether (DGEBA, Araldite® LY 556, Huntsman) cured with an anhydride curing agent methyl tetrahydrophtalic acid anhydride (MTHPA, Aradur® HY 917, Huntsman) and accelerated by an amine, 1-methyl-imidazole (DY070, Huntsman). The mixture of epoxy, hardener and accelerator is 100:90:1 parts per weight, respectively. BNPs used in this study are commercially available spray-dried nanoparticles with orthorhombic shape and primary particle size of approx.14 nm based on the manufacturer's datasheet (DISPERAL HP14, SASOL, Germany). First, suspensions of 30

wt% boehmite were provided and blended with DGEBA and further the hardener and accelerator are added to the blend. The concentrations used in this study is 0, 5 and 15 wt% BNP in 100:90:1 ratio of DGEBA, MTHPA and DY070, respectively. The epoxy mixture ratio used is the standard stoichiometric ratio (suggested by the manufacturer). The mixture is cured for 4 hours at 80 ˚C to reach gelation and 4 hours at 120 ˚C for post-curing. Dispersion and curing process was performed by Jux and coworker and described in details elsewhere [11, 12]. Please note that the samples used in this study are identical to those in above-mentioned publications. There, the reader can find more information about the dispersion and other properties which are not mentioned in this work.

The surface of cured samples is cut with ultramicrotome to obtain a smooth surface. Before AFM measurements the surfaces of samples are ion-polished to reduce the contaminations and residues from microtome cutting.

6.2.2 Intermodulation AFM

Recently, dynamic AFM methods including usage of multi-frequency have been developed in nanomechanical studies of surfaces. In this work, we use one such multi-frequency method called Intermodulation AFM (ImAFM). In ImAFM the cantilever is excited with not only one frequency like in tapping mode but with two frequencies close to a resonance of the cantilever. Here, we choose frequencies 0.5 kHz above and below the frequency of the first flexural eigenmode of the cantilever. Away from the surface, the cantilever performs a beating motion. Engaged to the surface, the cantilever motion is distorted by the nonlinear tip-sample interaction which creates additional frequency components in the cantilever motion spectrum as shown in Appendix A. These frequency components are called intermodulation products (IMPs), or mixing products, since they appear at frequencies which are linear integer combinations of the drive frequencies. The amplitudes and phases of IMPs are measured during scanning with a multi-frequency lock-in amplifier. At each pixel, hundreds of oscillations are carried out starting from low amplitudes, reaching a maximum and decreased to zero. As this cycle takes less than few milli-seconds, ImAFM has the advantage of being much faster compared to the conventional Force-distance curves (FDC).

The IMPs are directly correlated to the tip-surface force. For a single pixel we can visualize this correlation with force quadrature curves which show the in-phase and out-of-phase component of the force with respect to the tip motion for each oscillation cycle [190]. The in-phase component F_I corresponds to the conservative part of the force describing the elastic behavior of the surface. The out-of-phase quadrature F_Q measures the dissipated energy

during a single oscillation cycle. Examples of F_I and F_Q curves are presented in Fig.6.1. $F_I(A)$ looks similar to those conventional force-distance curves: it consists of an attractive and repulsive regime. The amplitude in the beginning of the measuring cycle is low therefore there is no tip-surface interaction. With increasing the amplitude, tip and sample spends more time closer and the tip gets into attractive regime (positive values of F_I) which is due to van der Waals forces. With further increase of the amplitude, the tip makes contact with the surface and penetrates into it. In this region the tip experiences a net repulsive force (negative values of F_I). However, at this stage $F_I(A)$ cannot be treated directly as FDC curves since the force is plotted as a function of oscillation amplitude rather than tip position. Amplitude-dependence force spectroscopy (ADFS) uses the inverse Abel transform to converts $F_I(A)$ to a traditional force-tip position curves [103, 105]. The ADFS curves can be treated as FDC curves: the slope of the curve in the repulsive regime gives a quantitative measure of the stiffness describing the purely elastic responds of the measured sample volume. The force in attractive regime is mainly originate from van der Waals forces which are caused by dipole-dipole and dipole-induced dipole interactions between the tip and surface. Therefore, the work of attractive forces includes information about material changes which is independent from the surface mechanics.
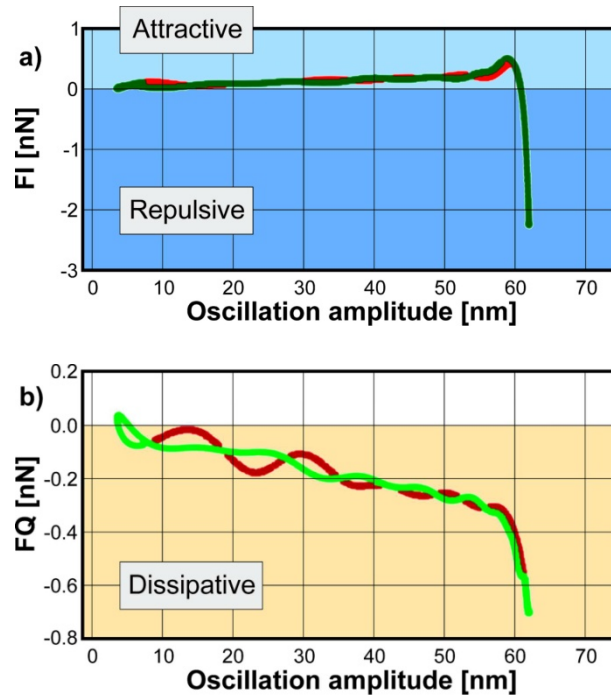

Fig.6.1. Reconstructed conservative F_I (a) and dissipative F_Q (b) forces on a polymer substrate. the red and green lines present the approach and retract curves, respectively

The $F_Q(A)$ describes the dissipative part of tip-surface interaction, which originates from viscous nature of the material [87].

For the analysis of spatially varying features, we create surface maps of the ADFS stiffness, the attractive force and the total energy dissipated during in a single pixel. It is noteworthy that the force quadrature curves shown in Fig.6.1 are measurements of single pixels whereas the maps show the measurement of a complete surface. Details about calculation of energy dissipation from multifrequency data can be found in Appendix B

ImAFM measurements were carried out using MFP3D microscope (Asylum Research, Santa Barbara, CA). A multi-frequency lock-in amplifier (Intermodulation Products, Segersta, Sweden) is used to generate the drive signals and measure the intermodulation spectra. The probes are HQ:NSC35 (Mikromasch, Wetzlar, Germany) with resonance frequency of 190 kHz (for section 6.3.1) and 202 kHz (for section 6.3.2), with tip radius lower than 20 nm.

6.2.3 Scanning kelvin probe microscopy

The vibrating capacitor or kelvin probe is a method to measure the contact potential difference (CPD) between a sample and tip also called surface potential V_{sp} [191]. The sample and probe behave as a capacitor plate with air as the dielectric in between. V_{sp} depends mainly on difference between work functions of probe and the sample. To obtain high lateral resolution surface potential maps, scanning kelvin probe microscopy (SKPM) is used. In this method, an AC signal excites the cantilever electrostatically at its resonance frequency. The potential difference between probe and the surface results in the mechanical oscillation of cantilever. The feedback loop nulls the oscillation by applying a bias voltage to the cantilever. This bias voltage is then collected as a contact potential difference (CPD). The corresponding equations and technical considerations are described in detail elsewhere [106]. SKPM is usually carried out as a dual-pass approach, performing two scans per line on the selected scan area. The first pass which includes the mechanical excitation of the cantilever (tapping mode) obtains the topography of the line. In the second pass, which is known as lift or nap mode, the topography information is used to maintain a defined distance from the surface which is known as nap height. Choosing a suitable nap height is crucial for increasing the resolution of SKPM while avoiding touching the surface during the second pass.

In this work we used MFP3D microscope (Asylum Research, Santa Barbara, CA) in SKPM mode. The gold-coated silicon probes with resonance frequency of 190.130 kHz, radius lower than 20 nm provide by are Mikromasch (Wetzlar, Germany) was used. During all SKPM measurements nap height is chosen to be 50 nm as the suitable height according to topographic features of the surface. The resulted scans shown in this article are corrected by offset plane with the purpose of enhancing the visibility of the contrast. Therefore, the scale

shown in SKPM images are different than the actual values. The measurements were carried out in air, at room temperature, using the first eigenmode frequency. Therefore no major subsurface sensitivity is expected since this would be mainly be the case when using the second eigenmode [192].

6.3 Results

In section 6.3.1, we focus on distinguishing particles, visualization of the interphase and determination of its stiffness. We use an epoxy/boehmite nanocomposite with 5wt% nanoparticles (EP/BNP5) as this weight percentage is high enough to show mechanical improvements in the macroscale meanwhile not so high that the particle agglomerations become dominant over the scanned surface [12]. We obtain the ImAFM stiffness and attractive forces of different phases of the nanocomposite including particles, interphase and matrix, meanwhile using potential map obtained by the SKPM mode as a complementary tool to verify the presence of particles.

In section 6.3.2, we quantify the effect of nanoparticles on the bulk matrix. The stiffness, work of attractive forces, and energy dissipation of the matrix phase in a high concentration nanocomposite with 15wt% BNPs are derived from ImAFM measurements and compared to those of neat epoxy.

6.3.1 ImAFM and SKPM studies on epoxy with 5 wt% BNP

Fig.6.2 shows AFM data acquired from a region located on the surface of EP/BNP5. The overview of a larger scan area is provided in Appendix C. The topography image (Fig.6.2 a) shows protrusions with different sizes. The main challenge is to distinguish the features related to presence of BNPs from nodular structures which are commonly observed in cured epoxy systems [193]. For this purpose, potential map obtained by the SKPM mode is used as a complementary tool to verify the presence of BNPs. Generally speaking, the potential values are related to the work function and electronic state of the surface which is actually a signal to measure the material contrast [188]. In Fig.6.2 b, the surface potential map shows contrast on the protrusions which verifies the presence of BNPs within these areas. Please note that in most conductive cantilevers, the entire bottom side of cantilever is coated with a conductive layer (gold). Therefore, the signal is not limited to the capacitance formed between the tip apex and the sample, but the entire cone is participating in producing the signal. Despite such limitations in the lateral resolution, SKPM clearly identifies compositional contrasts with the precision required in this work.
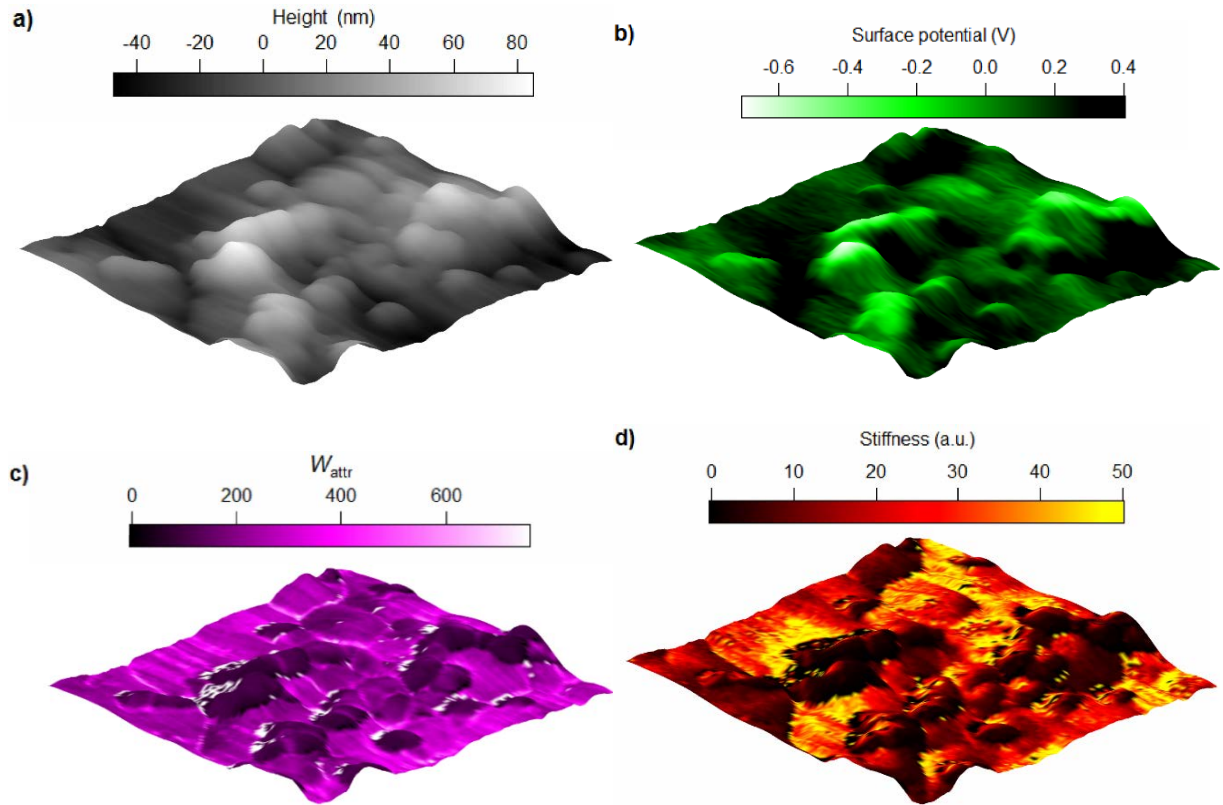
85

Fig.6. 2. a) 3-dimensional tapping mode topography b) Surface potential c) Work of attractive forces W_{attr} and d) stiffness maps of epoxy/boehmite nanocomposite with 5wt% nanoparticles. The scan sizes in all images are 860 nm x 860 nm. White pixels in W_{attr} show error.

Fig.6.2, c and d show work of attractive forces W_{attr} and stiffness maps, respectively, generated from ADFS curves. In a single ADFS curve obtained for each pixel, W_{attr} is calculated from the net attractive regime and the slope of the curve is proportional to stiffness. The W_{attr} map shows a clear contrast between the protrusions and the surrounding with a well-defined border. The area with sudden decrease in W_{attr} is located where the potential maps shows the presence of boehmite. Considering the van der Waals forces as the main driving force for net attractive regime, the low values of W_{attr} is an indication for a weaker van der Waals forces between the tip (gold) and BNPs than the epoxy. Van der Waals forces which are mainly originated from dipole-dipole and dipole-induced dipole interactions between tip and the surface, can be used as an additional information channel about the surface composition independent from its mechanics. Thus, when measuring the mechanical response with ImAFM, W_{attr} signal can be used to visualize material contrast.

Despite the existence of two distinguishable phases in Fig.6.2 c, the contrast in stiffness map Fig.6.4 d shows a variety of stiffness values in different distances from the protrusions. The area related to protrusions shows two phases, an area close to the center of protrusions with higher stiffness surrounded by an extremely low stiffness area (shown in black color). It is

noteworthy that the soft area is located at an immediate distance from nanoparticles located by potential and W_{attr} maps. Therefore, the soft area relates to the particle-polymer interphase.

It is noteworthy that the bulk matrix shows variations in stiffness in the scanned area. Blocks with high (yellow) and low (red) stiffnesses in bulk epoxy indicate the inhomogeneous nature of the matrix.

Since sudden height changes affect the force measurements, it is crucial to investigate the roll of topography artifacts in measured stiffnesses. Detailed analysis of topography-stiffness relation for the scanned surface is presented in Appendix D. This analysis demonstrates that except minor points with sudden changes of height and groove-like topographic features, most of topography changes and the stiffness values are independent from each other. Thus, by excluding the affected points of the scanned areas as error points, the remaining ADFS curves are independent from topography artifacts.

To precisely distinguish the stiffness of particles, interphase and polymer, several areas with the presence of nanoparticles are selected and analyzed separately (Appendix E). One of the selected areas is shown in the topography image (Fig.6.3 a) and the corresponding maps of surface potential and stiffness are presented in Fig.6.3 b and c, respectively. The surface potential distinguishes the nanoparticles from matrix however the interfacial region is not resolved in the potential map. Meanwhile, in the stiffness map, the existences of a soft region in the is clearly observable. In Fig.6.3 d, the ADFS curves of selected points with different distances from the particle are presented compared. Here it is also shown that the stiffness (slope) of the point in the interfacial region is drastically low. To precisely relate all the measured stiffness in the scanned area to different phase of the nanocomposite (particle, matrix and interphase), it is crucial to use the material contrast shown in surface potential map together with the stiffness map. For this purpose, we combined two information channels, the stiffness and potential histograms and plotted a two-dimensional histogram of stiffness and potential as shown in Fig.6.4. It is noteworthy that the measured points which were affected by sudden topographic changes are considered as error and excluded from the 2D histogram cloud.
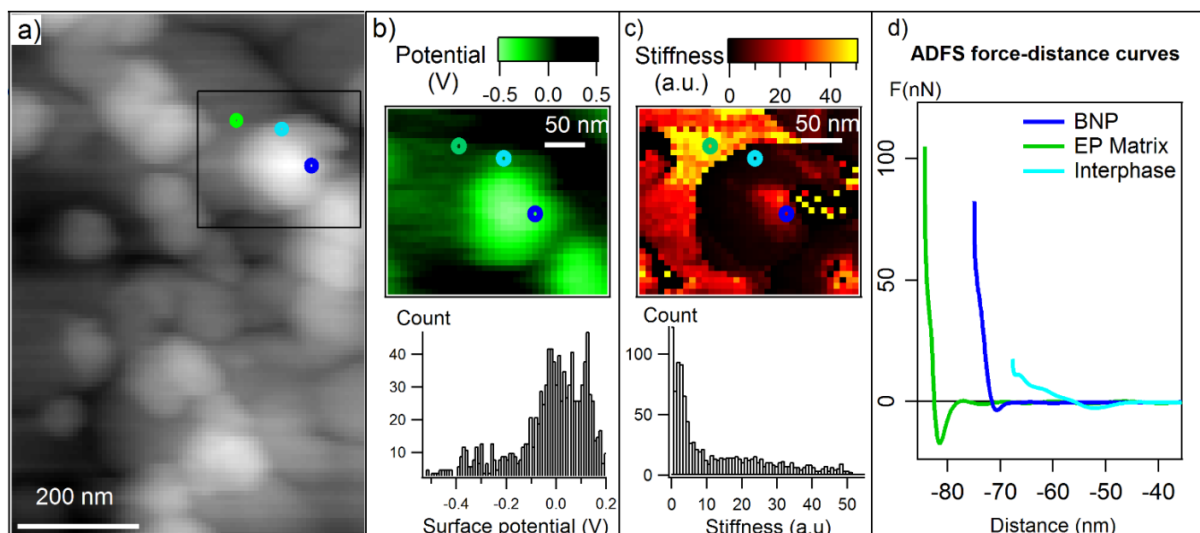
Fig.6.3. a) AFM tapping mode topography with the selected region of analysis marked with a square box, b) surface potential map and histogram and c) ADFS stiffness map and histogram of the selected area, d) ADFS curves related to three points shown with circle markers on the maps with the approximation of the location of BNPs (dark blue), epoxy matrix (green) and interphase (light blue).
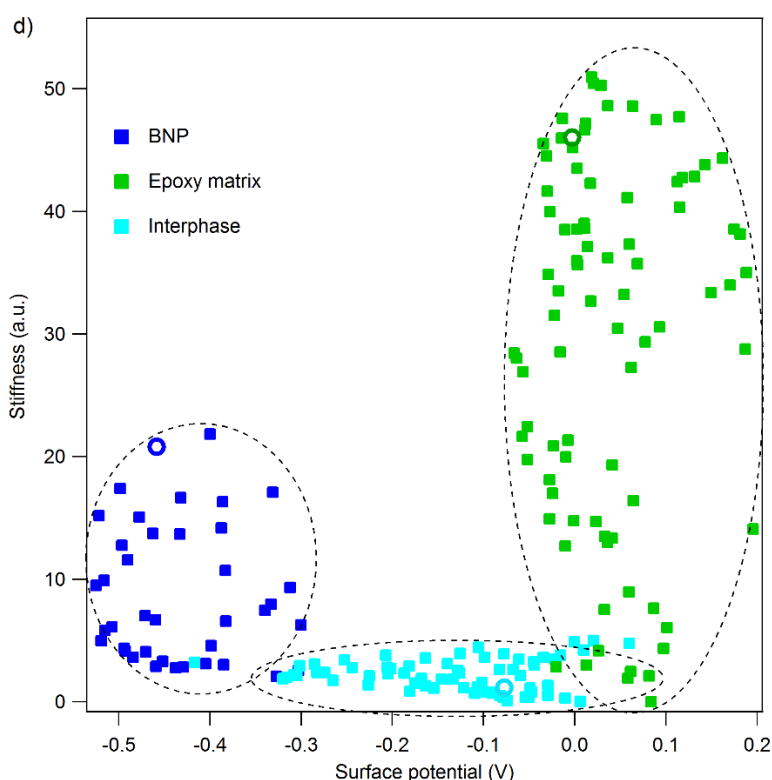
Fig.6.4. Two-dimensional histogram of stiffness vs. surface potential of the selected area (shown in Fig.6.3) of the scanned surface of EP/BNP 5. The dashed lines are used to help the eyes to distinguish between three different regions of the histogram.

In 2D histogram, the stiffness values are sorted based on the corresponding surface potential values and three distinguishable regions (marked with dashed circle lines in Fig.6.4) are

clearly observable on the histogram cloud. In the following, each region is discussed separately:

Dark blue points are related to pure BNP particles as they exhibit negative surface potential values (from -0.3 V to -0.5V). They have large distributions of stiffness varying from 5 up to 22. The variation of stiffness values in the area related to pure BNPs can be due to following reasons: i) Due to anisotropic nature of boehmite crystals, force curves obtained from different orientations show different stiffness values. ii) Particles which are present in the nanocomposites are in fact secondary particles which are formed by aggregation of several primary particles with the size of 14nms. Therefore, while in contact with the tip, several intra and inter-slippage between layers can occur which helps the deformation and results in apparent stiffness values which may be lower than the actual values.

Green points are related to pure matrix far from the particle according to their surface potential values. In this area, potential values are mostly positive and have a narrower distribution (between -0.05 and 0.2 V) compared to that of BNPs. The stiffness variation in epoxy matrix is high the values are distributed between 5 to 50. The broad distribution of stiffness in epoxy phase is due to following reasons: Inhomogeneous phases in epoxy-anhydride cured systems which has been already reported in several studies [38, 194]. Local changes in stoichiometric ratio which results in changes in the chemical structure of the network density and thus affect the mechanical properties of the epoxy.

The light blue cloud is related to the matrix in the immediate proximity of particles. This interfacial region has a gradient potential, but no gradient in stiffness is observed. The potential values start from low values in vicinity of particles (-0.3 V) increasing up to 0.05 V when getting close to the pure matrix. In all distances from the particle the interphase shows a stiffness value between 1 to 5. Thus, the soft interphase appears like a phase segregation which can be due to several effects. One is the preferential absorption of one of epoxy components (DGEBA monomers or anhydride curing agents) on the surface of BNPs.

One surprising observation is that the average stiffness of BNP particles is lower than that of epoxy phase. Contradictory to the structural stiffness of boehmite calculated by simulation which suggest a of modulus 136-267 GPa with respect to plane orientation, Fankhänel and coworkers reported an experimental average modulus of 10 GPa [162]. This behavior is suggested to be due to the slippage behavior between the layers and weak interlayer bonding. Nevertheless, knowing that the neat anhydride-cured epoxy has a Young's modulus of

approx. 3.3 GPa [13, 15], it is expected that in our nanocomposite system, particles exhibit higher stiffness values than the polymer matrix. To understand this unexpected inversion of stiffness between filler and matrix, in the next section, properties of the matrix phase of EP/BNP nanocomposites are investigated and compared with neat cured-epoxy.

6.3.2 ImAFM studies on neat epoxy and epoxy with 15 wt% BNP

Fig.6.5. compares the topography image of neat cured epoxy and epoxy/BNP nanocomposite with 15wt% particle content (EP/BNP15), respectively. Moreover, an overview of the particle distribution in EP/BNP15 is provided by operating scanning electron microscopy in transmission mode (Appendix F). Although larger agglomerates were scarcely observed, the majority of surface contains particles in form of agglomerates with the size of less than 100 nm similar to what is observed in Fig.6.4 b. The area shown here in Fig.6.4 b was selected carefully to avoid large agglomerates.

In Fig.6.6, the W_{attr} of neat epoxy and EP/BNP15 are compared. As previously discussed, W_{attr} data channel shows contrast between BNPs and epoxy phase independent from the mechanical properties. Here as well, in the inset image of Fig.6.5, the W_{attr} image of EP/BNP15 shows contrast between BNP and polymer phase. The W_{attr} of neat epoxy also contains inhomogeneities which is due to well-known nodular structures of epoxy. Nevertheless, the surprising observation is that in EP/BNP15, the pure matrix phase in presence of BNPs has higher values of W_{attr} comparing to neat epoxy. The comparison of W_{attr} histograms shown in Fig.6.5 demonstrates 100% increase in W_{attr} for the matrix. This is a clear indication that BNPs induces physical/chemical alteration in epoxy which is worthwhile for further investigations.
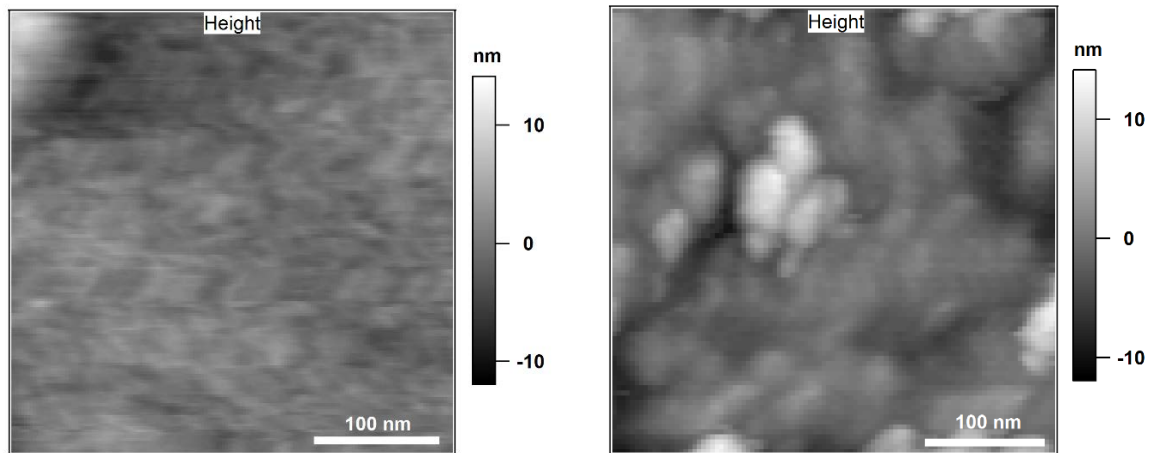
Fig.6.5. Tapping mode topography of 350 nm x 350nm scan area of neat epoxy (left) and epoxy with 15 wt% BNPs (EP/BNP15) (right)
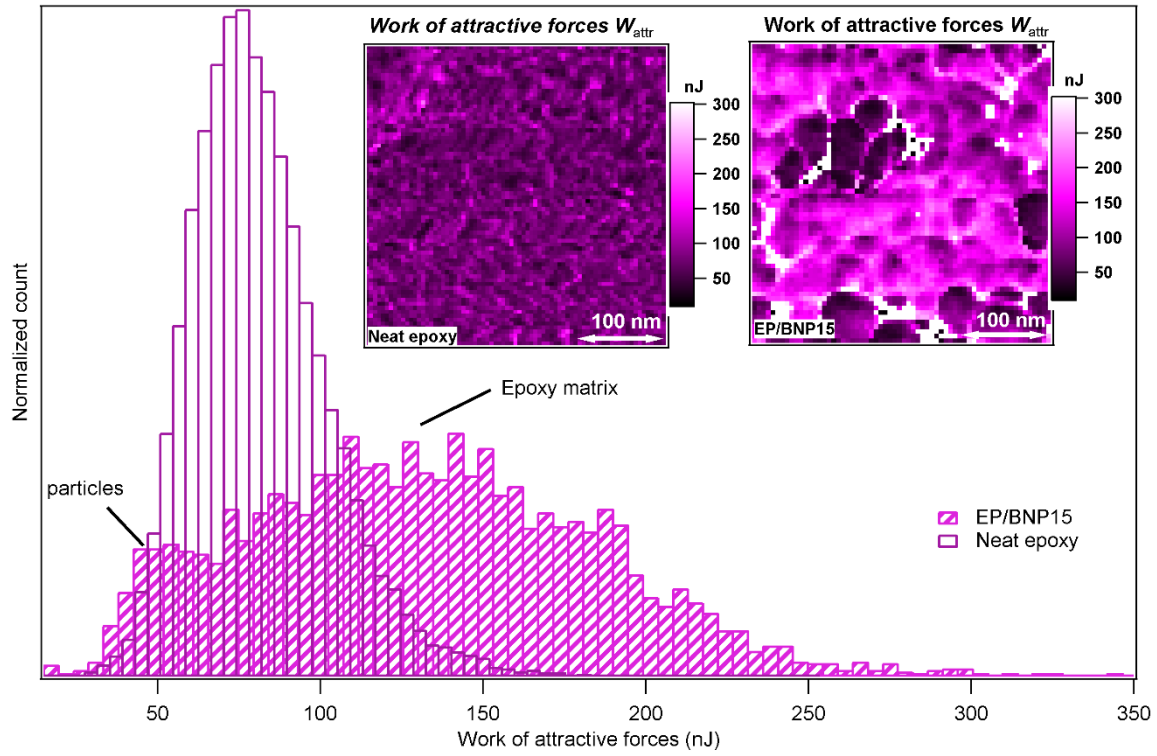
Fig.6.6. The comparison of the histograms of work of attractive forces W_{attr} in neat epoxy and EP/BNP15. The left-side inset image is W_{attr} map of neat epoxy and the right-side is W_{attr} map of EP/BNP15.

Fig.6.7 compares the stiffness of neat epoxy with epoxy matrix in EP/BNP15. The histograms show that the stiffnesses of nanoparticles are slightly higher than of neat epoxy, as expected. However, this relationship is inversed in EP/BNP15 in which matrix is stiffer than the particles. The inversed situation with particles softer than the epoxy matrix has been also observed in section 6.3.1. The comparison between the stiffness of matrix in EP/BNP 15 and neat epoxy reveals a 100% to 400% increase in matrix stiffness which occurs in the presence of boehmite. This is a significant property change of epoxy.
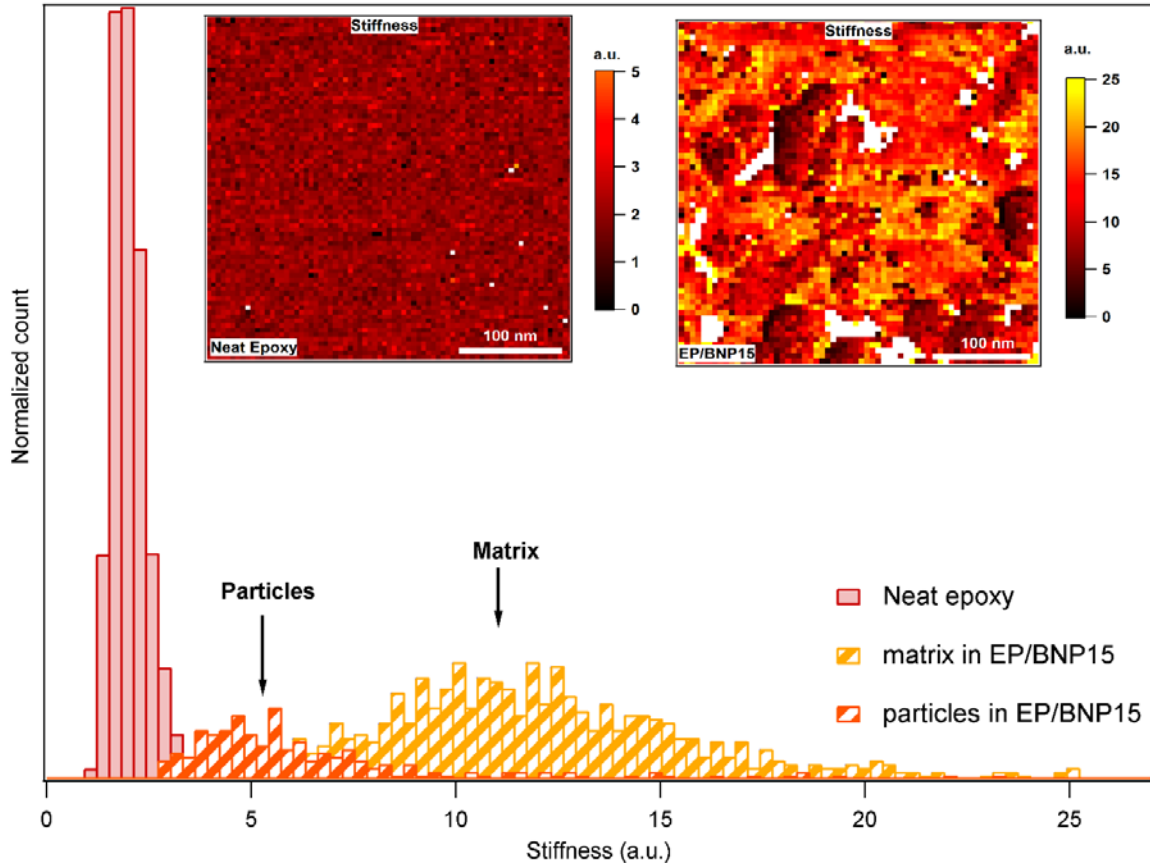
Fig.6.7. Comparison of stiffness histograms of neat epoxy and EP/BNP15. The left-side inset image related to stiffness map of neat epoxy and the right-side to EP/BNP15.

Fig.6.8 compares the energy dissipation maps of neat epoxy with EP/BNP15. It is observed that in EP/BNP15, the energy dissipation of particles is lower than of epoxy matrix. Clearly, long chains of polymer can dissipate the energy more than BNPs with crystal structures. However, comparing the peak values of energy dissipation histograms, it can be observed that epoxy matrix in EP/BNP15 shows an approx. 10% increase of energy dissipation compared to neat epoxy. This also indicates physical alteration of epoxy matrix as an effect of boehmite nanoparticles.
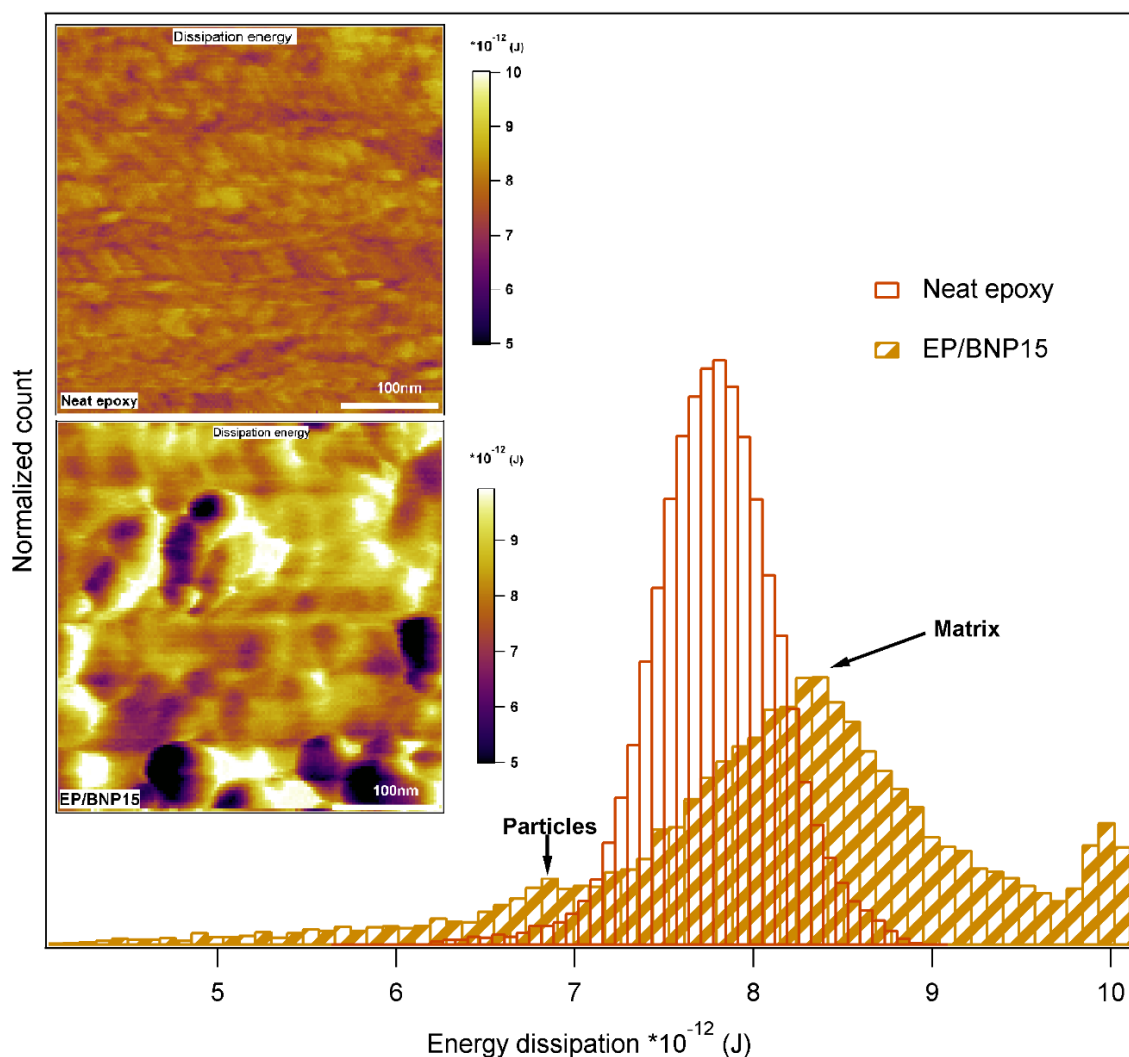
Fig.6.8. Comparison of energy dissipation histograms in neat epoxy and EP/BNP15. The top inset image related to energy dissipation map of neat epoxy and the bottom image to EP/BNP15.

6.4 Discussion

The analysis of ADFS curves in EP/BNP5 presented in section 6.3.1 demonstrated the formation of an interfacial region which has a significantly low stiffness. This region appears mostly as a block of soft material in the vicinity of particles rather than a region with stiffness gradient. One hypothesis is a disturbed crosslink density near the particles resulting in formation of a soft interphase. However, it has been demonstrated in several works on epoxy systems that the glassy state modulus does not reflect the crosslinking properties of the material, but exhibits the noncovalent bonding and inter and intra-molecular packing [71, 175]. They demonstrated that a low crosslinking density system can exhibit higher modulus at glassy state. Therefore, the disturbed crosslink density cannot explain the formation of soft interphase. Another hypothesis is the accumulation of one component of epoxy mixture (either DGEBA or anhydride hardener or both) on the surface of particles due to preferential

absorption, covalent or noncovalent bonding with boehmite, leading to a local phase segregation. In this case, the local stoichiometric ratio of epoxy and hardener can vary in bulk matrix and thus resulting in alteration of chemical and physical properties of the matrix. Further investigations on the chemical composition of the interphase are required to verify this hypothesis.

In section 6.3.2, the effect of BNPs on epoxy matrix is investigated. The significant increase in stiffness, attractive forces and energy dissipation in bulk matrix compared to neat epoxy demonstrated that boehmite induces physical, mechanical and chemical property alteration in anhydride-cured epoxy matrix. It was demonstrated that these property alterations in epoxy are not only limited to the interfacial region, but the bulk epoxy is affected significantly. The changes in epoxy matrix can affect the macroscopic properties of the composite more than what the interphase can do. Therefore, in addition to consideration of the modulus of interphase, the increased modulus of matrix must be taken into account when using theoretical models such as Halpin-Tsai [57, 195] when it comes to epoxy-boehmite nanocomposites or systems with similar observations. It is noteworthy that the stiffening effect of nanoparticles in crosslinked matrices has already been reported. Using ImAFM approach, they observed an increase of stiffness in PDMS matrix in the presence of silica nanoparticles.

Although BNPs alone has lower energy dissipation than polymer matrix (as seen in Fig.6.7), they induce changes in the matrix structure which resulted in the increase of energy dissipation in bulk polymer. The fracture toughness and critical energy release rate increase in epoxy-boehmite nanocomposites which was reported previously verifies this observation [12].

6.5 Conclusions

In this article, we applied different AFM-based methods to visualize property contrast and probe mechanical properties of nanoparticles, polymer matrix and the interphase in epoxy-boehmite nanocomposite systems. Multi-frequency intermodulation AFM (ImAFM) was used as a tool to measure forces together with scanning kelvin probe macroscopy (SKPM) as an additional information channel to show material contrast independent from the mechanics of the surface. ImAFM maps demonstrated stiffness contrast between polymer, particle and the interphase. SKPM shows potential contrast between boehmite nanoparticles and epoxy matrix. Combination of mechanical and surface potential values led to a more precise determination of the location and stiffness of interphase. The results demonstrated the presence of a soft block of polymer near the interfacial region with no visible stiffness

gradient. The stiffness of this region is considerably lower than both particles and polymer phase.

Moreover, the effect of boehmite on the matrix properties was investigated by focusing on stiffness and energy dissipation during the tip-surface interaction obtained from ImAFM force curves. A significant stiffening effect of boehmite nanoparticles on anhydride-cured DGEBA was demonstrated. Meanwhile, the presence of boehmite resulted in increase of energy dissipation. We suggest that boehmite cause structural alteration of matrix by inducing local changes in stoichiometric ratio of the epoxy and hardener due to preferential surface absorption, covalent or non-covalent bonding between boehmite particles and mixture components.

Acknowledgment

Chapter 7: Short- and long-range mechanical and chemical interphases caused by interaction of boehmite (γ-AlOOH) with anhydride-cured epoxy resins

This chapter is reproduced with permission from the accepted manuscript of: **Ghasem Zadeh Khorasani, Media**; Elert, Anna-Maria; Hodoroaba, Vasile-Dan; Agudo Jácome, Leonardo; Altmann, Korinna; Silbernagl, Dorothee; Sturm, Heinz. "Short- and Long-Range Mechanical and Chemical Interphases Caused by Interaction of Boehmite (γ-AlOOH) with Anhydride-Cured Epoxy Resins." *Nanomaterials* 9.6 (2019): 853.

*Supporting information is given in Appendix III

DOI: https://doi.org/10.3390/nano9060853

Media Ghasem Zadeh Khorasani [1,2,*], **Anna-Maria Elert** [1], **Vasile-Dan Hodoroaba** [1], **Leonardo Agudo Jácome** [1], **Korinna Altmann** [1], **Dorothee Silbernagl** [1] and **Heinz Sturm** [1,3]

[1] Bundesanstalt für Materialforschung und -prüfung (BAM), D-12205 Berlin, Germany; anna-maria.elert@bam.de (A.-M.E.); Dan.Hodoroaba@bam.de (V.-D.H.); Leonardo.Agudo@bam.de (L.A.J.); Korinna.Altmann@bam.de (K.A.); dorothee.silbernagl@bam.de (D.S.); Heinz.Sturm@bam.de (H.S.)

[2] Department of Polymer Materials and Technology, Technical University Berlin, D-10587 Berlin, Germany

[3] Department of Mechanical Engineering and Transport Systems, Technical University Berlin, D-10587 Berlin, Germany

[*] Correspondence: media.ghasem-zadeh-khorasani@bam.de; Tel.: +49-30-8104-4714

Abstract

Understanding the interaction between boehmite and epoxy and formation of their interphases with different mechanical and chemical structures is crucial to predict and optimize the properties of epoxy-boehmite nanocomposites. Probing the interfacial properties with atomic force microscopy (AFM)-based methods, especially particle-matrix long-range interactions is challenging. This is due to size limitations of various analytical methods in resolving nanoparticles and their interphases, overlap of interphases, and the effect of buried particles that prevent the accurate interphase property measurement. Here, we develop a layered model system in which the epoxy is cured in contact with a thin layer of hydrothermally synthesized boehmite. Different microscopy methods are employed to evaluate the interfacial properties. With intermodulation atomic force microscopy (ImAFM) and amplitude dependence force spectroscopy (ADFS), which contain information about stiffness, electrostatic and van der Waals forces. a soft interphase was detected between epoxy and boehmite layer. Surface potential maps obtained by scanning Kelvin probe microscopy (SKPM) revealed another interphase about one order of magnitude larger than the mechanical interphase. The AFM-infrared spectroscopy (AFM-IR) technique reveals that the soft interphase consists of unreacted curing agent. The long-range electrical interphase is attributed to the chemical alteration of the bulk epoxy and formation of new absorption bands.

Keywords: Epoxy nanocomposites, boehmite, interphase, Intermodulation AFM, SKPM, AFM-IR

7.1. Introduction

Introducing boehmite nanoparticles (BNPs) as a nanofiller in polymer nanocomposites and the investigation of the associated property enhancements has been the focus of many recent studies [10, 130, 131, 196-198]. Addition of BNPs to epoxy resins results in remarkable improvement in Young's modulus, flexural modulus, thermal conductivity, compressive strength, dimensional stability and fracture toughness [12-15, 115, 144, 145, 199]. Also when the BNP-epoxy is used as matrix in carbon-fiber reinforced composites, remarkable enhancement of the fiber-matrix interphase was reported [16].

It is noteworthy that the curing agent plays an important role in the properties of the nanocomposite since each curing agent can interact differently with boehmite nanoparticles. The different interaction between BNPs and epoxy components results in property variations not only at the interface between polymer and filler but also the bulk properties of the cured polymer can vary significantly [200, 201].

Chemical and physical interactions at the polymer-nanoparticle interface and formation of an interphase with different properties than those of both filler and matrix phase has a major effect on property improvement in polymer nanocomposites. Formation of additional soft or hard phases as a result of particle-matrix interactions leads to new energy dissipation pathways and significant improvements in damage tolerance, crack resistance and fracture toughness of the nanocomposite. Therefore, an in-depth understanding of interfacial characteristics at short and long distances from the interphase of nanoparticles is crucial. Numerical and empirical approaches show that strong bonding between a homogeneous polymer and nanoparticles generates a "mechanical interphase", which is usually short-range in nature, and that the modulus gradient of the interphase does not exceed more than a few nanometers [58, 78, 184, 202]. In a heterogenous polymer mixture consisting of resin and hardener, each molecule interacts with nanoparticles in different ways. Besides local distortions of the curing process due to confinement effects, chemical interactions between polymer and nanoparticles as well as preferential adsorption of one component can occur in a thermosetting matrix with nanofillers [66]. Based on functional groups on the surface of the filler, one compound is energetically preferred and therefore one reactant is accumulated at the interphase. The preferential adsorption leads to stochiometric changes in the curing mixture, if only on a smaller scale. As a result, a "chemical interphase" is defined, which can exceed considerably the range of nanometers [203].

Several hypotheses regarding the interphase properties of epoxy-BNP nanocomposites have been proposed. Arlt et al. suggested that a mechanical interphase may form around BNPs, which is hypothesized to be a result of disturbed crosslinking around the particles [13]. This argument is indirect and based on the topography of the surface after washing away the soft residues. Numerical studies of Fankhänel et al. showed that a soft interphase results from the high number of particle-matrix bonds [204]. The width of the interphase obtained from their simulations does not exceed more than a few tens of angstroms.

Atomic force microscopy (AFM) provides direct visualization and measurement of the interphase properties. Different AFM modes have been used to probe the mechanics of the interphase. AFM force-distance curves (FDC) offers a suitable approach for probing the interphase between thin films, where the vertical resolution is more important than the lateral resolution [161]. AFM in different modes, such as force modulation [67]or displacement modulation [101], has been used to probe the local stiffness of interphases of fiber reinforced

polymers. With the development of intermodulation AFM (ImAFM), it is possible to record a complete force curve at each image pixel with significantly reduced surface damage [105].

Recently, we showed that the analysis of ImAFM force curves enables to visualize the formation of the mechanical interphase as well as probing the van der Waals and dissipative forces which indicated the short– and long-range alteration of bulk epoxy in the presence of BNPs [200]. However, a precise probing of mechanical interphases and obtaining enough data within the scale of such small nanoparticles (less than 20 nm) are still challenging even with AFM approaches with a lateral resolution of a few tens of nanometers. Moreover, when probing the surface of a nanocomposite sample even with low volume fractions, long-range chemical interphases can overlap. Since the abovementioned force measurement approaches are not sub-surface sensitive, the effect of buried particles under the surface can be overlooked in the measurements and results in wrong interpretation of long-range interphases and bulk properties. Therefore, in this study we aim to probe short- and long-range interfacial properties on a two-dimensional layered model sample with a controlled geometry. Having a layer of crystalline boehmite, approx.1000 nm thick, growing normal to the substrate plane will result in high specific surface area and produce a localized interphase with more pronounced mechanical and chemical property difference than boehmite and bulk epoxy. Thus, the effect of overlapping interphases and buried particles in the bulk polymer is minimized and measuring the thickness of affected areas becomes more feasible. Besides implementing ImAFM to study the mechanical interphases, we show how scanning Kelvin probe microscopy (SKPM) and AFM-IR can be used to detect and characterize the long-range effect of boehmite on the formation of chemically altered phases in the bulk epoxy.

7.2. Experimental

7.2.1. Materials and sample preparation

The sample preparation process is schematically shown in Fig.7.1. First, a 100 nm layer of aluminum is deposited on the surface of a pre-cured epoxy substrate (EP1, Fig.7.1 a) using a physical vapor deposition (PVD) system (Edwards auto 306, Warley, UK).

The second step is the hydrothermal synthesis of boehmite (HydBo): formation of boehmite by boiling distilled water on aluminum has been described elsewhere [205-207]. It was suggested that boehmite is produced via the reaction of aluminum ions migrating from the metal, reacting with hydroxyl ions and precipitating back onto the substrate [205]. More recent studies demonstrated that the size and morphology of crystals can be controlled by variation of precursors, synthesis temperature, time and pH value [160, 208].

Here, we boiled the substrates with aluminum coating with distilled water at 120˚C, under high pressure (1.9 bars). The pH value was adjusted to 10 by adding NH_3 to the water solution. The solution containing the sample was transferred to a Teflon container, sealed and heated for one hour. The sample was washed, dried at room temperature overnight and further characterized by SEM (Fig.7.1 c). As seen in Fig.7.1 c the outer region of boehmite consists of nanostructured (in form of interconnected) lamellas interlocking in various directions in which the (100) planes are parallel to the substrate surface. Similar morphology of boehmite was reported when preparing boehmite coating by hydrolysis of AlN [209].

X-ray photoelectron spectroscopy (XPS) results show that the chemical composition of HydBo is in good agreement with commercially available BNP. (for more details, see Appendix A).
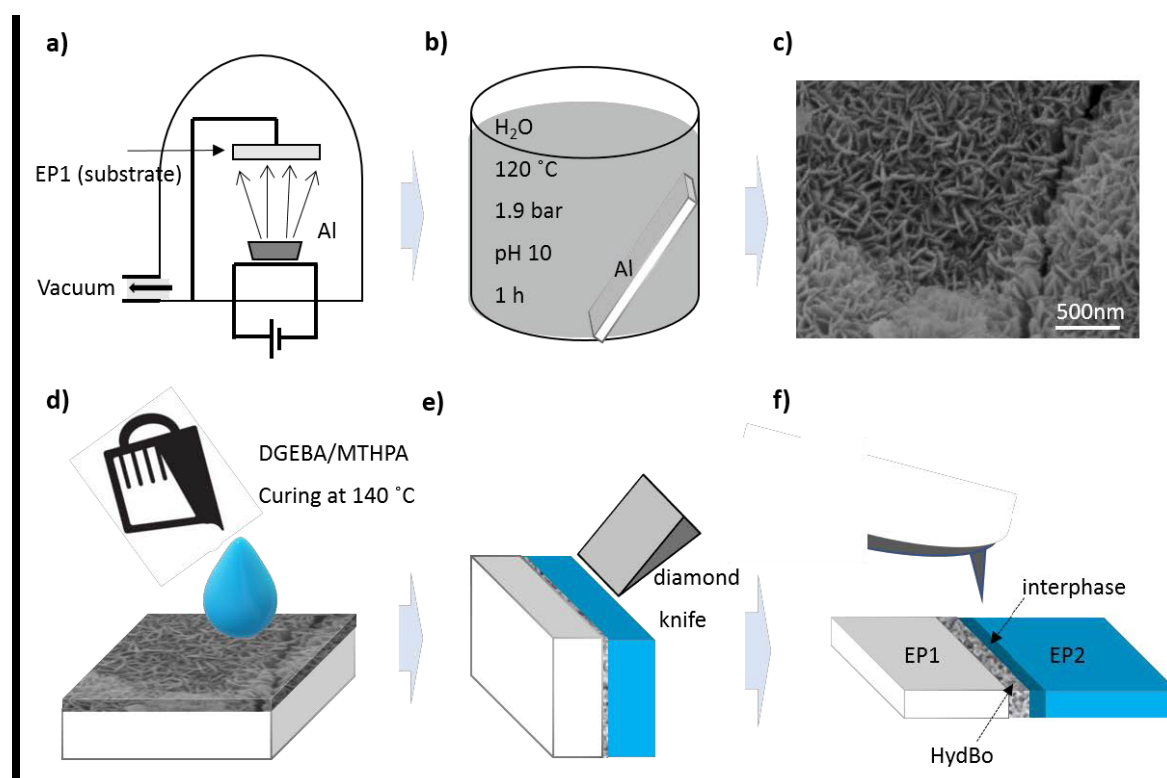
Fig.7.1 Schematic of the preparation of EP1/HydBo/EP2 model sample. a) Physical vapor deposition of aluminum on the epoxy substrate EP1, b) Hydrothermal synthesis of the boehmite layer from the aluminum coating in distilled water, c) Top view SEM image of the hydrothermally synthesized boehmite (HydBo), d) Preparation of the interacting epoxy layer, e) Ultramicrotomy of the cross-sectional surface of the layered structure. f) Evaluation of the microtomed sample with AFM-based and SEM/EDX methods.

In the next step, a polymer mixture consisting of resin, hardener and accelerator is prepared, poured to the surface of HydBo in a silicone mold and cured to form the interactive epoxy surface (EP2 (Fig.7.1 d). The epoxy systems used in this study for both the substrate (EP1)

and the interactive layer EP2 are identical, consisting of Bisphenol-A-diglycidyl ether (DGEBA, Araldite® LY 556, Huntsman) cured with anhydride curing agent methyl tetrahydrophtalic acid anhydride (MTHPA, Aradur® HY 917, Huntsman) and accelerated by an amine, 1-methyl-imidazole (DY070, Huntsman). The mixing ratio of epoxy, hardener and accelerator (by weight) is 100:90:1parts, respectively. The mixtures were cured for 4 hours at 80 ˚C to reach gelation and 4 hours at 140 ˚C for post-curing. EP1 has a different temperature history and curing conditions compared to EP2, since it was present during the evaporation of aluminum, the hydrothermal process and the curing of EP2. Thus, the two epoxies are not expected to exhibit identical properties. EP1 was used as the substrate to enhance the cutting procedure and easily access of the cross-sectional surface for further measurements. The cross-sectional surface of the sample was further cut using an ultramicrotome (Leica Ultracut UCT) equipped with a diamond knife (DiATOME) (Fig.7.1 e). For SEM and transmission electron microscopy (TEM) measurements, slices of approx. 100 nm in thickness were cut from the cross-sectional sample and were used with no extra conductive coating.

7.2.2 Characterization methods for short- and long-range mechanical and chemical interphases

Different AFM-based methods were used to obtain physical, mechanical and chemical properties of the material (Fig.7.1 f). For high resolution mechanical characterization of the surface, intermodulation AFM (ImAFM) was carried out. In this method, the cantilever is excited with two frequencies close to the resonance of the cantilever f_0. Here, we chose frequencies 0.5 kHz above and below the frequency of the first flexural eigenmode of the cantilever ($f_1 = f_0$- 0.5 kHz and $f_2 = f_0$+ 0.5 kHz). The resulting free oscillation of the cantilever is in the form of a beating wave. This motion is distorted by the nonlinear tip-sample interaction when the tip comes close to the surface. As a result, additional frequency components in the cantilever motion appear, which are called intermodulation products (IMPs). During the scan, amplitudes and phases of IMPs are measured with a multi-frequency lock-in amplifier. At each scan pixel, the oscillation of the cantilever is recorded through a cycle takes less than a few milliseconds. Each cycle starts from low amplitudes, reaches a maximum and decreases back to zero. At the beginning of the oscillation cycle, the amplitude is low, therefore, there is no tip-surface interaction (the tip does not sense the sample yet). When the amplitude increases, the tip first starts sensing the electrostatic forces of the sample, followed by the attractive van der Waals forces. Further increasing the amplitude results in the contact of the tip with the sample surface and further penetration into the surface. In this region the tip experiences a net repulsive force that gives information about the surface

stiffness. The force obtained at this stage is a function of amplitude, thus, it cannot be treated directly as conventional force-distance curves. Amplitude-dependence force spectroscopy (ADFS) uses the inverse Abel transform to convert the curve to a traditional force-distance [103, 105] In the latter, the slope of the curve in the repulsive regime gives a quantitative measure of the stiffness and the forces in attractive regime are related to electrostatic and van der Waals forces.

The second AFM-based method used in this study is scanning Kelvin probe microscopy (SKPM). In this method, a capacitor plate forms between tip and surface, where their potential difference is measured with air as the dielectric in between. Surface potential mainly depends on the difference between the work functions of tip and the sample. SKPM provides a high lateral resolution map of surface potential which can be used to probe heterogeneous phases with different structural and compositional properties. The cantilever is excited electrostatically at its resonance frequency by applying an AC signal. Due to the potential difference between the tip and surface, the cantilever begins to oscillate mechanically. By applying a bias voltage to the cantilever, the oscillation is cancelled out. This bias voltage is then collected, from which the surface potential is calculated. The corresponding equations and technical considerations are described in details elsewhere [106]. The measurements are carried out as dual pass approach in which two scans per line were performed. The first scan obtains the topography, which is used in the second scan to maintain a certain distance from the surface while measuring the potential.

For ImAFM and SKPM measurements in this study, a MFP3D microscope (Asylum Research, Santa Barbara, CA) was implemented. The gold-coated silicon probes provided by Mikromasch (Wetzlar, Germany) with a radius lower than 20 nm and resonance frequency f_0 = 185 kHz. During all SKPM measurements, the nap height is chosen to be 50 nm as the suitable height according to topographic features of the surface. The measurements were carried out in air, at room temperature, using the first eigenmode frequency.

AFM based infrared spectroscopy (AFM-IR) is a hybrid technique where chemical characterization provided by infrared (IR) spectroscopy can be obtained at the spatial resolution of AFM. [109-112] This is achieved by using the gold-coated tip of AFM to locally detect thermal expansion of a sample resulting from local absorption of IR radiation. Therefore, the AFM cantilever acts in this method as the IR detector, allowing the AFM-IR technique to overcome the spatial resolution limits of conventional IR microscopy. A tunable infrared laser is applied as the source of IR radiation. The IR light is focused onto a sample

region in the proximity of the AFM tip. If the laser is set to a wavelength that corresponds to an absorption wavelength of the sample, the sample sees a rapid thermal expansion by absorbing the light. The resulted expansion causes a force impulse on the tip of the cantilever, inducing an oscillation of the cantilever, whose amplitude can be detected. By tuning the repetition rate of the laser to match one of the contact mode resonance frequencies of the AFM cantilever, more sensitive and faster measurements are possible. By measuring the AFM probe oscillation amplitude response to IR absorption as a function of wavelength, it is possible to readily create IR absorption spectra of nanoscale regions of the sample surface.

The AFM-IR data were obtained using a NanoIR2s (Bruker / Anasys Instruments) coupled with a multichip QCL source (MIRcat, Daylight Solutions; tunable repetition rate range of 0–500 kHz; spectral resolution of 0.1 cm^{-1}) covering the range from 900 cm^{-1} to 1900 cm^{-1}. An Au-coated silicon probe (tapping AFM-IR cantilever, Anasys Instruments–spring constant 1–3 nN m^{-1}) was employed.

The scanning electron microscope (SEM) was of type Zeiss Supra 40 (Zeiss, Oberkochen, Germany) being equipped with a Schottky field emitter and a high-resolution InLens detector for the secondary electrons. Additionally, the SEM was also operated in the STEM-in-SEM (or T-SEM) mode, by using a dedicated, transmission sample holder which uses typical TEM grids of 3 mm diameter. The sample was prepared as a microtome-slice (see Fig.7.1) on a carbon TEM grid without any additional coating. Various beam voltages (3, 5, 10 and 20 kV) were applied in order to catch both the best surface morphology and reasonable excitation of the X-ray lines considered for EDS analysis (line scans and hyperspectral maps) across the layered structure. The EDS system used was of type Ultra Dry SDD EDS (Silicon drift detector energy dispersive X-ray spectrometer) from Thermo Fisher Scientific (Waltham, MA, USA) with a nominal active area of detector of 100 mm^2. More details on the dedicated arrangement SEM/STEM-in-SEM/EDS can be found in [210].

For X-ray photoelectron spectroscopy (XPS) measurements a Sage 100 (SPECS, Germany) was used. The angle between X-ray source and analyzer was 54.9°. The axis of the analyzer forms an angle of 18° with the sample surface normal. The samples were analyzed with non-monochromatic Al Kα radiation at a pressure of less than $3*10^{-7}$ mbar. The measurement area was 1 x 3 mm^2. The spectra were taken at a current of 18 mA, and 10 kV and 20 eV pass energy in fixed analyzer transmission mode. The results are a mean value of two measurements. The software CasaXPS was used to fit recorded signals.

7.3. Results and discussion

7.3.1 Morphology of the interfacial region

The microtomed cross-sectional surface of the layered sample is first analyzed using scanning electron microscopy (SEM) and presented in Fig.7.2. The average thickness of HydBo layer is approx. 1 μm. The interface between HydBo and epoxy is flatter on the left side (i.e. to EP1) of HydBo. Due to the morphology of the crystals in the outer region, no well-defined border between EP2 and HydBo is observed. As seen in the inset image of Fig.7.2, in the outer region of the boehmite layer towards EP2 (right side) the crystal growth orientation is rather perpendicular to the plane of the substrate (EP1). There, boehmite crystals show thin nanoplatelets and needle-like morphology approx. in length. This morphology was also confirmed by transmission electron microscopy (see Appendix B). Due to the high surface area of such nanostructures in the outer region of the layer, a pronounced interaction between boehmite and epoxy within this region is expected (marked with a dashed oval in Fig.7.2). Thus, this board region is the area of interest in further AFM measurements. In the following, we analyze the mechanical and physical properties of epoxy (EP2), preferentially in this interfacial region.
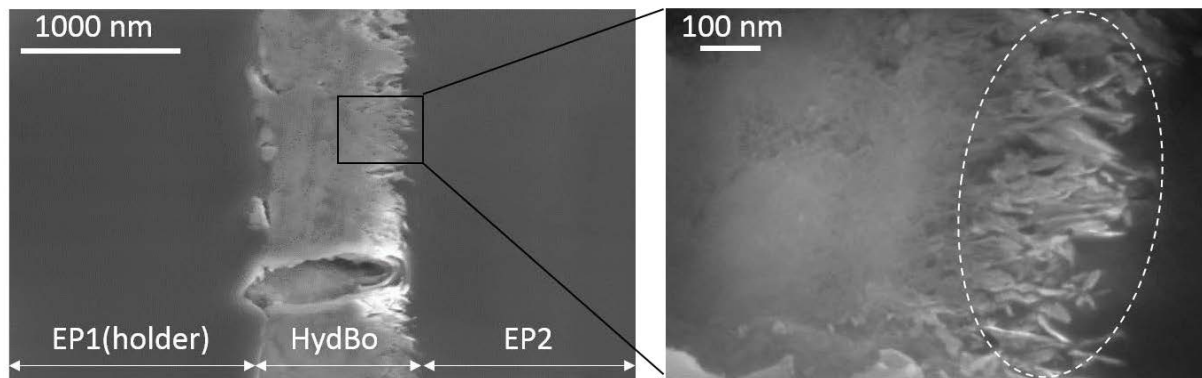
Fig.7.2 3 kV SEM micrograph of the cross-sectional surface of EP1/HydBo/EP2 layered structure prepared as microtome slice on a hollow TEM grid (without additional coating).

7.3.2. Intermodulation AFM analysis

The interfacial region described above was measured by means of ImAFM, as shown in Fig.7.3. The inset image of Fig.7.3 shows the AFM tapping mode topography of the cross-sectional surface of the sample. The topography image is consistent with the SEM micrograph in which the morphology of HydBo layer is distinguishable from the epoxy. By implementing ImAFM, ADFS force curves are obtained for each pixel of the scanned area. Fig.7.3 presents the average curves from different regions of the scanned area including bulk EP2 (red), bulk HydBo (green) and the interfacial region (blue). It is observed that these curves have different

characteristics in both attractive and repulsive regimes. As mentioned before, the repulsive regime occurs when the tip comes in contact with the sample surface due to the applied force (distance < 0, far right in Fig.7.3), and the slope of the curve in this region represents the stiffness of the sample. In the attractive regime, the tip experiences net attractive forces of different nature, mainly governed by electrostatic and the van der Waals forces (distance> 0). The electrostatic forces can be originated by either the dissociation of the surface groups or by absorption of ions onto the surface [211]. The influence of electrostatic forces is of long-range nature and observable in tip-sample separation distances above 20 nm , whereas van der Waals forces affect the tip in immediate distances to the surface [212]. In the vicinity of the surface, due to the van der Waals forces, the tip experiences the jump-to-contact [88]. Here, we use the force offset at jump-to-contact, which is here named F_{JC}, to map the van der Waals forces. The distance at which the slow zero-force offset starts, named d_{EF}, is here used to map the intensity of electrostatic forces and the distribution of surface charges of the sample. Since the forces in the attractive regime are independent of mechanical properties of the sample, the maps of electrostatic and van der Waals forces can be used as complementary channels of information to observe material contrast and to precisely distinguish the stiffness of organic and inorganic phases in the composite, as well as locating the mechanical interphase.
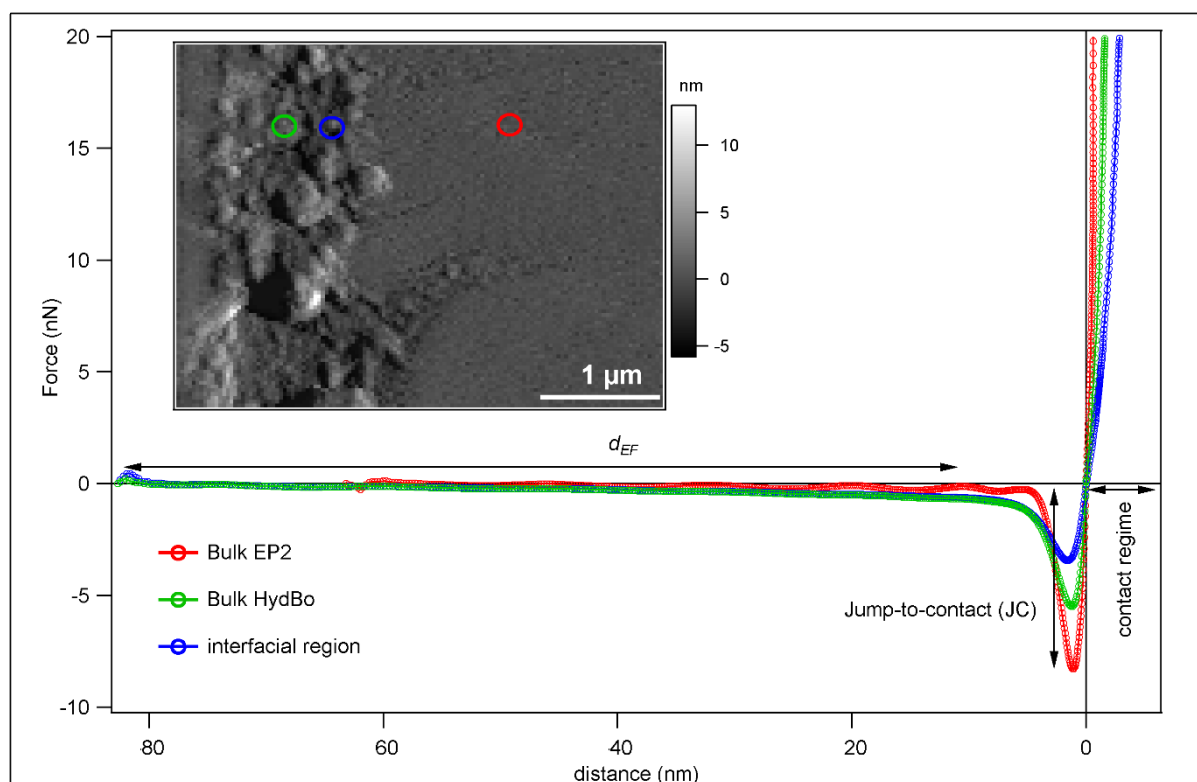

Fig.7.3 Averaged force-distance curves from ADFS measurements on point locations shown in the inset image (topography). See text for details.

Fig.7.4a and b show the maps of F_{JC} and d_{EF}, respectively. The map of stiffness, which is obtained by linear fit of the curve in the repulsive regime, is presented in Fig.7.4 c. The map of d_{EF} shows the material contrast between bulk epoxy and bulk HydBo layer. In the map of F_{JC}, the interfacial region appears more pronounced, whereas bulk HydBo and bulk epoxy do not differ significantly.

The stiffness map (Fig.7.4 c) shows a similar contrast to the F_{JC} map (Fig.7.4 a), where the interfacial region has a very low stiffness compared to bulk HydBo and bulk epoxy. There is no significant stiffness contrast between bulk epoxy and bulk HydBo. This is in agreement with previous findings, where the stiffness values of cured epoxy and boehmite in nanocomposites did not show a remarkable difference [200]. The soft area at the interfacial region, which is approx. 100-200 nm thick, coincides with the location of the HydBo's outer shell (nanoplatelets described in Fig.7.2). These results show that where structures of boehmite with high surface area are exposed to a curing epoxy, a soft interphase is formed as a result of the interaction between epoxy components and boehmite surface. It is noteworthy that additional studies of the mechanical properties of bulk epoxy (EP2) with the AFM force-distance curves (FDC) approach did not show any long-range (over 1 μm) stiffness gradient in the bulk epoxy (see Appendix C).

The formation of the soft interphase around BNPs in epoxy matrix with approx. 50 nm thickness was previously reported [200]. It was hypothesized to be due to either disturbed crosslinking, confinement effects or to preferential absorption of epoxy component (either DGEBA or anhydride hardener) leading to a local phase segregation in the vicinity of boehmite surface [200]. In section 3.5, AFM-IR measurements provide information about the chemical composition of the soft interphase.
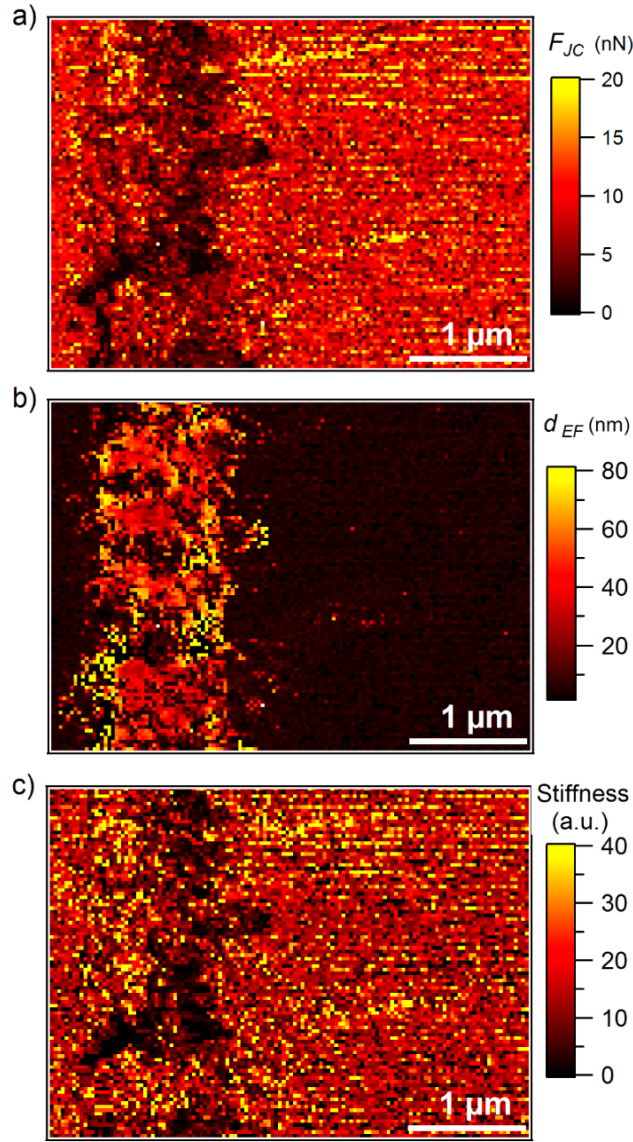
Fig.7.4 Maps of a) attractive force (jump-to-contact height), b) attractive force (electrostatic force), and c) stiffness of the cross-section of EP1(left)/HydBo/EP2 (right) model sample.

7.3.3. Surface potential measurements

Although bulk epoxy and bulk HydBo do not show a clear contrast in stiffness, their surface charges do show a remarkable contrast as observed previously in the d_{EF} map. For a better evaluation of the electrical properties, the sample was examined with SKPM. A larger scanned area (20 µm x 20 µm) enabled to visualize the long-range effects as seen in Fig.7.5. In the topography image (Fig.7.5 a), the morphology of the HydBo layer is distinguished from the epoxy layers. In the potential map (Fig.7.5 b), in addition to the potential difference between HydBo and bulk epoxy, a considerable potential gradient is also present, whereas on the EP2 side it extends over a wide region.

107
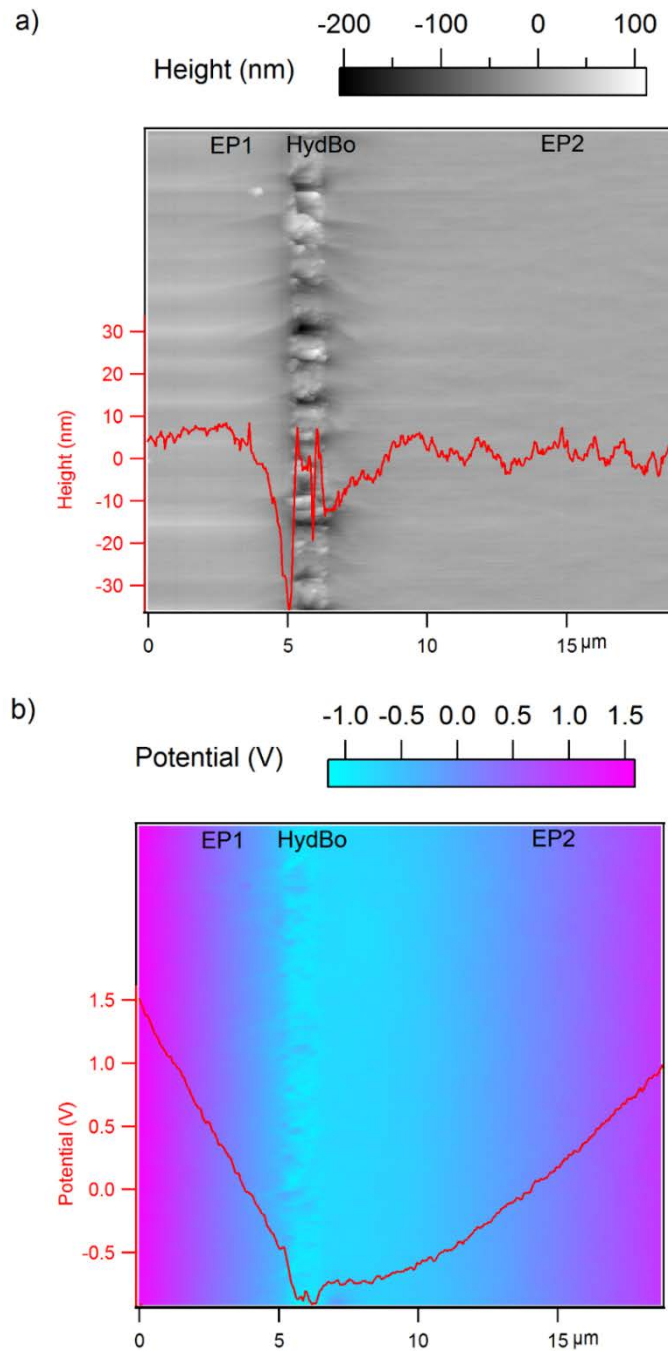
Fig.7.5 Maps of a) topography and b) surface potential of the cross-section of EP1/HydBo/EP2 model sample. The line profiles are presented in red color.

It was previously reported that in epoxy-boehmite nanocomposites, epoxy exhibits higher potential values than boehmite [200]. The difference in the width of potential gradient toward EP1 and EP2 is due to their different preparation histories. Due to the diffusion of aluminum through the surface of EP1 during the thermal deposition and further possible chemical bonding with the epoxy, a gradient in potential is expected at the interface of EP1 and HydBo. However, the gradient between HydBo and EP2 is five times broader than that of EP1. Such a

long-range interaction was unexpected, mainly since no long-range mechanical interphase was observed in force-distance curve measurements on the similar scanned area and the soft interphase around was only formed around the outer shell of HydBo with a less than 1 μm thickness. Therefore, we hypothesized that the nature of such long-range potential gradient obeys chemical alterations in the bulk epoxy. This could be either the result of diffusion of HydBo nanostructures far into the bulk EP2 during the preparation/curing, or alteration of the curing chemistry of epoxy due to preferential absorption of epoxy components. These two hypotheses are further studied by elemental analysis using SEM-EDS and chemical analysis using AFM-IR, respectively.

7.3.4. Elemental analysis via EDS (energy dispersive X-ray spectroscopy)

A representative SEM image of the cross-sectional surface of the EP1/HydBo/EP2 system together with an EDS linescan with Al K, C K and O K X-ray line intensities are shown in Fig.7.6. An EDS hypermap (containing an EDS spectrum in each pixel) has been acquired over the area imaged in Fig.7.6 as an alternative to a conventional linescan (see appendix D), in order to avoid beam damage due to long acquisition times for an analysis point. From the 256 x 196 pixels EDS hypermap acquired for 5 min, after 67 frames with only 4.4 s/frame, the EDS linescan shown in Fig.7.6 has been extracted by summing the net X-ray intensities (after spectral background subtraction) along the direction parallel to the HydBo layer. Thus, good counting statistics has been attained at gentle conditions (i.e. at high scan speed of the electron beam). It should be noted that the preparation of the thin, electron-transparent slice by microtomy has resulted in a reduction of the spatial resolution of EDS from the conventional micrometer range down to below 100 nm [41] There is a clear asymmetry in the signals of Al, O and C at the interphases of EP1 and EP2 with HydBo layer. This is due to different morphology of HydBo layer as observed in Fig.7.2. At the left side of the HydBo layer, in which the boehmite shows a more compact morphology, the intensity of the Al and O signals are higher (and the edge becomes sharper) than on the frayed right side which interacts with EP2. Furthermore, on the right side of HydBo, where the long-range (~10 μm) potential gradient has been observed (see Fig.7.5), the intensity of Al signal drops immediately at the interphase of EP2 and goes to zero approx. 1 μm away from the HydBo layer. This demonstrates that no significant long-range diffusion of boehmite into the bulk of the epoxy material is observed and thus this hypothesis does not explain the formation of the long-range potential gradient.
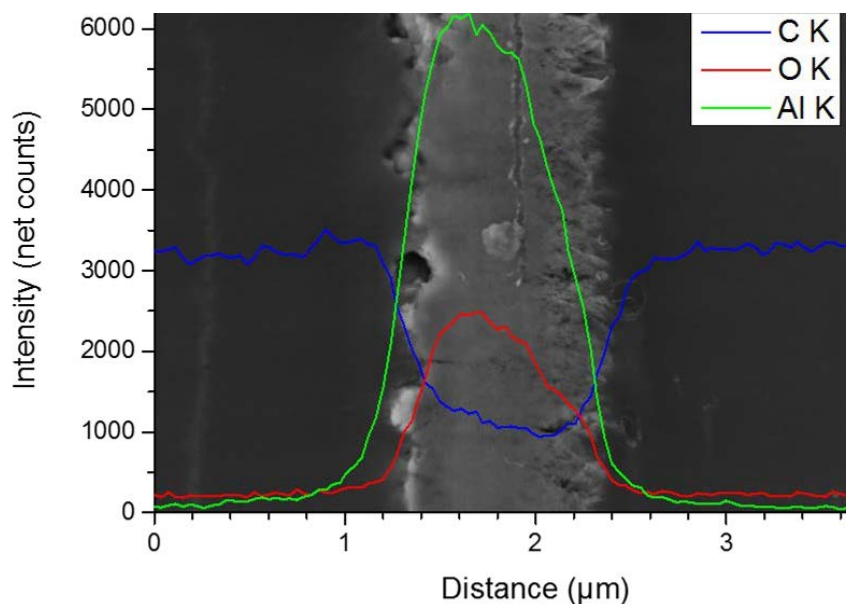
Fig.7.6: 3 kV SEM micrograph of the cross-section of EP1(left)/HydBo/EP2(right) and a 20 kV EDS linescan with C K, O K and AL K signals as net intensities (after spectral background subtraction). The EDS linescan has been extracted from a 256 x 196 pixel hypermap (appendix D) over the imaged area and after summing all the net X-ray intensities along the direction parallel with the HydBo layer in order to get good counting statistics under gentle excitation conditions.

It is noteworthy that the net intensity of C K line inside the HydBo layer is not zero. This could be explained by diffusion of epoxy inside the HydBo volume during the preparation and curing. However, a small contribution of carbon from surrounding epoxies (EP1 or EP2) might be co-excited by the X-rays generated in the not perfectly compact HydBo layer. The non-zero carbon signal in the HydBo layer has been observed also in other EDS linescans measured at different locations over the HydBo layer in the conventional linescan mode (point-by-point). It is reasonable to assume that EP2 components are absorbed physically or interact chemically with the surface of HydBo with its inherent roughness of at least 100 nm (Fig.7.2). Additionally, EP2 components penetrate through the porous surface structure of the HydBo layer. If this interaction is selective, meaning that one component (resin or hardener) is more likely to interact with HydBo layer, a long-range chemical alteration of the bulk EP2 occurs consequently, which can result in the long-range potential gradient in EP2. Since a direct correlation between the carbon signal to the diffusion of epoxy into the HydBo layer is not conclusive from the EDS measurements, we further examine this hypothesis by investigating local chemical structure of the epoxy using AFM-IR.

7.3.5. AFM-IR analysis

Prior to AFM-IR, ATR-IR spectroscopy on pure DGEBA, MTHPA, HydBo and the cured epoxy were carried out (see Appendix E). The carbonyl group usually shows a strong

intensity of absorption in the infrared spectrum C=O, which makes it useful to identify the anhydride component. The absorbance peaks at 1779 cm^{-1} and 1860 cm^{-1} are attributed to symmetric and asymmetric stretch of C=O, respectively. Depending on the intra- and intermolecular factors, these peaks can show deviations. Intermolecular hydrogen-bridging between C=O and an external component can result in a slight decrease of absorption frequency. The curing of epoxy with anhydride results in formation of an ester band at 1739 cm^{-1} and disappearance of the asymmetric stretch of carbonyl[20]. This information is further used to interpret the AFM-IR results.

Local IR signals were collected from the cross-sectional surface of EP1/HydBo/EP2 sample at different distances (0, 1, 5 and 15 μm) from HydBo layer. The spectra taken from the points with similar distance to HydBo are averaged and plotted in Fig.7.7. The absorbance at 1077cm^{-1} is a typical boehmite band which is not overlapped with the absorbance of epoxy and, thus, in our experiment it is used to identify the existence of boehmite [213]. It is observed that this absorption peak is not only present in the HydBo layer, as expected, but also in the epoxy domain up to 1 μm away from the HydBo and no absorption is observed at further distances (5 μm and 15 μm). This confirms that the diffusion of particles in the bulk polymer is only limited to short distances as also observed with EDS, where the aluminum signal was only pronounced up to 1 μm away from HydBo so that no boehmite was detected in the bulk EP2.
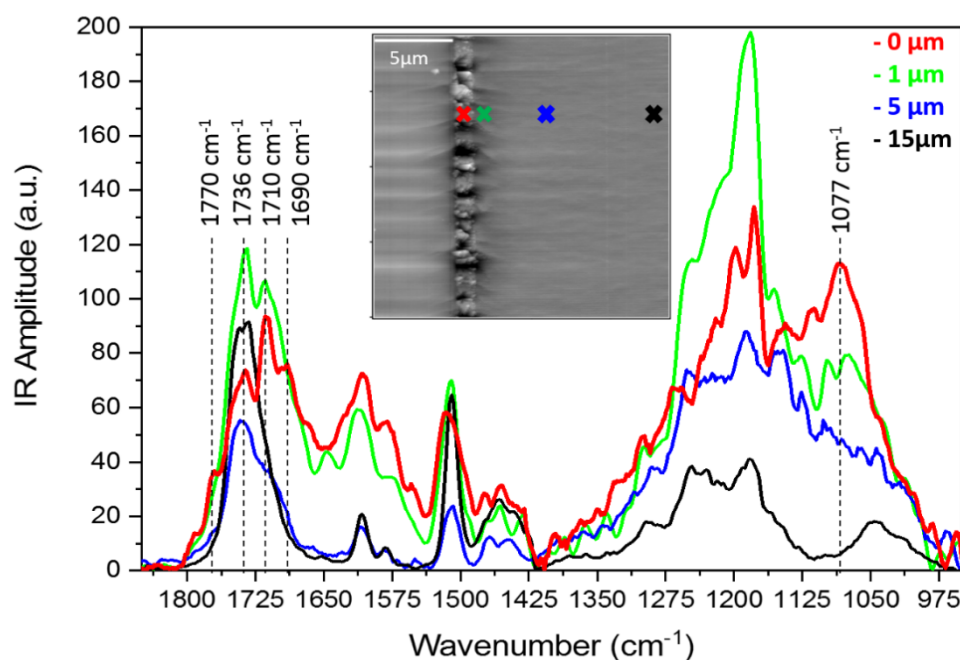
Fig.7.7 AFM-IR spectra from point measurements shown in the inset AFM topography image of the cross-sectional surface of EP1/HydBo/EP2 model sample.

Besides the ester band at 1736 cm^{-1}, which associates to the curing of epoxy with anhydride, an additional shoulder at 1770 cm^{-1} in the spectrum taken from the outer region of HydBo (0 µm) indicates the existence of unreacted anhydride absorbed by the HydBo layer. This peak gradually decreases with increasing distance from the interface and disappears completely at distances larger than 15 µm. The latter is the same distance where the potential gradient was observed in Fig.7.5. The presence of unreacted anhydride in the vicinity of HydBo indicates that the resin-hardener ratio is locally imbalanced and consequently the curing and chemical properties of the epoxy network are also affected at long distances (up to 15 µm) from the interface. The absorbance bands at 1510 cm^{-1} and 1608 cm^{-1} associate to the presence of the aromatic rings of DGEBA, which exists in all spectra including the spectrum obtained from the outer region of HydBo layer (0 µm). Hence, DGEBA is also present within the HydBo layer. Since all the characteristic absorption bands related to oxirane (831, 915 and 3057 cm^{-1}) are either overlapped with absorption of other species or out of the frequency limitation of AFM-IR, it is not possible to distinguish if the DGEBA component in these spectra is unreacted or part of a polymer chain.

It is noteworthy that there is a clear absorbance peak at 1712 cm^{-1} and 1690 cm^{-1}, which also gradually disappears up to 15 µm away from the HydBo layer. The absorbance peak at 1712 cm^{-1} was also observed in FTIR measurements when pure MTHPA hardener was mixed with

BNPs, whereas the mixture of pure DGEBA and BNPs did not result in the emergence of any additional peaks (see Appendix E, Fig.E3). The shift of absorption frequencies to 1712cm^{-1} and 1690 cm^{-1}can be attributed to the stretch of carbonyl bonds due to hydrogen bridging or chemical bonding to the hydroxyl groups of boehmite Another possible reason can be the water molecules, absorbed on the surface of HydBo layer or trapped inside the layered structure of crystals: the hydrolysis of anhydride results in formation of hydroxyl-anhydrides that in turn result in a side reaction pathway of carboxyl-epoxy polyesterification [24]. The hydroxyl anhydride can further result in hydrogen-bonding that may explain the absorbance band at 1690 cm^{-1}.

7.4. Discussion

The soft interphase with 100-200 nm thickness in the outer region of HydBo is attributed to the soft interphase forms surrounding the particles in epoxy-BNP nanocomposites shown in our previous studies [200]. The chemical composition of the soft interphase is different from the bulk epoxy due to the existence of excess anhydride hardener that did not participate in any reaction as observed in the AFM-IR spectrum taken from this region. Formation of an additional absorption band (1710 cm^{-1}) at the interphase, which is possibly related to species of anhydride with intra- or intermolecular H-bonding, also confirms the altered chemistry of the epoxy in this region. Moreover, in the previous studies, mechanical properties of bulk epoxy including the stiffness, energy dissipation and crosslinking density were also affected by BNPs [200, 201]. Here, measurements on a layered model system showed the chemical alteration of bulk epoxy. The AFM-IR results showing the preferential absorption of anhydride hardener and altered chemistry of the bulk support the hypotheses of distortion of stoichiometric ratio in the bulk. Therefore, further studies need to assess the effect of altered epoxy-hardener ratio on the bulk properties such as stiffness, chemical structure, crosslink density and energy dissipation, and correlate them with the presented results.

Although the location of potential gradient and chemical alteration coincide, there is insufficient proof to conclude that the chemical alteration is the cause of potential gradient in the bulk epoxy. Therefore, other possible mechanisms for such long-range potential gradients must be considered. One possible mechanism is the transfer of charges (single ions or ions on particles or charge particle) from the HydBo into the epoxy layer. At the interface of HydBo and EP2, sharp needle-like nanostructures of boehmite grown up perpendicular to the EP2 plane possibly enhance the injection and transfer of the trapped electrons to the bulk epoxy. Another consideration for the long-range potential gradient is the change in number of traps

and localized energy states of the bulk epoxy. As an effect of disturbed stoichiometric-ratio and altered curing chemistry in the vicinity of boehmite, the resulting polymer network may have less traps for energy, which results in lower values of surface potential than for the bulk epoxy. To investigate the effect of trapping states and the mechanism of charge transfer, surface potential measurements must be carried out in an open-loop fashion with no voltage feedback, where the DC bias of the tip can be varied. In this case, where tip and sample come into contact at a point, electrons or holes can be injected and the change of the potential values will provide information about the charge traps [214].

7.5. Conclusion

The interaction between boehmite and epoxy was investigated successfully by designing a layered epoxy/boehmite/epoxy model sample. The hydrothermally synthesized boehmite coats the first epoxy layer (substrate). The outer morphology of the hydrothermally synthesized boehmite is in the form of nanoplatelets and nanoneedles perpendicular to the plane. This outer region comes in contact with the mixture of the resin and the hardener (second epoxy layer) while curing and, thus, formation of interphases is expected to be observed in this region. Intermodulation AFM provided maps of stiffness, electrostatic and van der Waals forces. The contrast in the stiffness map revealed the formation of a soft phase with 100-200 nm thickness between the outer region of boehmite layer and the epoxy. The soft interphase was hypothesized to be caused by preferential absorption of unreacted anhydride hardener molecules on the surface of boehmite. This hypothesis was in finally proven by AFM-IR showing the correlated absorption peaks. In Nature and man-made composites, synergistic material properties combining high stiffness, strength and toughness are often attributed to a very complex role of the soft interface and to a hierarchical structure based on mechanically inferior H- bonds [215-217]. Such a soft interphase often acts as an advanced binder allowing the energy dissipation and suppressing catastrophic crack propagation, thus promoting the toughness of the epoxy nanocomposite as previously reported [12].

Using scanning Kelvin probe microscopy, a long-range interphase with a potential gradient width of over 10 μm was detected. Based on SEM-EDS measurements, boehmite particles did not diffuse far into the bulk epoxy and thus this effect does not play a role in the long-range potential gradient in the bulk epoxy. However, the distribution of carbon in the elemental analysis might indicate that polymer molecules penetrated in the boehmite layer and thus we hypothesized that as result of a selective interaction between boehmite surface and epoxy

components, the bulk polymer network is chemically altered, and this may give rise to the long-range potential interphase. AFM-IR investigations demonstrate the formation of a new absorption band at 1710 cm^{-1} at the interface up to few microns far into the bulk epoxy. The location of this chemical alteration coincides with the electrical interphase, demonstrating the long-range interaction and bulk effect of the presence of boehmite. Further studies are required to understand other possible mechanisms such as bulk electrical formation and the consequence of preferential absorption of the hardener, which is hypothesized to alter the local stoichiometric balance of epoxy-anhydride systems. The presented model system and techniques open possibilities to investigate the interfacial properties of different kinds of polymer and inorganic interphases and study the effect of different surface modifications on the interphase properties.

Acknowledgement

Concluding remarks

The primary hypotheses of this dissertation have been introduced in chapter 3. Here, on basis of new findings presented in Chapter 4, 5, 6 and 7 the verification of these hypotheses is discussed. In the outlook, new hypotheses as the basis of ongoing research and future investigations are introduced.

Hypthesis.1: The inclusion of BNPs as stiff fillers with higher Young's modulus than that of the epoxy matrix results in increase of the composite Young's modulus.

For years, the increase of the total tensile modulus of epoxy/BNP nanocomposites has been mainly attributed to the reinforcing effect of BNPs as highly stiff ceramic fillers. Assuming high stiffness values for BNPs was mainly based on few theoretical calculations, suggesting a Young's modulus of 138 to 156 GPa for boehmite. Without a precise experimentally obtained value for the Young's modulus of BNPs in the literature, using the simple theoretical mechanical models such as rule of mixture and Halpin-Tsai for such nanocomposite is impossible. Therefore, the first goal was to obtain more realistic value of Young's modulus of boehmite determined by suitable experimental approaches. Using AFM-based force-distance curve approaches, it was shown that the average Young's modulus of boehmite does not exceed 10 GPa. This value significantly deviates from the previously calculated values via simulation (see Chapter 4). Such a low Young's modulus of BNP significantly weakens the hypothesis 1 which claims Young's modulus of the BNPs is responsible for the enhanced modulus of nanocomposite. The new experimental value as the Young's modulus of BNPs (10 GPa) was taken into account for calculation of the total modulus of the nanocomposite using Halpin Tsai model and compared with experimental modulus values of the nanocomposite. Results show the deviation of the behavior of the composite particularly in case of high particle mass fractions from the theoretical values (see Appendix I SM2). Therefore, this assumption of hypothesis 1 based on classical theoretical models does not hold for epoxy/BNP nanocomposites, due to more complex interaction mechanisms. The competing reinforcement mechanisms may originate from formation of a strong interphase or alteration of bulk epoxy matrix properties in the presence of BNPs, which is addressed next.

Hypothesis 2: The inclusion of BNPs in epoxy, results in alteration of the structure and properties of bulk epoxy, including the crosslinking density and Young's modulus.

Further in Chapter 5, nanomechanical properties of the matrix phase in epoxy/BNP nanocomposites with various BNP loadings has been studies via nanoscale stiffness mapping

of the composite surface. additionally, dynamic mechanical behavior of the nanocomposite especially above glass transition which mainly reflects the behavior of the pure polymer matrix independent for the particles. The nanoscale mechanical maps have shown that the epoxy matrix becomes stiffer in the presence of BNPs especially at high loadings. Additionally, the decrease of glass transition temperature and crosslink density of the epoxy with inclusion of BNPs are clear indications of structural and network alteration in epoxy. Therefore, neat epoxy and the epoxy matrix phase in the nanocomposites are different in both structure and properties. These observations confirm the hypothesis 2. Such alteration can be caused from an alternative curing mechanism and network formation of the polymer as result of the interaction with BNPs. Moreover, it is concluded that the Young's modulus of epoxy cannot be considered as a constant when applying the theoretical models and thus resulting in the theoretical mismatch with experimental results. The alteration of Young's modulus of matrix at high BNP loadings affects the overall behavior of the nanocomposites.

Hypothesis 3: *the increase of fracture toughness and failure resistance in epoxy/BNP nanocomposites is mainly due to formation of a soft interphase with different network structure than the bulk. Formation of a soft interphase results in enhancing the energy dissipation and damping mechanisms in the nanocomposite.*

In Chapter 6 the interphase properties are directly investigated on the surface of cured nanocomposites, utilizing two AFM modes and multiple information channels. The particles and the particle-matrix interfacial region were identified and the topographical artifacts which leads to misinterpretation of the location of the phases was eliminated. The hypothesis of formation of soft interphases around the particle has been verified via the ImAFM stiffness mappings: a homogeneously soft interphase with few tens of nanometers thickness, with no gradient properties was observed near BNPs. Moreover, additional information regarding the local properties of epoxy has been extracted via mapping of the dissipative energy on the surface of the nanocomposites. The results show that the energy dissipation of the epoxy matrix in the presence of BNPs is considerably higher than the neat epoxy. This observation can be correlated to the increase of fracture toughness. Thus, besides the formation of a soft energy dissipating interphase, the alteration of the bulk epoxy structure as an effect of interaction with BNP amplifies to the energy dissipation mechanism all over the material.

Hypothesis 4: *The preferential absorption of epoxy components (resin or the hardener) toward the BNPs results in formation of an interphases with different chemical structure than the bulk. In this case, the interphase may consist of either excess epoxy or hardener molecules*

which did not participate in the crosslinking reaction of bulk epoxy. Moreover, such preferential absorbance results in formation and coexistence of multiple interphases (chemical and mechanical) with different thicknesses.

The shortcoming of the nanoscale study of nanocomposite samples with random distribution of particles is the overlap of interphases and the effect of hidden, buried particles under the surface: Therefore, more precise determination of interphase properties requires a layer model sample with a defined structure. In Chapter 7, the design of a layered model sample is proposed, consisting of a boehmite layer sandwiched between two epoxy layers, one as the holder (with no interactive interphase) and the other is interacting with boehmite and forming an interphase. This model sample provides a large, easy to access interfacial region, eliminating the shortcomings of the nanoscale measurements on the nanocomposite samples. Investigations has been carried out to determine the stiffness, surface potential and chemical composition of the epoxy at different distances from the interfacial region. The interphase in the model sample is a soft homogeneous phase with a thickness of approx. 100 nm. In addition to this mechanical interphase, an electrical properties interphase is also observed which exceeds the interfacial region and reach the bulk epoxy over 10 micrometers away from the boehmite layer. These observations confirm the hypothesis of coexistence of multiple interphases with different natures and different thicknesses as result of interaction of BNPs with epoxy. The potential difference which is mainly attributed to the chemical composition differences is correlated to the previously observed alteration of the bulk epoxy. Therefore, the hypothesis of chemical alteration of bulk epoxy due to interaction with boehmite gets stronger. In the end, using the AFM-IR method to probe the local chemical composition of sample clearly confirms that the soft interphase has an altered chemical structure. It consists of an amount of unreacted anhydride and formation of an additional absorption band possibly related to species of anhydride with intra- or intermolecular hydrogen-bonding at the interphase shows that the interphase indeed has a different chemical structure than the bulk epoxy. Based on these findings, it is confirmed that a) preferential adsorption of anhydride hardener into the BNP phase, b) alteration of the chemical structure of the epoxy and coexistence of multiple interphases are the reasons for formation of soft interphase and disturbed network density of bulk epoxy, respectively.

Outlook

As previously discussed, one important conclusion in this dissertation is preferential interaction of BNPs with anhydride. This results in formation of soft interphase around BNPs,

alteration of the bulk properties of epoxy matrix and consequently of the total properties of the nanocomposites. The mechanism behind such an interaction between anhydride and BNPs is still an open question. One possibility is that the hydroxyl groups on the surface of BNPs bond chemically or via hydrogen-bridging with the carboxyl group of the anhydride. Another possibility is the reaction of interlayer water molecules of BNPs with anhydride. The hydrolysis of anhydride results in formation of hydroxyl-anhydrides that in turn may result in a side reaction pathway of carboxyl-epoxy polyesterification. Nevertheless, more investigations are required to identify the mechanism behind the interaction of anhydride hardener and BNPs. Ongoing investigations are carried out with analytic approaches such as IR spectroscopies and liquid state NMR. For this purpose, model experiments are designed to investigate possible chemical interactions between BNPs and single components of epoxy system (resin, hardener and accelerator) individually and further the effect of BNPs on the curing kinetics.

Moreover, the preferential adsorption of one component of the epoxy matrix results in stoichiometric imbalance in the epoxy-hardener system. The consequent of such stoichiometric changes is formation of more than one separate or interconnected networks with different thermal and mechanical properties (e.g Young's modulus and T_g). To verify this hypothesis, it is necessary to investigate the effect of altered epoxy-hardener stoichiometric ratio on the local and bulk properties of nanocomposite. In the future investigations, model samples in which the stoichiometric ratio is systematically altered are made. The stiffness, chemical structure, thermal properties, crosslink density of the model samples are assessed and further correlated to the local and bulk properties of BNP nanocomposites.

Appendix I: Supporting material for Chapter 5

SM1:
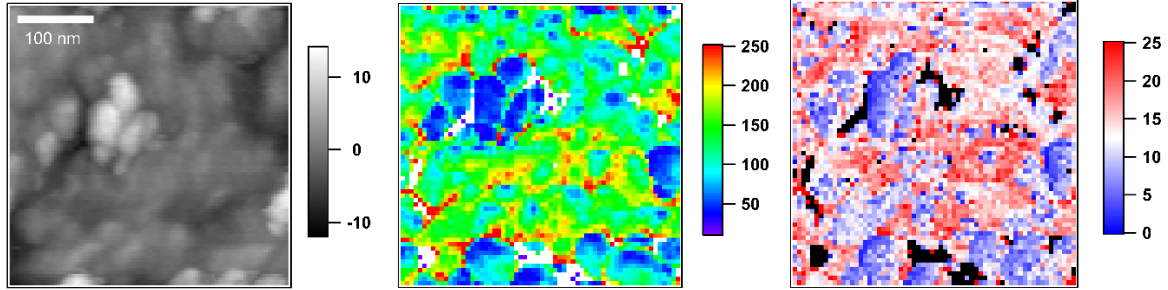
SM1.1 Tapping mode topography (left) and ImAFM work of attractive forces W_{attr}(middle) and stiffness map of EP/BNP15. White pixels on the on W_{attr} map and black pixels on stiffness map indicates error. The color scale units of topography, W_{attr} and stiffness map are nm, nJ and arbitrary unit, respectively.
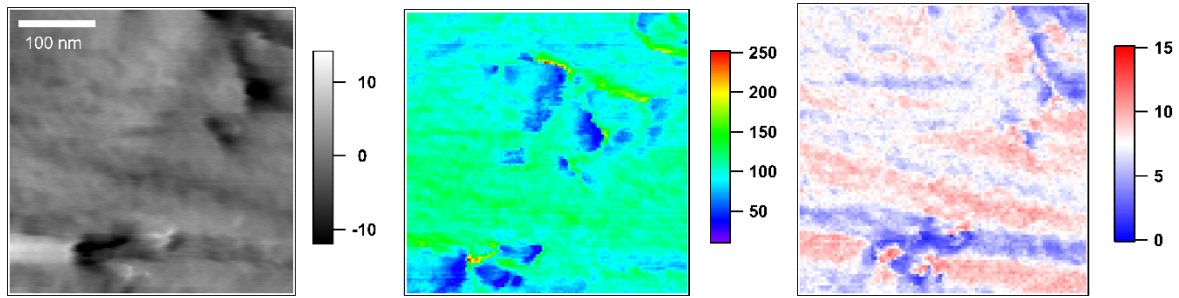
SM1.2 Tapping mode topography (left) and ImAFM work of attractive forces W_{attr}(middle) and stiffness map of EP/BNP2.5. The color scale units of topography, W_{attr} and stiffness map are nm, nJ and arbitrary unit, respectively.

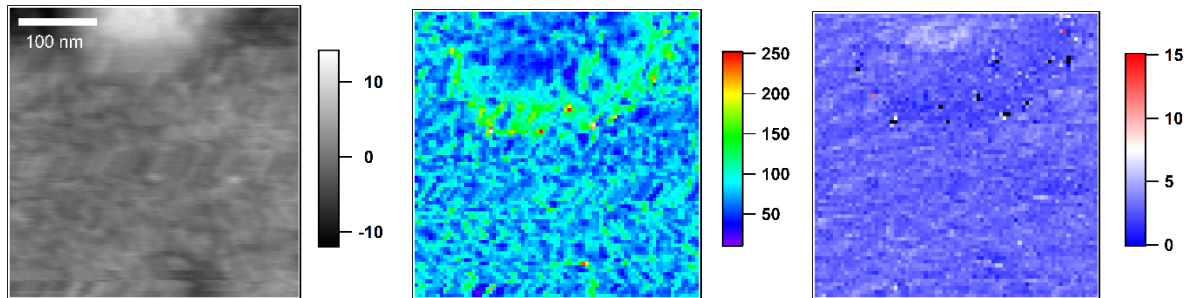SM1.3 Tapping mode topography (left) and ImAFM work of attractive forces W_{attr}(middle) and stiffness map of of neat epoxy EP. The color scale units of topography, W_{attr} and stiffness map are nm, nJ and arbitrary unit, respectively.

SM2: Comparison of experimental data with Halpin-Tsai model

It was assumed that the drastic increase of elastic modulus of composite E_c with BNP is due to contribution of elastic modulus of BNPs which is in the range of 10 GPa. Halpin-Tsai and experimental moduli are in the good agreement for only low particle concentrations (less than 5wt%). This shows that for low particle concentrations E_{BNP} is the main reason for increased modulus of the composites. However, from 5wt% Halpin-Tsai cannot follow the drastic increase of modulus. The disagreement between theoretical models and experimental mechanical behavior has been already observed in studies on several nanocomposite systems as it was usually attributed to the interphase modulus and also percolation of interphase. However, we believe that alteration of the modulus of matrix E_m as observed in our study is the reason for the disagreement with the theoretical model. Treating E_m as a variable parameter has never been taken into account in any theoretical modifications of Halpin-Tsai and hence it is noteworthy to be considered when such a behavior is observed.
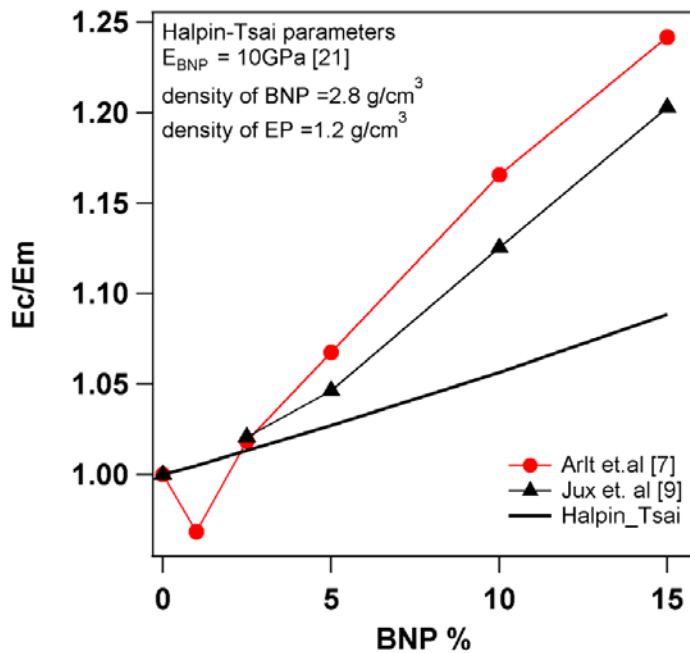
SM2. comparison of experimental elastic modulus of the EP/BNP nanocomposites from previous studies with the theoretical model Halpin-Tsai

SM3: Supplementary DMTA results
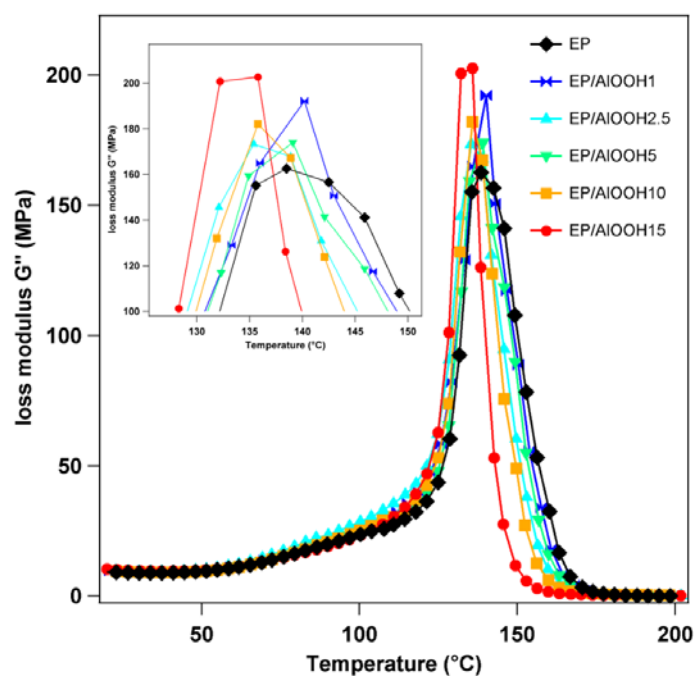
SM3.1 Loss modulus spectra of anhydride-cured epoxy with different BNP mass fraction (first run)
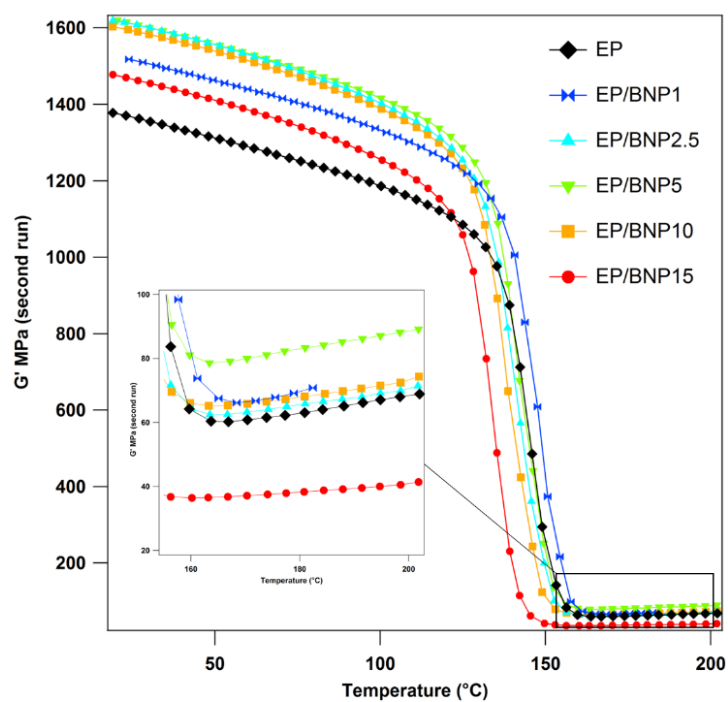
SM3.2 Shear storage modulus of anhydride-cured epoxy with different BNP concentrations (second run)
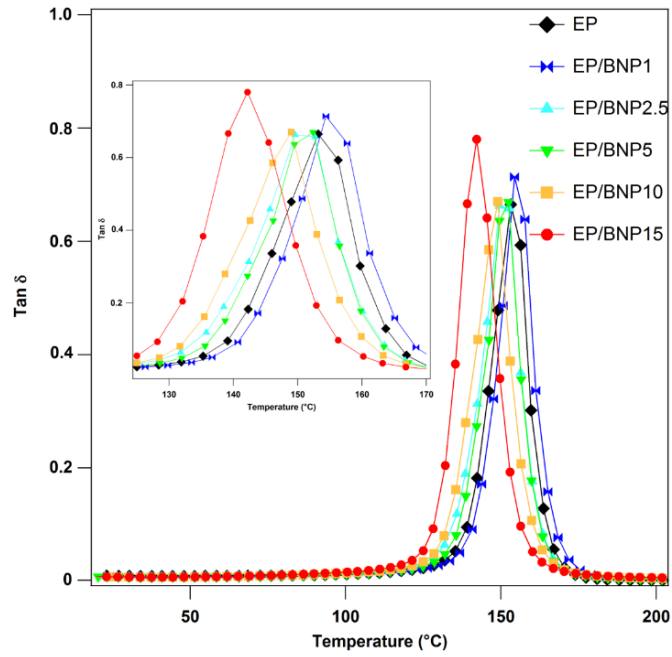
SM3.3 loss tangent of anhydride-cured epoxy with different BNP concentrations (second run)
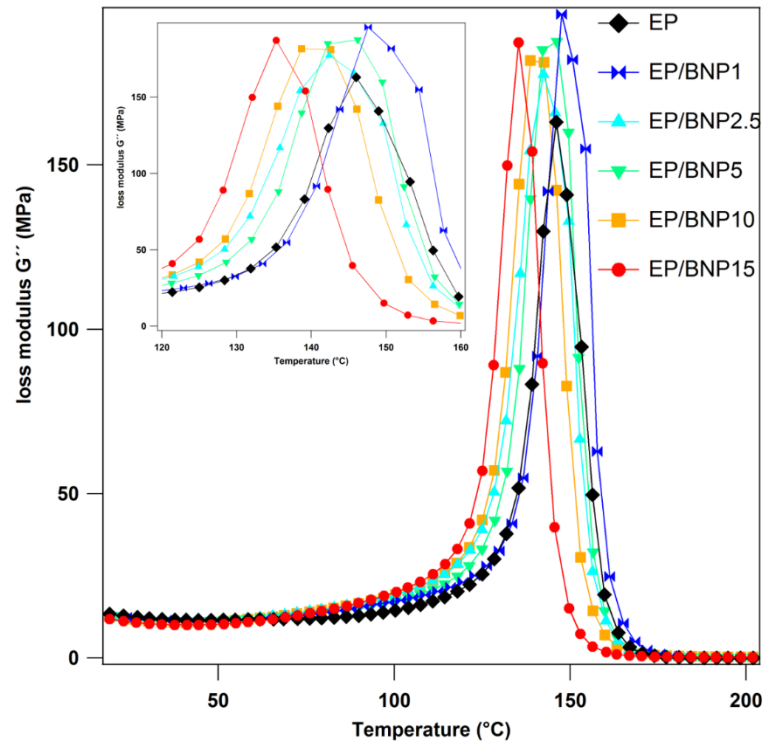
SM3.4 loss modulus spectra of anhydride-cured epoxy with different BNP mass fractions (second run)

the quantitative analysis of the *tan* δ and storage modulus of the second run for all compositions are evaluated from second run spectra (SM4,5 and 6) and listed in Table 2. For all compositions, T_g did not show any significant change from first to second run. However, the width of *tan* δ peak drops for all samples to a minimum value of 14 K. This is the width

which the EP/BNP15 nanocomposite has already reached during the first run and seems to be the minimum value that can be reached.

Table 2. Analysis of storage shear modulus and *tan* δ curves of the dynamic mechanic spectra for each composition (second run)

composition	Storage modulus G´ at room temperature (MPa)	Absolute value of Energetic elasticity G_e (MPa)	Crosslinking density v (mol m^{-3}) $*10^6$	Glass transition temperature T_g (˚C)	Width of half-height (K)	Peak Height (a.u.)
EP	1378	52	8.3	153	14	0.66
EP/BNP1	1518	80	9.17	154	14	0.71
EP/BNP2.5	1619	40	8.45	150	15	0.66
EP/BNP5	1620	45	10.64	152	14	0.66
EP/BNP10	1603	29	8.7	149	14	0.67
EP/BNP15	1478	17	4.9	142	14	0.78

Comparison of the crosslinking density values of first run with second run in Table 1 and Table 2 shows that for all compositions, the crosslinking densities are shifted to higher values while G_e shows a considerable decrease. Following the argumentation of Pohl et al. [42], a decrease in G_e values implies that the response of the network is more entropic. High values of G_e during the first measurement implies that the elastic response of samples at rubbery state was govern more energetically. According to Pohl et al., energy contribution G_e can be originated from physical entanglements and intermolecular forces. Thus, a decrease of G_e values in the second run implies that by exposure to high temperature, chemical crosslinks replace the physical interactions.

unfilled epoxy in the second run shows 10% increase in glassy state storage modulus compared to the first run. Nevertheless, for EP/BNP15, the difference between glassy state modulus in first and second run is only around 2%. Also, the increase of crosslinking density in second measurement for EP/BNP15 is small compared to unfilled epoxy and other compositions. It is noteworthy that 5wt% nanocomposite (EP/BNP5) has a distinctive behavior as exposure to high temperatures affects the mechanical properties of this composition more than others: The measurements in second run show that both crosslinking

density and glassy-state modulus reaches the maximum value among all other compositions. In composites less than 5wt% (EP/BNP1 and EP/BNP2.5), the changes in crosslinking density is not considerably large. Thus, somewhere between 5wt% and 10wt%, the crosslinking density starts to decrease and reaches its minimum value at 15wt% particle concentration. Therefore, a particle concentration between 5% to 10% appears to be a critical composition. The same tendency is observed in glassy state modulus from the second run. At low concentrations, the glassy state modulus increases and reaches a maximum value for EP/BNP5 then shows a slight trend of decrease for higher concentrations. The reason behind the behavior is not yet understood. However, a concentration threshold makes it reasonable to assume two competing effects of network formation, resulting a higher crosslinking at a BNP content between 5% and 10%.

SM4.Thermogravimetric analysis

To characterize the pyrolysis behavior (thermal decomposition) of the materials thermogravimetric analysis (TGA) was employed. Figure SM4 shows the mass loss rate curves of a pure epoxy and nanocomposites with various BNPs content. A minor decomposition process of approximately 0.2 wt% for the unfilled epoxy to 0.7 wt% for the nanocomposite with the highest BNPs content at ca.150 °C corresponds to the pyrolysis or desorption of the anhydride, which did not take part in the cross-linking reaction. Furthermore, at ca. 250 °C another decomposition reaction is observed as a change in the mass loss curve of about 2.5 to 4 wt% for the pure EP to the EP/BNP15, respectively. This results from the thermal degradation of the un-reacted DGEBA monomer. The decomposition products at 150 and 250 °C were investigated with a Mass Spectrometer (MS). At the lower temperature the gas contained CO_2, which is a typical decomposition product of an un-reacted anhydride bonds, whereas at the higher temperature phenyl group was detected, resulting from a decomposition of the un-crosslinked DGEBA monomer. A more detailed discussion about the TGA-MS results will be publish elsewhere. The main step of approximately 90 wt% for EP, decreasing with increasing BNPs content to 70 wt% for EP/BNP15, corresponds to the degradation temperature (T_{deg}) of the samples. A shift of the T_{deg} from approximately 408 °C for EP to 388 °C for EP/BNP15 indicates that the introduction of BNPs causes an earlier decomposition of the composites, which might result from a change in the network structure, as the nanofiller is added to the matrix. The last step in the mass loss curve for all the samples corresponds to the oxidation of the material. Lastly, the incorporation of the BNPs leads to an increase in the char yield as expected than the inorganic BNP do not decompose completely.

This clearly proves that all experiments with temperatures up to 200°C are not superimposed by problems of the thermal degradation of the different networks.
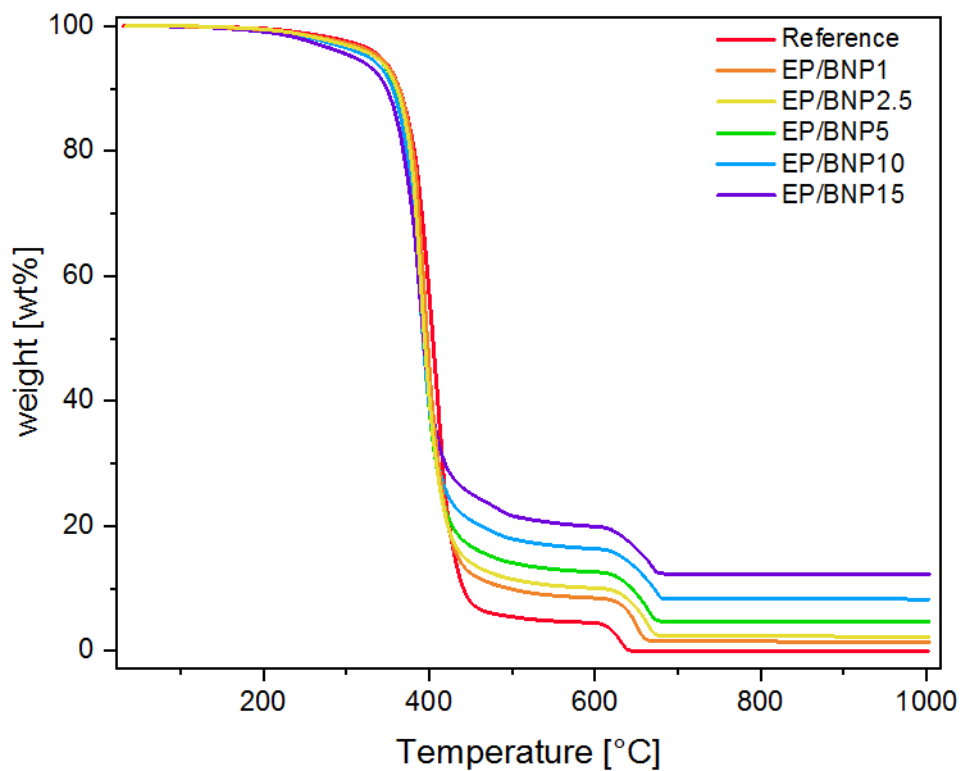
SM 4 : TGA thermograms of neat epoxy (reference) and epoxy/BNP nanocomposites.

Appendix II: Supporting material for Chapter 6

Appendix A
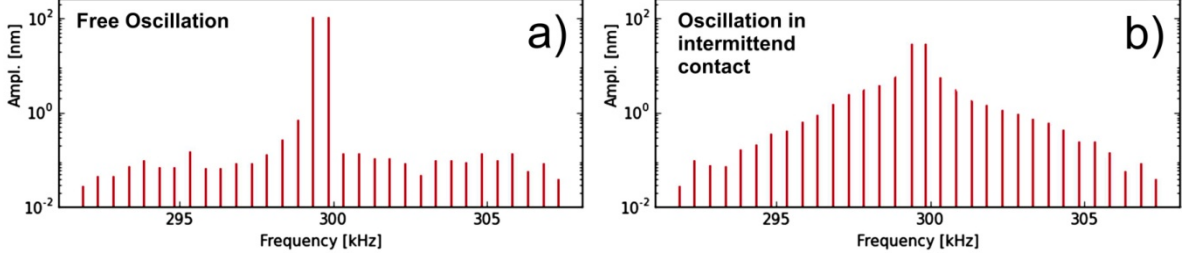
Figure A 1: Free oscillation (a) and oscillation in intermittent contact (b) of a cantilever with $f_0 =$ 299.6 kHz on a polymer surface.

Appendix B

Energy dissipation in multifrequency AFM:

In conventional dynamic atomic force microscopy (AFM) a sharp tip at the end of a micro-cantilever oscillates sinusoidally close to a surface of a sample. The phase difference between the tip oscillation and the drive force or the tip motion far away from the surface is can be related to the energy or power dissipated by the tip-surface interaction. Thus, the (oscillation) phase signal is often considered as a valuable channel of information giving compositional contrast between different surface materials.

Recently, a variety of multifrequency AFM methods have been developed giving detailed insight into the tip-surface interaction. However, the in multifrequency AFM the tip motion is no longer purely sinusoidal and thus the equations relating dissipated energy and phase signal in conventional dynamic AFM do not hold for multifrequency AFM methods like Intermodulation AFM. Here, we show how similar relations can be derived for general multifrequency techniques allowing for simple computation of the energy dissipated directly from the measured tip motion spectrum. Generally, the energy E_{dis} dissipated by the tip-surface force F_{ts} is given by the integral

$$E_{dis} = \int_C F_{ts}(z)dz$$

where C is the trajectory of the tip in the z coordinate. This expression can be written as a parametric integral,

$$E_{dis} = \int_C^T F_{ts}(t)\dot{z}dt$$

where T is the period of the tip motion and the dot denotes derivation with respect to time t. We introduce the

time-reversed velocity which is defined as $\dot{z}-t= \dot{z}(-t)$ which yields

$$E_{dis} = \int_C^T F_{ts}(t)\dot{z}-(0-t)dt$$

This integral can be identified as a convolution and allows by the Fourier convolution theorem us to establish a relation between the dissipated energy E_{dis} and the spectrum of the tip motion,

$$E_{dis} = F^{-1}\{-i\omega \hat{F}_{ts} \cdot \hat{z}^*\}(0)$$

where F is the Fourier operator, i is the complex unit, f is the frequency variable, the hat denotes a Fourier transformed quantity and the star the complex conjugate. In the last step we have used that the Fourier transform of the time-reversed velocity can be expressed as

$$\dot{z}-(\omega)=-i\omega\hat{z}^*(\omega).$$

With the cantilever transfer function $\hat{G}$, we can determine the spectrum of the tip-surface force $\hat{F}_{ts}$ from the measured tip-motion spectrum close to the surface $\hat{z}$ and far away from the surface $\hat{z}_{free}$,

$$\hat{F}_{ts} = \hat{G}^{-1}(\hat{z} - \hat{z}_0)$$

In case of a linear single mode cantilever, the transfer function is given by

$$\hat{G}(\omega) = \frac{\omega_0^2/k}{\omega_0^2 - \omega^2 + i\frac{\omega_0\omega}{Q}}$$

where ω_0 is the angular resonance frequency, k is the spring constant and Q is the quality factor of the cantilever. The dissipated energy E_{dis} now becomes

$$E_{dis} = F^{-1}\{-i\omega\hat{G}|\hat{z}|^2\}(0) - F^{-1}\{-i\omega\hat{G}\hat{z}_0\hat{z}^*\}(0).$$

With this relation we can determine the energy dissipated by the tip-surface force during one period of the tip motion directly from the measured free and engaged tip motion spectra.

Appendix C: Overview of nanoparticle distribution in EP/BNP5

Based on the contrasts observed in Figure A.2, particles tend to form agglomerates in the average size 100 nms. since the primary particle size is 14 nm, what we refer here as particles as actually secondary particles in the form of aggregation of few 10 primary particles.
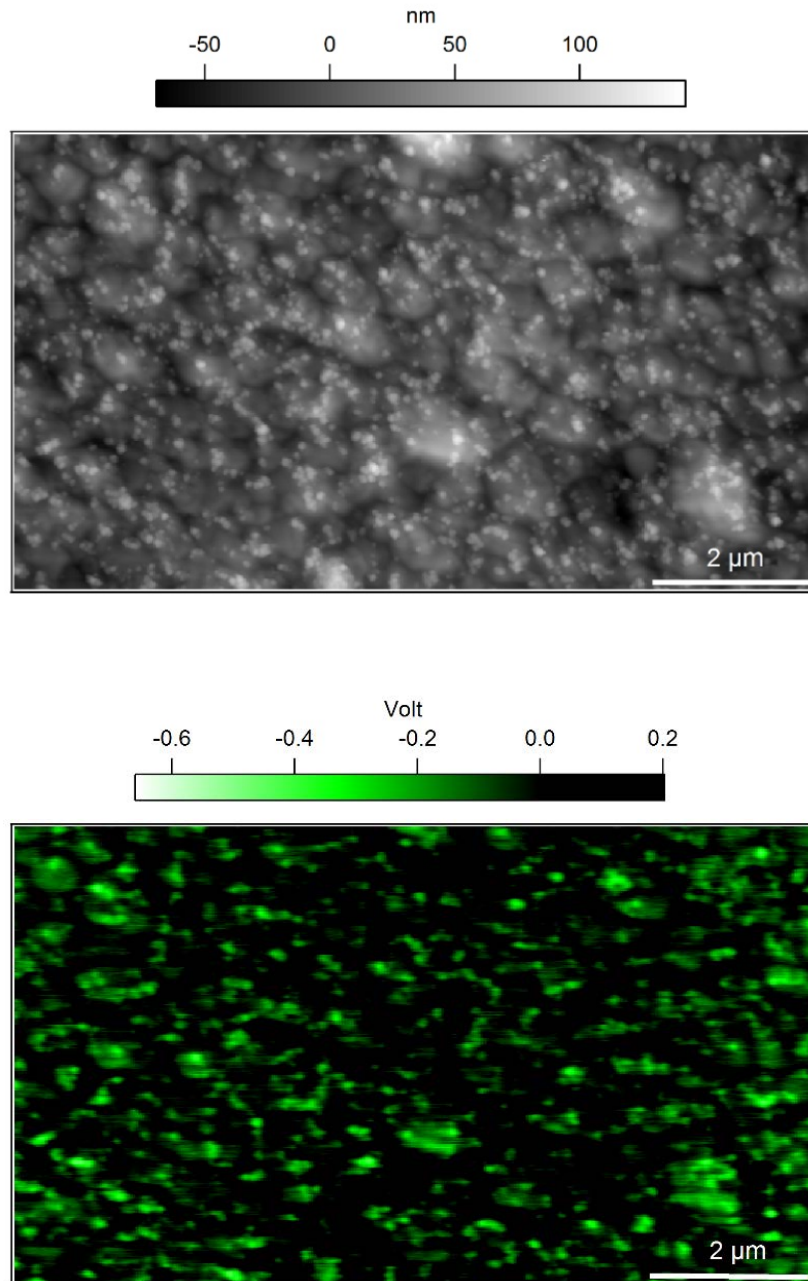
Figure A.2. Tapping mode topography (top) and SKPM surface potential map (bottom) of a 10μm x 6μm scan area of EP/BNP5

Appendix D

Analysis of topography artifacts in measured stiffness

sudden height changes can cause artefacts in topography and force measurements, known convolution effect [218]. Here we study the effect of topography changes on force measurements including stiffness and attractive forces. The first derivative of the topography is calculated and plotted over the force measurement values. Figure 11 shows the histogram of

stiffness and work of attractive forces versus the histogram of topography (first derivative). For both highly negative and positive values of height derivative which indicates areas of with extreme up and downhills in topography, W_{attr} shows low values, however in flat areas (where the derivative is zero or close to zero) W_{attr} exhibit both low and high values. It can be concluded that expect the highly extreme topography changes, the values of W_{attr} are not affected by topography changes. The same can be observed for stiffness: Zero values of stiffness which we take as error occur all over the surface from flat to sharply angled. Also, in flat areas the stiffness can vary from 0 to 100.

Topography features rarely cause artifacts in Potential measurement as in SKPM the tip is kept far from the surface and does not come into contact with the surface.
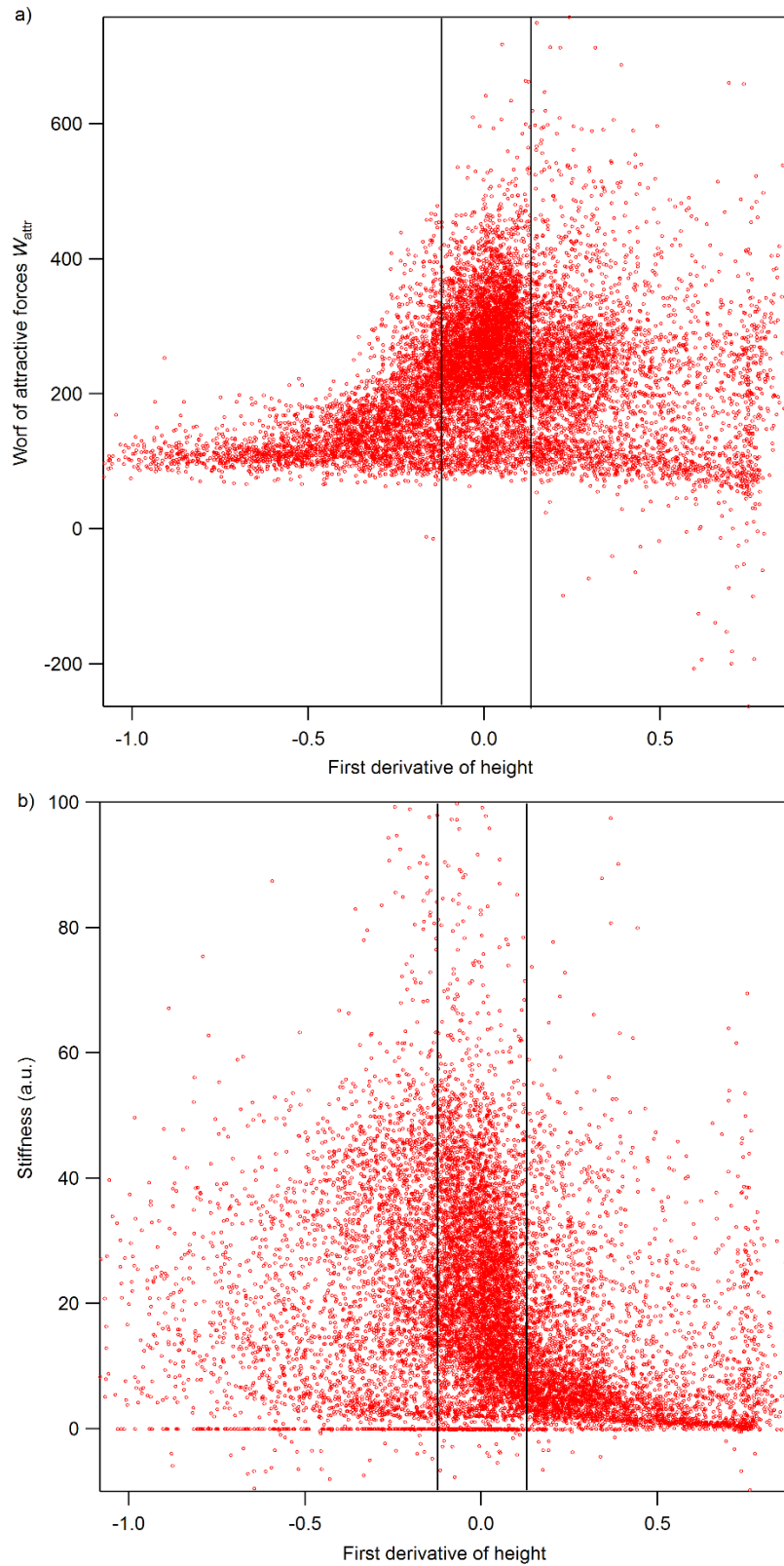
Figure 5: the effect of topography changes on ImAFM force measurement. a) histogram of ImAFM stiffness and b) work of attractive force W_{attr} versus the histogram first derivative of height obtained from tapping mode.

131

Appendix E

Analysis of stiffness-potential relationship of a selected area

a)

b)

c)

d)

e)

f)
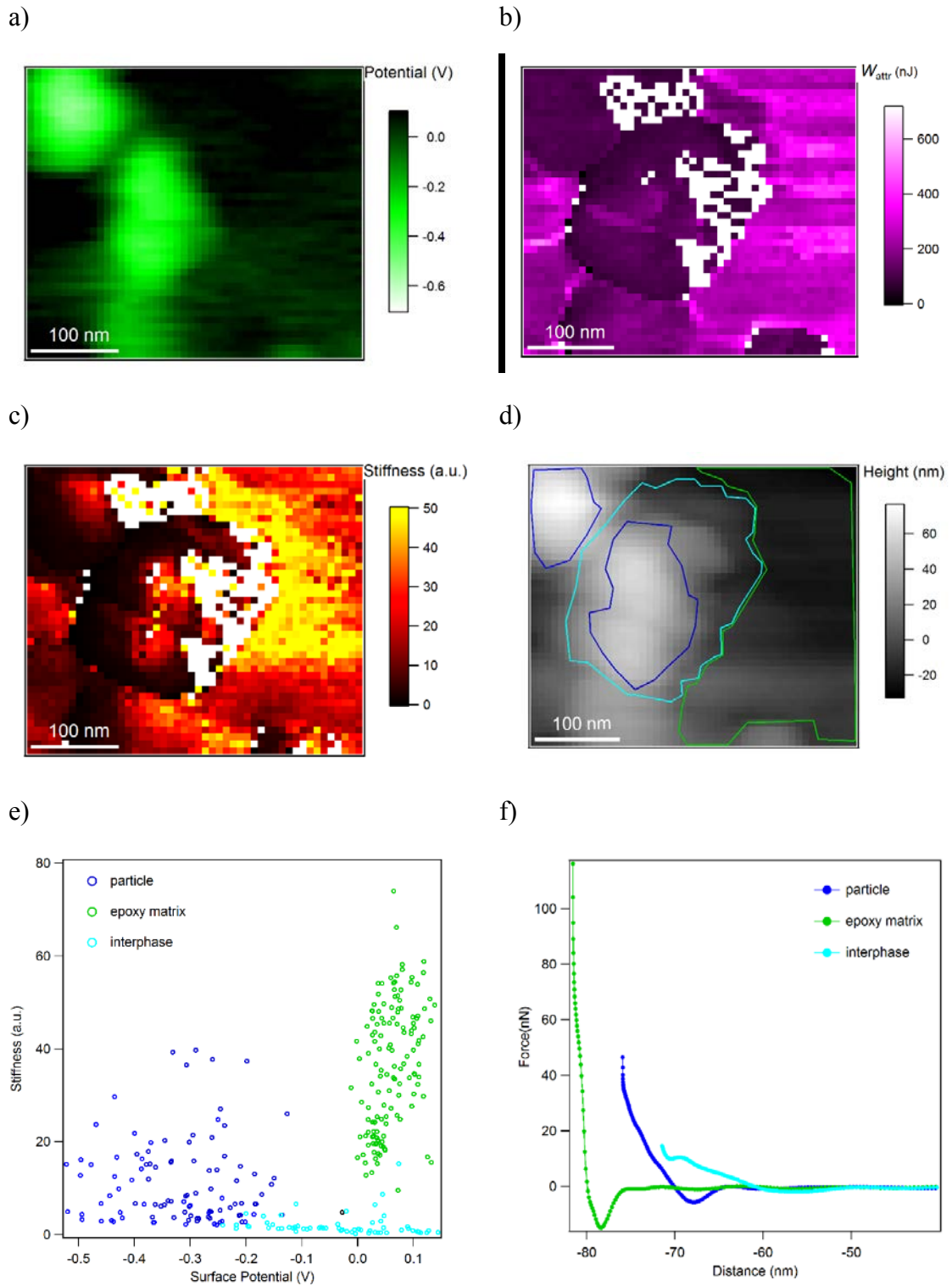
Figure A.4: a) Surface potential, b) work of attractive forces W_{attr} and c) the stiffness map of a selected area from Figure 2 scans. d) The corresponding topography of the scanned area where the domains of particle, interphase and pure matrix are distinguished by traces with dark blue, light blue

and green color, respectively. e)2D histogram of stiffness vs. potential. .f) typical ADFS curves related to particles(dark blue), interphase (light blue) and pure matrix(green). White pixels in b) and c) indicate error pixels

Appendix F

T-SEM micrograph of a 100 nm thick microtome cut of the EP/BNP15:

200nm
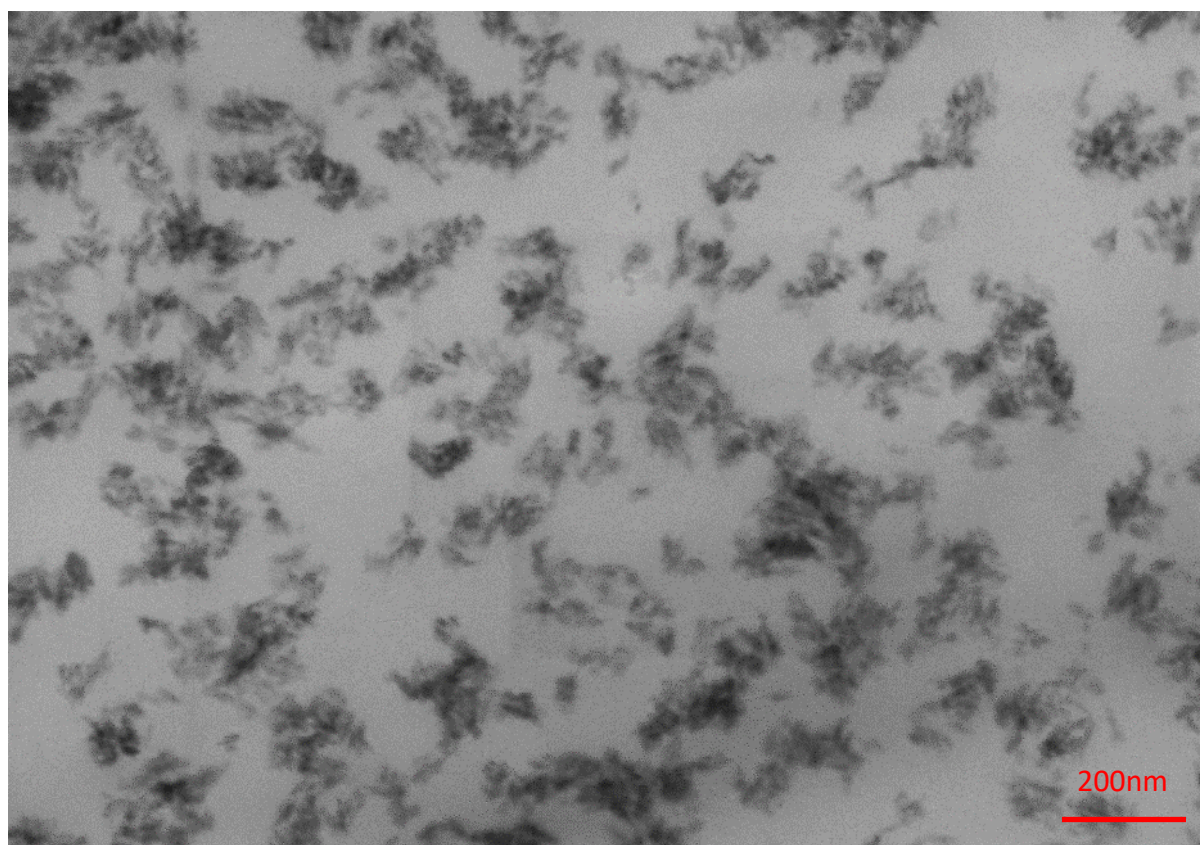
Appendix III: Supporting material for chapter 7

Appendix 1

We verified the chemical structure of HydBo with XPS and compared it with commercially available boehmite nanoparticles (Disperal HP14, Sasol, Germany). During the XPS measurement, the sample is irradiated with X-rays, enabling the removal of near-core electrons from existing atoms. These electrons will be detected and are characteristic of the corresponding atoms. XPS is a surface sensitive method due to working under ultra-high vacuum, where the main information depth is about 5-7 nm. As seen in Fig. 8, the Al 2p peaks show no significant difference. The binding energy of commercially available boehmite NP is 74.3 eV, and 74.4 eV for HydBo. According to previous studies, O 1s spectra provide more information about the crystal structure, hydroxyl groups and absorbed water of boehmite [219]. When comparing the O 1s peaks of the purchased and self-produced HydBo, it becomes clear that both are very similar. The O 1s peak was fitted in both cases. Signals were found for the Al-O-Al and the Al-OH bond at 532.2 and 531.0 eV for the commercially available boehmite. In the HydBo, the binding energies are shifted by 0.2 eV to higher binding energies. The percentage ratios of Al-O-Al to Al-OH for both boehmite types are shown in Table 1. The percentage contents of the HydBo are minimally lower because the sample still contains residual water from the production process.
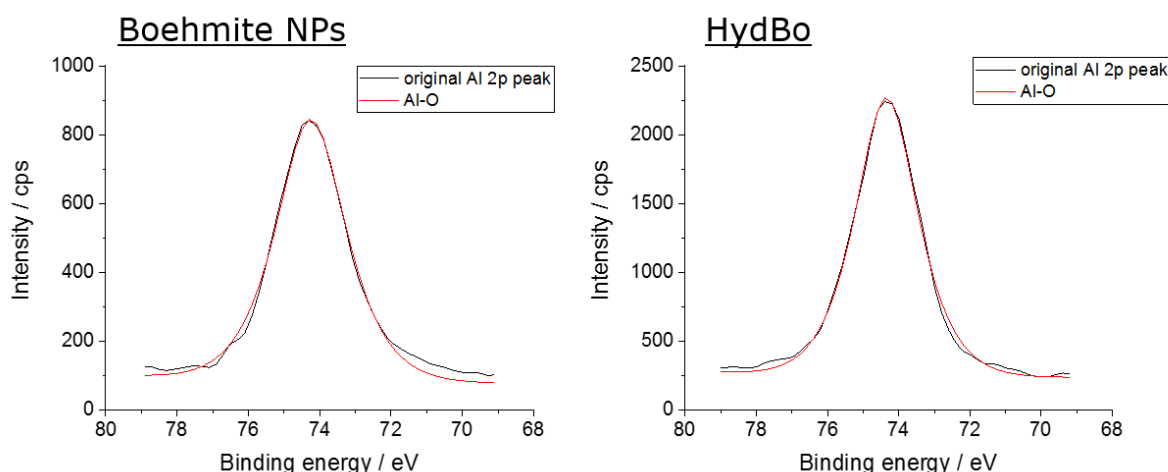
Fig. 8 Comparison of Al p2 peak of commercial boehmite NPs (left) and hydrothermally synthesized boehmite layer on epoxy substrate (right)
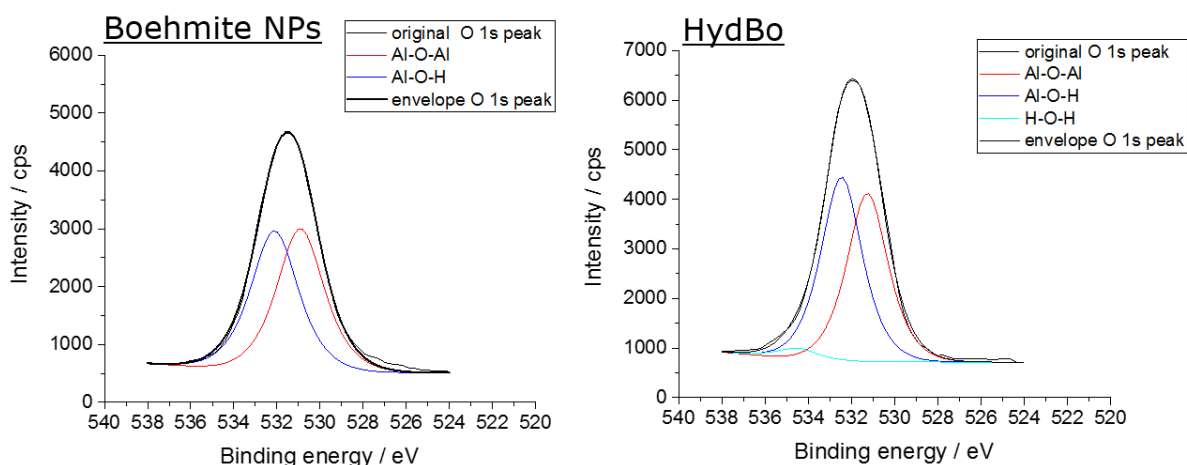
Fig. 9 Comparison O 1s peak of commercial boehmite NPs (left) and hydrothermally synthesized boehmite layer on epoxy substrate (right)

Table 1: Comparison of the percentage ratios of the fitted O 1s peaks

Sample	Al-O-Al in %	Al-O-H in %	H_2O
Commercially available boehmite (BNP)	49.7	50.3	-
HydBo	48.2	49.7	2.1

Appendix 2

An ultramicrotome cut of EP1/HydBo/EP2 with 100 nm nominal thickness was examined using a 2200 FS (JEOL, Japan) transmission electron microscope (TEM) working at an acceleration voltage of 200 keV. The morphology of the outer shell of HydBo (Fig. 10, left) is consistent with SEM micrographs (Fig. 2), demonstrating the needle- and platelet-like structures with low crystallinity (Fig. 10, right).
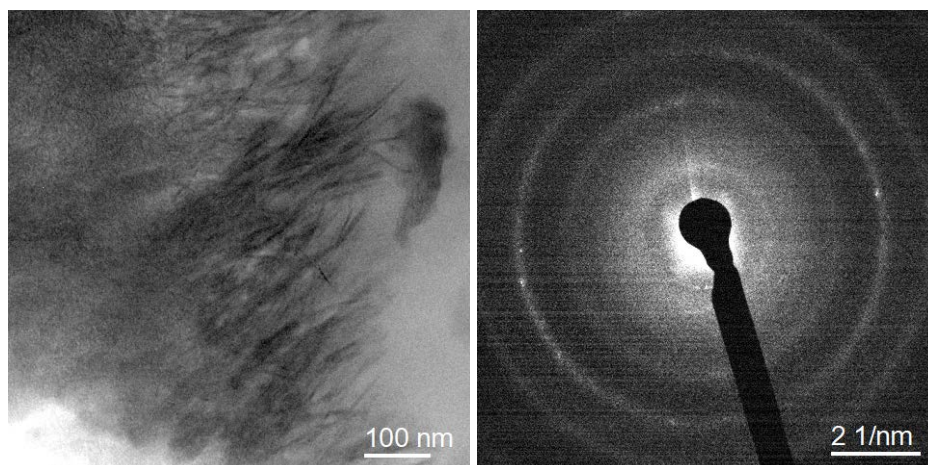
Fig. 10: Bright field (BF) TEM micrograph of the outer region of HydBo layer in EP2 medium (left) diffraction pattern showing crystallinity of region in on the left (right).

Appendix 3

Conventional AFM (force distance curves, FDC) was carried out on the cross-sectional surface of EP1/HYdBo/EP2 using a silicon probe with spring constant of 50 nN/nm, resonance frequency of 329.43 kHz (Nanosensors, Switzerland). The average force-distance curves (repulsive regime) and the FDC stiffness map are presented in Fig.11. A comparison of force-distance curves from EP1 and EP2 in bulk (away from interphase) shows that the Young's moduli of epoxies on both sides are similar. The FDC map taken from different distances from the boehmite layer does not show any significant changes in the stiffness values. Thus, it can be concluded that despite having a long-range (10 μm) chemical interphase between HydBo and epoxy, the mechanical interphase is not observable in this range.
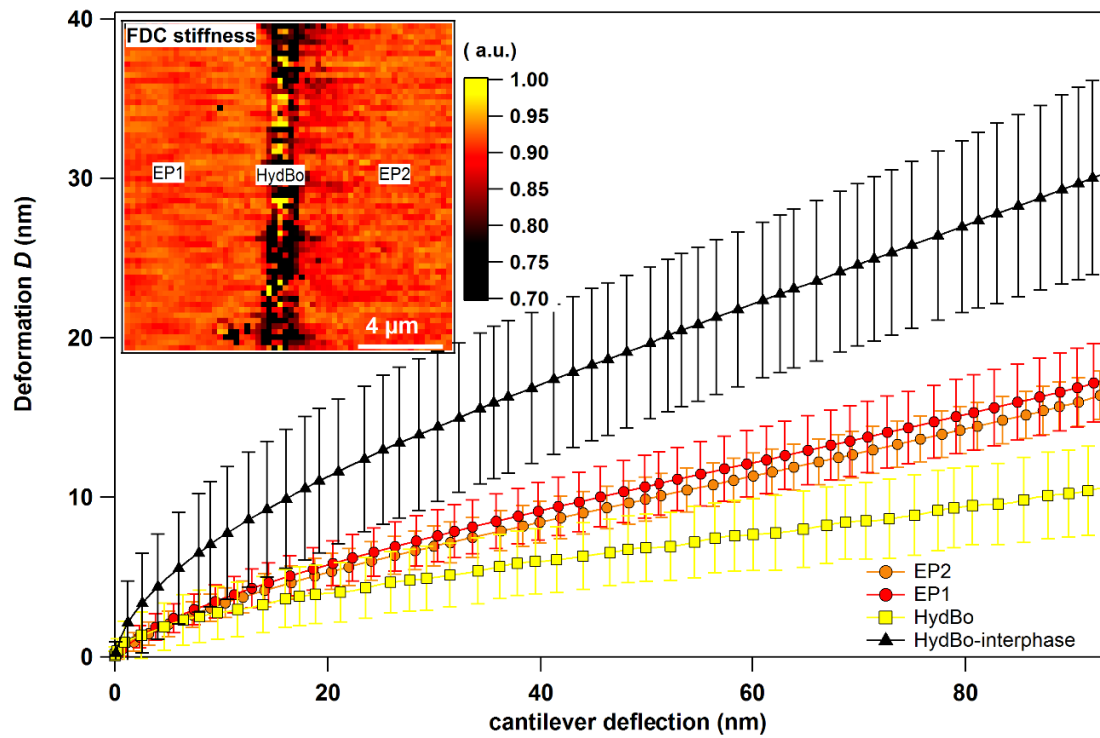
Fig. 11 FDC stiffness map (inset image) and average force-distance curves of the cross-sectional surface of EP1/HydBo/EP2

Appendix 4
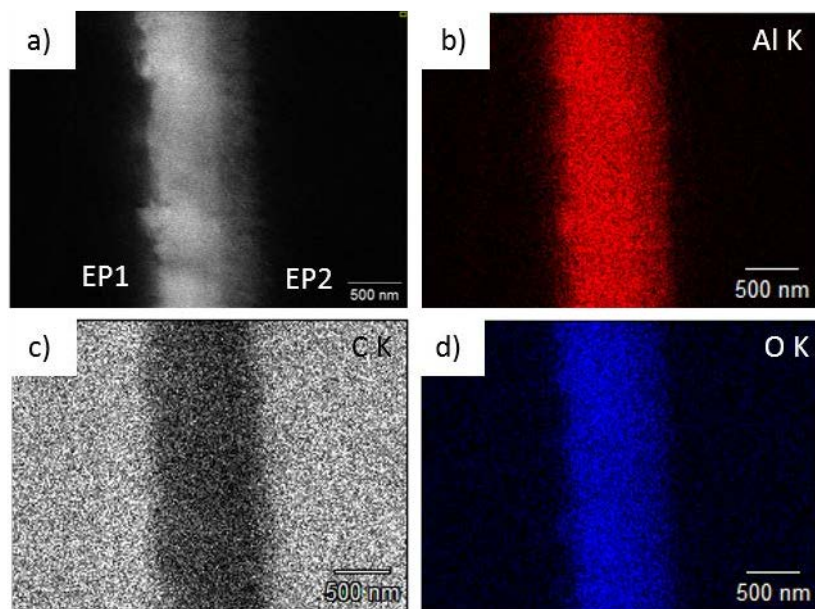
Fig. 12 a) 20 kV SEM micrograph of the microtome-slice EP1(left)/HydBo/EP2(right) sample and the corresponding net X-ray intensities of b) aluminum (Al K), c) carbon (C K) and d) oxygen (O K) extracted from an 20 kV EDS hypermap of 256 x 192 pixels after acquisition of 67 frames @ 4.4 s/frame.

Appendix 5

Attenuated total reflection infrared (ATR/IR) spectra were collected using an FT-IR spectrometer (Smart Orbit; Thermo Fischer Scientific; Karlsruhe, Germany) at room temperature. Fig. 12 shows the IR spectra of anhydride-cured epoxy as well as individual components of the epoxy including pure resin, anhydride hardener as well as pure BNP (powder). The most pronounced peak results from the reaction between oxirane groups of DGEBA with MTHPA and the formation of an ester band at 1739 cm^{-1}.

The mixture of DGEBA with BNP via three roll milling is examined with ATR, whereas no specific change in the spectrum regarding any possible reaction was found. (Fig. 13). However, evaluating the IR spectrum of the mixture of MTHPA with BNPs prepared by three roll milling (Fig. 14) shows that boehmite and anhydride react even at room temperature and thus an additional absorption at 1710 cm^{-1} regarding either a chemical bond or an H-bond appears after mixing. This information confirms that boehmite interacts more preferentially with anhydride component than with the DGEBA resin.
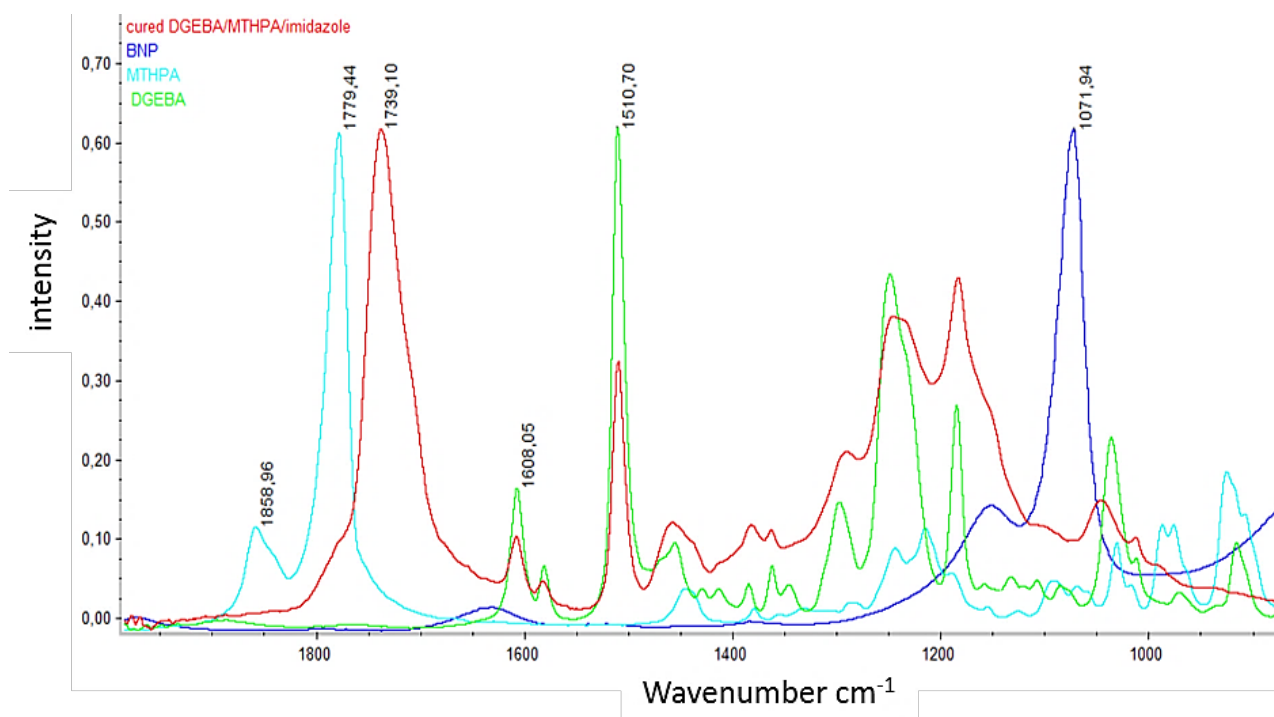
Fig. 13 Room temperature ATR-IR spectra of BNPs, epoxy resin DGEBA, anhydride hardener MTHPA and the thermally cured DGEBA/MHTPA/imidazole(accelerator) with 100:90:1 mixing ratio and 120 curing temperature.
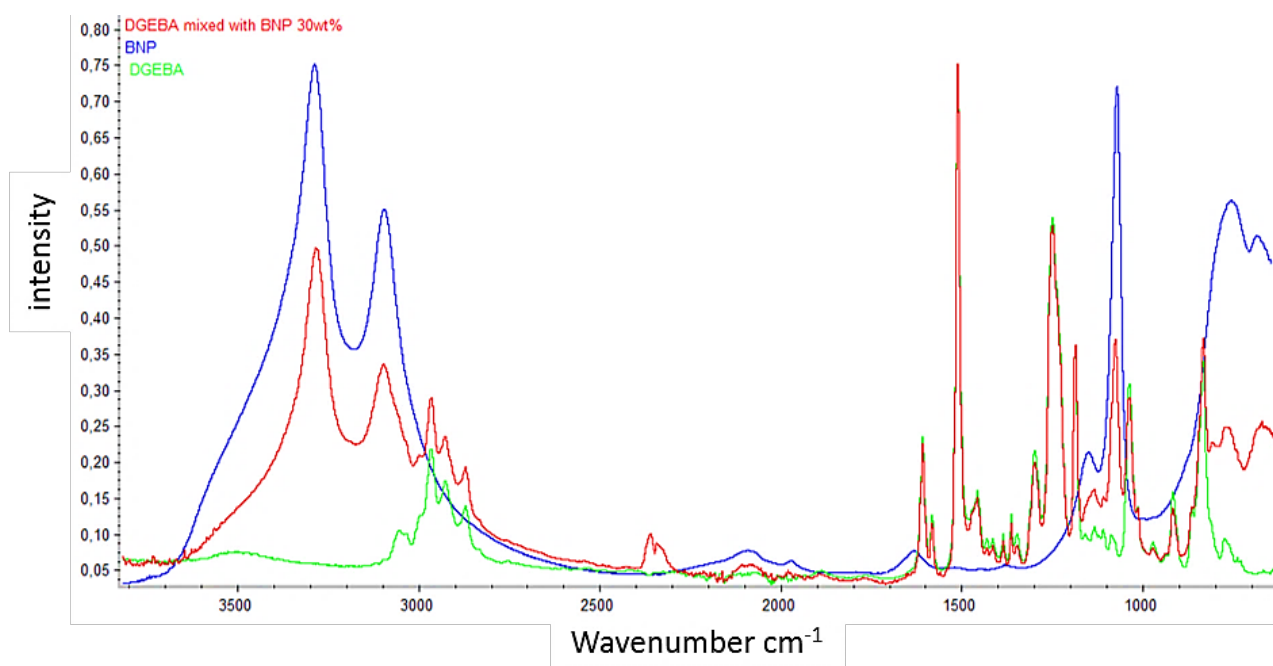
Fig. 14 Room temperature ATR-IR spectra of BNPs, epoxy resin DGEBA and the masterbatch mixture of BNPs and DGEBA.
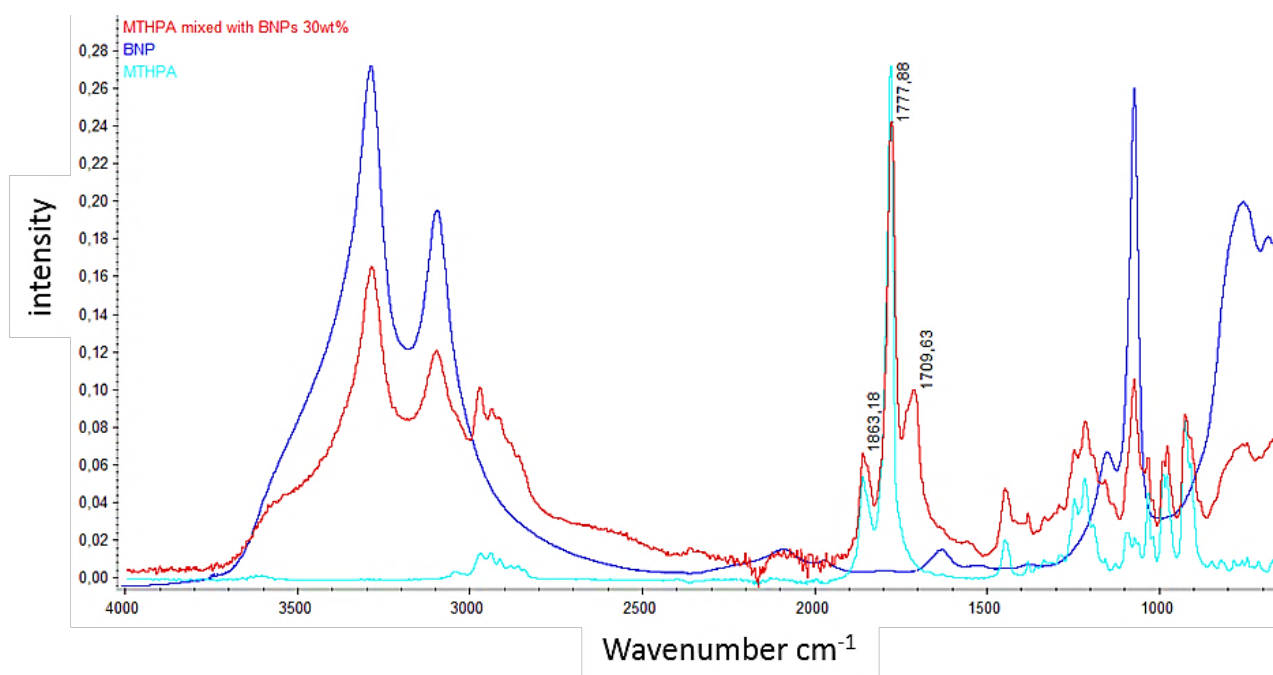
Fig. 15 Room temperature ATR-IR spectra of BNPs, anhydride hardener and the masterbatch mixture of BNPs and MTHPA.

List of main abbreviations and symbols

A	Area
a	Contact radius
A	amplitude
Å	Angstrom
ADFS	Amplitude dependence force spectroscopy
a_{DMT}	Contact radius calculated by DMT theory
AFM	atomic force microscopy
AFM-IR	AFM-infrared spectroscopy
a_{Hertz}	Contact radius calculated by Hertz theory
a_{JKR}	Contact radius calculated by JKR theory
AM	Amplitude modulation
ATR-IR	Attenuated total reflectance infrared spectroscopy
BDS	Broadband dielectric spectroscopy
BNPs	Boehmite nanoparticles
C	capacitance
CFRPs	carbon fiber-reinforced polymers
CNT	carbon nanotubes
d	density
d	diameter
D	deformation
d	deflection
DETA	diethylenetriamine
DGEBA	bisphenol A diglycidyl ether
DMTA	dynamic mechanical thermal analysis
DSC	as differential scanning calorimetry
E´	storage modulus
E´´	loss modulus
E_c	elastic modulus of the composite
E_{diss}	Energy dissipation
EDX	Energy dispersive X-ray spectroscopy
E_f	elastic modulus of the fiber
E_F	Fermi level energy
E_{FS}	Fermi level energy of the sample
E_{FT}	Fermi level energy of the tip
E_m	elastic modulus of the matrix
ESBO	epoxidized soy bean oil
E_{tot}	Reduced elastic modulus
F	force

f_0	resonance frequency
f_1	Intermodulation Drive 1 frequency
f_2	Intermodulation Drive 2 frequency
F_c	Cantilevers force
FDC	AFM force-distance curves
FDC	Force-distance curve
F_{drive}	Driving force
F_I	Conservative force
f_{IMP}	Frequency of intermodulation product
F_{JC}	Jump to contact force
FM	Frequency modulation
FMM	Force modulation microscopy
F_Q	Dissipative force
FT-IR	Fourier transform infrared spectroscopy
F_{ts}	Tip-sample force
FV	Force volume
G	Transfer function
G	shear modulus
$G*$	Complex shear modulus
G'	storage shear modulus
G''	loss shear modulus
G'	storage shear modulus
G_e	energetic part of modulus
GeoB	Geological boehmite
G_r	Shear modulus in the rubbery state
H-DGBEBA	hydrogenated DGEBA
HydBo	Hydrothermally synthesized boehmite
ImAFM	Intermodulation AFM
JC	Jump to contact
k	sample's spring constant
K_B	Boltzmann constant
k_c	Cantilever's spring constant
k_{eff}	effective spring constant
l	length
M_C	average molecular weight of chains between crosslink points
MDFEM	molecular-dynamic finite element method
MIR	mid-infrared spectroscopy
MPD	m-phenylenediamines
MTHPA	methyl tetrahydrophthalic anhydride
NIR	near-infrared spectroscopy
NMR	Nuclear magnetic resonance

NPs	nanoparticles
P	Power of oscillation
PDS	power density spectrum
PeakforceQNM	Peak Force quantitative nanomechanical mapping
PEEK	Polyether ether ketone
PFM-AFM	Pulsed force mode atomic force microscopy
PMMA	Poly (methyl methacrylate)
pN	Pico newton
PNCs	polymer nanocomposites
POSS	polyoctahedral silsesquioxanes
PVD	physical vapor deposition
Q	Cantilever's quality factor
QCL	Quantum cascade laser
R	gas constant
ROM	rule of mixture
S	stiffness
SFPO	single fiber pull-out tests
SKPM	scanning Kelvin Probe microscopy
T	(absolute) temperature
T_2	hydrogen spin-spin relaxation time
T_2^P	hydrogen spin-spin relaxation time plateau value
tan δ	damping ratio
TEM	Transmission electron microscopy
T_g	glass transition temperature (range)
TGA	Thermogravimetric analysis
T_m	melting temperature (range)
V	voltage
V_{AC}	AC voltage
V_{DC}	DC voltage
vdW	van der Waals
V_{sp}	Surface potential difference between tip and sample
W	Work of adhesion
W_{attr}	Work of attractive forces
W_{vdW}	van der Waals work
X_{NIR}	degree of conversion measured by NIR
XPS	x-ray photoelectron spectroscopy
XRD	X-ray diffraction
δ	cantilever's deflection
Δf	half power band width of the resonance peak

ΔH	reaction enthalpy
ΔH_R	residual enthalpy of post-curing
υ	crosslink density
υ_s	Poisson ratio of the sample
υ_{tip}	Poisson ratio of the tip
Φ	Work function
Φ_s	Work function of the sample
Φ_t	Work function of the tip
ω	frequency
ω_0	Resonance frequency
E	elastic modulus
Φ	front factor
Φ_f	volume fraction of the fiber
Φ_m	volume fraction of the matrix
ν_P	Poisson's ratio
ξ	shape parameter

References

[1]   F. Barthelat and R. Rabiei, "Toughness amplification in natural composites," *Journal of the Mechanics and Physics of Solids,* vol. 59, no. 4, pp. 829-840, 2011.

[2]   R. Cahn and B. Harris, "Newer forms of carbon and their uses," *Nature* vol. 221, no. 5176, p. 132, 1969.

[3]   C. Soutis, "Carbon fiber reinforced plastics in aircraft construction," *Materials Science and Engineering: A* vol. 412, no. 1-2, pp. 171-176, 2005.

[4]   R. Stewart, "Automotive composites offer lighter solutions," *Reinforced Plastics,* vol. 54, no. 2, pp. 22-28, 2010.

[5]   A. K. Naskar, J. K. Keum, and R. G. Boeman, "Polymer matrix nanocomposites for automotive structural components," *Nature nanotechnology* vol. 11, no. 12, p. 1026, 2016.

[6]   M. Bhattacharya, "Polymer nanocomposites—a comparison between carbon nanotubes, graphene, and clay as nanofillers," *Materials,* vol. 9, no. 4, p. 262, 2016.

[7]   J. Njuguna and K. Pielichowski, "Polymer nanocomposites for aerospace applications: properties," *Advanced Engineering Materials,* vol. 5, no. 11, pp. 769-778, 2003.

[8]   M. Naebe *et al.*, "Mechanical property and structure of covalent functionalised graphene/epoxy nanocomposites," *Scientific reports,* vol. 4, p. 4375, 2014.

[9]   B. K. Kim, J. W. Seo, and H. M. Jeong, "Morphology and properties of waterborne polyurethane/clay nanocomposites," *European Polymer Journal,* vol. 39, no. 1, pp. 85-91, 2003.

[10]   J. Karger-Kocsis and L. Lendvai, "Polymer/boehmite nanocomposites: A review," *Journal of Applied Polymer Science,* vol. 135, no. 24, 2017, doi: 10.1002/app.45573.

[11]   M. Jux, B. Finke, T. Mahrholz, M. Sinapius, A. Kwade, and C. Schilde, "Effects of Al (OH) O nanoparticle agglomerate size in epoxy resin on tension, bending, and fracture properties," *Journal of Nanoparticle Research,* vol. 19, no. 4, p. 139, 2017.

[12]   M. Jux, J. Fankhänel, B. Daum, T. Mahrholz, M. Sinapius, and R. Rolfes, "Mechanical properties of epoxy/boehmite nanocomposites in dependency of mass fraction and surface modification-An experimental and numerical approach," *Polymer,* 2018.

[13]   C. Arlt, "Wirkungsweisen nanoskaliger Böhmite in einem Polymer und seinem Kohlenstofffaserverbund unter Druckbelastung," Otto-von-Guericke Universität Magdeburg, 2011.

[14]   S. Duwe, C. Arlt, S. Aranda, U. Riedel, G. J. C. S. Ziegmann, and Technology, "A detailed thermal analysis of nanocomposites filled with SiO2, AlN or boehmite at varied contents and a review of selected rules of mixture," vol. 72, no. 12, pp. 1324-1330, 2012.

[15]   W. Exner, C. Arlt, T. Mahrholz, U. Riedel, and M. Sinapius, "Nanoparticles with various surface modifications as functionalized cross-linking agents for composite resin materials," *Composites Science and Technology,* vol. 72, no. 10, pp. 1153-1159, 2012.

[16]   P. Drescher, M. Thomas, J. Borris, U. Riedel, and C. Arlt, "Strengthening fibre/matrix interphase by fibre surface modification and nanoparticle incorporation into the matrix," *Composites Science and Technology,* vol. 74, pp. 60-66, 2013.

[17]   S. C. Ligon-Auer, M. Schwentenwein, C. Gorsche, J. Stampfl, and R. Liska, "Toughening of photo-curable polymer networks: a review," *Polymer Chemistry,* vol. 7, no. 2, pp. 257-286, 2016.

[18]   I. Hamerton, *Recent developments in epoxy resins.* iSmithers Rapra Publishing, 1996.

144

[19]   E. Dümichen *et al.*, "Analyzing the network formation and curing kinetics of epoxy resins by in situ near-infrared measurements with variable heating rates," *Thermochimica acta,* vol. 616, pp. 49-60, 2015.

[20]   X. Fernàndez-Francos, S. G. Kazarian, X. Ramis, and À. J. A. s. Serra, "Simultaneous monitoring of curing shrinkage and degree of cure of thermosets by attenuated total reflection Fourier transform infrared (ATR FT-IR) spectroscopy," vol. 67, no. 12, pp. 1427-1436, 2013.

[21]   S. T. Cholake *et al.*, "Quantitative analysis of curing mechanisms of epoxy resin by mid-and Near-Fourier transform Infra red Spectroscopy," *Defence Science Journal,* vol. 64, no. 3, pp. 314-321, 2014.

[22]   V. Trappe, W. Burchard, and B. Steinmann, "Anhydride-cured epoxies via chain reaction. 1. The phenyl glycidyl ether/phthalic acid anhydride system," *Macromolecules,* vol. 24, no. 17, pp. 4738-4744, 1991.

[23]   A. Mauri, N. Galego, C. Riccardi, and R. Williams, "Kinetic Model for Gelation in the Diepoxide− Cyclic Anhydride Copolymerization Initiated by Tertiary Amines," *Macromolecules,* vol. 30, no. 6, pp. 1616-1620, 1997.

[24]   X. Fernàndez-Francos, X. Ramis, and A. Serra, "From curing kinetics to network structure: A novel approach to the modeling of the network buildup of epoxy– anhydride thermosets," *Journal of Polymer Science Part A: Polymer Chemistry,* vol. 52, no. 1, pp. 61-75, 2014.

[25]   G. Lachenal, A. Pierre, and N. Poisson, "FT-NIR Spectroscopy: trends and application to the kinetic study of Epoxy/triamine system (Comparison with DSC and SEC Results)," *Micron,* vol. 27, no. 5, pp. 329-334, 1996.

[26]   K. Wudy and T. Budde, "Reaction kinetics and curing behavior of epoxies for use in a combined selective laser beam melting process of polymers," *Journal of Applied Polymer Science,* vol. 136, no. 7, p. 46850, 2019.

[27]   L. E. Nielsen, "Cross-linking–effect on physical properties of polymers," *Journal of Macromolecular Science, Part C,* vol. 3, no. 1, pp. 69-103, 1969.

[28]   P. Flory, "Principles of polymer chemistry Ithaca," *Cornell University,* 1953.

[29]   C. M. Ofner III and W. A. Bubnis, "Chemical and swelling evaluations of amino group crosslinking in gelatin and modified gelatin matrices," *Pharmaceutical research,* vol. 13, no. 12, pp. 1821-1827, 1996.

[30]   A. Kenyon and L. Nielsen, "Characterization of network structure of epoxy resins by dynamic mechanical and liquid swelling tests," *Journal of Macromolecular Science— Chemistry,* vol. 3, no. 2, pp. 275-295, 1969.

[31]   A. Mujtaba *et al.*, "Mechanical properties and cross-link density of styrene–butadiene model composites containing fillers with bimodal particle size distribution," *Macromolecules,* vol. 45, no. 16, pp. 6504-6515, 2012.

[32]   C. G. Fry and A. C. Lind, "Determination of crosslink density in thermoset polymers by use of solid-state proton NMR techniques," *Macromolecules,* vol. 21, no. 5, pp. 1292-1297, 1988.

[33]   H. Heinze, K. Schmieder, G. Schnell, and K. Wolf, "The Temperature Shift of the Second Order Transition of Natural Rubber by Crosslinking," *Rubber Chemistry and Technology,* vol. 35, no. 3, pp. 776-793, 1962.

[34]   E. DiMarzio and J. J. J. R. N. B. S. A. Gibbs, "On the second-order transition of a rubber," *Res. Nat. Bur. Stand. A* vol. 68, pp. 611-617, 1964.

[35]   M. Rubinstein and R. H. Colby, *Polymer physics*. Oxford University Press New York, 2003.

[36]   G. Levita, S. De Petris, A. Marchetti, and A. Lazzeri, "Crosslink density and fracture toughness of epoxy resins," *Journal of materials science,* vol. 26, no. 9, pp. 2348-2352, 1991.

[37]   W. Stark, "Investigation of the curing behaviour of carbon fibre epoxy prepreg by Dynamic Mechanical Analysis DMA," *Polymer Testing,* vol. 32, no. 2, pp. 231-239, 2013.

[38]   H. Kishi, T. Naitou, S. Matsuda, A. Murakami, Y. Muraji, and Y. Nakagawa, "Mechanical properties and inhomogeneous nanostructures of dicyandiamide-cured epoxy resins," *Journal of Polymer Science Part B: Polymer Physics,* vol. 45, no. 12, pp. 1425-1434, 2007.

[39]   M. Drumm, C. Dodge, and L. Nielsen, "Cross Linking of a Phenol-Formaldehyde Novolac-Determiantion by Dynamic-Mechanical Measurements," *Industrial Engineering Chemistry,* vol. 48, no. 1, pp. 76-81, 1956.

[40]   J. Kalantar and L. Drzal, "The bonding mechanism of aramid fibres to epoxy matrices," *Journal of materials science,* vol. 25, no. 10, pp. 4186-4193, 1990.

[41]   T. Ionescu, V. Mavrantzas, D. J. Keffer, and B. Edwards, "Atomistic simulation of energetic and entropic elasticity in short-chain polyethylenes," *Journal of Rheology* vol. 52, no. 2, pp. 567-589, 2008.

[42]   G. Pohl, H. Goering, and D. Joel, "ON THE DETERMINATION OF NETWORK DENSITY IN POLYURETHANES," *Plaste und Kautschuk,* vol. 30, no. 4, pp. 196-200, 1983.

[43]   D. Edwards, "Polymer-filler interactions in rubber reinforcement," *Journal of Materials Science,* vol. 25, no. 10, pp. 4175-4185, 1990.

[44]   T. Zheng *et al.*, "Studies on Curing Kinetics and Tensile Properties of Silica-Filled Phenolic Amine/Epoxy Resin Nanocomposite," *Polymers,* vol. 11, no. 4, p. 680, 2019.

[45]   T. Jin-hua, L. Guo-qin, C. Huang, and S. Lin-jian, "Mechanical properties and thermal behaviour of LLDPE/MWNTs nanocomposites," *Materials Research,* vol. 15, no. 6, pp. 1050-1056, 2012.

[46]   B. P. Grady, *Carbon nanotube-polymer composites: manufacture, properties, and applications*. John Wiley & Sons, 2011.

[47]   M. A. Rafiee, J. Rafiee, Z. Wang, H. Song, Z.-Z. Yu, and N. Koratkar, "Enhanced mechanical properties of nanocomposites at low graphene content," *ACS nano,* vol. 3, no. 12, pp. 3884-3890, 2009.

[48]   M. Biswas and S. S. Ray, "Recent progress in synthesis and evaluation of polymer-montmorillonite nanocomposites," in *New polymerization techniques and synthetic methodologies*: Springer, 2001, pp. 167-221.

[49]   H. Zou, S. Wu, and J. Shen, "Polymer/silica nanocomposites: preparation, characterization, properties, and applications," *Chemical reviews,* vol. 108, no. 9, pp. 3893-3957, 2008.

[50]   Y. Sun, Z. Zhang, K. S. Moon, and C. Wong, "Glass transition and relaxation behavior of epoxy nanocomposites," *Journal of Polymer Science Part B: Polymer Physics,* vol. 42, no. 21, pp. 3849-3858, 2004.

[51]   M. K. Corbierre, N. S. Cameron, M. Sutton, K. Laaziri, and R. B. Lennox, "Gold nanoparticle/polymer nanocomposites: dispersion of nanoparticles as a function of capping agent molecular weight and grafting density," *Langmuir,* vol. 21, no. 13, pp. 6063-6072, 2005.

[52]   B. J. Ash, R. W. Siegel, and L. S. Schadler, "Mechanical behavior of alumina/poly (methyl methacrylate) nanocomposites," *Macromolecules,* vol. 37, no. 4, pp. 1358-1369, 2004.

[53] J. Halpin, "Stiffness and expansion estimates for oriented short fiber composites," *Journal of Composite Materials,* vol. 3, no. 4, pp. 732-734, 1969.

[54] T. Mori and K. Tanaka, "Average stress in matrix and average elastic energy of materials with misfitting inclusions," *Acta metallurgica,* vol. 21, no. 5, pp. 571-574, 1973.

[55] D. Paul and L. M. Robeson, "Polymer nanotechnology: nanocomposites," *Polymer,* vol. 49, no. 15, pp. 3187-3204, 2008.

[56] T. Fornes and D. R. Paul, "Modeling properties of nylon 6/clay nanocomposites using composite theories," *polymer,* vol. 44, no. 17, pp. 4993-5013, 2003.

[57] Y. Zare, "Development of Halpin-Tsai model for polymer nanocomposites assuming interphase properties and nanofiller size," *Polymer Testing,* vol. 51, pp. 69-73, 2016.

[58] R. Qiao and L. C. Brinson, "Simulation of interphase percolation and gradients in polymer nanocomposites," *Composites Science and Technology,* vol. 69, no. 3, pp. 491-499, 2009.

[59] L. H. Sharpe, "The interphase in adhesion," *The Journal of Adhesion,* vol. 4, no. 1, pp. 51-64, 1972.

[60] M. Piggott, "Tailored interphases in fibre reinforced polymers," *MRS Online Proceedings Library Archive* vol. 170, 1989.

[61] J. Williams, M. Donnellan, M. James, and W. Morris, "Properties of the interphase in organic matrix composites," *Materials Science and Engineering: A,* vol. 126, no. 1-2, pp. 305-312, 1990.

[62] J. Huang, C. He, X. Liu, J. Xu, C. S. Tay, and S. Y. Chow, "Organic–inorganic nanocomposites from cubic silsesquioxane epoxides: direct characterization of interphase, and thermomechanical properties," *Polymer,* vol. 46, no. 18, pp. 7018-7027, 2005.

[63] M. VanLandingham, R. Dagastine, R. Eduljee, R. McCullough, and J. J. C. P. A. a. s. Gillespie Jr, "Characterization of nanoscale property variations in polymer composite systems: 1. Experimental results," *Composites Part A: applied science and manufacturing,* vol. 30, no. 1, pp. 75-83, 1999.

[64] S. Yu, S. Yang, and M. Cho, "Multi-scale modeling of cross-linked epoxy nanocomposites," *Polymer,* vol. 50, no. 3, pp. 945-952, 2009.

[65] L. T. Drzal, "Composite Property Dependence on the Fiber, Matrix, and the Interphase," presented at the NASA. Langley Research Center Tough Composite Mater.; p. p 227-243, 1984.

[66] J. Chung, M. Munz, and H. Sturm, "Stiffness variation in the interphase of amine-cured epoxy adjacent to copper microstructures," *Surface and interface analysis,* vol. 39, no. 7, pp. 624-633, 2007.

[67] E. Mäder, K. Mai, and E. Pisanova, "Interphase characterization in polymer composites-monitoring of interphasial behavior in dependence on the mode of loading," *Composite Interfaces,* vol. 7, no. 3, pp. 133-147, 2000.

[68] K. Elabshihy, "Characterization of epoxy/copper interphases using nanoindentation," *Doctoral thesis,TU Berlin,* 2016.

[69] A. B. Pangelinan, "Surface induced molecular weight segregation in thermoplastic composites," 1992.

[70] J. Lesko, K. Jayaraman, and K. Reifsnider, "Gradient interphase regions in composite systems," in *Key Engineering Materials*, 1996, vol. 116: Trans Tech Publ, pp. 61-86.

[71] V. Gupta, L. Drzal, C. C. Lee, and M. Rich, "The temperature-dependence of some mechanical properties of a cured epoxy resin system," *Polymer Engineering & Science,* vol. 25, no. 13, pp. 812-823, 1985.

[72] L. T. Drzal, M. J. Rich, and P. F. Lloyd, "Adhesion of graphite fibers to epoxy matrices: I. The role of fiber surface treatment," *The Journal of Adhesion,* vol. 16, no. 1, pp. 1-30, 1983.

[73] A. Garton, W. T. Stevenson, and S. Wang, "Interfacial reactions in carbon—epoxy composites," *British polymer journal,* vol. 19, no. 5, pp. 459-467, 1987.

[74] E. Fitzer, K.-H. Geigl, W. Hüttner, and R. Weiss, "Chemical interactions between the carbon fibre surface and epoxy resins," *Carbon,* vol. 18, no. 6, pp. 389-393, 1980.

[75] S.-G. Hong and J.-S. Tsai, "The adsorption and curing behaviors of the epoxy/amidoamine system in the presence of metal oxides," *Journal of thermal analysis and calorimetry,* vol. 63, no. 1, pp. 31-46, 2001.

[76] J. Kelber, J. Rogers Jr, B. Banse, and B. Koel, "Interaction of dimethylamine with clean and partially oxidized copper surfaces," *Applied Surface Science,* vol. 44, no. 3, pp. 193-204, 1990.

[77] F. Boerio and D. Ondrus, "Effect of substrates on the structure of polymer interphases: II. Epoxyanhydride adhesives cured against aluminum and copper," *Journal of colloid interface science,* vol. 139, no. 2, pp. 446-456, 1990.

[78] Z. Wang, Z. Wang, H. Yu, L. Zhao, and J. Qu, "Controlled network structure and its correlations with physical properties of polycarboxyl octaphenylsilsesquioxanes-based inorganic–organic polymer nanocomposites," *RSC Advances,* vol. 2, no. 7, pp. 2759-2767, 2012.

[79] H. Wu and C. Claypool, "An analytical approach of the microbond test method used in characterizing the fibre-matrix interface," *Journal of Materials Science Letters,* vol. 10, no. 5, pp. 260-262, 1991.

[80] K. Mai, E. Mäder, and M. Mühle, "Interphase characterization in composites with new non-destructive methods," *Composites Part A: Applied Science Manufacturing,* vol. 29, no. 9-10, pp. 1111-1119, 1998.

[81] T. Bogetti, T. Wang, M. VanLandingham, and J. Gillespie Jr, "Characterization of nanoscale property variations in polymer composite systems: 2. Numerical modeling," *Composites Part A: applied science manufacturing,* vol. 30, no. 1, pp. 85-94, 1999.

[82] Z. Wang, Q. Lv, S. Chen, C. Li, S. Sun, and S. Hu, "Effect of Interfacial Bonding on Interphase Properties in SiO2/Epoxy Nanocomposite: A Molecular Dynamics Simulation Study," *ACS applied materials & interfaces,* vol. 8, no. 11, pp. 7499-7508, 2016.

[83] B. Cappella, H. Sturm, and S. Weidner, "Breaking polymer chains by dynamic plowing lithography," *Polymer,* vol. 43, no. 16, pp. 4461-4466, 2002.

[84] J. L. Hutter and J. Bechhoefer, "Calibration of atomic-force microscope tips," *Review of Scientific Instruments,* vol. 64, no. 7, pp. 1868-1873, 1993.

[85] T. R. Rodrıguez and R. García, "Theory of Q control in atomic force microscopy," *Applied Physics Letters,* vol. 82, no. 26, pp. 4821-4823, 2003.

[86] S. M. Walley, "Historical origins of indentation hardness testing," *Materials Science and Technology,* vol. 28, no. 9-10, pp. 1028-1044, 2012.

[87] P. M. Claesson *et al.*, "From force curves to surface nanomechanical properties," *Physical Chemistry Chemical Physics* vol. 19, no. 35, pp. 23642-23657, 2017.

[88] H.-J. Butt, B. Cappella, and M. Kappl, "Force measurements with the atomic force microscope: Technique, interpretation and applications," *Surface science reports,* vol. 59, no. 1, pp. 1-152, 2005.

[89] B. Cappella, S. K. Kaliappan, and H. Sturm, "Using AFM force− distance curves to study the glass-to-rubber transition of amorphous polymers and their elastic− plastic

properties as a function of temperature," *Macromolecules,* vol. 38, no. 5, pp. 1874-1881, 2005.

[90]   H. Hertz, "On the contact of elastic solids," *Reine Angew. Mathematik,* vol. 92, pp. 156-171, 1881.

[91]   K. L. Johnson, K. Kendall, and A. Roberts, "Surface energy and the contact of elastic solids," *Proceedings of the royal society of London. A. mathematical and physical sciences,* vol. 324, no. 1558, pp. 301-313, 1971.

[92]   B. V. Derjaguin, V. M. Muller, and Y. Toporov, "Effect of contact deformations on the adhesion of particles," *Journal of colloid and interface science,* vol. 53, no. 2, pp. 314-326, 1975.

[93]   M. Radmacher, J. P. Cleveland, M. Fritz, H. G. Hansma, and P. K. Hansma, "Mapping interaction forces with the atomic force microscope," *Biophysical journal,* vol. 66, no. 6, pp. 2159-2165, 1994.

[94]   S.-L. Gao, E. Mäder, and S. F. Zhandarov, "Carbon fibers and composites with epoxy resins: Topography, fractography and interphases," *Carbon,* vol. 42, no. 3, pp. 515-529, 2004.

[95]   S. Magonovº, V. Elings, and M. Whangbo, "Phase imaging and stiffness in tapping-mode atomic force microscopy," *Surface science,* vol. 375, pp. L385-L391, 1997.

[96]   H. U. Krotil, T. Stifter, H. Waschipky, K. Weishaupt, S. Hild, and O. Marti, "Pulsed force mode: a new method for the investigation of surface properties," *Surface and Interface Analysis,* vol. 27, no. 5-6, pp. 336-340, 1999.

[97]   B. Pittenger, N. Erina, and C. Su, "Quantitative mechanical property mapping at the nanoscale with PeakForce QNM," *Application Note Veeco Instruments Inc,* pp. 1-12, 2010.

[98]   T. Young, M. Monclus, T. Burnett, W. Broughton, S. Ogin, and P. Smith, "The use of the PeakForceTM quantitative nanomechanical mapping AFM-based method for high-resolution Young's modulus measurement of polymers," *Measurement Science and Technology,* vol. 22, no. 12, p. 125703, 2011.

[99]   P. Maivald *et al.*, "Using force modulation to image surface elasticities with the atomic force microscope," *Nanotechnology,* vol. 2, no. 2, p. 103, 1991.

[100]   M. Radmacher, R. Tillmann, and H. Gaub, "Imaging viscoelasticity by force modulation with the atomic force microscope," *Biophysical journal,* vol. 64, no. 3, pp. 735-742, 1993.

[101]   M. Munz, H. Sturm, E. Schulz, and G. Hinrichsen, "The scanning force microscope as a tool for the detection of local mechanical properties within the interphase of fibre reinforced polymers," *Composites Part A: Applied Science,* vol. 29, no. 9-10, pp. 1251-1259, 1998.

[102]   Parksystems. "Force Modulation Microscopy." https://www.parksystems.com/images/spmmodes/mechanical/Force-Modulation-Microscopy-(FMM).pdf

[103]   D. Platz, E. A. Tholén, D. Pesen, and D. B. Haviland, "Intermodulation atomic force microscopy," *Applied Physics Letters,* vol. 92, no. 15, p. 153106, 2008.

[104]   D. B. Haviland, "Quantitative force microscopy from a dynamic point of view," *Current Opinion in Colloid & Interface Science,* vol. 27, pp. 74-81, 2017.

[105]   D. Platz, D. Forchheimer, E. A. Tholén, and D. B. Haviland, "Interaction imaging with amplitude-dependence force spectroscopy," *Nature communications,* vol. 4, p. 1360, 2013.

[106]   M. Nonnenmacher, M. o'Boyle, and H. K. Wickramasinghe, "Kelvin probe force microscopy," *Applied physics letters,* vol. 58, no. 25, pp. 2921-2923, 1991.

[107] W. Melitz, J. Shen, A. C. Kummel, and S. Lee, "Kelvin probe force microscopy and its application," *Surface science reports,* vol. 66, no. 1, pp. 1-27, 2011.

[108] M. Rohwerder and F. Turcu, "High-resolution Kelvin probe microscopy in corrosion science: scanning Kelvin probe force microscopy (SKPFM) versus classical scanning Kelvin probe (SKP)," *Electrochimica Acta,* vol. 53, no. 2, pp. 290-299, 2007.

[109] A. Dazzi, R. Prazeres, F. Glotin, and J. Ortega, "Local infrared microspectroscopy with subwavelength spatial resolution with an atomic force microscope tip used as a photothermal sensor," *Optics letters,* vol. 30, no. 18, pp. 2388-2390, 2005.

[110] A. Dazzi, R. Prazeres, F. Glotin, and J. M. Ortega, "Subwavelength infrared spectromicroscopy using an AFM as a local absorption sensor," *Infrared physics & technology,* vol. 49(1-2), pp. 113-121, 2006.

[111] A. Dazzi, "Sub-100-nanometer infrared spectroscopy and imaging based on a near-field photothermal technique (PTIR)," *Biomedical Vibrational Spectroscopy,* pp. 291-312, 2008.

[112] A. Dazzi, C. B. Prater, Q. Hu, D. B. Chase, J. F. Rabolt, and C. Marcott, "AFM–IR: combining atomic force microscopy and infrared spectroscopy for nanoscale chemical characterization," *Applied spectroscopy,* vol. 66, 12, pp. 1365-1384, 2012.

[113] S. Morsch, Y. Liu, S. B. Lyon, and S. R. Gibbon, "Insights into epoxy network nanostructural heterogeneity using AFM-IR," *ACS applied materials & interfaces,* vol. 8, no. 1, pp. 959-966, 2015.

[114] S. Morsch, S. Lyon, P. Greensmith, S. Smith, and S. Gibbon, "Mapping water uptake in organic coatings using AFM-IR," *Faraday discussions,* vol. 180, pp. 527-542, 2015.

[115] A. Kyritsis *et al.*, "Polymer dynamics in epoxy/alumina nanocomposites studied by various techniques," *Journal of Applied Polymer Science,* vol. 121, no. 6, pp. 3613-3627, 2011.

[116] P. B. Messersmith and E. P. Giannelis, "Synthesis and characterization of layered silicate-epoxy nanocomposites," *Chemistry of materials,* vol. 6, no. 10, pp. 1719-1725, 1994.

[117] J. Brown, I. Rhoney, and R. A. Pethrick, "Epoxy resin based nanocomposites: 1. Diglycidylether of bisphenol A (DGEBA) with triethylenetetramine (TETA)," *Polymer International,* vol. 53, no. 12, pp. 2130-2137, 2004.

[118] E. Vassileva and K. Friedrich, "Epoxy/alumina nanoparticle composites. I. Dynamic mechanical behavior," *Journal of Applied Polymer Science,* vol. 89, no. 14, pp. 3774-3785, 2003.

[119] B. Wetzel, P. Rosso, F. Haupert, and K. Friedrich, "Epoxy nanocomposites–fracture and toughening mechanisms," *Engineering fracture mechanics,* vol. 73, no. 16, pp. 2375-2398, 2006.

[120] T. V. Kosmidou, A. Vatalis, C. Delides, E. Logakis, P. Pissis, and G. Papanicolaou, "Structural, mechanical and electrical characterization of epoxy-amine/carbon black nanocomposites," *Express Polymer Letters,* vol. 2, no. 5, pp. 364-372, 2008.

[121] O. Zabihi, M. Ahmadi, and M. Naebe, "One-pot synthesis of aminated multi-walled carbon nanotube using thiol-ene click chemistry for improvement of epoxy nanocomposites properties," *RSC Advances,* vol. 5, no. 119, pp. 98692-98699, 2015.

[122] H. Miyagawa and L. T. Drzal, "Thermo-physical and impact properties of epoxy nanocomposites reinforced by single-wall carbon nanotubes," *Polymer,* vol. 45, no. 15, pp. 5163-5170, 2004.

[123] A. Yasmin, J. Luo, J. Abot, and I. M. Daniel, "Mechanical and thermal behavior of clay/epoxy nanocomposites," *Composites Science and Technology,* vol. 66, no. 14, pp. 2415-2422, 2006.

[124] S. B. Sinnott, "Chemical functionalization of carbon nanotubes," *Journal of Nanoscience and Nanotechnology,* vol. 2, no. 2, pp. 113-123, 2002.

[125] Sasol, "Dispersal HP14," *Brunsbüttel, Germany,* 2014.

[126] T. S. Halbach and R. Mülhaupt, "Boehmite-based polyethylene nanocomposites prepared by in-situ polymerization," *Polymer,* vol. 49, no. 4, pp. 867-876, 2008.

[127] T. S. Halbach, Y. Thomann, and R. Mülhaupt, "Boehmite nanorod-reinforced-polyethylenes and ethylene/1-octene thermoplastic elastomer nanocomposites prepared by in situ olefin polymerization and melt compounding," *Journal of Polymer Science Part A: Polymer Chemistry,* vol. 46, no. 8, pp. 2755-2765, 2008.

[128] W. Brostow, T. Datashvili, B. Huang, and J. Too, "Tensile properties of LDPE+ boehmite composites," *Polymer Composites,* vol. 30, no. 6, pp. 760-767, 2009.

[129] W. Brostow, T. Datashvili, D. Kao, and J. Too, "Tribological properties of LDPE+ boehmite composites," *Polymer Composites,* vol. 31, no. 3, pp. 417-425, 2010.

[130] P. Blaszczak, W. Brostow, T. Datashvili, and H. E. H. Lobland, "Rheology of low-density polyethylene+ Boehmite composites," *Polymer composites,* vol. 31, no. 11, pp. 1909-1913, 2010.

[131] R. C. Streller, R. Thomann, O. Torno, and R. Mülhaupt, "Morphology, crystallization behavior, and mechanical properties of isotactic poly (propylene) nanocomposites based on organophilic boehmites," *Macromolecular Materials Engineering,* vol. 294, no. 6-7, pp. 380-388, 2009.

[132] Y. Cai, M. Zhao, H. Wang, Y. Li, and Z. Zhao, "Synthesis and properties of flame-retardant poly (vinyl alcohol)/pseudo-boehmite nanocomposites with high transparency and enhanced refractive index," *Polymer degradation and stability,* vol. 99, pp. 53-60, 2014.

[133] C. Özdilek, K. Kazimierczak, D. van der Beek, and S. J. Picken, "Preparation and properties of polyamide-6-boehmite nanocomposites," *Polymer,* vol. 45, no. 15, pp. 5207-5214, 2004.

[134] V. M. Khumalo, J. Karger-Kocsis, and R. Thomann, "Polyethylene/synthetic boehmite alumina nanocomposites: structure, thermal and rheological properties," *Express Polym Lett,* vol. 4, no. 5, pp. 264-274, 2010.

[135] V. Khumalo, J. Karger-Kocsis, and R. Thomann, "Polyethylene/synthetic boehmite alumina nanocomposites: structure, mechanical, and perforation impact properties," *Journal of Materials Science,* vol. 46, no. 2, pp. 422-428, 2011.

[136] G. Droval, I. Aranberri, J. Ballestero, M. Verelst, and J. Dexpert-Ghys, "Synthesis and characterization of thermoplastic composites filled with γ-boehmite for fire resistance," *Fire and Materials,* vol. 35, no. 7, pp. 491-504, 2011.

[137] E. S. Ogunniran, R. Sadiku, S. Sinha Ray, and N. Luruli, "Morphology and thermal properties of compatibilized PA12/PP blends with boehmite alumina nanofiller inclusions," *Macromolecular Materials and Engineering,* vol. 297, no. 7, pp. 627-638, 2012.

[138] E. S. Ogunniran, R. Sadiku, S. Sinha Ray, and N. Luruli, "Effect of boehmite alumina nanofiller incorporation on the morphology and thermal properties of functionalized poly (propylene)/polyamide 12 blends," *Macromolecular Materials and Engineering,* vol. 297, no. 3, pp. 237-248, 2012.

[139] D. Pedrazzoli, V. Khumalo, J. Karger-Kocsis, and A. Pegoretti, "Thermal, viscoelastic and mechanical behavior of polypropylene with synthetic boehmite alumina nanoparticles," *Polymer testing,* vol. 35, pp. 92-100, 2014.

[140] D. Pedrazzoli, F. Tuba, V. Khumalo, A. Pegoretti, and J. Karger-Kocsis, "Mechanical and rheological response of polypropylene/boehmite nanocomposites," *Journal of Reinforced Plastics and Composites,* vol. 33, no. 3, pp. 252-265, 2014.

[141] J. Karger-Kocsis, V. Khumalo, T. Bárány, L. Mészáros, and A. Pegoretti, "On the toughness of thermoplastic polymer nanocomposites as assessed by the essential work of fracture (EWF) approach," *Composite Interfaces,* vol. 20, no. 6, pp. 395-404, 2013.

[142] R. El Hage, A. Viretto, R. Sonnier, L. Ferry, and J.-M. Lopez-Cuesta, "Flame retardancy of ethylene vinyl acetate (EVA) using new aluminum-based fillers," *Polymer degradation and stability,* vol. 108, pp. 56-67, 2014.

[143] J. Zhang, Q. Ji, P. Zhang, Q. Kong, and Y. Xia, "Preparation and Characterization of Poly (ethylene Terephthalate)/Boehmite Nanocomposites," *Polymers & Polymer Composites,* vol. 19, no. 6, p. 469, 2011.

[144] T. Sun, Z. Wu, Q. Zhuo, X. Liu, Z. Wang, and H. Fan, "Surface functionalized boehmite sheets filled epoxy composites with enhanced mechanical and thermal properties," *Polymers for Advanced Technologies* vol. 25, no. 12, pp. 1604-1609, 2014.

[145] Z. Wu, Q. Zhuo, T. Sun, and Z. Wang, "Mechanical properties of epoxy resins reinforced with synthetic boehmite (AlOOH) nanosheets," *Journal of Applied Polymer Science,* vol. 132, no. 5, 2015.

[146] N. Shahid, R. G. Villate, and A. R. Barron, "Chemically functionalized alumina nanoparticle effect on carbon fiber/epoxy composites," *Composites Science and Technology,* vol. 65, no. 14, pp. 2250-2258, 2005.

[147] C. Esposito Corcione and M. Frigione, "Cure kinetics and physical characterization of epoxy/modified boehmite nanocomposites," *Journal of adhesion science* vol. 31, no. 6, pp. 645-662, 2017.

[148] I. Topolniak, V.-D. Hodoroaba, D. Pfeifer, U. Braun, and H. Sturm, "Boehmite Nanofillers in Epoxy Oligosiloxane Resins: Influencing the Curing Process by Complex Physical and Chemical Interactions," *Materials,* vol. 12, no. 9, p. 1513, 2019.

[149] M. Sangermano, F. Deorsola, D. Fabiani, G. Montanari, and G. Rizza, "Epoxy-boehmite nanocomposites as new insulating materials," *Journal of applied polymer science,* vol. 114, no. 4, pp. 2541-2546, 2009.

[150] D. Abliz, T. Jürgens, T. Artys, and G. Ziegmann, "Cure kinetics and rheology modelling of boehmite (AlOOH) nanoparticle modified epoxy resin systems," *Thermochimica acta,* vol. 669, pp. 30-39, 2018.

[151] X. Bokhimi, J. Toledo-Antonio, M. Guzman-Castillo, and F. Hernandez-Beltran, "Relationship between crystallite size and bond lengths in boehmite," *Journal of Solid State Chemistry,* vol. 159, no. 1, pp. 32-40, 2001.

[152] A. Kiss, G. Keresztury, and L. Farkas, "Raman and ir spectra and structure of boehmite (γ-AlOOH). Evidence for the recently discarded D172h space group," *Spectrochimica Acta Part A: Molecular Spectroscopy,* vol. 36, no. 7, pp. 653-658, 1980.

[153] D. Tunega, H. Pašalić, M. Gerzabek, and H. Lischka, "Theoretical study of structural, mechanical and spectroscopic properties of boehmite (γ-AlOOH)," *Journal of Physics: Condensed Matter,* vol. 23, no. 40, p. 404201, 2011.

[154] Y. Noel, R. Demichelis, F. Pascale, P. Ugliengo, R. Orlando, and R. Dovesi, "Ab initio quantum mechanical study of γ-AlOOH boehmite: structure and vibrational spectrum," *Physics and Chemistry of Minerals,* vol. 36, no. 1, pp. 47-59, 2009.

[155] R. C. Streller, "Boehmite als Nanofüllstoffe für Polypropylen-Nanocomposites und Nanopartikel-modifizierte Polypropylen/Kautschuk-Blends," *Freiburg: Albert-Ludwigs-Universitaet Freiburg im Breisgau,* 2008.

[156] M. Digne, P. Sautet, P. Raybaud, H. Toulhoat, and E. Artacho, "Structure and stability of aluminum hydroxides: a theoretical study," *The Journal of Physical Chemistry B,* vol. 106, no. 20, pp. 5155-5162, 2002.

[157] Jmol, "an open-source Java viewer for chemical structures in 3D," *http://www.jmol.org/.*

[158] J. Q. Wang, J. L. Liu, X. Y. Liu, M. H. Qiao, Y. Pei, and K. N. Fan, "Hydrothermal transformation of bayerite to boehmite," *Science of Advanced Materials,* vol. 1, no. 1, pp. 77-85, 2009.

[159] C. Doss and R. Zallen, "Raman studies of sol-gel alumina: finite-size effects in nanocrystalline AlO (OH)," *Physical Review B,* vol. 48, no. 21, p. 15626, 1993.

[160] K. Okada, T. Nagashima, Y. Kameshima, A. Yasumori, and T. Tsukada, "Relationship between formation conditions, properties, and crystallite size of boehmite," *Journal of colloid and interface science,* vol. 253, no. 2, pp. 308-314, 2002.

[161] D. Silbernagl and B. Cappella, "Reconstruction of a hidden topography by single AFM force–distance curves," *Surface Science,* vol. 603, no. 16, pp. 2363-2369, 2009.

[162] J. Fankhänel *et al.*, "Mechanical Properties of Boehmite Evaluated by Atomic Force Microscopy Experiments and Molecular Dynamic Finite Element Simulations," *Journal of Nanomaterials,* vol. 2016, 2016.

[163] T. Kruckenberg and R. Paton, *Resin transfer moulding for aerospace structures.* Springer Science & Business Media, 2012.

[164] C. May, *Epoxy resins: chemistry and technology.* CRC press, 1987.

[165] B. C. Kim and S. W. Park, "Fracture toughness of the nano-particle reinforced epoxy composite," *Composite structures,* vol. 86, no. 1-3, pp. 69-77, 2008.

[166] K. W. Putz, M. J. Palmeri, R. B. Cohn, R. Andrews, and L. C. Brinson, "Effect of cross-link density on interphase creation in polymer nanocomposites," *Macromolecules,* vol. 41, no. 18, pp. 6752-6756, 2008.

[167] C. D. Wood, A. Ajdari, C. W. Burkhart, K. W. Putz, and L. C. Brinson, "Understanding competing mechanisms for glass transition changes in filled elastomers," *Composites Science and Technology,* vol. 127, pp. 88-94, 2016.

[168] O. Zabihi, M. Aghaie, and K. Zare, "Study on a novel thermoset nanocomposite form DGEBA–cycloaliphatic diamine and metal nanoparticles," *Journal of thermal analysis and calorimetry,* vol. 111, no. 1, pp. 703-710, 2013.

[169] M. Abdalla, D. Dean, D. Adibempe, E. Nyairo, P. Robinson, and G. Thompson, "The effect of interfacial chemistry on molecular mobility and morphology of multiwalled carbon nanotubes epoxy nanocomposite," *Polymer,* vol. 48, no. 19, pp. 5662-5670, 2007.

[170] V. D. Hodoroaba, S. Rades, and W. Unger, "Inspection of morphology and elemental imaging of single nanoparticles by high-resolution SEM/EDX in transmission mode," *Surface and interface analysis,* vol. 46, no. 10-11, pp. 945-948, 2014.

[171] J. Chung, M. Munz, and H. Sturm, "Amine-cured epoxy surface morphology and interphase with copper: an approach employing electron beam lithography and scanning force microscopy," *Journal of adhesion science and technology,* vol. 19, no. 13-14, pp. 1263-1276, 2005.

[172] K. Dušek, "Are cured thermoset resins inhomogeneous?," *Die Angewandte Makromolekulare Chemie: Applied Macromolecular Chemistry and Physics,* vol. 240, no. 1, pp. 1-15, 1996.

[173] M. Ghasem Zadeh Khorasani, D. Silbernagl, D. Platz, and H. sturm, "Insights into nano-scale physical and mechanical properties of epoxy/boehmite nanocomposite using different AFM modes," *to be published*.

[174] H. Huang, "Local surface mechanical properties of PDMS-silica nanocomposite probed with Intermodulation AFM," 2017.

[175] H. Ishida and D. J. Allen, "Mechanical characterization of copolymers based on benzoxazine and epoxy," *Polymer,* vol. 37, no. 20, pp. 4487-4495, 1996.

[176] M. Sharifi, C. Jang, C. Abrams, and G. Palmese, "Toughened epoxy polymers via rearrangement of network topology," *Journal of Materials Chemistry A,* vol. 2, no. 38, pp. 16071-16082, 2014.

[177] A. Seidel, *Characterization and analysis of polymers*. John Wiley & Sons, 2008.

[178] N. Amdouni, H. Sautereau, J.-F. Gerard, and J.-P. Pascault, "Epoxy networks based on dicyandiamide: effect of the cure cycle on viscoelastic and mechanical properties," *Polymer,* vol. 31, no. 7, pp. 1245-1253, 1990.

[179] M. Ghasem Zadeh khorasani, D. Silbernagl, A. M. Elert, and H. Sturm, "Interphase investigations on 2-D model sample of epoxy-boehmite nanocomposite using AFM-based approaches.," 2018(to be published).

[180] M. Morell, X. Ramis, F. Ferrando, Y. Yu, and A. Serra, "New improved thermosets obtained from DGEBA and a hyperbranched poly (ester-amide)," *Polymer,* vol. 50, no. 23, pp. 5374-5383, 2009.

[181] W. Chen *et al.*, "Interfacial structure and performance of rubber/boehmite nanocomposites modified by methacrylic acid," *Polymer,* vol. 52, no. 19, pp. 4387-4395, 2011.

[182] J. Karger-Kocsis and L. Lendvai, "Polymer/boehmite nanocomposites: A review," *Journal of Applied Polymer Science*.

[183] E. Voyiatzis, M. Rahimi, F. Müller-Plathe, and M. C. Böhm, "How thick is the polymer interphase in nanocomposites? Probing it by local stress anisotropy and gas solubility," *Macromolecules* vol. 47, no. 22, pp. 7878-7889, 2014.

[184] A. P. Holt *et al.*, "Dynamics at the polymer/nanoparticle interface in poly (2-vinylpyridine)/silica nanocomposites," *Macromolecules,* vol. 47, no. 5, pp. 1837-1843, 2014.

[185] H. Hu, L. Onyebueke, and A. Abatan, "Characterizing and modeling mechanical properties of nanocomposites-review and evaluation," *Journal of minerals and materials characterization and engineering,* vol. 9, no. 04, p. 275, 2010.

[186] P. J. Purohit, D.-Y. Wang, A. Wurm, C. Schick, and A. Schönhals, "Comparison of thermal and dielectric spectroscopy for nanocomposites based on polypropylene and layered double hydroxide–proof of interfaces," *European Polymer Journal,* vol. 55, pp. 48-56, 2014.

[187] P. Schmutz and G. Frankel, "Corrosion study of AA2024-T3 by scanning kelvin probe force microscopy and in situ atomic force microscopy scratching," *Journal of the Electrochemical Society* vol. 145, no. 7, pp. 2295-2306, 1998.

[188] M. Salerno and S. Dante, "Scanning Kelvin Probe Microscopy: Challenges and Perspectives towards Increased Application on Biomaterials and Biological Samples," *Materials,* vol. 11, no. 6, p. 951, 2018.

[189] M. J. Cadena, R. G. Reifenberger, and A. Raman, "High resolution subsurface imaging using resonance-enhanced detection in 2nd-harmonic KPFM," *Nanotechnology,* vol. 29, no. 40, p. 405702, 2018.

[190] D. Platz, D. Forchheimer, E. A. Tholén, and D. B. J. B. j. o. n. Haviland, "Interpreting motion and force for narrow-band intermodulation atomic force microscopy," *Beilstein Journal of Nanotechnology* vol. 4, p. 45, 2013.

[191] L. Kelvin, "V. Contact electricity of metals," *Dublin Philosophical Magazine Journal of Science,* vol. 46, no. 278, pp. 82-120, 1898.

[192] O. A. Castañeda-Uribe, R. Reifenberger, A. Raman, and A. J. A. n. Avila, "Depth-sensitive subsurface imaging of polymer nanocomposites using second harmonic Kelvin probe force microscopy," vol. 9, no. 3, pp. 2938-2947, 2015.

[193] J. L. Racich and J. A. Koutsky, "Nodular structure in epoxy resins," *Journal of Applied Polymer Science,* vol. 20, no. 8, pp. 2111-2129, 1976.

[194] K. Dušek, J. Pleštil, F. Lednický, and S. Luňák, "Are cured epoxy resins inhomogeneous?," *Polymer,* vol. 19, no. 4, pp. 393-397, 1978.

[195] J. Affdl and J. Kardos, "The Halpin-Tsai equations: a review," *Polymer Engineering & Science,* vol. 16, no. 5, pp. 344-352, 1976.

[196] G. Camino, A. Maffezzoli, M. Braglia, M. De Lazzaro, M. Zammarano, and Stability, "Effect of hydroxides and hydroxycarbonate structure on fire retardant effectiveness and mechanical properties in ethylene-vinyl acetate copolymer," *Polymer Degradation,* vol. 74, no. 3, pp. 457-464, 2001.

[197] E. Wawrzyn, B. Schartel, A. Karrasch, C. Jäger, and stability, "Flame-retarded bisphenol A polycarbonate/silicon rubber/bisphenol A bis (diphenyl phosphate): Adding inorganic additives," *Polymer degradation,* vol. 106, pp. 74-87, 2014.

[198] A. Laachachi, M. Ferriol, M. Cochez, J.-M. L. Cuesta, D. Ruch, and Stability, "A comparison of the role of boehmite (AlOOH) and alumina (Al2O3) in the thermal stability and flammability of poly (methyl methacrylate)," *Polymer Degradation,* vol. 94, no. 9, pp. 1373-1378, 2009.

[199] C. T. Vogelson, Y. Koide, L. B. Alemany, and A. R. Barron, "Inorganic− organic hybrid and composite resin materials using carboxylate-alumoxanes as functionalized cross-linking agents," *Chemistry of materials,* vol. 12, no. 3, pp. 795-804, 2000.

[200] M. Ghasem Zadeh Khorasani, D. Silbernagl, D. Platz, and H. Sturm, "Insights into nano-scale physical and mechanical properties of epoxy/boehmite nanocomposite using different AFM modes," *Polymers,* vol. 11, no. 2, p. 235, 2019.

[201] M. G. Z. Khorasani, D. Silbernagl, P. Szymoniak, V.-D. Hodoroaba, and H. Sturm, "The effect of boehmite (AlOOH) on nanomechanical and thermomechanical properties correlated to crosslinking density of epoxy in epoxy/boehmite nanocomposites," *Polymer,* vol. 164, pp. 174-182, 2019.

[202] T. V. Ndoro, M. C. Böhm, and F. Müller-Plathe, "Interface and interphase dynamics of polystyrene chains near grafted and ungrafted silica nanoparticles," *Macromolecules,* vol. 45, no. 1, pp. 171-179, 2011.

[203] M. Munz, B. Cappella, H. Sturm, M. Geuss, and E. Schulz, "Materials contrasts and nanolithography techniques in scanning force microscopy (SFM) and their application to polymers and polymer composites," in *Filler-Reinforced Elastomers/Sanning Force Microscopy*: Springer, 2003, pp. 87-210.

[204] J. Fankhänel, A. Kempe, and R. Rolfes, "Simulating atomic force microscopy for the determination of the elastic properties of nanoparticle reinforced epoxy resin," in *Proceedings of the 7th European Congress on Computational Methods in Applied Sciences and Engineering (ECCOMAS Congress' 16)*, 2016.

[205] R. Hart, "A study of boehmite formation on aluminium surfaces by electron diffraction," *Transactions of the Faraday Society*

vol. 50, pp. 269-273, 1954.

[206] R. Harrington and H. Nelson, "An electron diffraction study of anodic films," *Trans. Am. Inst. Min. Metall. Pet. Eng,* vol. 137, p. 62, 1940.

[207] J. Bryan, "The action of boiling distilled water on aluminium," *Journal of the Society of Chemical Industry,* vol. 69, no. 6, pp. 169-173, 1950.

[208] X. Zhang *et al.*, "Size and Morphology Controlled synthesis of boehmite nanoplates and crystal growth mechanisms," *Crystal Growth Design,* vol. 18, no. 6, pp. 3596-3606, 2018.

[209] A. Kocjan, A. Dakskobler, and T. Kosmac, "Superhydrophobic nanostructured boehmite coatings prepared by AlN powder hydrolysis," *International Journal of Applied Ceramic Technology,* vol. 8, no. 4, pp. 848-853, 2011.

[210] V.-D. Hodoroaba, C. Motzkus, T. Macé, and S. Vaslin-Reimann, "Performance of high-resolution SEM/EDX systems equipped with transmission mode (TSEM) for imaging and measurement of size and size distribution of spherical nanoparticles," *Microscopy and Microanalysis,* vol. 20, no. 2, pp. 602-612, 2014.

[211] H.-J. J. B. J. Butt, "Measuring electrostatic, van der Waals, and hydration forces in electrolyte solutions with an atomic force microscope," vol. 60, no. 6, pp. 1438-1444, 1991.

[212] A. Rosa-Zeiser, E. Weilandt, S. Hild, O. J. M. S. Marti, and Technology, "The simultaneous measurement of elastic, electrostatic and adhesive properties by scanning force microscopy: pulsed-force mode operation," vol. 8, no. 11, p. 1333, 1997.

[213] J. J. Fripiat, H. J. Bosmans, and P. G. J. T. J. o. P. C. Rouxhet, "Proton mobility in solids. I. Hydrogenic vibration modes and proton delocalization in boehmite," vol. 71, no. 4, pp. 1097-1111, 1967.

[214] R. Borgani, L. K. Pallon, M. S. Hedenqvist, U. W. Gedde, and D. B. Haviland, "Local charge injection and extraction on surface-modified Al2O3 nanoparticles in LDPE," *Nano letters,* vol. 16, no. 9, pp. 5934-5937, 2016.

[215] T. Giesa, M. Arslan, N. M. Pugno, and M. J. Buehler, "Nanoconfinement of spider silk fibrils begets superior strength, extensibility, and toughness," *Nano letters,* vol. 11, no. 11, pp. 5038-5046, 2011.

[216] M. A. Meyers, P.-Y. Chen, A. Y.-M. Lin, and Y. Seki, "Biological materials: structure and mechanical properties," *Progress in Materials Science,* vol. 53, no. 1, pp. 1-206, 2008.

[217] P. Fratzl, H. S. Gupta, F. D. Fischer, and O. Kolednik, "Hindered crack propagation in materials with periodically varying Young's modulus—lessons from biological materials," *Advanced Materials,* vol. 19, no. 18, pp. 2657-2661, 2007.

[218] J. Shen, D. Zhang, F.-H. Zhang, and Y. Gan, "AFM tip-sample convolution effects for cylinder protrusions," *Applied Surface Science,* vol. 422, pp. 482-491, 2017.

[219] J. T. Kloprogge, L. V. Duong, B. J. Wood, and R. L. Frost, "XPS study of the major minerals in bauxite: gibbsite, bayerite and (pseudo-) boehmite," *Journal of colloid and interface Science,* vol. 296, no. 2, pp. 572-576, 2006.